Tissue Interaction and Spatial Pattern Formation

Gerhard C. Cruywagen

Lincoln College
Oxford

A thesis submitted in partial fulfilment of the requirements for the degree of Doctor of Philosophy at the University of Oxford

Trinity Term 1992

Abstract

Gerhard C. Cruywagen, Lincoln College, Oxford.
A thesis submitted in partial fulfilment of the requirements for
the degree of Doctor of Philosophy at the University of Oxford.
Trinity Term 1992.

Tissue Interaction and Spatial Pattern Formation

The development of spatial structure and form on vertebrate skin is a complex and poorly understood phenomenon. We consider here a new mechanochemical tissue interaction model for generating vertebrate skin patterns. Tissue interaction, which plays a crucial role in vertebrate skin morphogenesis, is modelled by reacting and diffusing signal morphogens. The model consists of seven coupled partial differential equations, one each for dermal and epidermal cell densities, four for the signal morphogen concentrations and one for describing epithelial mechanics. Because of its complexity, we reduce the full model to a small strain quasi-steady-state model, by making several simplifying assumptions.

A steady state analysis demonstrates that our reduced system possesses stable time-independent steady state solutions on one-dimensional spatial domains. A linear analysis combined with a multiple time-scale perturbation procedure and numerical simulations are used to examine the range of patterns that the model can exhibit on both one- and two-dimensions domains. Spatial patterns, such as rolls, squares, rhombi and hexagons, which are remarkably similar to those observed on vertebrate skin, are obtained.

Although much of the work on pattern formation is concerned with synchronous spatial patterning, many structures on vertebrate skin are laid down in a sequential fashion. Our tissue interaction model can account for such sequential pattern formation. A linear analysis and a regular perturbation analysis is used to examine propagating epithelial contraction waves coupled to dermal cell invasion waves. The results compare favourably with those obtained from numerical simulations of the model. Furthermore, sequential pattern formation on one-dimensional domains is analysed; first by an asymptotic technique, and then by a new method involving the envelopes of the spatio-temporal propagating solutions. Both methods provide analytical estimates for the speeds of the wave of propagating pattern which are in close agreement with those obtained numerically. Finally, by numerical simulations, we show that our tissue interaction model can account for two-dimensional sequential pattern formation. In particular, we show that complex two-dimensional patterns can be determined by simple quasi-one-dimensional patterns.

Acknowledgements

I begin by expressing my sincere gratitude to my two supervisors. Firstly, I thank Prof. J.D. Murray, FRS, who introduced me to biological pattern formation. Without his enthusiasm and encouragement this thesis would never have come into existence. Secondly, I thank Dr. P.K. Maini for his advice and comments, especially during the second part of my research. His patience and sense of humour during the many fruitful discussions we had were a great source of motivation. I am also grateful to Dr. P. Grindrod whose helpful ideas and comments made the work in Chapter 6 possible.

I am indebted to the Rhodes Trust, Oxford, not only for their financial funding but also for their continual moral support. I would furthermore like to express my gratitude to the South African Foundation for Research Development for their financial assistance, as well as Lincoln College and the Mathematical Institute for providing various travel and book grants.

My thanks also go to my fellow graduate students, including Debbie Benson, Dr. Daniel Bentil, Dr. Meghan Burke, Vivi Carstensen, Mark Groves, Dr. Mark Lewis, Gideon Ngwa, Robert Payne, Joe Pitt-Francis, Faustino Sanchez-Garduno and Dr. Jonathan Sherratt who have made the Centre for Mathematical Biology such an enjoyable and productive place to work in. I learned much from talking to the many visitors the Centre had, in particular I thank Dr. Wendy Brandts and Dr. James Sneyd.

Finally, I must thank my parents and family for their continual interest, support and encouragement throughout the past three years.

What has been achieved is but the first step; we still stand in the presence riddles, but not without hope of solving them. And riddles with the hope of solution — what more can a scientist desire.

H. Spemann (1927)

Contents

Introduction

The development of a multicellular organism from a single initial cell is one of the most intriguing phenomena in the natural sciences. From this initial cell springs forth a complete well organized entity consisting of a variety of organs and tissue types. How the embryonic cells become ordered into a collection of spatial structures and forms, a process called morphogenesis, is one of the central issues in developmental biology.

Genes play a crucial role in initiating development and in acting as precursors to pattern formation processes, but genetics, alone, cannot explain the actual mechanisms involved in producing pattern and structure. It is clear that a complex interaction of chemical, mechanical and electrical phenomena underlies the process of morphogenesis.

The exact mechanisms governing pattern formation are not well understood and differ from organism to organism and from organ to organ. We examine here the organization and formation of structure on the vertebrate skin as one example of the various pattern formation processes that operate. Specialized structures such as hair, scales, feathers and glands are distributed over the skin in a highly orderly fashion. This gives rise to two important questions. Firstly, what are the mechanisms involved in the formation of the individual appendages? Secondly, how is their orderly distribution determined? We address these two fundamental questions theoretically here via a mathematical modelling approach. In this way we hope to gain a better understanding of skin pattern formation in particular and, ultimately, in morphogenesis as a whole.

Experimental investigation into morphogenesis has increased our knowledge of some aspects of pattern formation. Mathematical models can be of assistance in these investigations, since they provide a formalized framework for the theories and hypotheses that are constructed from experimental results. This is, however, not the only objective of mathematical modelling. Not only can

mathematical models improve our understanding of the mechanisms involved, but they can also assist us in examining the roles of specific submechanisms in determining the final patterns. Such investigations could suggest new experiments and could thus trigger new areas of research. The ultimate measure of a model's success is in its ability to predict hitherto unrecognized behaviours.

We begin our investigation in Chapter 1 by considering the wide range of mathematical and theoretical models that have been proposed for skin pattern formation. Vertebrate skin is composed of two basic layers, the dermis and the epidermis. Since these two layers have vastly different properties, proposed mechanisms vary from visco-elastic stress-strain models to reaction-diffusion and chemotaxis models, each emphasizing a different feature of skin morphogenesis. In the light of these models, as well as recent experimental results, we propose new improved models for both the dermal and epidermal layers.

It has now been shown experimentally that interaction between the dermal and epidermal layers is an integral component of vertebrate skin pattern formation. In Chapter 2 we therefore introduce a new tissue interaction model, based on diffusing signal chemicals, for modelling skin patterning. However, due to the complex nature of morphogenesis, this model is extremely involved. So, several simplifying assumptions are introduced to get a much simpler and more streamlined caricature version which, nevertheless, still encapsulates the key features of the full model. A linear analysis of this reduced model suggests that patterned solutions are indeed possible under appropriate conditions.

That our reduced tissue interaction model can indeed give rise to stable steady state patterns in one spatial dimension is demonstrated by a steady state analysis of the nonlinear system in Chapter 3. Both a multiple time-scale bifurcation analysis and numerical simulation are used to examine the nature of the one-dimensional solutions.

In Chapter 4 we extend our investigations to two-dimensional domains. A linear analysis forms the basis of a much more involved nonlinear perturbation analysis. This, combined with detailed numerical simulations, give an indication

of the large range of structures possible on rectangular domains and how various model mechanisms are involved in their determination.

Not only can pattern formation be explained by the tissue interaction model, but travelling wavefronts, acting as precursors to many developmental processes, can in fact be simulated. In Chapter 5 we present a detailed investigation, based on a perturbation analysis and numerical simulations, to examine the dermal cell invasion wave coupled to an epithelial contraction wave which our model exhibits.

Although only synchronous patterning is normally considered in pattern formation models, often embryonic patterns, including skin structures, are laid down in a sequential fashion. In Chapter 6 we investigate such one-dimensional sequential patterning. An asymptotic technique, incorporating the method of steepest descents, is used for analysing the propagation of one-dimensional patterned solutions. For analysing the speed of propagation a new method, involving the envelopes of the propagating solutions is introduced. This method has several advantages over the asymptotic technique.

A key question is whether our tissue interaction system can model sequential patterning on two-dimensional domains, thus mimicking vertebrate skin morphogenesis. This question is addressed in Chapter 7 where we propose two possible mechanisms for such sequential patterning. Numerical investigations based on experimental results indicate which of the two mechanisms is more likely to operate. It is shown that, under appropriate conditions, our proposed tissue interaction system can indeed simulate sequential skin pattern formation.

Finally, we summarize the results in the Conclusion.

Chapter 1

Models for Skin Organ Pattern Formation

1.1 Introduction

A large variety of mathematical models have been proposed to describe pattern formation processes during morphogenesis. Of these, the most widely studied models are the reaction-diffusion systems pioneered by Turing (1952). He demonstrated that a system of two hypothetical reacting and diffusing chemicals, called morphogens, could evolve to a spatially heterogeneous steady state pattern. In the early embryo, such morphogen pre-patterns could be involved in the subsequent development of structure and form. The pre-patterns may be interpreted by the cells which then differentiate according to a pre-programmed set of rules. This is the concept of *positional information* proposed by Wolpert (1969, 1971, 1981). For examples and applications of such reaction-diffusion systems see the books by Murray (1977, 1989), Fife (1979) and Meinhardt (1982).

Experimentalists have so far been unable to identify, with certainty, suitable candidates for the morphogens on which this theory is based. Calcium has been suggested by Goodwin (1984) and ammonia by Bradbury & Gross (1989). Also, experiments on the chick limb bud suggest that retinoic acid could be the morphogen that provides the positional signal in limb development, see, for example, Tickle *et al.* (1982) and Bricell & Tickle (1989). Kay *et al.* (1984) have isolated a morphogen in the slime mould, *Dictyostelium.* The existence of morphogens, however, still remains a controversial issue.

Another, but very different, approach to pattern formation was first used

by Oster *et al.* (1983) (for further examples see also Murray & Oster 1984a, 1984b and Murray 1989). They developed *mechanochemical* models to describe pattern formation in which it is assumed that mechanical morphogenetic movements of cells and related tissue create structure and form. Three features of the mechanochemical models give them a distinct advantage over the more traditional reaction-diffusion systems. Firstly, the mechanochemical models are based on known experimental facts about embryonic cells and tissue. By experimentally altering the biological behaviour of the tissue one can test and compare the mathematical predictions with the biology. This would lead to improvements of our mathematical model and ultimately a better understanding of morphogenesis. A second advantage of mechanochemical mechanisms is that they have the potential for self correction. A developing embryo's capability of adjusting to many outside disturbances is reflected in these models. In the reaction-diffusion mechanisms any external disturbance of the pre-pattern would naturally disrupt the developmental process seriously. Finally, the mechanical shaping of tissue which occurs during embryogenesis forms an integral part of the mechanochemical models. In the chemical theory of morphogenesis the mechanics of tissue is not addressed at all.

For the above reasons we therefore mainly adopt the mechanochemical approach throughout this thesis.

In the next section we describe the necessary biological details of skin morphogenesis needed to understand the mathematical models we construct in Sections 1.3 and 1.4. As we shall explain in Section 1.2, vertebrate skin is composed of two layers, namely the dermal and the epidermal layers. We discuss models for dermal pattern formation in Section 1.3, while epidermal models are considered in Section 1.4. In each of these sections we give a brief review of the relevant mechanochemical models published so far. Based on new experimental evidence we then propose new improved mathematical models for each of these layers.

1.2 General Biology of Skin Morphogenesis

We present in this section a short summary of the biological details necessary for constructing the mathematical models; however, for a detailed account of the biology involved the textbooks by Walbot & Holder (1987) and Gilbert (1988) should be consulted.

During early embryogenesis cells can be classified into two general types, mesenchymal (fibroblast) and epithelial. Epithelial cells are usually not motile and are packed together in sheets. Mesenchymal cells, on the other hand, are motile and move about in the intercellular space between and on epithelial layers.

During morphogenesis these cells undergo a combination of events such as division, differentiation, adhesion, migration and death. The coordination of these activities is crucial for the pattern formation processes. Intercellular communication plays an important role in organizing and controlling these events.

Cells in the embryo receive a specific set of instructions to specify their role during development and in the final organism. Some of these instructions are cued by chemical molecules secreted from one group of cells to influence the fate of others. Such chemicals have been isolated by, for example, Kimelman & Kirschner (1987) in the *Xenopus* (a species of frog) embryo. The chemical mediators are so rapidly taken up by receptor cells or destroyed and immobilized by extracellular enzymes that they only act on cells in their immediate neighbourhood — so called paracrine signalling. Usually a steadily increasing concentration switches on some or other response from the receptor cells as soon as a certain threshold concentration has been reached. The chemical signals act at very low concentrations, less than $10^{-8}M$. A good review on chemical signalling can be found in Alberts *et al.* (1989).

We are specifically interested in vertebrate skin pattern formation. Vertebrate skin is composed of two basic layers: an ectodermal epithelium, the epidermis, consisting of columnar cells, overlies a mesodermal mesenchyme, the

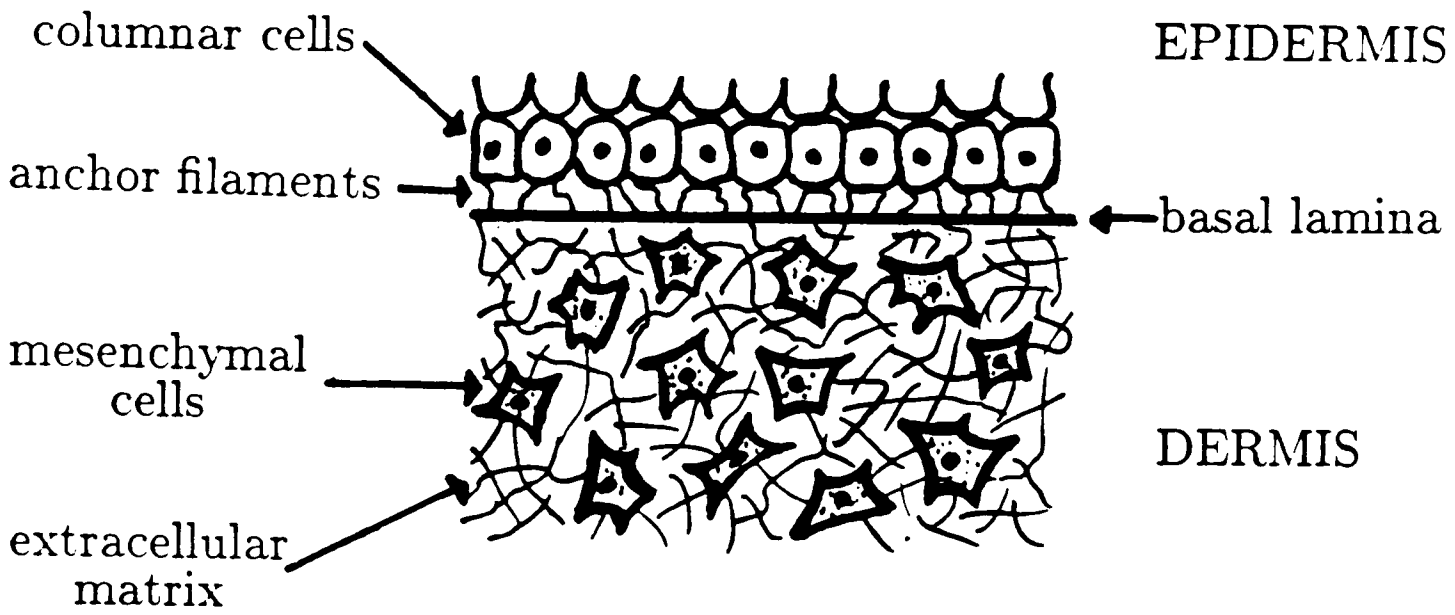

Figure 1.1: Schematic representation of the cross section of chick skin around day 6 of gestation. An epidermis, consisting of columnar cells overlies the dermis, consisting of mesenchymal cells. These mesenchymal cells move about in the extracellular matrix. The epidermis is attached to the basal lamina which separates the epidermal layer from the dermal layer.

dermis. These two layers are separated by the fibrous basal lamina (see Figure 1.1).

Epithelial cells array themselves into sheets and may present a very regular *paving stone* appearance when viewed from the apical side. Each epithelial cell has a definite polarity, with the apical surface facing the external medium. Just beneath the apical surface a circumferential complex of junctions bind the epithelial cells tightly to one another and seals the embryo from the outside environment. The basal surface faces the basal lamina. The epidermal layer of cells can fold, roll, invaginate and deform as a whole, but there is very little movement of the densely packed individual cells.

The much thicker dermis consists of mesenchymal cells, connective tissue, collagen fibres, blood, lymph vessels, sensory nerves and so on. The mesenchymal cells are loosely packed and they move around on a jelly-like tissue called the extracellular matrix, which we shall refer to as the ECM (Hay 1981). Mesenchymal cells can attach to the ECM via finger-like filopodia with which they

can exert large traction forces on the ECM (Harris *et al.* 1981).

During skin development sweat glands, hair follicles, feather germs and/or other skin structures grow down from the epidermis into the dermis. Although the models considered here are of general applicability to vertebrate skin, we shall concentrate on feather germ formation on the chick back. This has been widely studied by authors such as Wessells (1965), Davidson (1983a, 1983b) and Chuong & Edelman (1985a, 1985b). The several stages of feather formation are described in Sengel's (1976) book.

The first feather rudiments on the chick back become visible six days after egg fertilization. A feather primordia consists of a thickening of the epidermis, called a placode, and a condensation of the dermal cells, called a papilla. A placode is seen by the elongation and thickening of the columnar basal cells, perpendicular to the skin. The dermal condensations are largely due to cell migration, with localized proliferation playing a secondary role.

The chick's feather primordia appear sequentially. Initially we have a periodic row of feather buds along the dorsal midline. New buds are added anteriorly (towards the head) and posteriorly (towards the tail) causing it to grow in length. Lateral rows of feather buds then appear sequentially from the dorsal row outwards but at a much slower rate. The primordia of the new lateral rows are equidistant from two neighbouring primordia of the preceding row so that a *chessboard* pattern arises. Although the word *hexagonal* is normally used to describe the spatial arrangement of feather follicles, a better description of the pattern at the time of initiation would be *chessboard*, as is also pointed out by Nagorcka (1986) (see Figure 1.2).

Note that we are interested in the initial patterning stage where induction between the dermal papillae and epithelia placodes induce the formation of the feather buds.

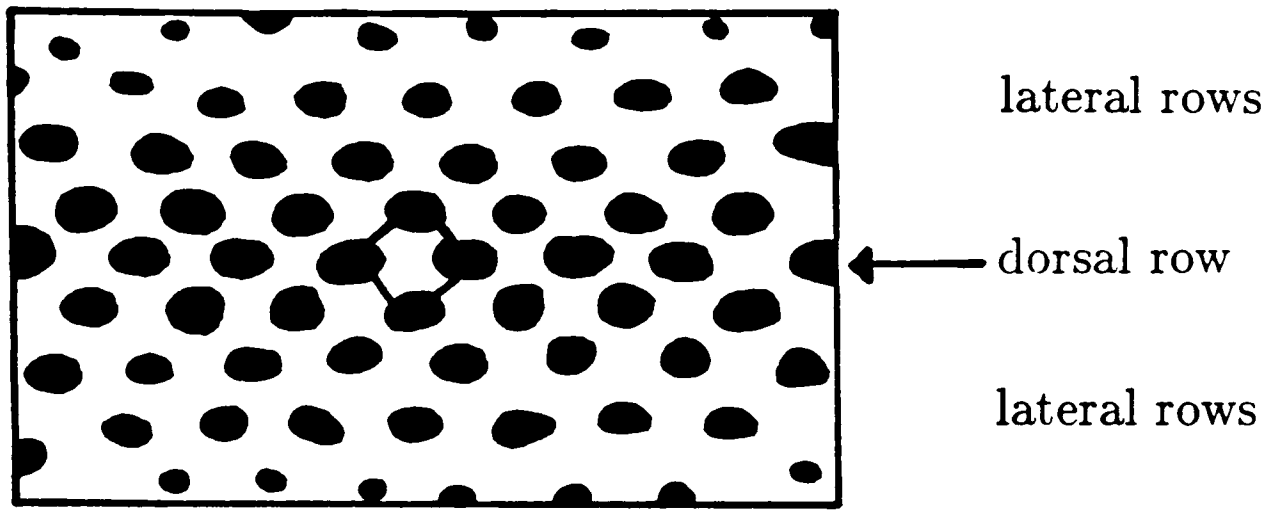

Figure 1.2: Tracings of the *chessboard* pattern of primordia on the back of a 10–11 day old chick. As illustrated, we have a square pattern, rather than a hexagonal pattern. Redrawn from Nagorcka (1986).

1.3 Models for Dermal Morphogenesis

Murray *et al.* (1983) (see also Oster *et al.* 1983 and Murray & Oster 1984a, 1984b) first proposed a mechanochemical model for mesenchymal morphogenesis. Their model is based on the interaction between motile cells and the extracellular matrix on which these cells move. It consists of three equations: a conservation equation for cell population density; a mechanical balance equation for the forces between the cells and ECM; and thirdly, an equation governing the conservation of the ECM. Cell-cell adhesion mechanisms have not been addressed by these models.

It now seems that cell-cell adhesion mechanisms play a crucial role in morphogenetic processes as discussed, for example, by Edelman (1984, 1985, 1986, 1988) in his *Morphoregulator Hypothesis.* In Section 1.3.1 we propose a new, but very simple model, based on this *Morphoregulator Hypothesis.* This model is generalized in Section 1.3.2 to account for various other mechanisms which are believed to be important during the initial stages of dermal morphogenesis. The generalized version of the model will be used in the next chapter in constructing the tissue interaction model.

1.3.1 A Cell-Cell Adhesion Model

Ever since the early studies by Wilson (1907), Holtfreter (1943, 1944), Moscana (1952), and others demonstrated tissue- and species-specific sorting of embryonic cells, it has been believed that specialized adhesive properties of cells play a fundamental role in morphogenesis. The importance of cell-cell adhesion in developmental processes has now been shown in several experimental systems. In *Dictyostelium*, for example, at least two separate mechanisms for cell-cell adhesion operate (Beug *et al.* 1970, 1973), for other examples see McClay & Ettensohn (1987). More important to us is Edelman's suggestion in his *Morphoregulator Hypothesis* that cell-cell adhesion mechanisms control skin organ morphogenesis.

Background Biology

Cell-cell adhesion is mediated by molecules called cell adhesion molecules, or CAMs in short. CAMs are large glycoprotein molecules found on the cell surface and are synthesized by the cell. They can be classified into two general groups, the primary CAMs and the secondary CAMs. The two primary CAMs, neural cell adhesion molecules (N-CAMs) and liver cell adhesion molecules (L-CAMs), appear early in developing tissue and could therefore play a crucial role in pattern formation. Binding of N-CAM and L-CAM is homophylic, which means that a CAM on one cell binds to the same CAM on another cell. The N-CAM binding mechanism is calcium (Ca^{2+}) independent whereas that of L-CAM is Ca^{2+}-dependent.

The CAMs undergo certain changes in expression or in chemical properties during development. These changes, collectively termed local cell surface modulation, have a remarkable influence on the rate and strength of the binding mechanisms. In vesicle binding experiments only a two-fold change in the surface concentration of N-CAM leads to a greater than thirty-fold change in the rate of homophylic binding (Hoffman & Edelman 1983, Grumet & Edelman

1988). Hoffman & Edelman (1983) also showed that chemical modulation can result in a three- to four-fold change in the CAMs' homophylic binding rate. The implication is that cell surface modulation of CAMs could have a major effect on cell movement.

How do CAMs function in relation to morphogenesis? It has been demonstrated that blocking primary CAMs by antibodies *in vitro* and also *in vivo*, disrupts the morphogenetic processes dependent on cellular adhesion. For example, it is sufficient to block only N-CAM binding in neurons to disrupt neural patterns in a variety of tissues (Edelman 1985). Epithelial cells in the chick embryo skin are L-CAM positive during the placode formation stage. Gallin *et al.* (1986) showed that antibodies to L-CAM perturb the inductive interactions between the epidermis and dermis and alter the feather bud pattern formation. (We shall discuss this example in more detail in the next chapter.) From these experiments the importance of CAMs in morphogenesis is evident.

We also know that different CAMs are expressed in sequential schedules in different organs during development. Examples of this spatio-temporal expression of CAMs during tissue growth are numerous — it has been seen in the nervous system, muscle, gut and kidney (see Edelman 1988). Chuong & Edelman (1985a, 1985b) discuss the repeated expression of CAMs during feather formation.

According to the *Morphoregulatory Hypothesis*, the CAMs at the cell surface act either as regulators or *steersman* for the primary morphogenetic processes. Thus the sequential CAM expression together with local cell surface modulation play a direct role in cell movement and deformation. This hypothesis assumes a set of mechanisms exists that control the action of the CAM regulatory genes. We have seen that small changes in CAM expression can have drastic effects on their functioning, so small changes in the CAM regulatory mechanisms could have a major influence on the patterns. How these genes are triggered is still unknown; morphogens are possible candidates (see for, example, Edelman 1984).

We are interested in the feather germ initiation stage, specifically on the

chick back. Experiments by Chuong & Edelman (1985a) (see also Edelman *et al.* 1985) emphasize the importance of N-CAM during the formation of dermal papillae. At the earliest stage of feather germ formation a thin layer (3 to 10 cells thick) of dermal cells is uniformly N-CAM positive. Dermal condensations form directly underneath the epidermal placodes and at about the same time as the placode development. The cells inside the dermal condensations stain brightly for N-CAM. The loosely orientated mesenchymal cells in the surrounding tissue become N-CAM negative, while cells that are increasingly N-CAM positive lie in between. Once initiated the dermal clusters can accumulate more cells, possibly by the means of CAM adhesion mechanisms — a behaviour akin to chemotaxis. The smallest initial N-CAM positive dermal cluster observed consisted of about ten cells.

These observations support our hypothesis that pattern formation is the result of CAM expression and modulation on cell surfaces. We now construct a model to describe such mesenchymal morphogenesis in terms of cell-cell adhesion.

Mathematical Model

We define the field variables:

$$\begin{aligned} n(\boldsymbol{x},t) &= \text{the density of mesenchymal cells at position } \boldsymbol{x} \text{ and time } t; \\ a(\boldsymbol{x},t) &= \text{the density of expressed N-CAMs on cells at position } \boldsymbol{x} \text{ and} \\ &\quad \text{time } t. \end{aligned}$$

The latter is probably dependent on the concentration of a chemical signal as we shall explain below.

The general conservation law for cell density is

$$\frac{\partial n}{\partial t} = -\nabla \cdot \boldsymbol{J}_n + \text{mitosis},$$

where $\boldsymbol{J}_n$ represents the flux of cells — the number of cells crossing a unit volume in a unit time. The flux is made up of taxis and diffusion contributions

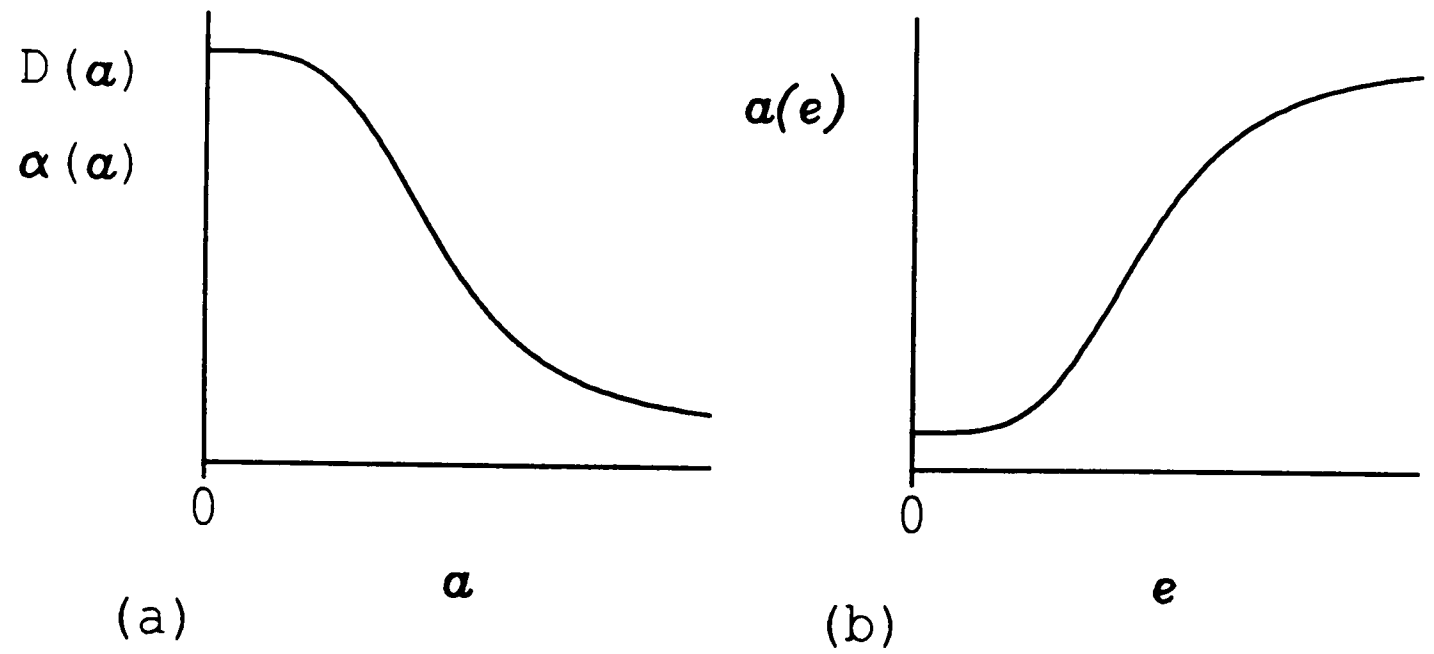

Figure 1.3: Qualitative sigmoidal curves simulating biological switch mechanisms. (a) Increasing the concentration of expressed N-CAM, a, turns off the taxis and diffusion factors, D and α, respectively. (b) As the morphogen concentration, e increases, the chemotactic factor, a, and therefore the chemotaxis, is switched on.

which we now discuss.

Taxis: The main contribution to cell flux is cell-cell attraction, an aggregative process, which tends to organize cell populations by enhancing cell movement into regions of higher cell density. Cells move about in a random-like way in the dermis — some of them bind to neighbouring cells, while others break their bonds. The bonds between cells with a high density of expressed N-CAMs are much stronger and stay longer attached. So, we assume that cells tend to move up a gradient of N-CAM expression.

The cell flux will be higher in regions of higher cell density, because there are more cells to move up the N-CAM gradient. We model this chemotactic flux by

$$\boldsymbol{J}_{\text{taxis}} = n\alpha(a)\nabla a,$$

where $\alpha(a)$, the chemotactic factor, is a function of the N-CAM concentration. As the N-CAM density increases the cells become more firmly attached to each other which restricts their movements, and so α is modelled as a switch-like function of a, qualitatively as in Figure 1.3(a).

Diffusion: Cells disperse randomly in a homogeneous medium which we take to be isotropic. We model this flux due to random motion with Fickian diffusion,

$$\boldsymbol{J}_{\text{diffusion}} = -D(a)\nabla n,$$

where D, the diffusion coefficient, is dependent on the N-CAM density a. When the cells express a high concentration of N-CAM they are firmly linked. This inhibits random cell movement and aggregation, so we model $D(a)$ as a switch function similar to $\alpha(a)$ as in Figure 1.3(a).

In classical diffusion cells respond to the local cell density by moving down a concentration gradient. Diffusion has a stabilizing effect; hence cell populations tend to a spatially homogeneous distribution. In the morphogenetic situations considered here, we expect the effect of diffusion to be relatively small compared to the other mechanisms involved and therefore we shall often set $D = 0$.

Mitosis: We assume that the mesenchymal cells proliferate until a limiting density $\bar{n}$ is reached. This can be adequately modelled by logistic growth,

$$\text{mitotic rate} = rn(\bar{n} - n),$$

where r and $\bar{n}$ are positive constants. This form exhibits a typical sigmoidal proliferation rate observed experimentally in many cell populations.

Incorporating all these effects, the equation for cell conservation is

$$\frac{\partial n}{\partial t} = \nabla \cdot D(a)\nabla n - \nabla \cdot n\alpha(a)\nabla a + rn(\bar{n} - n).$$

1.3.2 A General Cell Aggregation Model

In the above model mesenchymal cell aggregation is explained in terms of cell-cell adhesion mechanisms. Although such an explanation is appealing, there is no conclusive evidence in support of this theory. We therefore examine some other aggregation mechanisms that have been proposed. By incorporating these

different ideas into our model we develop a very general model for dermal morphogenesis which contains the basic features of the various proposed mechanisms.

A cell migration mechanism which has received a lot of attention in the literature is chemotaxis — the process where cells move up a chemical gradient (see Zigmond 1989 for a discussion). The amoebae of the slime mold *Dictyostelium*, for example, move up a gradient of cyclic AMP. This aggregation process in the slime mold is further assisted by the expression of CAMs at the cell adhesion centres (Gerisch 1986). A similar process could be involved in papillae formation: dermal cells move up a chemical gradient, while the N-CAM functions as a binding mechanism in the papillae.

Changes in the composition of the extracellular matrix and in its structure can have remarkable effects on cell movement. It is known that cells move in the direction of the most adhesive part of the extracellular matrix (Oster *et al.* 1983). This movement up an adhesive gradient is called haptotaxis. The cells are very sensitive to adhesion differences in the extracellular matrix — they move up gradients of as low as 1 percent (Devreotes & Zigmond 1988). For example, the substratum density can change mechanically due to the cell traction forces on the extracellular matrix. This sets up a matrix gradient which can induce cells to move towards higher density regions because of the availability of more adhesive sites (see, for example, Murray 1989). Also, the chemical composition of the extracellular matrix could be altered due to the influence of, or reaction with, a chemical or morphogen and as a result its adhesion capabilities could change. Sengel *et al.* (1985) have shown that during feather morphogenesis both fibronectin (adhesive) and collagen (structural) components of the extracellular matrix exhibit a heterogeneous distribution related to the developing feather germs.

Models similar to the cell-cell adhesion model can be constructed for each of these mechanisms. Since it is not known which of these mechanisms is responsible for dermal cell movement, or even whether or not it is a combination of all of

them (Erikson 1990), we now propose a general, reaction diffusion-chemotaxis model to simulate cell movement in the dermis.

We introduce a new variable,

$$e(\boldsymbol{x}, t) = \text{the concentration of a chemical at position } \boldsymbol{x} \text{ and time } t.$$

The fact that the cells in papillae express more N-CAM than the surrounding cells is an important justification for the existence of such a signal chemical. Some cells in the dermis receive a signal for expressing N-CAM, while others do not receive the same signal. This message is most probably involved in initiating aggregation. So, we replace the taxis term in the last equation with the chemotactic term

$$\boldsymbol{J}_{\text{chemotaxis}} = n\alpha(e)\nabla a(e),$$

where the chemical $e(\boldsymbol{x}, t)$ switches on cell-taxis. Whether this morphogen increases the expression of N-CAM and/or increases the ECM adhesiveness is not germane in our simple model. Alternatively the morphogen could simply be a normal chemo-attractant as is the case in *Dictyostelium* aggregation.

Usually the taxis mechanism would be switched on when $e(\boldsymbol{x}, t)$ passes a certain critical threshold concentration. Strictly speaking therefore $a(e(\boldsymbol{x}, t))$ should be modelled by a sigmoidal curve which simulates this switch mechanism, see Figure 1.3(b). However, for convenience we incorporate the function $a(e)$ into the chemotactic factor $\alpha(e)$ so that the full general equation is

$$\frac{\partial n}{\partial t} = \nabla \cdot D(e)\nabla n - \nabla \cdot n\alpha(e)\nabla e + rn(\bar{n} - n), \tag{1.1}$$

where D and α are now functions of the chemical concentration e. For simplicity, however, as a first approximation we shall assume, in what follows, that D and α are constants.

1.4 Models for Epithelial Morphogenesis

The first mechanical model for epithelial morphogenesis was proposed by Odell *et al.* (1981). They used a finite element approach to model the epithelium

as a sheet of discrete cells adhering to the basal lamina. In their model it is assumed that each cell has the ability to undergo contraction which controls the cell shape and ultimately the morphogenetic movements of the epithelial sheet.

Several continuum mechanochemical models have been developed from this initial model. Currently the most widely used models are those based on a cytogel contractility mechanism. In Section 1.4.1 we propose such a cytogel model to explain early epithelial morphogenesis.

More recently, as an alternative to the cytogel models, a cortical tractor mechanism has been proposed by various authors. However, as we shall demonstrate in Section 1.4.2, there are serious problems associated with these models. We subsequently make a suitable adaption of the original cortical tractor model mechanism to construct a new workable alternative, which we shall call the cortical flow model.

A generalized mechanochemical model, compatible with both the cytogel and cortical flow models, is then derived in Section 1.4.3. Since this model encapsulates the basic features of both the cytogel and cortical flow models we shall use this generalized version in the tissue interaction model in Chapter 2.

1.4.1 The Cytogel Model

A continuum mechanical model based on the original model of Odell *et al.* (1981) was developed by Murray & Oster (1984b) (see also Oster & Odell 1984 and Murray 1989). The model we propose here is similar to the latter. For the biological details refer to Alberts *et al.* (1989).

Although macromolecular protein fibres, called actin filaments, are distributed throughout the cytoplasm of an animal cell, there is a particularly dense network in the cortex. This cortical layer is situated below a cell's plasma (outer) membrane and is believed to be largely responsible for cell movements and deformation. The actin filaments are linked by myosin crossbridges, also made up of protein, and collectively they constitute the cell's cytoskeleton.

The cytoskeleton is a dynamic structure which can contract actively by regulating the assembling and disassembling of the crosslinking fibres. When the network is weakly linked the cytoplasm liquifies — a process known as solation — whereas when it is strongly linked it gelates. By regulating this sol-gel equilibrium the cell can exhibit a large variety of motile phenomena and shape changes (Odell *et al.* 1981).

The local concentration of free calcium, Ca^{2+}, in the cytogel is directly responsible for the sol-gel transition and the degree of actomyosin crosslinking (see, for example, Korn & Hammer 1988). The Ca^{2+} is released into the cytogel from special intracellular calcium-sequestering compartments. At low Ca^{2+} levels the cytogel is crosslinked and is in the gel-state. As the free Ca^{2+} concentration rises crosslinking in the gel is encouraged and the cytoskeleton starts to contract actively. However, if the Ca^{2+} level gets too high the cytogel solates and the crosslinking network breaks apart and cannot support any stress. So there is a window of free Ca^{2+} concentration which is optimal for contractile activity (Murray & Oster 1984b, Oster & Odell 1984).

Ca^{2+} is, however, only one link in a very complex biochemical scheme regulating contraction. Extracellular signals are usually necessary to stimulate the calcium release from the sequestering compartments (see, for example, Berridge 1988). We therefore assume, for the purpose of our model, that the amount of free calcium is a function of an extracellular morphogen concentration, say s.

We model the epithelial sheet of cells as a two-dimensional, visco-elastic continuum of cytogel. The model involves three field variables:

$N(\boldsymbol{x},t)$ = the epithelial (cell) density at position $\boldsymbol{x}$ and time t;

$\boldsymbol{u}(\boldsymbol{x},t)$ = the displacement vector at time t of a material point in the epithelial layer which was initially at position $\boldsymbol{x}$;

$s(\boldsymbol{x},t)$ = the concentration of a chemical at position $\boldsymbol{x}$ and time t.

Force Balance Equation for Cytogel Contractility

We expect the cytogel contractility mechanism to adhere to Newtonian dynamics and derive accordingly a two-dimensional force balance equation. As we are dealing with a system at a very low Reynolds number, the elastic forces dominate inertial terms (Oster *et al.* 1983) — the motion of cells instantly ceases when the applied forces are removed (Purcell 1977). The inertial terms are therefore negligible in the equation for the cytogel mechanics. The active traction forces generated in the tissue are thus in equilibrium with the visco-elastic restoring forces and any external forces present. We write the force balance equation as

$$\nabla \cdot \boldsymbol{\sigma} + \boldsymbol{R} = \mathbf{0}.$$

where $\boldsymbol{\sigma} = (\boldsymbol{\sigma}_{ij})$, $1 \leq i, j \leq 2$, is the stress tensor of the cytogel continuum and $\boldsymbol{R}$ represents the external body forces acting on the cytogel.

In keeping with the classical theory of elasticity (see Landau & Lifshitz 1970) we consider stresses and forces as being exerted on a small cytogel element by the *surrounding* body. These stresses and forces are thus measured in the direction of the outward normal to the sides of the body element. Note that, according to Newton's third law, this element exerts in turn an equal, but opposite force on the surrounding material. In some earlier works there were confusion about the direction in which the active contraction stress should be measured.

We must now model the various contributions to $\boldsymbol{\sigma}$ and $\boldsymbol{R}$. Since both passive and active stresses are present in the cytogel we write

$$\boldsymbol{\sigma} = \boldsymbol{\sigma}_{\text{passive}} + \boldsymbol{\sigma}_{\text{active}}.$$

Note that the passive stress tensor consists of two components, the cytogel elasticity and the cytogel viscosity, so

$$\boldsymbol{\sigma}_{\text{passive}} = \boldsymbol{\sigma}_{\text{elastic}} + \boldsymbol{\sigma}_{\text{viscous}}.$$

Cytogel Elasticity: Conventionally, according to Hooke's Law, the stress at a point, in an isotropic medium, is a function only of the strain and dilation at

that point, namely

$$\boldsymbol{\sigma}_{\text{elastic}} = \frac{E}{(1+\upsilon)}(\boldsymbol{\varepsilon} + \frac{\upsilon}{1-2\upsilon}\theta \boldsymbol{I}),$$

where the strain tensor

$$\boldsymbol{\varepsilon} = \frac{1}{2}(\nabla \boldsymbol{u} + \nabla \boldsymbol{u}^T),$$

and the dilation

$$\theta = \nabla \cdot \boldsymbol{u}.$$

E is the passive elastic modulus, $\boldsymbol{I}$ is the unit tensor and υ is *Poisson's ratio* (Landau & Lifshitz 1970).

This linear form of the stress tensor is of course not valid for a material as complex as biological tissue. For example, as the cytogel commences to contract, the amount of overlap of the actin filaments increases and the number of myosin crossbridges increases. As a result the fibres grow stronger. When a fibrous material is stretched the fibres also tend to align in the direction of the stress and the effective elasticity increases. However, when the Ca^{2+}-concentration is high the cytogel solates and so we model the elastic modulus E as a decreasing function of the chemical s (Murray 1989), see Figure 1.4(a).

Fibrous materials are also characterized by non-local elastic interactions, since the fibres can transmit stress between points in the cytogel quite far apart. This is because the actin fibres thread through the cytoplasm over relatively long distances. We include the effect of long range elastic stresses by higher order terms of the form

$$-\frac{E(s)}{1+\upsilon}\left(\beta_1 \nabla^2 \boldsymbol{\varepsilon} + \frac{\upsilon}{1-2\upsilon}\beta_2 \nabla^2 \theta \boldsymbol{I}\right),$$

where β_1 and β_2 are constants. Oster & Odell (1984) used a similar expression in their cytogel model. To ensure that the above expression represents passive elasticity, β_1 and β_2 must be positive. The long range elastic stresses are, however, much smaller than the local stresses so that $\beta_1, \beta_2 \ll 1$. (For a pedagogical discussion of long range effects see Murray (1989).)

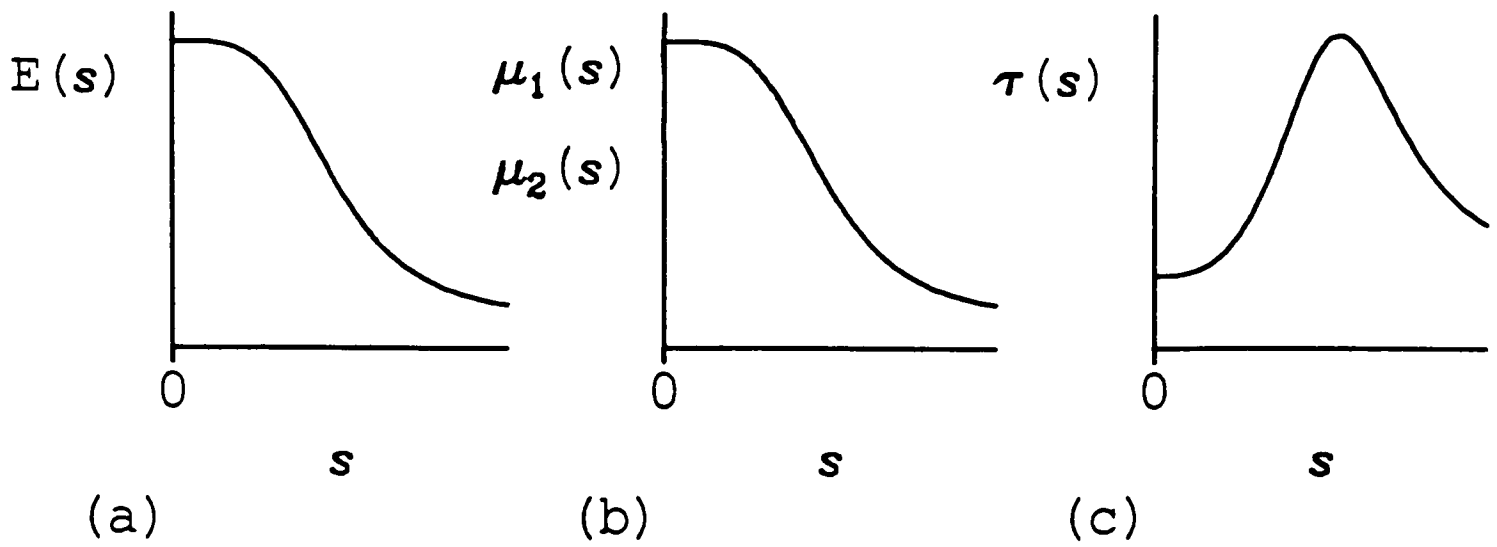

Figure 1.4: The nonlinear dependence of the parameters in the stress tensor on the variables θ and s. In (a) and (b) the precipitous drop in the elastic modulus E, and viscosities μ_1, μ_2, occurs when the gel solates. (c) The dependence of the active traction τ, on the morphogen s.

The elastic stress tensor is therefore

$$\boldsymbol{\sigma}_{\text{elastic}} = \frac{E(s)}{1+v}\left[\boldsymbol{\epsilon} - \beta_1\nabla^2\boldsymbol{\epsilon} + \frac{v}{1-2v}(\theta - \beta_2\nabla^2\theta)\boldsymbol{I}\right].$$

Cytogel Viscosity: We model the viscous stress associated with cytogel motion as

$$\boldsymbol{\sigma}_{\text{viscous}} = \mu_1\frac{\partial\boldsymbol{\epsilon}}{\partial t} + \mu_2\frac{\partial\theta}{\partial t}\boldsymbol{I},$$

where μ_1 and μ_2 are the shear and bulk viscosities respectively (Landau & Lifshitz 1970, Flügge 1975). As before this equation is only valid for an isotropic material. Since the behaviour of the cytogel changes as the concentration of the morphogen $s(\boldsymbol{x},t)$ varies we assume that both the viscosity coefficients, μ_1 and μ_2, are functions of $s(\boldsymbol{x},t)$. For example, the solation of the cytogel causes the severing of the fibre network and therefore causes a precipitous drop in the viscosities of μ_1 and μ_2, see Figure 1.4(b).

Active Contraction Stress: As explained above the active contraction stress of the actin-myosin network is triggered by the local free Ca^{2+} concentration.

Since we assume that a chemical message $s(\boldsymbol{x}, t)$ switches on the Ca^{2+} release mechanism, we model the active contraction stress as

$$\boldsymbol{\sigma}_{\text{active}} = \tau(s)\boldsymbol{I},$$

where $\tau(s)$ is the active traction. The dependence of the contraction stress on the morphogen s is illustrated in Figure 1.4(c). The onset of contraction is rather sudden and, as we are only interested in the window of optimal contraction, we model $\tau(s)$ as a sigmoidal function of the form

$$\tau(s) = \frac{\tau s^2}{1 + ks^2},$$

(see Murray & Oster 1984b and Oster & Odell 1984). The sharpness of the switch is controlled by the positive parameter k, while the strength of the traction mechanism is reflected by the positive constant τ.

Body Forces: Movement of the cytogel is restricted by the attachment of the cortical fibres to the cell membrane and the subcortical cytoskeleton. The movement of the epithelial layer is also inhibited by its attachment to the basal lamina which in turn is attached via tethers through the extracellular matrix. We model these restraining forces as a simple linear spring, by setting

$$\boldsymbol{R} = -\rho\boldsymbol{u},$$

where ρ is the parameter reflecting the strength of the attachments.

The force balance equation then is

$$\nabla \cdot \left\{ \frac{E(s)}{1+\upsilon} \left[\boldsymbol{\varepsilon} - \beta_1 \nabla^2 \boldsymbol{\varepsilon} + \frac{\upsilon}{1-2\upsilon}(\theta - \beta_2 \nabla^2 \theta)\boldsymbol{I} \right] + \right.$$

$$\left. \mu_1(s)\frac{\partial \boldsymbol{\varepsilon}}{\partial t} + \mu_2(s)\frac{\partial \theta}{\partial t}\boldsymbol{I} + \tau(s)\boldsymbol{I} \right\} = \rho \boldsymbol{u} \ . \tag{1.2}$$

By measuring the force taken to stretch the cytogel in a given direction one can determine the relationship between the elastic uni-directional stress and the dilation. Oster & Odell (1984) have shown that this relationship is linear for

small strains and because we shall be primarily concerned with the small strain behaviour of the epithelial layer (see Section 2.3) we model E as a constant rather than a function of the dilation θ. To decrease the complexity, in the work that follows we shall also assume, as a first approximation, that μ_1 and μ_2 are constants.

Epithelial Cell Conservation

We assume that the epithelial cell density is directly proportional to the epithelial material density. The general conservation equation for the cell density is

$$\frac{\partial N}{\partial t} = -\nabla \cdot \boldsymbol{J}_N,$$

where $\boldsymbol{J}_N$ is the cell flux.

The most important contribution to cell flux is convection. Because the cells are attached we have no random dispersal – as the sheet deforms, the position of single cells stays fixed in relation to their neighbours. The convective flux is equal to the cell density times the mean epithelial velocity,

$$\boldsymbol{J}_{\text{convection}} = N\frac{\partial \boldsymbol{u}}{\partial t},$$

and so

$$\frac{\partial N}{\partial t} = -\nabla \cdot N\frac{\partial \boldsymbol{u}}{\partial t}. \tag{1.3}$$

Equations (1.2) and (1.3) constitute the field equations for our cytogel model for epithelial pattern formation.

1.4.2 A Cortical Flow Model

We begin this section by describing the different cortical tractor theories for cell propulsion. These theories are then related to epithelial pattern formation and a model mechanism proposed by Cheng *et al.* (1986) (see also Jacobson *et al.* 1985, 1986) is discussed. We show, however, that their model cannot give rise

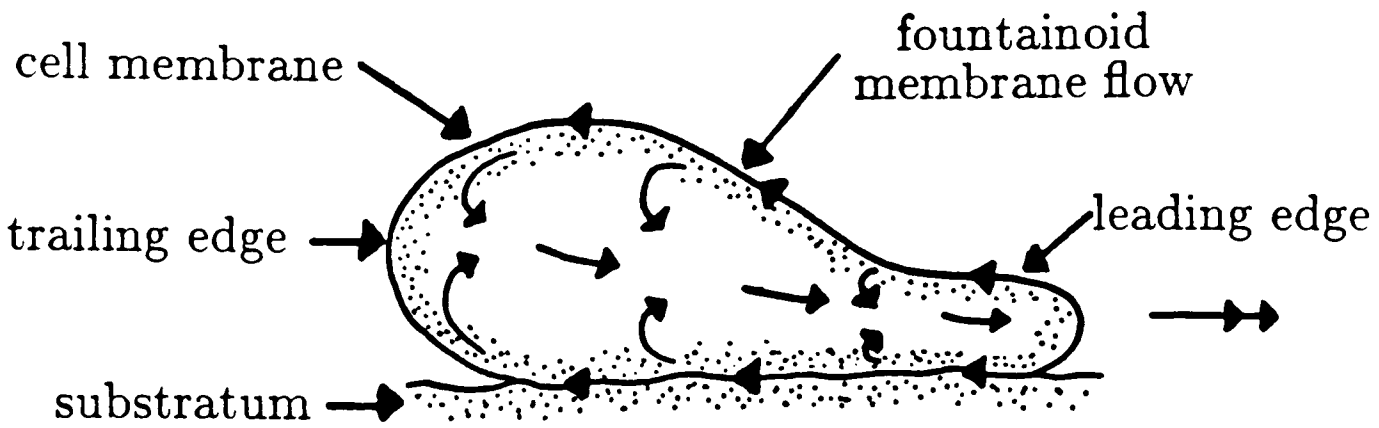

Figure 1.5: Sketch of the model of Abercrombie *et al.* (1970) for cell locomotion based on a fountainoid flow of cell membrane.

to spatial patterns as predicted. Subsequently we propose a possible alternative model linked to the cortical flow mechanism observed in individual cells.

Cell Locomotion Theories

Abercrombie *et al.* (1970) proposed a model for fibroblast cell locomotion based on the flow of a cell's plasma membrane. In their experimental work they showed that a particle attached to the cell membrane flows backwards, in the opposite direction of the cell movement. Similar marking experiments have been carried out by other authors, for example Harris & Dunn (1972) and Dembo & Harris (1981). These experiments suggest the existence of a continuous membrane flow from the leading edge to the trailing edge of a moving cell. In some way this membrane must be re-absorbed at the back of the cell to be transferred through the cytoplasm to the front where it is reinserted as membrane (see Figure 1.5). In fact, Abercrombie *et al.* (1970) suggested that a cell's propulsive mechanism is therefore similar to that of a tank. The cell membrane could be seen as a continuous flexible sheet analogous to a tank's caterpillar.

There are mainly two reasons why this model has recently fallen out of favour. Firstly, it has been shown that the speed of membrane flow decreases towards the trailing edge of the cell. Therefore the membrane cannot function

as the equivalent of a tank thread (Bretscher 1987). Secondly, Ambrose (see the discussion after the paper by Petris & Raff 1981) reasoned that since the plasma membrane is viscous, it does not have the mechanical properties necessary for propulsion.

Consequently alternative models for cortical flow propelled cell locomotion have been proposed. Since it is still a controversial issue whether the cell membrane flows or whether the movements, observed on the cell membrane, are the result of an internal flow in the cell, there are mainly two propulsion theories in the literature.

Bretscher (1984, 1987, 1989) believes in the fountainoid flow of the cell membrane as described above. The plasma membrane is ingested at the trailing edge of the cell and then transported as vesicles (small sacs) across the cytoplasm and reinserted at the front. He reasons that the flow is the result of diffusion of lipids and proteins in the plasma membrane. They diffuse from a high concentration at the leading edge, where they are inserted, towards a lower concentration at the trailing edge. Some of the proteins, for example the CAMs, act as adhesion and junctional structures. As they flow along the membrane they attach and detach to the outer substratum. When they are bound to the rigid extracellular matrix they cannot diffuse with the membrane and act as *feet* that provide the thrust for cell motion. The flowing membrane pushes against these feet and this generates the locomotive forces.

Several authors, for example Sheetz *et al.* (1989), Bray & White (1988) and Darnel *et al.* (1986), support the alternative cytoskeletal model. They believe that the cell membrane does not flow, but that the locomotive force is generated by the contractile system of actin filaments in the cortical layer. The cell adhesion structures in the membrane interact with the contracting and relaxing cortex and are thus actively pulled to the tail of the cell. In a similar way as in the previous model the adhesion structures attach to the substratum and then act as feet that pull the cell along. The cortex contraction mechanism could be driven by a cycle of events involving the solation of the actomyosin

cortical gel followed by the osmotic expansion and active contraction of the cortex. Such a mechanism would be related to the model we proposed in Section 1.4.1 (see also, Oster 1984).

For our purposes it is not crucial which one of the above two models is correct. The driving mechanism of adhesive structures attaching to the substratum and pulling the cell forward, is essentially the same in both cases. We shall simply call this driving mechanism the *cortical tractor.*

Cell motility can be stimulated by ionic leaks, for example Ca^{2+}, and can be inhibited by blocking ionic channels (see Zigmond 1978, Snyderman & Goetzl 1981). Consequently it is reasonable to assume, in terms of our model mechanism, that the concentration of an ionic stimuli is proportional to the cortical tractor velocity of a cell — the higher the ionic concentration the higher the velocity of the cortical tractor and the faster the cell moves.

Critique of Proposed Cortical Tractor Models

Jacobson *et al.* (1985) applied the cortical tractor model of Cheng *et al.* (1986) to cells in the epidermal layer. They explained the epithelial sheet movement during morphogenesis in terms of the cortical tractor activities of individual cells. According to their hypothesis epidermal cells have a cortical flow pattern, analogous to that of fibroblast cells as discussed above, directed from the basal to apical ends of the cells (see Figure 1.6). The basal surface of each cell may be active, but the cells stay firmly attached via their apical junctions. They deduced that, because of the cortical tractoring of the epithelial cells, each cell is trying to crawl down on its neighbours. Gradients in a chemical signal, resulting in gradients of cortical tractor speed, can therefore give rise to the various patterning effects seen in epithelial morphogenesis. A similar model was used by Jacobson *et al.* (1986) to explain neurulation in amphibians.

Cheng *et al.* (1986) modelled the cortical tractor mathematically with a finite element force balance equation. They assumed that a shear force, vertical to the epithelial sheet, arises from a difference in the cortical tractor velocities

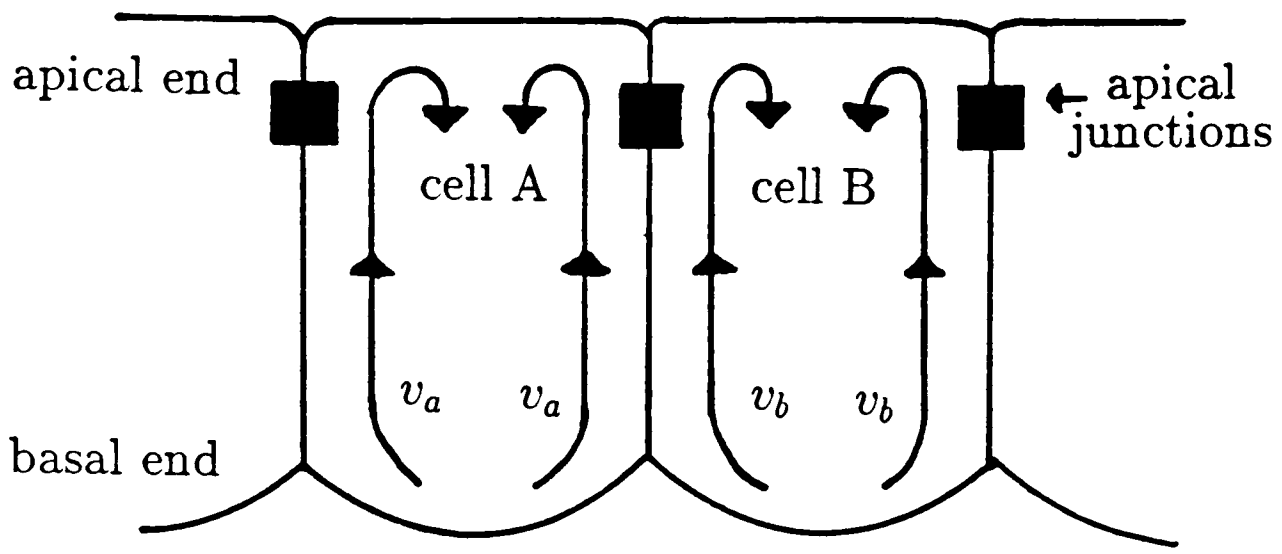

Figure 1.6: The cortical tractor mechanism for epidermal cells. A difference in the cortical tractor velocities of cell A and cell B could activate the basal ends of the cells.

of adjacent cells (Figure 1.6). More specifically, if v_a and v_b are the cortical tractor speeds of adjacent cells this shear force is

$$\eta|v_a - v_b|,$$

where η is the shear modulus. This active force is counteracted by the viscoelastic restoring forces. However, as we shall explain, such a model mechanism is unable to produce relevant deformations of the epithelial sheet.

Let us consider the hypothetical case of an isolated pair of neighbouring cells A and B as is shown in Figure 1.7. The two cells have different cortical tractor velocities and are attached with adhesion structures circulated by their cortical flows — there is no apical junction. Without loss of generality we can assume that only cell A has a cortical tractor flow. Cell A's attachments to cell B are pulled in the direction of flow and provides a thrust to the right, for cell A. At the same time cell B experiences a reaction force to the left.

There are now two possibilities. In the first case we assume that cell B's attachments to cell A are not swept along with the cortical flow of cell A and are fixed to the non-flowing cell membrane of A — the cytoskeletal model. In

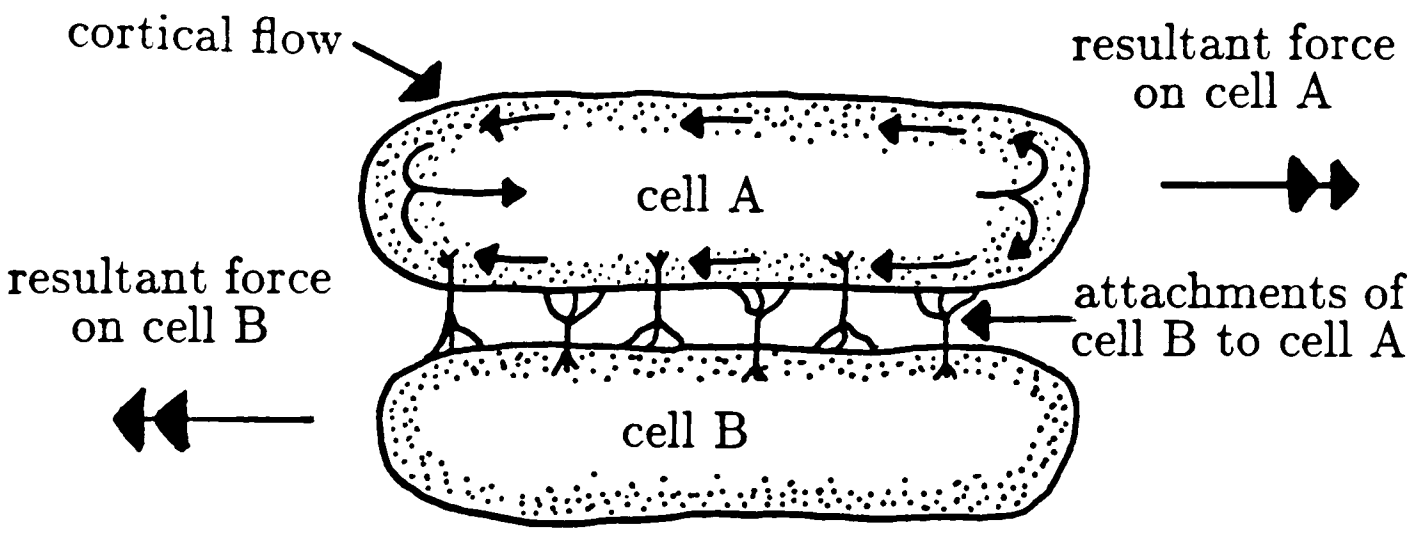

Figure 1.7: A hypothetical example of two fibroblast cells trying to move in relation to each other. Cell A is pushed to the right by its cortical flow, while cell B is pushed to the left.

this case, since B is firmly attached to A, there will be no resultant force on the system and thus nothing happens. This is analogous to pushing someone away from yourself, while he is still holding onto you.

Secondly, suppose we assume that the attachments of cell B to cell A move with the membrane flow of cell A (Bretscher's model), or is pulled along by the cortical contraction/release mechanism (cytoskeletal model) of cell A. In this case, because of action-reaction forces, cell A will be pushed to the right and similarly, cell B will be pushed to the left. This mechanism is very similar to the original caterpillar locomotion model of Abercrombie *et al.* (1970). Since this type of substratum independent movement has been seen in assemblies of *Dictyostelium* amoebae (Sternfield & David 1981) our proposed propulsion mechanism could be correct. Odell & Bonner (1986) presented a mathematical model for *Dictyostelium* crawling based on this tank propulsion mechanism — their model would therefore also be valid for our theoretical system.

As a next step, we must investigate whether this latter mechanism can cause epithelial sheet deformations. We look at a similar system, but with the added constraint that the cells are fixed at their apical ends. Now, as a result of cell A's cortical tractoring, it is stretched basally, while cell B is compressed towards the

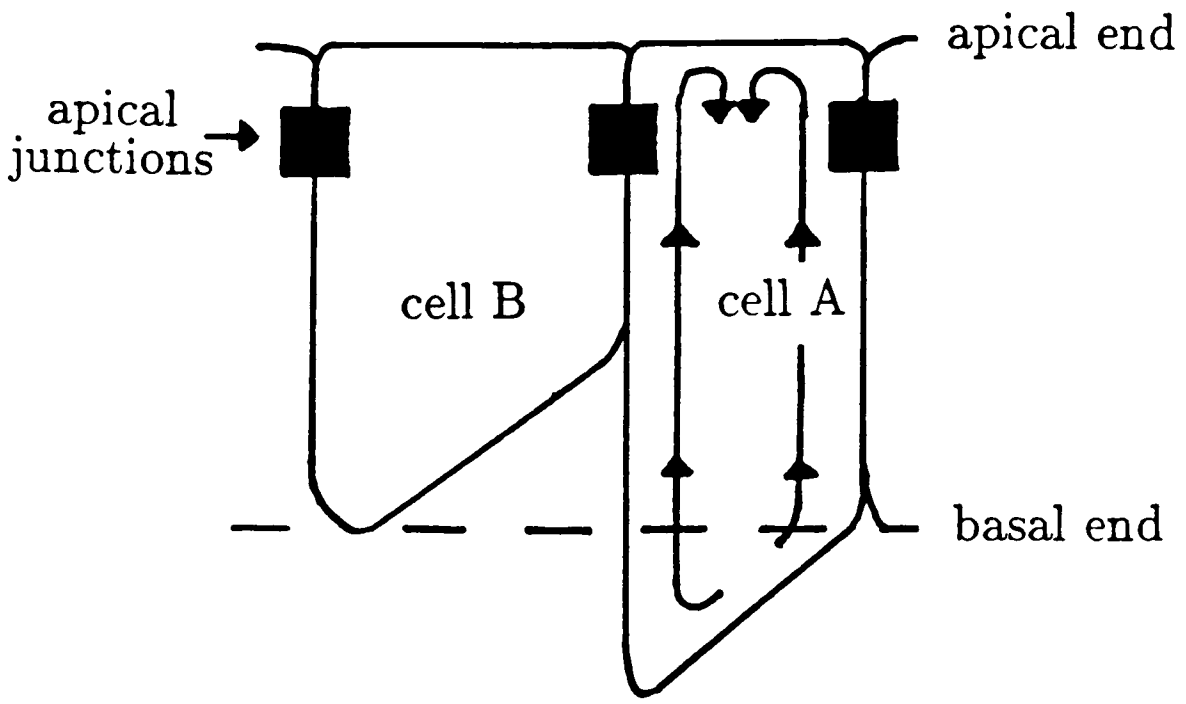

Figure 1.8: The cortical flow in cell A elongates it basally and compresses cell B apically.

apical end as is shown in Figure 1.8. Therefore, if we have a row of epithelial cells in conjunction with a linear gradient in signal chemical concentration, which induces cortical tractor activity, we should get a saw-tooth like pattern as seen in Figure 1.9. Apparently a linear gradient in a chemical, controlling the cortical tractor mechanism, can therefore not give rise to the observed patterns in the epithelium, as was proposed by Cheng *et al.* (1986) and Jacobson *et al.* (1985, 1986). Although a nonlinear gradient in a signal chemical might be responsible for epithelial patterns, the saw-tooth like appearance of the epithelial layer of cells will persist. Since such saw-tooth patterns are not observed in experimental systems it seems unlikely that their proposed mechanism is operative.

Furthermore, Cheng *et al.* (1986) wrote a finite difference mechanical balance equation for the vertical stretching of cells. By assuming that the cell widths stay fixed the equation was converted into a horizontal continuum field equation. However, because they used the principle of cell volume conservation in constructing the model, this transformation cannot be valid. Stretched cells become narrower and therefore, their finite element framework is not fixed, but

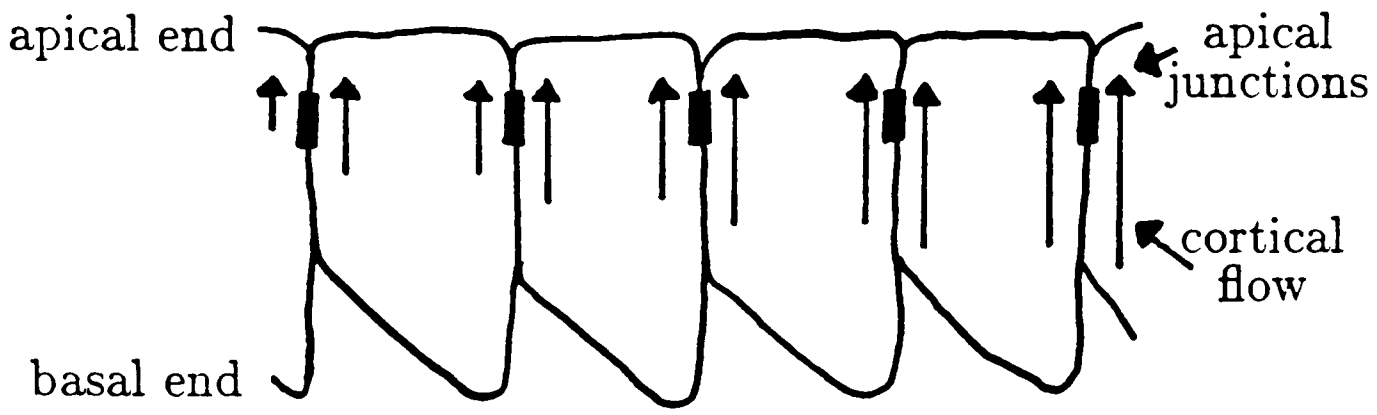

Figure 1.9: Saw-tooth like pattern expected in the epithelial layer due to a linear gradient in chemical concentration increasing from the left to the right.

moves in the horizontal plane.

A New Cortical Flow Model

We now describe a model based on a cortical flow mechanism which could explain the change of epithelial cells from their cuboidal shape to columnar shape.

We consider the same scenario as described above — the epithelial cells are fixed at their apical ends. However, we impose the additional constraint, used in the cytogel model of Section 1.4.1, that the epithelial cells are firmly attached to the basal lamina via adhesion tethers. These attachments prevent any movement that can result from the mechanical cortical tractor forces. Furthermore, we assume that the visco-elastic joint membrane between adjacent cells does not flow, as is the case in the cytoskeletal model.

The shear forces caused by the cortical tractor flow in cell A could now stretch the joint plasma membrane in an apical direction to elongate the two cells. If, for instance, the cortical tractor speeds of cells A and B are respectively v_a and v_b then a shear force

$$\eta \frac{(v_a + v_b)}{2},$$

with η the shear modulus, stretches the joint membrane. This stretching is

balanced by the visco-elastic restoring forces of the membrane. A gradient in a signalling chemical concentration, which determines the flow velocity of the cells' cortical tractors, could now give rise to a similar gradient in cell heights and so could be responsible for spatial patterns.

Because of cell volume conservation, an apical stretching cell will narrow and therefore induce horizontal forces in the epithelial sheet by pulling adjacent cells closer to itself. In our model the forces exerted by the elongation of the cells to the left and right of cell B will be functions of $(v_a + v_b)/2$ and $(v_b + v_c)/2$ respectively, where v_c is the cortical flow speed of cell C (which is adjacent to cell B). These cortical flow speeds are in turn functions of the signal chemical.

Similar to the cytogel model in Section 4.1.1 one could construct a continuum model consisting of a force balance equation for the horizontal stresses present in the epithelial sheet. We denote the cortical flow inducing signal chemical by $s(\boldsymbol{x}, t)$. Since the active traction in the sheet is effectively dependent on the chemical concentration s the horizontal active traction stress is modelled by a function τ of s. By including the contributions of the visco-elastic restoring stresses as well as the body forces an equation similar to (1.2) can be constructed.

Biologically this model, which we shall call the *cortical flow* model, seems much more acceptable than the cortical tractor model of Cheng *et al.* (1986). Apart from the cell-cell adhesion and junctional structures, there are also the actin fibres threading through the epithelial cells over relatively long distances. Since these fibres join epidermal cells into a coherent sheet, individual cell and membrane movement, as is required by the cortical tractor model, does not really seem plausible.

1.4.3 A General Model

A generalized model for epithelial morphogenesis, encapsulating the features of both the cytogel and cortical flow models is now proposed. Our model is based

on the biological observations and interpretations as reported by Belintsev *et al.* (1987).

We know that during epithelial morphogenesis some cells undergo an apical to basal elongation, or so called polarization, where their length-width ratio could change from 1 to a ratio of about 2.2 (Petrov & Beloussov 1984). Here we are not concerned with the mechanisms causing this cell polarization; whether it is due to cytogel contraction or cortical flow as described in the previous two sections, or some totally different mechanism, is not crucial to our model. Instead, we follow the generalized argument that polarizing cells induce tangential destabilizing stresses which are consequently responsible for epithelial pattern formation.

The existence of lateral elastic tensions in epithelial sheets have been demonstrated by Beloussov *et al.* (1975). In dissection-explantation experiments, passive deformations, where the columnar shaped cells return towards their original cuboidal shapes, have been detected. Belintsev *et al.* (1987) suggested that these deformations are passive relaxation of mechanical tensions pre-existing in the intact tissue. Furthermore, Beloussov *et al.* (1975) showed that these lateral tensions are due to the narrowing polarizing cells. Some minutes after an isolated piece of epithelia has relaxed, lateral tensions start to build up again. He demonstrated that these tensions are caused by a new polarizing domain appearing in the isolated fragment, which then stretches the surrounding cells.

On the other hand, we also know that lateral tensions in the epithelial sheet influence the polarization of cells. Kolega (1986) showed that cell elongation can be suppressed by stretching an isolated fragment of epithelia. This suggests that the stretching caused by polarized regions can inhibit polarization in other regions.

Belintsev *et al.* (1987) used a *hidden* parameter, to describe cell polarization, in a kinetic equation for simulating pattern formation in the epithelium. We believe that pattern formation can be described more realistically by the continuum mechanical force balance equation used in Section 1.4.1. The force balance

equation (1.2) reflects the various horizontal stresses present in the epithelial sheet. We assume that cells polarize in response to a chemical message, s. The active traction stress $\tau(s)$, a function of s, results from the tension created by the narrowing cells. The active traction is balanced by the restraining tethers attached to the basal lamina, by the long and short range elastic restoring forces and also by viscous restoring forces. Although the epithelial layer is able to exhibit viscous properties, in subsequent chapters we shall usually neglect these viscous effects.

The experimental work of Kolega (1986), described above, hinted at the importance of long range elastic stresses. Plickert (1980) showed that in the case of budding in marine hydrozoa, epithelial cells can sense whether distant cells are polarized or not. He induced placodes mechanically at irregular intervals. In response the epithelial layer then reorganized itself and the placodes were formed at the expected positions. Long range effects therefore seem crucial for global order and shape.

We shall show in the next chapter that long range effects are also crucial in our mathematical model. By omitting them our model cannot produce a coherent reproducible pattern, whereas with long range elastic forces included, our model also exhibits the same reorganization abilities as observed in the hydrozoa.

Chapter 2

A Tissue Interaction Model

2.1 Introduction

It is now well established that tissue interactions play a major role in the developing embryo. Most morphogenetic processes depend on the chemical and mechanical interaction between different tissue types (Wessells 1977). That skin pattern formation is no exception is demonstrated by the experimental evidence which we discuss in Section 2.2. It has been shown that communication between the epithelial and dermal layers is crucial during skin appendage formation.

The majority of skin pattern formation models proposed so far is, however, only concerned with either dermal or epidermal morphogenesis. In the light of recent experimental results we propose in Section 2.3 a model in which interaction between the two skin layers plays a fundamental role. The dermal and epithelial models, as described in Chapter 1, form the framework for this model.

The full tissue interaction model is very involved and extremely difficult to analyze, so, in Section 2.4 the model is reduced to a simple *small strain quasi-steady-state* system which, nevertheless, still retains the essential features of the full model.

A linear stability analysis of the small strain quasi-steady-state model is performed in Section 2.5 which gives an indication of the parameter space wherein spatial patterns are possible. We also explain in biological terms why pattern formation can only occur in a certain parameter space.

We examine three simplified versions of the linear model in Section 2.6 to determine which features of our model are important for coherent patterns to develop. A simple linear model which can give rise to pattern formation is subsequently considered in more detail.

2.2 The Biology of Tissue Interaction

In Sections 1.3.1 and 1.4.1 we saw examples of how the behaviour of cells is influenced by an external input — both mesenchymal CAM expression as well as cytogel contraction are affected by chemical signals. In this section we shall discuss, in more detail, the ways in which sets of cells influence the behaviour of other nearby cell populations. In particular, we shall look at epithelial and mesenchymal cell communication during skin morphogenesis which mainly involves *action-at-close-range*, or so called *proximate* interactions (see, for example, Gilbert 1988).

There are two types of proximate interactions: *instructive* interactions and *permissive* interactions. In instructive interactions specific instructions are given by one group of cells to another. For example, if one places the optic vesicle of the embryonic eye adjacent to a part of the head ectoderm, which in the normal course of development would have formed skin, then specific information is passed to that region of the ectoderm so that a lens rather than skin develops (McKeehan 1951).

On the other hand, in permissive interactions no specific instructions are passed, but development proceeds, however, only in the presence of another tissue. Epithelial cell mitosis, for instance, usually occurs only in the presence of adjacent embryonic mesenchyme (Gilbert 1988).

Several authors, for example Rawles (1963), Dhouailly (1973, 1975), Sengel (1976) and Dhouailly & Maderson (1984), have demonstrated the importance of instructive interaction between the epithelial layer and the mesenchymal layer during embryonic skin pattern formation.

Dhouailly (1973, 1975) studied this interaction by combining epidermal and dermal tissues from three different classes of animals — reptiles (lizards), birds (chicks) and mammals (mice). Her recombination experiments suggest that messages originate from the dermis to influence the patterns formed in the epidermis. For example, chick dermis explanted with any type of epidermis,

forms the type of appendage specific to the epidermis, but the typical shape, size and distribution are similar to that seen in feather bud formation.

Note that there are two possible ways in which such instructions can be passed from the mesenchyme to the epithelia (and vice versa) (Saxén *et al.* 1976). Firstly, they could be sent via soluble signals, so called paracrine signalling as is discussed in Section 1.2. Secondly, because of direct contact between epithelial and mesenchymal cells, signals could be transmitted mechanically. It is, however, not known which mechanism, if not both, is involved in relaying these instructions — no signalling molecules have been isolated as yet.

The experiments of Gallin *et al.* (1986), mentioned in Section 1.3.1, provide firm evidence of signals being passed from the epidermal to the dermal layer during skin development. We shall now discuss their results in more detail. It is known that explanted 6-day old dorsal chick skin, in organ culture, develops the expected chessboard array of feather germs. By adding anti-L-CAM antibodies at the time of explant, after 3 days, the N-CAM linked dermal papillae no longer develop a chessboard pattern, but merge into stripes with a different symmetry as can be seen in Figure 2.1. The antibodies were then removed and the tissue allowed to grow for another $7\frac{1}{2}$ days. Instead of the usual chessboard pattern a *cobblestone*-like array of plaques, with a more variable distribution, was formed.

As mentioned in Section 1.3.1 the epidermal layer is L-CAM positive during placode formation, while the dermal layer is free of L-CAMs. Functional tests also showed that anti-L-CAM inhibits epithelial cell condensations *in vitro*, but has no influence on the N-CAM linked dermal condensations. The anti-L-CAM fragments thus can have no direct influence on pattern formation in the dermis. The change in the behaviour of the mesenchymal cells when the epidermis is perturbed, must therefore be the result of altered instructions received from the epidermis.

Although it appears as if L-CAM is involved in relaying the signal, it seems unlikely that L-CAM itself acts in the role of a messenger (Gallin *et al.* 1986). The anti-L-CAM antibodies could either directly perturb the instructions which

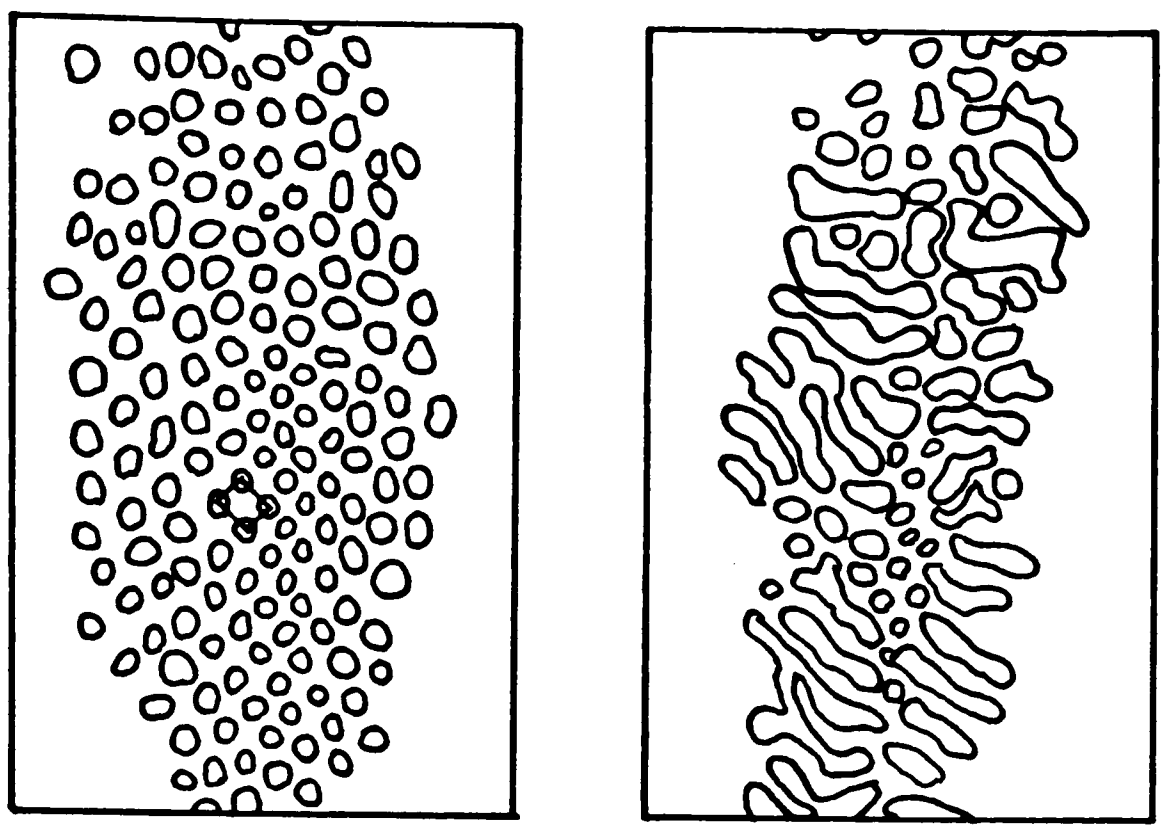

(a) (b)

Figure 2.1: Tracings of 7-day old chick embryo skin condensations cultured for three days. (a) The unperturbed chessboard pattern, with a typical square element highlighted, while in (b) anti-L-CAM fragments were cultured with the skin to give a cobblestone pattern (Redrawn from Gallin *et al.* 1986).

are sent to the dermis, or they could change the mechanical properties of the epithelial cells, thus influencing the instructions indirectly. The latter explanation seems more plausible, since L-CAMs play an important role in collectively linking the epithelial cells into a sheet. Disrupting these bonds should disrupt the mechanical behaviour of the epithelial layer.

It is evident from the experiments discussed that signals are not only relayed from the dermis to the epidermis and *vice versa*, but they are actually involved in the morphogenetic processes themselves. This fact is incorporated into the mathematical model which we propose in the next section.

2.3 The Tissue Interaction Model

Nagorcka (1986) proposed a tissue interaction mechanism to model the formation of feathers, scales and hair follicles. It consists of a reaction-diffusion system in the epidermis controlled by a switch mechanism situated in the dermis. The reacting diffusing morphogens provide the *positional information* (see Section 1.1) for epidermal patterning and also induce dermal condensations. This model is based on the earlier models of Nagorcka & Mooney (1982, 1985), Nagorcka (1984) and Mooney & Nagorcka (1985). Not only do these models depend on the positional information hypothesis, but a very delicately tuning is necessary for creating stable patterns.

A quasi-mechanochemical tissue interaction model, related to the above one, was proposed by Nagorcka *et al.* (1987). In this model a mechanochemical system for the dermal layer is coupled to an epidermal reaction-diffusion system. Numerical simulations demonstrated that these equations can generate regular complex spatially patterned solutions. This was confirmed by a detailed analytical study of a similar system by Shaw & Murray (1990).

We propose here a very different tissue interaction model involving mechanochemical cell movements activated by paracrine signalling. The model is based on the experimental evidence and proposals of Chuong & Edelman (1985a). We believe that this model is biologically more realistic than previous models. Crucially it does *not* use the concept of *positional information.*

As a result of their tissue interaction experiments, Chuong & Edelman (1985a) proposed that a specific factor produced by the L-CAM positive dermal cells, perhaps a hormone or peptide, triggers the formation of dermal condensations. This factor acts as a chemotactic agent and/or stimulates N-CAM expression to induce N-CAM linked papillae. The recombination experiments of Dhouailly (1973, 1975) suggest that, similarly, a dermally produced signal is involved in epidermal patterning by determining the shape, size and distribution of the placodes. Chuong & Edelman (1985a) therefore proposed that

epidermal placode formation is induced by a factor produced by the developing dermal condensations. When the placode and papilla formation of a feather germ is completed, the inductive factors are modified so as to halt the dermal aggregation and epithelial traction. Since these factors can still be active in lateral neighbouring tissue, periodic feather germ patterns could thus be formed in a self propagating manner.

A computer model was constructed by Gallin *et al.* (1986) to simulate this process. In their model, a signal E_s produced by the L-CAM linked epidermal cells increases the mitotic rate, aggregation and N-CAM expression of the mesenchyme. A dermal signal D_s, produced by the N-CAM positive condensations, in turn, induces placode formation in the epithelium. The dermal signal also downregulates the production of E_s which should then halt the papilla formation and therefore also the placode formation. Although the signals E_s and D_s are treated as diffusible morphogens, acting as intercellular chemical signals, the model is also consistent with direct cell-cell signalling, whether chemical or mechanical.

Their computer simulation involved 9600 epithelial cells and 3850 mesenchymal cells which acted on signals, and again released signals, in cyclic patterns. The cellular response to morphogen signals was modelled stochastically. The results they obtained were in good agreement with their experimental observations.

We propose a continuum tissue interaction model based on this discrete model of Gallin *et al.* (1986). Our model involves six field variables in space and time. The epidermal variables are:

$N(\boldsymbol{x},t)$ = the epidermal cell density at position $\boldsymbol{x}$ and time t;

$\hat{e}(\boldsymbol{x},t)$ = the epidermal concentration of a signal morphogen, produced in the epidermis, at position $\boldsymbol{x}$ and time t;

$\hat{s}(\boldsymbol{x},t)$ = the epidermal concentration of a signal morphogen, received from the dermis, at position $\boldsymbol{x}$ and time t.

Similarly, the variables for the dermis are:

$n(\boldsymbol{x},t)$ = the dermal cell density;

$s(\boldsymbol{x},t)$ = the dermal concentration of a signal morphogen produced in the dermis;

$e(\boldsymbol{x},t)$ = the dermal concentration of a signal morphogen received from the epidermis.

(We distinguish morphogen variables and related constants specific to the epidermal layer from those of the dermal layer by using the hat symbol.)

The chemical $\hat{e}(\boldsymbol{x},t)$, produced in the epidermal layer, is modelled as a diffusible morphogen. The morphogen diffuses from a high concentration in the epidermis, across the basal lamina, to a lower concentration in the dermis. This morphogen, represented by $e(\boldsymbol{x},t)$ in the dermis, then induces papilla formation. Similarly $s(\boldsymbol{x},t)$ is the diffusible morphogen signal produced in the dermal layer which then diffuses through the basal membrane to the epidermal layer. In the epidermis this morphogen, represented as $\hat{s}(\boldsymbol{x},t)$, induces placode formation. The scenario is sketched in Figure 2.2. Four reaction-diffusion type equations are used to serve as conservation equations for the four morphogens $\hat{e}$, $\hat{s}$, e and s.

Conservation Equation for $\hat{e}$ in the Epidermis

The random movement of the epidermally produced morphogen $\hat{e}$ is modelled with the classical Fickian diffusion term. Our conservation equation for this chemical is therefore

$$\frac{\partial \hat{e}}{\partial t} = \hat{D}_e \nabla^2 \hat{e} + \text{production} - \text{dermal signal} - \text{degradation},$$

where the positive constant $\hat{D}_e$ is the epidermal diffusion coefficient of $\hat{e}$.

We assume that $\hat{e}$ is produced by the epidermal cells and that its production can be altered by the morphogen signal $\hat{s}$ received from the dermal layer. We

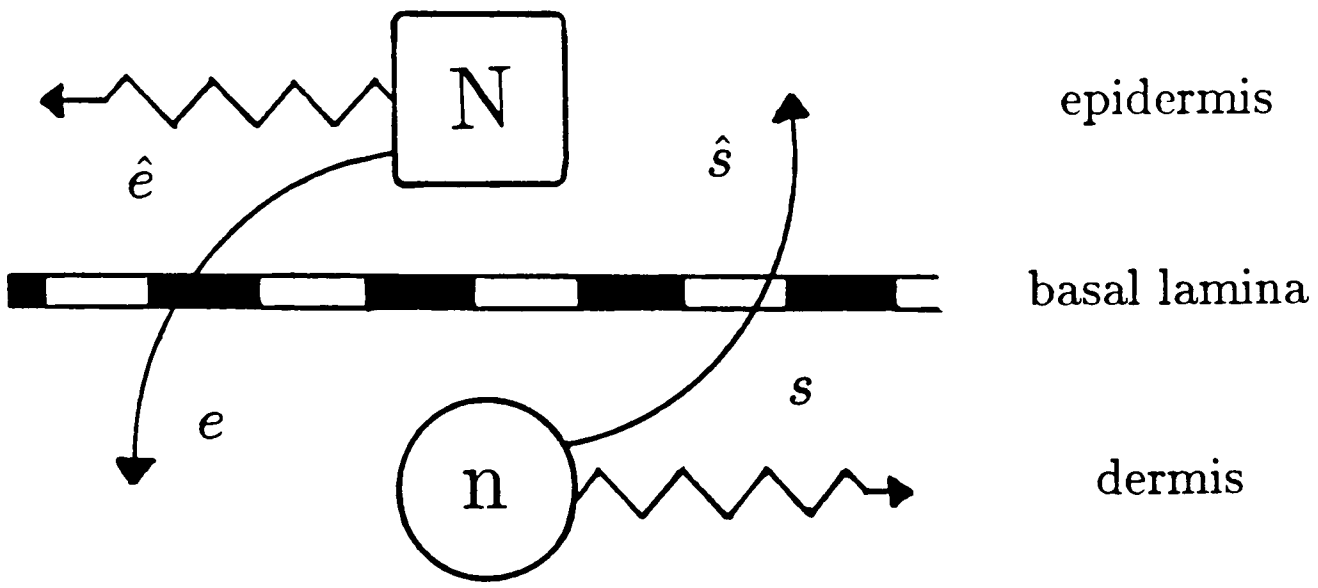

Figure 2.2: A sketch of the tissue interaction mechanism. The dermal cells n, produce a morphogen s, which diffuses to the epidermis where it is denoted by $\hat{s}$. Similarly $\hat{e}$, produced by the epidermal cells N, diffuses to the dermis where it is denoted by e.

model the production as a function f of N and $\hat{s}$,

$$\text{production} = f(N, \hat{s}).$$

During paracrine signalling the chemical molecules are rapidly degraded by enzymes and so we model the degradation term by

$$\text{degradation} = \hat{\gamma}\hat{e},$$

where the positive constant $\hat{\gamma}$ is a measure of the degradation rate.

The morphogen $\hat{e}$, diffuses across the basal lamina to the dermal layer where it is represented by the variable e. This loss of $\hat{e}$ from the epidermis is modelled by the term

$$\text{dermal signal} = P_e(\hat{e} - e),$$

where P_e is the positive diffusion constant.

Conservation Equation for e in the Dermis

The dermal morphogen e, is similarly modelled as a diffusing chemical. Since this morphogen diffuses from the epidermis to the dermis, we have the conservation equation for e as

$$\frac{\partial e}{\partial t} = D_e \nabla^2 e + P_e(\hat{e} - e) - \text{metabolism},$$

where D_e is the dermal diffusion constant for e and is positive.

The signalling molecules attach to the mesenchyme receptor cells and are metabolized by them. We assume that this metabolism is proportional to the receptor cell density n, and the chemical concentration e, and thus

$$\text{metabolism} = \gamma n e,$$

where the positive constant γ is the metabolic rate.

We can derive identical conservation equations for the dermally produced morphogen s, and the epidermal signal $\hat{s}$. In these equations the respective diffusion constants are D_s and $\hat{D}_s$, the degradation and metabolism constants are ν and $\hat{\nu}$, and the basal membrane diffusion constant is P_s. All the parameters are non-negative. The production of the chemical s is modelled by a function $g(n, e)$.

We have now established the signalling mechanisms for our tissue interaction model and so the next step is to introduce the cell conservation equations and the mechanochemical force balance equation. The interaction mechanism we described here is based on a continuum tissue interaction model proposed by Edelman, Murray, Odell & Oster (unpublished, 1986). To model the actual cell movements, they used the epidermal cortical tractor model of Cheng *et al.* (1986) coupled with a dermal chemotaxis equation.

However, in Section 1.4.2 we discussed the problems associated with the cortical tractor model of Cheng *et al.* (1986). Therefore, for modelling epithelial sheet movements, we use instead the general mechanochemical system described in Section 1.4.3 (see equations (1.2) and (1.3)). There it is assumed that the

active contraction stress is induced by a chemical signal. In our tissue interaction model we make the assumption that the active contraction is triggered by the signal chemical $\hat{s}$, originating from the dermis.

For the dermal cells we use the general chemotaxis equation (1.1). In Section 1.3.3 we modelled the taxis as being induced by an external signalling chemical. Here we assume that the taxis is caused by the signal morphogen e, originating from the epidermis.

The full tissue interaction system is now given by the following equations: The epidermal cell equations are

$$\nabla \cdot \Big\{ \frac{E}{1+\upsilon} \Big[\boldsymbol{\varepsilon} - \beta_1 \nabla^2 \boldsymbol{\varepsilon} + \frac{\upsilon}{1-2\upsilon} (\theta - \beta_2 \nabla^2 \theta) \boldsymbol{I} \Big] + \mu_1 \frac{\partial \boldsymbol{\varepsilon}}{\partial t} + \mu_2 \frac{\partial \theta}{\partial t} \boldsymbol{I} + \frac{\tau \hat{s}^2}{1 + c\hat{s}^2} \boldsymbol{I} \Big\} = \rho \boldsymbol{u} \ , \tag{2.1a}$$

$$\frac{\partial N}{\partial t} = -\nabla \cdot N \frac{\partial \boldsymbol{u}}{\partial t}, \tag{2.1b}$$

and the epidermal morphogen equations are

$$\frac{\partial \hat{e}}{\partial t} = \hat{D}_e \nabla^2 \hat{e} + f(N, \hat{s}) - P_e(\hat{e} - e) - \hat{\gamma} \hat{e}, \tag{2.2a}$$

$$\frac{\partial \hat{s}}{\partial t} = \hat{D}_s \nabla^2 \hat{s} + P_s(s - \hat{s}) - \hat{\nu} N \hat{s}. \tag{2.2b}$$

The dermal chemotaxis equation is

$$\frac{\partial n}{\partial t} = D \nabla^2 n - \alpha \nabla \cdot n \nabla e + r n (\bar{n} - n), \tag{2.3a}$$

and the dermal morphogen equations are

$$\frac{\partial s}{\partial t} = D_s \nabla^2 s + g(n, e) - P_s(s - \hat{s}) - \nu s, \tag{2.4a}$$

$$\frac{\partial e}{\partial t} = D_e \nabla^2 e + P_e(\hat{e} - e) - \gamma n e. \tag{2.4b}$$

Nondimensional System

Nondimensionalizing the above system of equations reduces the number of parameters and also defines nondimensional parameter groupings. These parameter groupings are biologically significant, since they show which biological parameters have equivalent effects.

Let T_0 and L_0 be typical time and length scales respectively, $\bar{N}$ and $\bar{n}$ typical average cell densities and s_0 and e_0 typical morphogen concentrations. Define the nondimensional quantities

$$t^* = \frac{t}{T_0}, \qquad \boldsymbol{x}^* = \frac{\boldsymbol{x}}{L_0}, \qquad \boldsymbol{u}^* = \frac{\boldsymbol{u}}{L_0}, \qquad N^* = \frac{N}{\bar{N}}, \qquad n^* = \frac{n}{\bar{n}},$$

$$\hat{s}^* = \frac{\hat{s}}{s_0}, \qquad s^* = \frac{s}{s_0}, \qquad \hat{e}^* = \frac{\hat{e}}{e_0}, \qquad e^* = \frac{e}{e_0},$$

$$\mu_1^* = \frac{\mu_1(1+\upsilon)}{ET_0}, \qquad \mu_2^* = \frac{\mu_2(1+\upsilon)}{ET_0}, \qquad \tau^*(\hat{s}^*) = \frac{\tau s_0^2(1+\upsilon)}{E},$$

$$c^* = cs_0^2, \qquad \beta_1^* = \frac{\beta_1}{L_0^2}, \qquad \beta_2^* = \frac{\beta_2}{L_0^2}, \qquad \rho^* = \frac{\rho L_0(1+\upsilon)}{E},$$

$$\hat{D}_e^* = \frac{\hat{D}_e T_0}{L_0^2}, \qquad f^*(N^*, \hat{s}^*) = \frac{f(N, \hat{s})T_0}{e_0}, \qquad P_e^* = P_e T_0, \qquad \hat{\gamma}^* = \hat{\gamma} T_0,$$

$$\hat{D}_s^* = \frac{\hat{D}_s T_0}{L_0^2}, \qquad P_s^* = P_s T_0, \qquad \hat{\nu}^* = \hat{\nu}\bar{N} T_0,$$

$$D^* = \frac{DT_0}{L_0^2}, \qquad r^* = r\bar{n}T_0, \qquad \alpha^* = \frac{\alpha e_0 T_0}{L_0^2},$$

$$D_s^* = \frac{D_s T_0}{L_0^2}, \qquad g^*(n^*, e^*) = \frac{g(n,e)T_0}{s_0}, \qquad P_s^* = P_s T_0, \qquad \nu^* = \nu T_0,$$

$$D_e^* = \frac{D_e T_0}{L_0^2}, \qquad P_e^* = P_e T_0, \qquad \gamma^* = \gamma\bar{n}T_0.$$

Dropping the asterisks for algebraic convenience the dimensionless epidermal cell equations are

$$\nabla \cdot \Big\{ \boldsymbol{\epsilon} - \beta_1 \nabla^2 \boldsymbol{\epsilon} + \frac{\upsilon}{1-2\upsilon}(\theta - \beta_2 \nabla^2 \theta)\boldsymbol{I} + \mu_1 \frac{\partial \boldsymbol{\epsilon}}{\partial t} + \mu_2 \frac{\partial \theta}{\partial t}\boldsymbol{I} + \frac{\tau \hat{s}^2}{1 + c\hat{s}^2} \Big\} = \rho \boldsymbol{u}\,, \tag{2.5a}$$

$$\frac{\partial N}{\partial t} = -\nabla \cdot N \frac{\partial \boldsymbol{u}}{\partial t}, \tag{2.5b}$$

while the epidermal morphogen equations become

$$\frac{\partial \hat{e}}{\partial t} = \hat{D}_e \nabla^2 \hat{e} + f(N, \hat{s}) - P_e(\hat{e} - e) - \hat{\gamma}\hat{e}, \tag{2.6a}$$

$$\frac{\partial \hat{s}}{\partial t} = \hat{D}_s \nabla^2 \hat{s} + P_s(s - \hat{s}) - \hat{\nu} N \hat{s}. \tag{2.6b}$$

The dermal equations become

$$\frac{\partial n}{\partial t} = D\nabla^2 n - \nabla \cdot n\alpha \nabla e + rn(1-n), \tag{2.7a}$$

$$\frac{\partial s}{\partial t} = D_s \nabla^2 s + g(n,e) - P_s(s - \hat{s}) - \nu s, \tag{2.7b}$$

$$\frac{\partial e}{\partial t} = D_e \nabla^2 e + P_e(\hat{e} - e) - \gamma n e. \tag{2.7c}$$

Note that by taking different values for T_0 we could study different time scales, for example, setting $T_0 = L_0^2/D$ would imply that we are using the cell diffusion time scale and so $D^* = 1$.

2.4 Small Strain Quasi-Steady-State System

The above set of seven coupled nonlinear differential equations is too complicated to lend itself to any useful analysis at this stage. In this section we show how the system can be reduced to only two coupled equations by making several reasonable simplifying assumptions. The essential features of our tissue interaction mechanism are, however, retained in this caricature model.

As a first step we can reduce the tensor equation (2.5a) to a scalar dilation equation in θ. Taking the divergence of (2.5a) and using the tensor identities

$$\nabla \cdot \boldsymbol{\varepsilon} = \text{grad}\ \theta - \text{curl curl}\ \boldsymbol{u},$$

$$\nabla \cdot (\text{curl}\ \boldsymbol{u}) = \mathbf{0}, \qquad \nabla \cdot (\theta \boldsymbol{I}) = \boldsymbol{I} \cdot \text{grad}\ \theta,$$

we have

$$\mu \frac{\partial}{\partial t} \nabla^2 \theta + \nabla^2 \theta - \beta \nabla^4 \theta + \nabla^2 \tau(\hat{s}) = \rho \theta,$$

where $\mu = \mu_1 + \mu_2$, $\beta = \beta_1 + \beta_2$ and μ, β, ρ and τ have been divided by $(1-\upsilon)/(1-2\upsilon)$.

In many embryological situations the changes in cell strain and cell density during pattern formation are small. We therefore make the simplifying assumption that the dilation θ, remains small during feather germ formation.

With this small strain approximation we linearize equation (2.5b) about the nondimensionalized steady state $N = 1$. With $N = 1 + \tilde{N}$, $|\tilde{N}| \ll 1$, we obtain

$$\frac{\partial \tilde{N}}{\partial t} = -\nabla \cdot \frac{\partial \boldsymbol{u}}{\partial t},$$

which gives, on integration,

$$N = 1 - \nabla \cdot \boldsymbol{u} = 1 - \theta. \tag{2.8}$$

Since $\theta \ll 1$ the epithelial cell density N, remains positive. We now substitute the linear form (2.8), relating the epidermal cell density N, to the dilation θ, into equations (2.6a) and (2.6b) to obtain a *small strain approximation* system.

In paracrine signalling the chemical molecules are either rapidly metabolized by receptor cells or degraded by enzymes, while the effect of the local morphogen diffusion is believed to be small. By isolating the more important processes we can simplify our system considerably. Hence we assume that the local morphogen diffusion effects are negligibly small compared to the metabolism, degradation, production and diffusion across the basal lamina of the morphogens and so we set $\hat{D}_e$, $\hat{D}_s$, D_s and D_e equal to zero.

We further assume that the free morphogen concentration in any layer stays constant with time — so $\hat{e}$, e, $\hat{s}$ and s are at their equilibrium states. This implies that the signalling morphogens are used up, degrade and diffuse to the adjacent layer at the same rate they diffuse into, and are produced in, a layer. This assumption is consistent with the concept of paracrine signalling. We thus have a *quasi-steady-state* model in which equations (2.6a), (2.6b), (2.7b) and (2.7c) become the four algebraic equations:

$$\begin{aligned} f(1-\theta, \hat{s}) &= P_e(\hat{e} - e) + \hat{\gamma}\hat{e}, \\ P_s(s - \hat{s}) &= \hat{\nu}(1-\theta)\hat{s}, \\ g(n, e) &= P_s(s - \hat{s}) + \nu s, \\ P_e(e - \hat{e}) &= \gamma n e. \end{aligned}$$

Eliminating s and $\hat{e}$ we can solve for $\hat{s}$ and e as functions of $1 - \theta$ and n.

The full *small strain quasi-steady-state* system therefore consists of two coupled nonlinear partial differential equations in θ and n, namely

$$\mu\frac{\partial}{\partial t}\nabla^2\theta + \nabla^2\theta - \beta\nabla^4\theta + \nabla^2\frac{\tau\hat{s}^2(1-\theta,n)}{1+c\hat{s}^2(1-\theta,n)} = \rho\theta, \tag{2.9a}$$

$$\frac{\partial n}{\partial t} = D\nabla^2 n - \alpha\nabla\cdot n\nabla e(1-\theta,n) + rn(1-n), \tag{2.9b}$$

where the functional forms of $\hat{s}$ and e are

$$\begin{aligned}\hat{s}(1-\theta,n) &= \frac{P_s g(n,e)}{\nu P_s + (\nu+P_s)\hat{\nu}(1-\theta)},\\ e(1-\theta,n) &= \frac{P_e f(1-\theta,\hat{s})}{\hat{\gamma}P_e + (\hat{\gamma}+P_e)\gamma n}.\end{aligned}$$

We also have the physically imposed condition $|\theta| < 1$.

So far we have not given detailed analytical expressions for the chemical production functions $f(1-\theta,\hat{s})$ and $g(n,e)$. Since our proposed tissue interaction mechanism is a model, the detailed forms of these functions are not important at this stage, only their qualitative forms. Gallin *et al.* (1986) suggested in their computer model that the morphogen s, diffusing from the dermis to the epidermis, could inhibit the production of the dermally produced morphogen $\hat{e}$. This effect was included by Edelman, Murray, Odell & Oster (unpublished, 1986) in their tissue interaction model by setting

$$f(1-\theta,\hat{s}) = \frac{k_0(1-\theta)}{1+k_1\hat{s}^2} = \frac{k_0 N}{1+k_1\hat{s}^2},$$

in which k_0 and k_1 are positive constants.

We, however, assume for simplicity that the production of both morphogens $\hat{e}$ and s are proportional to the respective cell densities $N\,(=1-\theta)$ and n, so that

$$f(1-\theta,\hat{s}) = k_e(1-\theta) \quad \text{and} \quad g(n,e) = k_s n,$$

where the positive constants k_e and k_s, are the nondimensional epidermal and dermal production rates respectively.

By making the following substitutions

$$\tau^* = \frac{\tau k_s^2}{\nu^2}, \qquad c^* = \frac{c k_s^2}{\nu^2}, \qquad \hat{\nu}^* = \frac{\hat{\nu}(\nu + P_s)}{\nu P_s},$$
$$\alpha^* = \frac{\alpha k_e}{\hat{\gamma}}, \qquad \gamma^* = \frac{\gamma(\hat{\gamma} + P_e)}{\hat{\gamma} P_e}, \tag{2.10}$$

the nonlinear model reduces to

$$\mu \frac{\partial}{\partial t} \nabla^2 \theta + \nabla^2 \theta - \beta \nabla^4 \theta + \tau \nabla^2 \frac{n^2}{[1 + \hat{\nu}(1 - \theta)]^2 + cn^2} = \rho \theta, \tag{2.11a}$$

$$\frac{\partial n}{\partial t} = D \nabla^2 n - \alpha \nabla \cdot n \nabla \frac{1 - \theta}{1 + \gamma n} + rn(1 - n), \tag{2.11b}$$

where we have omitted the asterisks for notational convenience.

2.5 Linear Stability Analysis

Here we examine the behaviour of a linear version of the small strain quasi-steady-state system. Not only does the linear analysis give a rough guide of how the nonlinear model will behave, it also enables us to predict parameter ranges in which spatially heterogeneous patterns could exist.

The equations (2.11) admit the spatially homogeneous steady states

$$n = 0, \quad \theta = 0 \quad \text{and} \quad n = 1, \quad \theta = 0.$$

Since we are interested in spatial pattern formation occuring in established cell populations, the first steady state is not of any interest at the moment. We consider only the steady state where the nondimensional cell densities, N $(= 1 - \theta)$ and n, are equal to unity.

We linearize about this steady state by setting

$$n = 1 + \tilde{n} \quad \text{and} \quad \theta = \tilde{\theta},$$

where $|\tilde{n}| \ll 1$ and $|\tilde{\theta}| \ll 1$. Ignoring higher order terms and dropping the tildes, the linearized equations are

$$\mu \frac{\partial}{\partial t} \nabla^2 \theta = \rho \theta - \nabla^2 \theta + \beta \nabla^4 \theta - P_1 \nabla^2 \theta - P_2 \nabla^2 n, \tag{2.12a}$$

$$\frac{\partial n}{\partial t} = D \nabla^2 n - rn + Q_1 \nabla^2 n + Q_2 \nabla^2 \theta, \tag{2.12b}$$

where

$$P_1 = \frac{2\tau\hat{\nu}(1+\hat{\nu})}{(1+2\hat{\nu}+\hat{\nu}^2+c)^2}, \tag{2.13a}$$

$$P_2 = \frac{2\tau(1+2\hat{\nu}+\hat{\nu}^2)}{(1+2\hat{\nu}+\hat{\nu}^2+c)^2}, \tag{2.13b}$$

$$Q_1 = \frac{\alpha\gamma}{(1+\gamma)^2}, \tag{2.13c}$$

$$Q_2 = \frac{\alpha}{1+\gamma}, \tag{2.13d}$$

are all positive.

We expand θ and n in their Fourier series and, using the principle of superposition, look for solutions $\boldsymbol{w}$ in the form

$$\boldsymbol{w} = \begin{pmatrix} \theta \\ n \end{pmatrix} \propto e^{(i\mathbf{k}\cdot\mathbf{x}+\lambda(k^2)t)},$$

where $\boldsymbol{k}$ is the wavevector, $k^2 = \boldsymbol{k}\cdot\boldsymbol{k}$. and $\lambda(k^2)$ is the growth rate of the spatial mode corresponding to the wavevector $\boldsymbol{k}$.

Substituting $\boldsymbol{w}$ into the linearized system (2.12) gives a set of two linear homogeneous equations which are solvable if and only if

$$\begin{vmatrix} -\mu k^2\lambda - \beta k^4 - (P_1+1)k^2 - \rho & -P_2k^2 \\ Q_2k^2 & \lambda + (D+Q_1)k^2 + r \end{vmatrix} = 0.$$

Solving this expression gives a quadratic for $\lambda(k^2)$, namely

$$a(k^2)\lambda^2 + b(k^2)\lambda + c(k^2) = 0,$$

where

$$\begin{aligned} a(k^2) &= \mu k^2, \\ b(k^2) &= (\mu D + \mu Q_1 + \beta)k^4 + (P_1 + 1 + \mu r)k^2 + \rho, \\ c(k^2) &= \beta(D+Q_1)k^6 - (P_2Q_2 - r\beta - DP_1 - P_1Q_1 - D - Q_1)k^4 \\ &\quad + (r + rP_1 + \rho D + \rho Q_1)k^2 + \rho r. \end{aligned}$$

We define the *dispersion relation* to be the the root $\lambda(k^2)$ of this quadratic with largest real part. From the point of view of linear stability we are only

interested in the root of $\lambda(k^2)$ with the largest real part, hence we consider the dispersion relation

$$\lambda(k^2) = \begin{cases} \dfrac{-b(k^2) + \Re\left(\sqrt{b^2(k^2) - 4a(k^2)c(k^2)}\right)}{2a(k^2)} & \text{if } k^2 \neq 0 \\ -r & \text{if } k^2 = 0. \end{cases} \tag{2.14}$$

The general solution to the linear system is therefore

$$\boldsymbol{w}(\boldsymbol{x}, t) = \int p_f(\boldsymbol{k}) \begin{pmatrix} 1 \\ M(k^2) \end{pmatrix} e^{(i\mathbf{k}\cdot\mathbf{x} + \lambda(k^2)t)}\, d\boldsymbol{k}, \tag{2.15}$$

where $p_f(\boldsymbol{k})$ is determined by a Fourier transform of the initial conditions $\boldsymbol{w}(\boldsymbol{x}, 0)$ and

$$M(k^2) = \frac{-Q_2 k^2}{\lambda(k^2) + (D + Q_1)k^2 + r}. \tag{2.16}$$

The steady state is linearly stable if $\Re\lambda(k^2) \leq 0$, because perturbations about the steady state will then tend to zero as $t \to \infty$. The linear analysis also predicts that only those spatial modes with wavenumbers satisfying $\Re\lambda(k^2) > 0$, will grow exponentially. Spatially heterogeneous solutions of the linear system are characterized by a dispersion relation satisfying $\Re\lambda(0) \leq 0$, but which exhibits a range of unstable modes corresponding to the eigenvalues k^2 with $\Re\lambda(k^2) > 0$. These modes grow initially, but then the higher order terms become important and our linear approximation is no longer valid.

Since $a(k^2)$ and $b(k^2)$ are positive for all non-zero values of k^2, $\Re\lambda(k^2)$ is positive if and only if $c(k^2)$ is negative for some non-zero k^2. The function $c(k^2)$ is a cubic in k^2 and according to Descartes' rule of signs, as it has two sign changes, the expression has either two positive real roots or none.

There is only one negative term in the expression for $c(k^2)$, which is also the only term in which the two parameters P_2 and Q_2 appear. These two destabilizing parameters, together with P_1 and Q_1, are involved in the tissue interaction mechanism of the model — P_1 and P_2 are the parameters which reflect the dermal to epidermal interaction, while Q_1 and Q_2 reflect the epidermal to dermal interaction. The parameters P_1 and Q_1, however, have a stabilizing effect.

The steady state can become linearly unstable only if both P_2 and Q_2 are non-zero. Thus two-way interaction is absolutely crucial for this model to exhibit spatially heterogeneous patterns. That neither the dermal nor epidermal model described above can give spatial patterns separately is an important feature of our model which distinguishes it from previous tissue interaction models.

This also correlates well with our physical understanding of the model. Assume that in a specific dermal region the cell density is slightly higher than in surrounding areas. Biologically this may arise due to the very small natural inhomogeneties present in embryos. Because of the higher cell density, the concentration of the locally produced morphogen, s, rises in this region. This chemical diffuses to the epidermal layer to become $\hat{s}$. The concentration of $\hat{s}$ will be higher in the epithelial tissue directly above the dermal condensation and consequently the traction in the epidermal sheet increases so that a region of polarized cells develops. Here, because of the higher epithelial cell density, more of the morphogen $\hat{e}$ is manufactured in the polarized region than in the neighbouring areas. Therefore a greater amount of the chemical $\hat{e}$ diffuses to the dermal layer directly below the polarized cells to enhance the aggregation process there. In this way we get the simultaneous formation of papillae and placodes due to the positive feedback mechanisms.

By switching off, say, the dermal signalling mechanism there will be no inductive factor for epidermal contractions. Thus the dermal cells receive a homogeneous morphogen signal from the epidermis and the chemotactically induced condensations cannot develop. Turning off the epidermal signalling mechanism leads to a similar scenario.

To understand how the stabilizing parameters P_1 and Q_1 come to appear in our dispersion relation (2.14) we must focus on the dermal equation with the stabilizing interaction term $Q_1\nabla^2 n$. Because of chemotaxis, dermal cells move towards regions of high morphogen concentration e. The dermal cells, which act as receptor cells, consume the chemical e at a rate proportional to the dermal cell density and the chemical concentration. In the dermal aggregation centres

both the cell density n, and the chemical concentration e, are high, so that e is rapidly metabolized by the cells. In the surrounding tissue where n and e are low the metabolism of e is minimal and the concentration of free morphogen rises. This inhibits the chemotaxis process and has a stabilizing effect. Hence, if the metabolic rate is large in comparison to the other processes then this stabilizing effect is dominant and spatial patterns cannot develop. Similar arguments can be used to explain the reason for the stabilizing term $P_1\nabla^2\theta$ in the epidermal equation.

We can deduce the qualitative effects of some of the various other terms in the model as regards to their pattern formation potential, by simply looking at the expressions for $b(k^2)$ and $c(k^2)$. This leads to a better heuristic understanding of the model mechanism with respect to pattern formation.

Since we require $c(k^2)$ to be negative we see that the long range effects, quantified by β, are stabilizing — if β increases $c(k^2)$ becomes more positive. The epithelial tethering, quantified by the parameter ρ, also stabilizes the solution. In the dermal layer we see that both the logistic form of cell proliferation, reflected by r, and the cell diffusion D, are stabilizing.

Ideally one should test these effects experimentally and compare the results with those predicted here. Would, for example, an experimental reduction of the dermal cell proliferation inhibit pattern formation as predicted here?

Although we have shown that, with the correct parameter choice, our model solution can indeed bifurcate from a homogeneous solution the parameters P_1, P_2, Q_1 and Q_2 are in fact complicated expressions of our actual nondimensional model parameters, see (2.13) and we therefore we still have to show that bifurcation is possible in terms of these original parameters.

This is done formally by showing that for any positive value k_c^2 of k^2, one can find a non-negative parameter space for which $c(k_c^2) < 0$. It is convenient for this purpose to write $c(k_c^2)$ in the form

$$c(k_c^2) = c_0 + c_1Q_1 - c_2Q_2,$$

where

$$
\begin{aligned}
c_0 &= \beta D k_c^6 + (r\beta + DP_1 + D)k_c^4 + (rP_1 + r + \rho D)k_c^2 + \rho r, \\
c_1 &= \beta k_c^6 + (P_1 + 1)k_c^4 + \rho k_c^2, \\
c_2 &= P_2 k_c^4,
\end{aligned}
$$

are all positive.

Assume $c(k_c^2) \geq 0$. We are thus in one of the following parameter spaces:

(i) $c_1 Q_1 - c_2 Q_2 < 0$.

Since Q_1 and Q_2 are linear in α, see (2.13c) and (2.13d), we can use α as a bifurcation parameter. By increasing α we can make the left hand side of the expression (i) arbitrarily large and negative so that $c(k_c^2)$ becomes negative.

(ii) $c_1 Q_1 - c_2 Q_2 \geq 0$ and $c_0 - c_2 \alpha < 0$.

Here, since from (2.13c) and (2.13d) we have

$$\lim_{\gamma \to 0^+} Q_1(\gamma) = 0 \quad \text{and} \quad \lim_{\gamma \to 0^+} Q_2(\gamma) = \alpha,$$

we can use γ as a bifurcation parameter. By decreasing γ we move into parameter space (i) and we can then increase α to make $c(k_c^2)$ negative. Alternatively, because of the second inequality in (ii), we can make $c(k_c^2)$ negative by only decreasing γ.

(iii) $c_1 Q_1 - c_2 Q_2 \geq 0$ and $c_0 - c_2 \alpha \geq 0$.

By decreasing the value of γ we can never get $c(k_c^2)$ negative. This can only be done by decreasing γ until we move into parameter space (i), where we can again use α as bifurcation parameter.

In summary, one can thus always move into an unstable domain of the parameter space by changing either one or both of the bifurcation parameters γ and α. By a similar series of arguments it can be demonstrated that by decreasing $\hat{\nu}$ and/or increasing τ, $c(k^2)$ can be made negative for some positive k^2.

Returning to the expressions of α, γ, τ and $\hat{\nu}$ in terms of the original parameters, see (2.10), we can now examine under what biological conditions bifurcation to spatial pattern is possible.

The parameter α will be large if the production rate of the chemical $\hat{e}$ (k_e in terms of the original parameter set), as well as the chemotactic effect (α) are large in comparison with the degradation of $\hat{e}$ ($\hat{\gamma}$). For the constant γ to be small the dermal cell metabolism (originally also γ) must be low and the diffusion across the basal lamina (P_e) must be sufficiently fast in comparison with the chemical degradation ($\hat{\gamma}$).

Analogues to the above, τ will be large if the production rate of the chemical s, and the epithelial traction effects are large in comparison to the degradation of s. The constant $\hat{\nu}$ is small if the epidermal cell metabolism is low and the diffusion of s across the basal lamina is fast in comparison with the degradation of s.

2.6 Simplified Linear Models

In the previous section we showed that the linear version of our model is indeed capable of spatial pattern formation. A short discussion of the role of the various terms was also given by looking at their contribution to the dispersion relation. Here we highlight the role of some of the more important terms in our linear system of equations (2.12) with regards to pattern formation by considering some special cases in which one or more of the factors affecting cell motion or mechanical equilibrium are neglected. We do this by setting various constants equal to zero and examining the resulting dispersion relations.

In embryogenesis coherent reproducible patterns develop from natural initial inhomogeneties — different embryos of the same species develop similar patterns. It is crucial that our model should be able to mimic this: for a given set of parameters the same pattern should develop independent of the initial conditions. In terms of our linear model this implies that only a very small

range of eigenvalues should be unstable so that patterns corresponding to these are the only ones that grow. By further imposing boundary conditions, as we shall do in the next two chapters, we can restrict the allowable patterns even further. However, if there is, instead, a large set of unstable eigenvalues, the patterns that would develop could be very different, even if the initial conditions are only perturbed slightly.

In the first case we analyze the linear model (2.12) when the epidermal long range effects are omitted by setting $\beta = 0$. Our dispersion relation now reduces to

$$\lambda(k^2) = \begin{cases} \dfrac{-b(k^2) + \Re\left(\sqrt{b^2(k^2) - 4a(k^2)c(k^2)}\right)}{2a(k^2)} & \text{if } k^2 \neq 0 \\ -r & \text{if } k^2 = 0. \end{cases}$$

where

$$\begin{aligned} a(k^2) &= \mu k^2, \\ b(k^2) &= (\mu D + \mu Q_1)k^4 + (P_1 + 1 + \mu r)k^2 + \rho, \\ c(k^2) &= -(Q_2P_2 - DP_1 - Q_1P_1 - D - Q_1)k^4 \\ &\quad + (r + rP_1 + \rho D + \rho P_1)k^2 + \rho r. \end{aligned}$$

It is easy to show that if $c(k_c^2) < 0$ for some k_c^2 then $c(k^2) < 0$ for all $k^2 > k_c^2$. We thus have an infinite range of allowable eigenvalues (Figure 2.3(a)). Contrary to our requirements the linear solution now depends critically on the initial conditions. It is therefore evident that long range elastic restoring forces are essential for obtaining a finite range of unstable eigenvalues. The fact that coherent reproducible patterns are only possible if we include long range effects is consistent with the experiments of Plickert (1980) and Kolega (1986) as was discussed in Section 1.4.1.

In the second example we omit the epithelial tethering and dermal proliferation by respectively setting $\rho = 0$ and $r = 0$. The functions $a(k^2)$, $b(k^2)$ and $c(k^2)$ appearing in the dispersion relation reduce to

$$a(k^2) = \mu k^2,$$

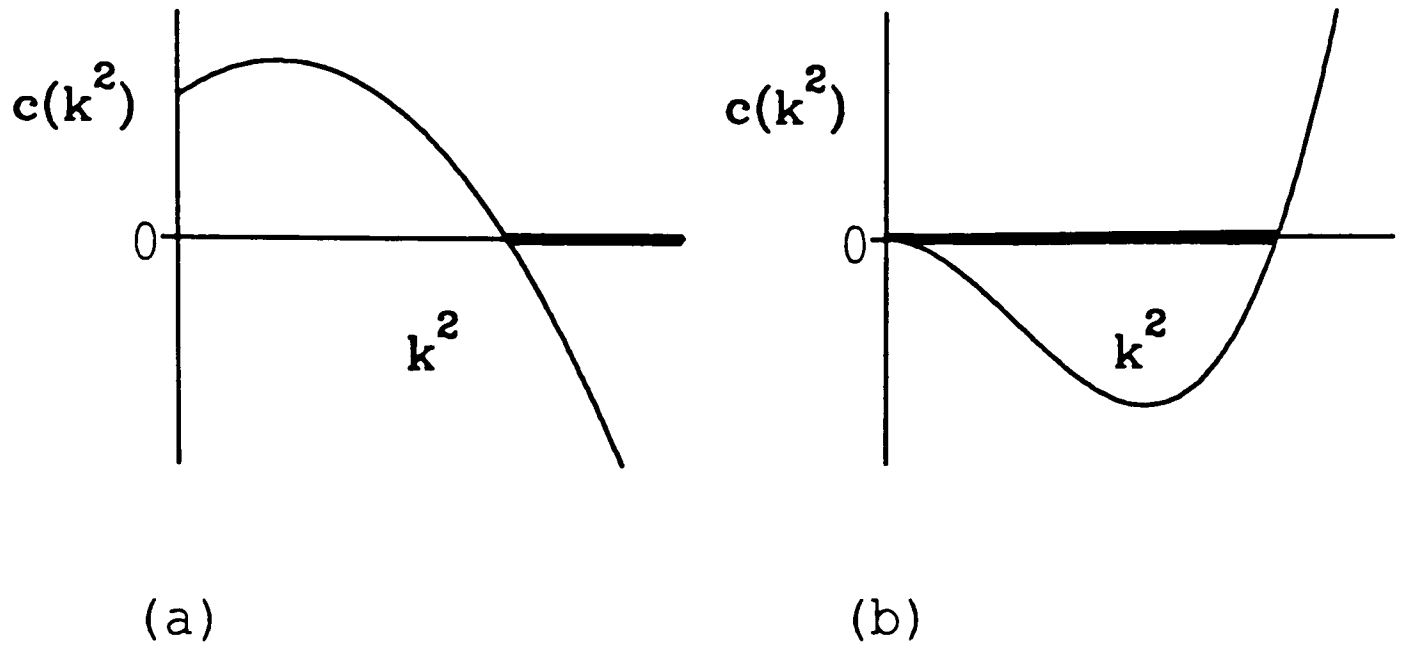

Figure 2.3: The forms of the function $c(k^2)$ when (a) $\beta = 0$ and (b) $\rho = 0,\ r = 0$. The steady state is unstable if $c(k^2) < 0$, since then $\lambda(k^2) > 0$.

$$\begin{aligned} b(k^2) &= (\mu D + \mu Q_1 + \beta)k^4 + (P_1 + 1)k^2, \\ c(k^2) &= \beta(D + Q_1)k^6 - (Q_2P_2 - DP_1 - Q_1P_1 - D - Q_1)k^4. \end{aligned}$$

In this case we see that if $c(k_c^2) < 0$ for some k_c^2 then $c(k^2) < 0$ for all $k^2 < k_c^2$. Thus the range of unstable eigenvalues will always include all the eigenvalues form zero up to the largest one (see Figure 2.3(b)). Isolation of a specific eigenvalue is therefore not possible if both $r = 0$ and $\rho = 0$. Either dermal cell proliferation, reflected by r, or epithelial tethering, reflected by ρ, is required.

With a parabolic-type dispersion relation one can easily select and isolate different unstable eigenvalue. We consider the simplest possible version of the linear model (2.12) with such a dispersion relation. Ignoring the epithelial sheet viscosity as well as dermal diffusion and proliferation, that is, setting μ, D and r to zero, our system reduces to

$$\nabla^2\theta - \beta\nabla^4\theta + P_1\nabla^2\theta + P_2\nabla^2 n = \rho\theta, \tag{2.17a}$$

$$\frac{\partial n}{\partial t} = Q_1\nabla^2 n + Q_2\nabla^2\theta. \tag{2.17b}$$

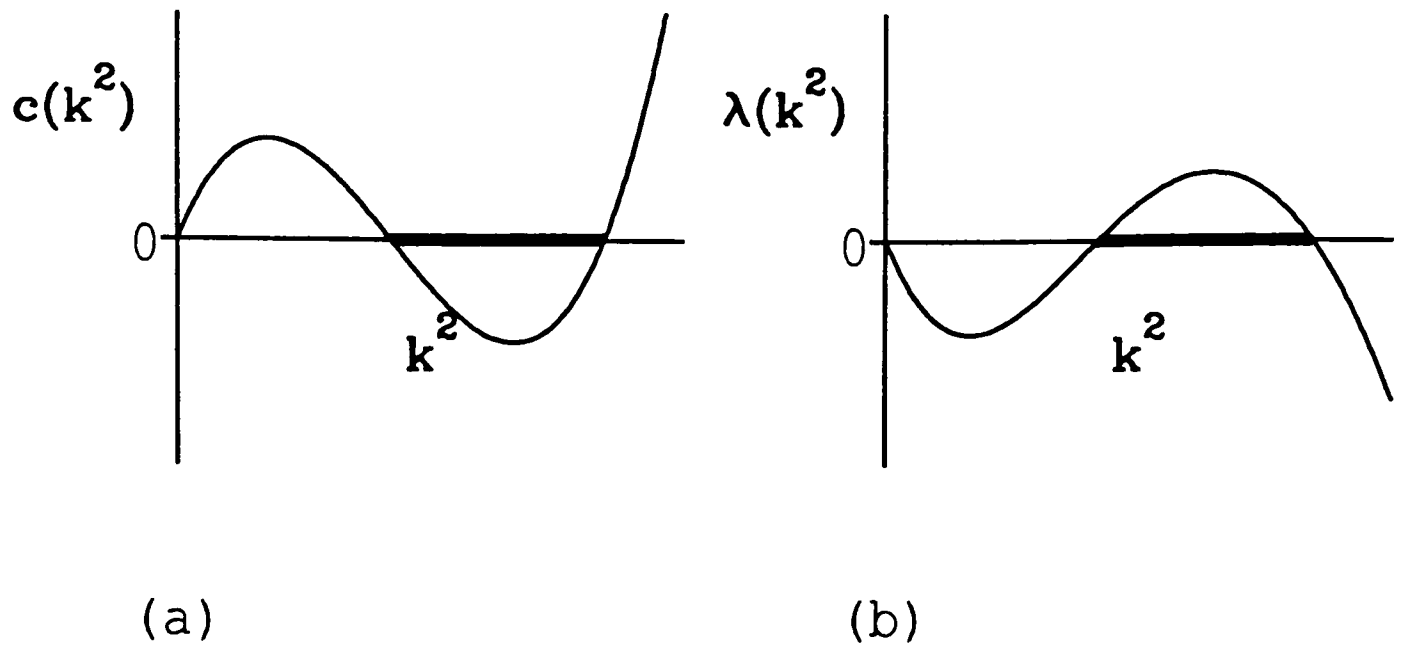

Figure 2.4: Forms of (a) the function $c(k^2)$ and (b) the dispersion relation $\lambda(k^2)$ if $\mu = D = r = 0$. The steady state is unstable if $\lambda(k^2) > 0$ and $c(k^2) < 0$.

The dispersion relation for this system is

$$\lambda(k^2) = -\frac{c(k^2)}{b(k^2)}, \tag{2.18}$$

where

$$\begin{aligned} b(k^2) &= \beta k^4 + (P_1 + 1)k^2 + \rho, \\ c(k^2) &= \beta Q_1 k^6 - (P_2 Q_2 - P_1 Q_1 - Q_1)k^4 + \rho Q_1 k^2. \end{aligned}$$

The steady state is unstable if and only if $c(k^2) < 0$ for some k^2 (see Figure 2.4). We now present a detailed analysis of this model.

The first necessary condition for $c(k^2)$ to be negative is

$$P_2 Q_2 - P_1 Q_1 - Q_1 > 0. \tag{2.19}$$

This condition is, however, not sufficient to satisfy $\Re\lambda(k^2) > 0$ as we additionally require that

$$c(k^2_{\min}) < 0,$$

where $k^2_{\min}$ is the value of k^2 for which $c(k^2)$ has a minimum value. To find $k^2_{\min}$ we must differentiate $c(k^2)$ in terms of k^2 and solve the resulting quadratic in

k^2. Since $c(k^2)$ is a cubic and since $c(k^2) \to \infty$ as $k^2 \to \infty$ the largest of the two roots is $k^2_{\min}$, so

$$k^2_{\min} = \frac{(P_2Q_2 - P_1Q_1 - Q_1) + \sqrt{(P_2Q_2 - P_1Q_1 - Q_1)^2 - 3\beta\rho Q_1^2}}{3\beta Q_1}. \tag{2.20}$$

Substituting this into $c(k^2)$, the second necessary condition simplifies to

$$(P_2Q_2 - P_1Q_1 - Q_1)^2 > 4\beta\rho Q_1^2. \tag{2.21}$$

We can now use either γ or $\hat{\nu}$ as the bifurcation parameter; here however we examine only the role of γ. Referring to the results obtained in the previous section,

$$\lim_{\gamma \to 0^+} Q_1(\gamma) = 0 \quad \text{and} \quad \lim_{\gamma \to 0^+} Q_2(\gamma) = \alpha,$$

it is easy to see that both the necessary conditions for spatial pattern (2.19) and (2.21) can be satisfied if γ is small enough. At the bifurcation point, where $\gamma = \gamma_c$, we require $c(k^2) = 0$, and so, writing Q_1 and Q_2 as functions of γ_c, we obtain

$$(P_2Q_2(\gamma_c) - P_1Q_1(\gamma_c) - Q_1(\gamma_c))^2 = 4\beta\rho Q_1^2(\gamma_c).$$

Substituting this into (2.20) we find the critical eigenvalue

$$k_c^2 = \frac{P_2Q_2(\gamma_c) - P_1Q_1(\gamma_c) - Q_1(\gamma_c)}{2\beta Q_1(\gamma_c)}.$$

Whenever $c(k^2) < 0$, the range of unstable eigenvalues is (k_-^2, k_+^2), where

$$k_\pm^2 = \frac{(P_2Q_2 - P_1Q_1 - Q_1) \pm \sqrt{(P_2Q_2 - P_1Q_1 - Q_1)^2 - 4\beta\rho Q_1^2}}{2\beta Q_1}.$$

We shall use these results in the next chapter to isolate specific unstable eigenvalues.

We note here that by including boundary conditions, only a discrete set from this range of unstable eigenvalues can go unstable. This will be discussed in full detail later on.

Chapter 3

One-Dimensional Solutions

3.1 Introduction

It is important, of course, that any pattern formation model exhibits solutions similar to those observed *in vivo*. In this chapter and the next we therefore use analytical and numerical techniques to examine the spatially patterned solutions which our small strain quasi-steady-state model allows. We begin this investigation by examining pattern formation in one-dimensional domains. This will form the basis for the analysis of two-dimensional spatial patterns in Chapter 4.

We consider the one-dimensional small strain quasi-steady-state problem

$$\mu\frac{\partial^3\theta}{\partial t\partial x^2}+\frac{\partial^2\theta}{\partial x^2}-\beta\frac{\partial^4\theta}{\partial x^4}+\tau\frac{\partial^2}{\partial x^2}\left\{\frac{n^2}{[1+\hat{\nu}(1-\theta)]^2+cn^2}\right\}=\rho\theta, \quad (3.1a)$$

$$\frac{\partial n}{\partial t}=D\frac{\partial^2 n}{\partial x^2}-\alpha\frac{\partial}{\partial x}\left\{n\frac{\partial}{\partial x}\left(\frac{1-\theta}{1+\gamma n}\right)\right\}+rn(1-n), \quad (3.1b)$$

on the spatial interval $(0, L)$, where L is positive. From the biological situation envisaged we could impose either zero-flux or periodic boundary conditions. To be specific we choose here the former, that is

$$\frac{\partial n(0,t)}{\partial x} = \frac{\partial n(L,t)}{\partial x}=0, \quad (3.2a)$$

$$\frac{\partial \theta(0,t)}{\partial x} = \frac{\partial \theta(L,t)}{\partial x}=0, \quad (3.2b)$$

$$\frac{\partial^3 \theta(0,t)}{\partial x^3} = \frac{\partial^3 \theta(L,t)}{\partial x^3}=0, \quad (3.2c)$$

where the last two conditions derive from the relationship $N = 1 - \theta$. These restrictions ensure that, in the absence of the dermal logistic growth term, both dermal and epithelial cell densities are conserved. So, there is no flux of

cells across the boundaries of the tissue considered. We now show that our linearized model, with these six boundary conditions, does indeed give rise to spatially patterned solutions.

The one-dimensional linear system, derived from equations (2.12), is

$$\mu \frac{\partial^3 \theta}{\partial t \partial x^2} = \rho\theta - \frac{\partial^2 \theta}{\partial x^2} + \beta \frac{\partial^4 \theta}{\partial x^4} - P_1 \frac{\partial^2 \theta}{\partial x^2} - P_2 \frac{\partial^2 n}{\partial x^2}, \tag{3.3a}$$

$$\frac{\partial n}{\partial t} = D \frac{\partial^2 n}{\partial x^2} - rn + Q_1 \frac{\partial^2 n}{\partial x^2} + Q_2 \frac{\partial^2 \theta}{\partial x^2}. \tag{3.3b}$$

Solutions of these equations satisfying the boundary conditions (3.2) are

$$\boldsymbol{w}(\boldsymbol{x}, t) = \begin{pmatrix} \theta \\ n \end{pmatrix} = \sum_{\tilde{k}} p_f(\tilde{k}) \begin{pmatrix} 1 \\ M(k^2) \end{pmatrix} e^{\lambda(k^2)t} \cos k\boldsymbol{x},$$

where the discrete wavenumbers k, are members of the sequence

$$k = \frac{\tilde{k}\pi}{L}, \qquad \tilde{k} = 0, 1, 2, \ldots,$$

$M(k^2)$ is as in (2.16), and $p_f(\tilde{k})$ is determined by a Fourier transform of the initial conditions in terms of $\cos k\boldsymbol{x}$. The spatially heterogeneous solution that emerges for large time, is the sum of the *modes*

$$p_f(\tilde{k}) \begin{pmatrix} 1 \\ M(k^2) \end{pmatrix} \cos k\boldsymbol{x},$$

corresponding to the *mode numbers* $\tilde{k}$ for which $\lambda((\pi\tilde{k}/L)^2) > 0$.

The aim of the rest of the chapter is to show that the nonlinear system similarly allows discrete patterned solutions to evolve with time and furthermore that these patterns reach a time-independent steady state. We begin by proving in Section 3.2, by means of a global steady state analysis, that a subproblem of our nonlinear reduced model (3.1) has steady state spatially patterned solutions in one spatial dimension. A more realistic version of the model is considered in Section 3.3 where we perform a nonlinear bifurcation analysis to obtain analytical approximations to the patterned solutions. In Section 3.4 this system is solved numerically using two different algorithms. The results are compared with the approximate solutions obtained in Section 3.3. We also show numerically that patterned solutions exist for the full small strain quasi-steady-state model (3.1).

3.2 Steady State Analysis

To demonstrate that our small strain quasi-steady-state system can indeed give rise to spatially heterogeneous solutions for certain parameter ranges, we consider a reduced version of the system in one space dimension. To this end we examine the following one-dimensional problem

$$\mu\frac{\partial^3\theta}{\partial t\partial x^2}+\frac{\partial^2\theta}{\partial x^2}-\beta\frac{\partial^4\theta}{\partial x^4}+\tau\frac{\partial^2}{\partial x^2}\left\{\frac{n^2}{[1+\hat{\nu}(1-\theta)]^2+cn^2}\right\}=0, \tag{3.4a}$$

$$\frac{\partial n}{\partial t}=-\alpha\frac{\partial}{\partial x}\left\{n\frac{\partial}{\partial x}\left(\frac{1-\theta}{1+\gamma n}\right)\right\}, \tag{3.4b}$$

where we have set D, r and ρ equal to zero in (3.1). We again impose the zero-flux boundary conditions (3.2). Without loss of generality we set $L=1$ and so consider the problem on the domain $(0,1)$. We now conduct a steady state analysis of the model to obtain the global behaviour of the solutions.

The steady state problem, after integrating (3.4a) twice and (3.4b) once with respect to x, is

$$\beta\theta''=\theta+\frac{\tau n^2}{[1+\hat{\nu}(1-\theta)]^2+cn^2}+k_0x+k_1 \tag{3.5a}$$

$$\alpha n\left(\frac{1-\theta}{1+\gamma n}\right)'=k_2, \tag{3.5b}$$

where the prime denotes differentiation with respect to x, and k_0, k_1 and k_2 are the constants of integration. Using the boundary conditions (3.2) one can show that $k_0=k_2=0$. Since a negative or zero dermal cell density is physically impossible, $n>0$, and so equation (3.5b) can be divided by n. Integrating the resulting equation leads to

$$\frac{1-\theta}{1+\gamma n}=k_3,$$

where k_3 is the integration constant. As before we assume that $\theta=0$, $n=1$ is the homogeneous steady state solution. Using this we determine k_3 and then solve for n in terms of θ which gives

$$n=1-\theta\left(1+\frac{1}{\gamma}\right).$$

Substituting this expression for n into (3.5a) and solving for k_1, using the steady state condition $\theta = 0$, we obtain a typical conservative system

$$\theta'' = F(\theta), \tag{3.6}$$

where

$$\beta F(\theta) = \theta + \frac{\tau[1-\theta(1+1/\gamma)]^2}{[1+\hat{\nu}(1-\theta)]^2 + c[1-\theta(1+1/\gamma)]^2} - \frac{\tau}{(1+\hat{\nu})^2+c}.$$

We can now introduce a potential defined by

$$V(\theta) = -\int F(\theta)d\theta.$$

The stationary points are given by $F(\theta) = 0$ and we observe that the *total energy*

$$\frac{1}{2}(\theta')^2 + V(\theta),$$

is constant along the orbits of the (θ, θ') phase plane (see, for example, Jordan & Smith 1987).

The function $F(\theta)$ admits three equilibrium states. One is $\theta = 0$ and the other two are

$$\theta = \frac{-\xi_1 \pm \sqrt{\xi_1^2 - 4\xi_0\xi_2}}{2\xi_2} \tag{3.7}$$

which are the roots of the quadratic

$$\xi_2\theta^2 + \xi_1\theta + \xi_0 = 0 \tag{3.8}$$

where

$$\begin{aligned}
\xi_2 &= -K\left[\hat{\nu}^2 + c\left(1+\frac{1}{\gamma}\right)^2\right], \\
\xi_1 &= 2K\left[\hat{\nu}(1+\hat{\nu}) + c\left(1+\frac{1}{\gamma}\right)\right] - \tau\left[1+2\hat{\nu}+\frac{1}{\gamma}\left(2+\frac{1}{\gamma}\right)(1+\hat{\nu})^2\right], \\
\xi_0 &= 2\tau(1+\hat{\nu})\left(1+\frac{1}{\gamma}+\frac{\hat{\nu}}{\gamma}\right) - K^2,
\end{aligned}$$

and

$$K = (1+\hat{\nu})^2 + c.$$

The resulting phase portrait depends critically on

$$\Delta = \xi_1^2 - 4\xi_0\xi_2. \tag{3.9}$$

Since the model parameters are all positive, the expression ξ_2 is always negative. The signs of ξ_0 and ξ_1 depend, however, on the parameter values. As bifurcation parameters we can, for example, choose either τ or γ.

If τ is large or if γ is small ξ_0 will be positive. Under these conditions $\Delta > \xi_1^2$ and so the roots (3.7) have opposite signs. Since

$$\lim_{\theta \to -\infty} F(\theta) = -\infty, \qquad \lim_{\theta \to \infty} F(\theta) = \infty,$$

the potential $V(\theta)$ has the qualitative form shown in Figure 3.1(a). The corresponding (θ, θ') phase portrait contains two saddle points which are the roots (3.7) as well as a centre at the origin, see Figure 3.1(b).

It is easy to see from the phase plane that our system (3.4) does have a global heterogenous steady state solution. For example, the trajectory AB as indicated in Figure 3.1(b), which starts out and finishes on the line $\theta' = 0$, satisfies the boundary conditions and corresponds to a simple gradient solution for $\theta(x)$, while the clockwise trajectory ABA, or in short AA, corresponds to a solution with a single hump, but on a domain twice as large. In fact, if the trajectory AA is traversed, say m times, we get a solution for $\theta(x)$ with m humps, but, of course, the domain is then m-times larger than that of the single hump solution.

In summary, we can therefore always find a parameter space so that spatially heterogeneous solutions exist for the small strain quasi-steady-state system. Furthermore, the solutions we obtained here are qualitatively similar to the approximate solutions and the numerical solutions we obtain in the next two sections for different versions of the time evolution system. In terms of our original model variables (see (2.10)) it means that if the epidermal traction is sufficiently large, the epidermal chemical diffusion is small enough or the chemical diffusion across the basal lamina is sufficiently fast, spatial pattern formation is possible.

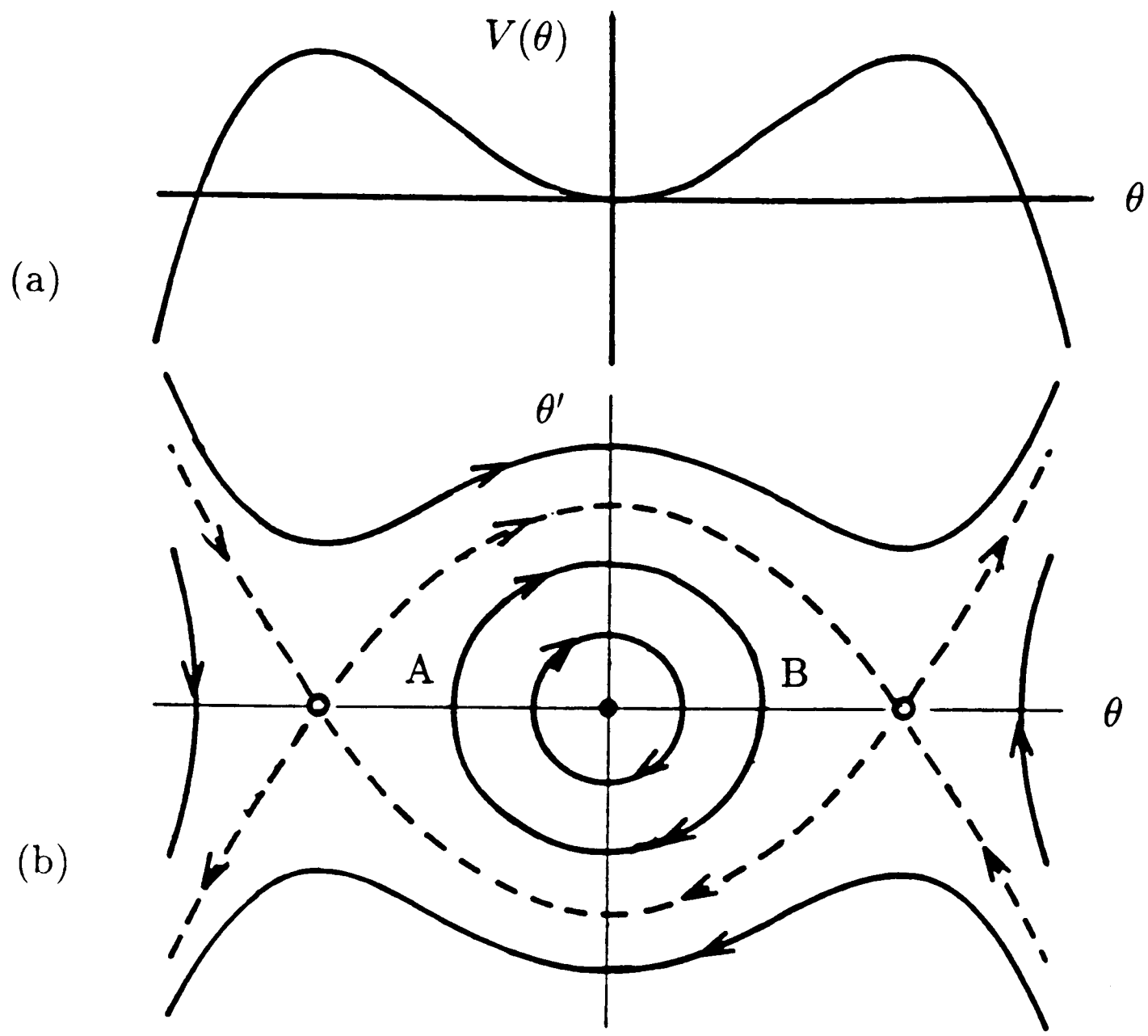

Figure 3.1: The behaviour of the steady state system (3.6) when $\Delta > \xi_1^2$. (a) The form of the potential $V(\theta)$. (b) The corresponding (θ, θ') phase portrait. The trajectory AB indicates a simple gradient solution in θ satisfying the boundary conditions (3.2).

We could further enhance our understanding of the model behaviour by determining the bifurcation diagrams for this system. For simplicity we only consider the case when the bifurcation parameter is τ, although γ could similarly be used as bifurcation parameter. For the purpose of the analysis the expression Δ, as in (3.9), is regarded as a function of τ.

In the above we have demonstrated that $\Delta(\tau) > \xi_1^2$ for large τ which implies that there are three steady states for equations (3.4), a stable one at $\theta = 0$ and two unstable ones of opposite signs. However, as τ decreases it passes through

two critical values, first through, say, τ_2 and then through τ_1, where $\Delta(\tau_2) = \xi_1^2$ and $\Delta(\tau_1) = 0$. At these critical values the number, stability and signs of the steady states change. In terms of the biological application of our model, we are interested only in non-negative values of τ and thus also of τ_1 and τ_2. Since the expression $\Delta(\tau)$ is a quadratic in τ and

$$\Delta(0) = -4cK^2\left(1 + \frac{1+\hat{\nu}}{\gamma}\right)^2 < 0,$$

τ_1 must be unique and positive as it is the positive root of $\Delta(\tau) = 0$. It is also easy to show that τ_2 has the unique positive value

$$\tau_2 = \frac{K^2}{2(1+\hat{\nu})(1+1/\gamma+\hat{\nu}/\gamma)}.$$

The system (3.4) has three different bifurcation diagrams depending on the following conditions:

(i) $\xi_1 > 0$ when $\Delta = \xi_1^2$.

As we decrease the value of τ towards τ_2, Δ approaches $\Delta = \xi_1^2$, and so from (3.7) it follows that the negative root of $F(\theta)$ tends to zero. At the point where $\tau = \tau_2$, this root indeed becomes zero so that $F(\theta)$ has a double zero and one positive root. By constructing the corresponding potential $V(\theta)$ here as we have done above, one can show that both the zero and positive steady states are unstable.

As τ decreases further, beyond τ_2, the zero root of $F(\theta)$ changes into a positive root (again refer to (3.7)) so that we now have one zero and two positive steady states.

When τ reaches τ_1 the two positive roots of $F(\theta)$ are equal so that we are left with only two steady states — one zero and one positive. For $\tau < \tau_1$ the two roots (3.7) are imaginary and the only remaining steady state is $\theta = 0$, which is also unstable. The detailed bifurcation diagram is illustrated in Figure 3.2(a).

Note that since

$$0 < \Delta(\tau) < \xi_1^2 \text{ when } \tau_1 < \tau < \tau_2,$$

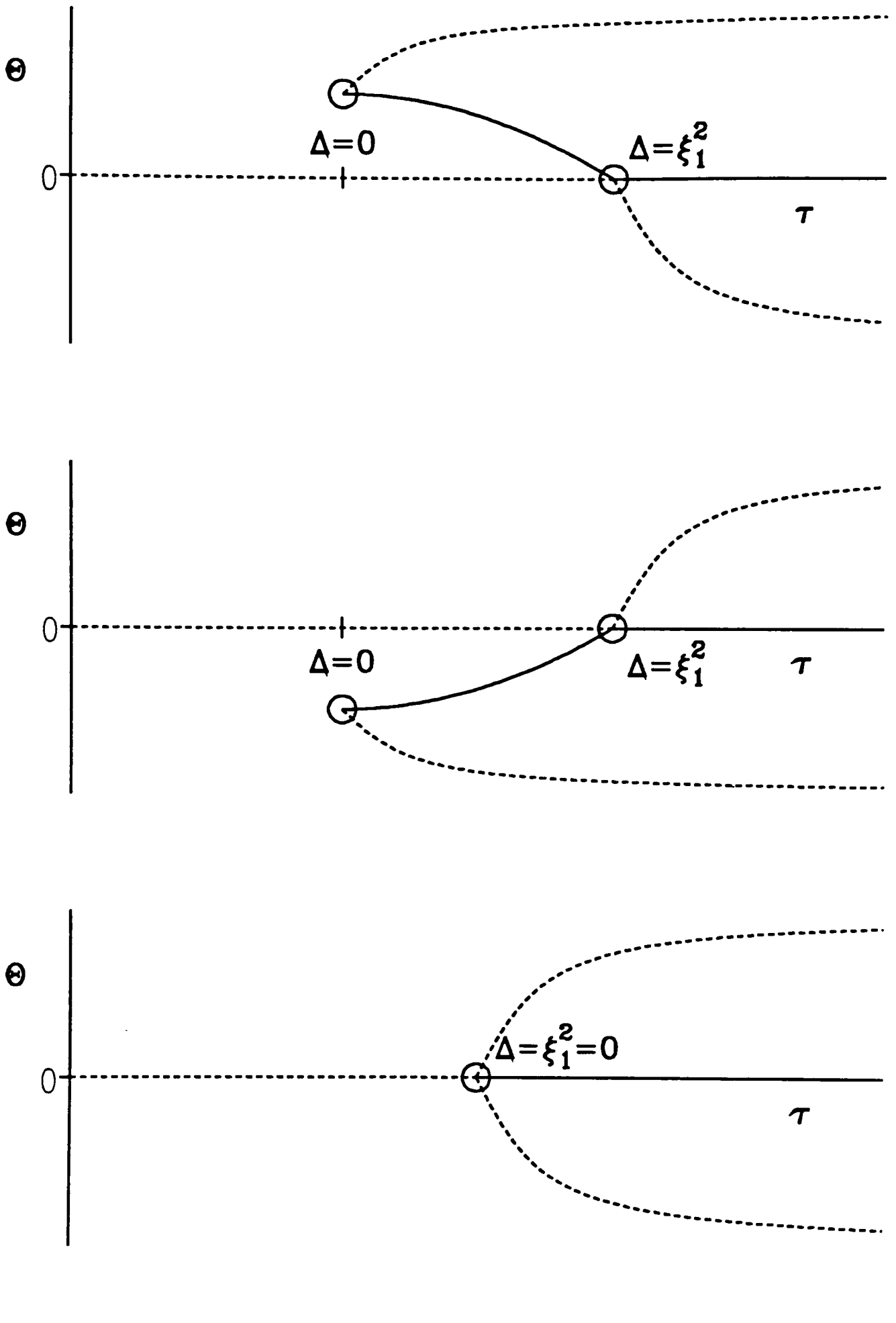

Figure 3.2: The bifurcation diagrams for the steady state system (3.6). The solid lines indicate the stable steady states and the broken lines the unstable steady states. (a) Case (i) where $\xi_1 > 0$ when $\Delta = \xi_1^2$. (b) Case (ii) where $\xi_1 < 0$ when $\Delta = \xi_1^2$. (c) Case (iii) where $\xi_1 = 0$ when $\Delta = \xi_1^2 = 0$. See the text for details.

we do not have to consider the effect on the bifurcation diagrams of a possible sign change of ξ_1 in this domain. For $\tau < \tau_1$ such a sign change does not matter since the roots (3.7) are imaginary.

(ii) $\xi_1 < 0$ when $\Delta = \xi_1^2$.

Here, as we decrease τ towards the value τ_2, the positive root of $F(\theta)$, rather than the negative root as in case (i), tends to zero. At $\tau = \tau_2$, $F(\theta)$ again has a double zero. For $\tau_1 < \tau < \tau_2$ we have two negative steady states and one zero steady state, rather than the two positive and one zero steady state as above. Similar to case (i), the two negative roots of $F(\theta)$ are equal when $\tau = \tau_1$ and become imaginary for $\tau < \tau_1$. The bifurcation diagram is drawn in Figure 3.2(b).

(iii) $\xi_1 = 0$ when $\Delta = \xi_1^2 = 0$.

This condition is only true in the special case when $\tau_1 = \tau_2$. As before for $\tau > \tau_2$, $F(\theta)$ has two non-zero real roots and one zero root. The two non-zero roots of $F(\theta)$, however, become imaginary when $\tau = \tau_1 = \tau_2$, and we are left with only the single steady state $\theta = 0$ when $\tau < \tau_2$. This is an unstable steady state as can be seen from the bifurcation diagram in Figure 3.2(c).

3.3 Nonlinear Bifurcation Analysis

The linear analysis of Section 2.6 showed that if $r = 0$, $D = 0$ and $\mu = 0$, we can arbitrarily select and isolate an eigenvalue for which the homogeneous steady state, $\theta = 0$ and $n = 1$, is unstable. In this section we derive an approximate analytical expression for the spatially heterogeneous solution of the corresponding nonlinear problem,

$$\frac{\partial^2\theta}{\partial x^2} - \beta\frac{\partial^4\theta}{\partial x^4} + \tau\frac{\partial^2}{\partial x^2}\left\{\frac{n^2}{[1+\hat{\nu}(1-\theta)]^2 + cn^2}\right\} = \rho\theta, \tag{3.10a}$$

$$\frac{\partial n}{\partial t} = -\alpha\frac{\partial}{\partial x}\left\{n\frac{\partial}{\partial x}\left(\frac{1-\theta}{1+\gamma n}\right)\right\}, \tag{3.10b}$$

which is system (3.1) but with r, D and μ set to zero.

This simplification is biologically realistic, because the dermal cell diffusion is very small compared to chemotaxis, cell proliferation appears to cease when pattern formation starts and the epidermal viscosity coefficient is believed to be relatively very small. This is also the simplest version of the small strain quasi-steady-state model for which mode isolation is possible, as was shown in Section 2.6.

Since the epithelial and dermal cell condensations which form during early chick skin morphogenesis are small, it is appropriate to examine equations (3.10) in the vicinity of the bifurcation point to spatially patterned solutions. In this region we can use a weakly nonlinear analysis to find small amplitude solutions for θ and n which indicate how the different parameters are involved in the evolving patterns. We follow the technique of Matkowsky (1970).

As is explained in Section 2.6, we can now use either γ or $\hat{\nu}$ as bifurcation parameters, however, as before we select γ. We assume that the system bifurcates to spatial patterns at the critical value $\gamma = \gamma_c$ with $k^2 = k_c^2$, where

$$\Re\lambda(k_c^2, \gamma_c) = 0 \text{ and } \Re\lambda(k^2, \gamma_c) < 0 \text{ if } k^2 \neq k_c^2.$$

As γ decreases below γ_c, the homogeneous steady state loses linear stability and both θ and n grow exponentially. Intuitively there are three time regimes involved as the solution evolves. Initially, while θ and n are still small, the solution grows linearly from the homogeneous steady state, as was discussed in Section 2.6. The solution, however, soon evolves into the second time regime when nonlinear effects come into play. As was demonstrated in the steady state analysis of the previous section the solution finally reaches a steady state for very large time — the third time regime. Since we are particularly interested in the steady state solution as time tends to infinity, we examine here the time evolution of the solution, using a multiple time scale perturbation procedure. The analysis is performed in general on an infinite spatial domain. The zero-flux boundary conditions (3.2), as required by the biology, will be introduced

at a later stage.

We examine the behaviour of the system in the neighbourhood of the critical eigenvalue k_c^2 where γ is just marginally smaller than the critical value γ_c, by setting

$$\gamma = \gamma_c + \epsilon\gamma_1 + \epsilon^2\gamma_2 + \epsilon^3\gamma_3 + \ldots \quad \text{where } 0 < \epsilon \ll 1. \tag{3.11}$$

We also set

$$t = T_1/\epsilon + T_2/\epsilon^2 + T_3/\epsilon^3 + \ldots, \tag{3.12}$$

thus introducing the time scales

$$T_1 = \epsilon t, \qquad T_2 = \epsilon^2 t, \qquad T_3 = \epsilon^3 t,$$

and so on.

The nonlinear system is now reduced to a hierarchy of linear equations by assuming power series expansions for θ and n,

$$\theta(x, \epsilon, T_1, \ldots) = \epsilon\theta_1(x, T_1, \ldots) + \epsilon^2\theta_2(x, T_1, \ldots) + \ldots, \tag{3.13a}$$

$$n(x, \epsilon, T_1, \ldots) = 1 + \epsilon n_1(x, T_1, \ldots) + \epsilon^2 n_2(x, T_1, \ldots) + \ldots. \tag{3.13b}$$

The variables θ and n are considered as functions of x, ϵ and T_i, $i = 1, 2, 3, \ldots$, thus ignoring the t-dependence except through T_i.

We begin the analysis by substituting these series expansions (3.11), (3.12) and (3.13) into the two interaction terms of the nonlinear system. For algebraic simplicity we initially set

$$\tilde{n}(x, \epsilon, T_1, \ldots) = 1 - n(x, \epsilon, T_1, \ldots),$$

so that the epidermal interaction term now becomes

$$\begin{aligned} \frac{\tau(1+\tilde{n})^2}{[1+\hat{\nu}(1-\theta)]^2 + c(1+\tilde{n})^2} \;=\; & p_0 + p_1\theta + p_2\tilde{n} + p_3\theta^2 + p_4\theta\tilde{n} + p_5\tilde{n}^2 \\ & + p_6\theta^3 + p_7\theta^2\tilde{n} + p_8\theta\tilde{n}^2 + p_9\tilde{n}^3 + O(\epsilon^4), \end{aligned}$$

where

$$p_0 = \tau\chi^{-1}, \qquad p_5 = \tau\chi^{-2}(\chi - 5c) + 4\tau\chi^3 c^2,$$
$$p_1 = 2\tau\chi^{-2}\hat{\nu}(1+\hat{\nu}), \qquad p_6 = 4\tau\chi^{-4}\hat{\nu}^3(1+\hat{\nu})(\chi - 2c),$$
$$p_2 = 2\tau\chi^{-2}(\chi - c), \qquad p_7 = 2\tau\chi^{-4}\hat{\nu}^2[4(1+\hat{\nu})^2(\chi - 3c) - \chi(\chi - 2c)],$$
$$p_3 = 3\tau\chi^{-3}\hat{\nu}^2(\chi - 2c), \qquad p_8 = 2\tau\chi^{-4}\hat{\nu}(1+\hat{\nu})[\chi(\chi - 10c) + 12c^2],$$
$$p_4 = 4\tau\chi^{-3}\hat{\nu}(1+\hat{\nu})(\chi - 2c), \qquad p_9 = 4\tau\chi^{-3}c(3c - \chi) - 8\tau\chi^4 c^3,$$

and

$$\chi = 1 + 2\hat{\nu} + \hat{\nu}^2 + c.$$

Similarly, the dermal interaction term is

$$\begin{aligned}\frac{\alpha(1-\theta)}{1+\gamma(1+\tilde{n})} &= [q_2 - (\gamma_1 + \epsilon\gamma_2 + \epsilon^2\gamma_3)\epsilon q_1 - (\gamma_1 + \epsilon\gamma_2 + \epsilon^2\gamma_3)\epsilon q_3] \\ &\quad - [q_1 + (\gamma_1 + \epsilon\gamma_2)\epsilon q_6]\tilde{n} - [q_2 - (\gamma_1 + \epsilon\gamma_2)\epsilon q_3]\theta \\ &\quad + q_1\theta\tilde{n} + q_4\tilde{n}^2 - q_5\tilde{n}^3 - q_4\theta\tilde{n}^2 + O(\epsilon^4),\end{aligned}$$

where

$$q_1 = \alpha\gamma_c\zeta^{-2}, \qquad q_4 = \alpha\gamma_c^2\zeta^{-3},$$
$$q_2 = \alpha\zeta^{-1}, \qquad q_5 = \alpha\gamma_c^3\zeta^{-4},$$
$$q_3 = \alpha\zeta^{-2}, \qquad q_6 = \alpha(1-\gamma_c)\zeta^{-3},$$

and

$$\zeta = 1 + \gamma_c.$$

Note here that $p_i = P_i$ and $q_i = Q_i$ for $i = 1, 2$, where P_i and Q_i are the interaction parameters in the linearized model, see (2.13).

The system of equations can now be written as

$$\mathcal{L}\begin{pmatrix}\theta \\ \tilde{n}\end{pmatrix} = \boldsymbol{G} + \boldsymbol{E} \tag{3.14}$$

where $\mathcal{L}$ is the linear operator which is $O(\epsilon)$, $\boldsymbol{G}$ is the function arising from the nonlinear terms in θ and n and $\boldsymbol{E}$ is the function arising from the time derivatives as well as the dependence of γ on ϵ. We have that

$$\mathcal{L} \equiv \begin{pmatrix} -\beta\frac{\partial^4}{\partial x^4} + (1+p_1)\frac{\partial^2}{\partial x^2} - \rho & p_2\frac{\partial^2}{\partial x^2} \\ q_2\frac{\partial^2}{\partial x^2} & q_1\frac{\partial^2}{\partial x^2} \end{pmatrix}.$$

In the analysis that follows the first and second components of a vector shall be denoted by the superscripts (1) and (2) respectively, for example

$$\boldsymbol{G} = \begin{pmatrix} G^{(1)} \\ G^{(2)} \end{pmatrix};$$

we have that

$$\begin{aligned} G^{(1)} &= -\frac{\partial^2}{\partial x^2}\left(p_3\theta^2 + p_4\theta\tilde{n} + p_5\tilde{n}^2 + p_6\theta^3 + p_7\theta^2\tilde{n} + p_8\theta\tilde{n}^2 + p_9\tilde{n}^3\right) + O(\epsilon^4), \\ G^{(2)} &= \frac{\partial}{\partial x}\left[\tilde{n}\frac{\partial}{\partial x}\left(-q_2\theta - q_1\tilde{n} + q_1\theta\tilde{n} + q_4\tilde{n}^2 - q_4\theta\tilde{n}^2 - q_5\tilde{n}^3\right)\right] \\ &\quad + \frac{\partial^2}{\partial x^2}\left(q_1\theta\tilde{n} + q_4\tilde{n}^2 - q_4\theta\tilde{n}^2 - q_5\tilde{n}^3\right) + O(\epsilon^4), \end{aligned}$$

and

$$\begin{aligned} E^{(1)} &= 0, \\ E^{(2)} &= \frac{\partial}{\partial x}\left[(\tilde{n}+1)\frac{\partial}{\partial x}\left\{(\gamma_1 + \gamma_2\epsilon)\epsilon q_3\theta - (\gamma_1 + \epsilon\gamma_2)\epsilon q_6\tilde{n}\right\}\right] \\ &\quad + \epsilon\frac{\partial\tilde{n}}{\partial T_1} + \epsilon^2\frac{\partial\tilde{n}}{\partial T_2} + O(\epsilon^4). \end{aligned}$$

We further define the matrix $\boldsymbol{L}_k$, arising from the action of the operator $\mathcal{L}$ on terms of the form e^{ikx}, as

$$\boldsymbol{L}_k = \begin{pmatrix} -\beta k^4 - (1+p_1)k^2 - \rho & -p_2k^2 \\ -q_2k^2 & -q_1k^2 \end{pmatrix}.$$

The series expansions (3.13) for $\theta(x, \epsilon, T_1, \ldots)$ and $n(x, \epsilon, T_1, \ldots)$ are now substituted into equation (3.14) and the coefficients are equated at each order, leading to a hierarchy of linear nonhomogeneous equations in the unknowns θ_i, n_i.

Equating coefficients of $O(\epsilon)$ gives

$$\mathcal{L}\begin{pmatrix} \theta_1 \\ n_1 \end{pmatrix} = \mathbf{0}.$$

We are in the vicinity of the bifurcation point and so we assume that eigenvalue k_c^2 is the dominant one (and for small enough ϵ, the only one) that grows on the long time scale. We further assume that our solutions are periodic with period $2\pi/k_c$. Since our interest is in the real solutions of the equation we have

$$\begin{pmatrix} \theta_1 \\ n_1 \end{pmatrix} = \begin{pmatrix} 1 \\ M \end{pmatrix}\left\{A(T_1, T_2)\cos k_c x + B(T_1, T_2)\sin k_c x\right\}, \qquad (3.15)$$

where

$$\boldsymbol{L}_{k_c}\begin{pmatrix}1\\M\end{pmatrix}=\boldsymbol{0}.$$

We specifically use the form $(1,M)^T$, because $\det(\boldsymbol{L}_{k_c})=0$. Solving for M gives

$$M=-\frac{q_2}{q_1}=-\frac{\gamma_c+1}{\gamma_c}.$$

The values of $A(T_1,T_2)$ and $B(T_1,T_2)$ are still to be determined. Note that although A and B are not only functions of T_1 and T_2, but also of T_3, T_4 and so on, we ignore this dependence here, since, as we shall see later, their values do not actually depend on these higher time scales.

At $O(\epsilon^2)$,

$$\mathcal{L}\begin{pmatrix}\theta_2\\n_2\end{pmatrix}=\boldsymbol{S},$$

where

$$\begin{aligned}
S^{(1)} &= -\frac{\partial^2}{\partial x^2}\left(p_3\theta_1^2+p_4\theta_1 n_1+p_5 n_1^2\right),\\
S^{(2)} &= \frac{\partial^2}{\partial x^2}\left(q_4 n_1^2+b_1\theta_1 n_1\right)\frac{\partial^2}{\partial x^2}\left(\gamma_1 q_3\theta_1-\gamma_1 q_6 n_1\right)\\
&\quad -\frac{\partial}{\partial x}\left[n_1\frac{\partial}{\partial x}\left(q_2\theta_1+q_1 n_1\right)\right]+\frac{\partial n_1}{\partial T_1}.
\end{aligned}$$

Substituting the expressions (3.15) for θ_1 and n_1 into the above equations gives

$$\begin{aligned}
\mathcal{L}\begin{pmatrix}\theta_2\\n_2\end{pmatrix} &= \begin{pmatrix}2k_c^2(p_3+p_4M+p_5M^2)\\0\end{pmatrix}\left[\left\{A^2(T_1,T_2)-B^2(T_1,T_2)\right\}\cos 2k_c x\right.\\
&\quad \left.+2A(T_1,T_2)B(T_1,T_2)\sin 2k_c x\right]\\
&\quad +\begin{pmatrix}0\\\delta_1\end{pmatrix}(Mq_6-q_3)k_c^2\{A(T_1,T_2)\cos k_c x+B(T_1,T_2)\sin k_c x\}\\
&\quad +\begin{pmatrix}0\\M\end{pmatrix}\left(\frac{\partial A(T_1,T_2)}{\partial T_1}\cos k_c x+\frac{\partial B(T_1,T_2)}{\partial T_1}\sin k_c x\right). \qquad (3.16)
\end{aligned}$$

The solution is composed of a complimentary function and a particular integral and so we write

$$\begin{pmatrix}\theta_2\\n_2\end{pmatrix}=\begin{pmatrix}\theta_2^h\\n_2^h\end{pmatrix}+\begin{pmatrix}\theta_2^p\\n_2^p\end{pmatrix}, \qquad (3.17)$$

where the complimentary part's solution is

$$\begin{pmatrix}\theta_2^h\\n_2^h\end{pmatrix}=\boldsymbol{C}\cos k_c x+\boldsymbol{D}\sin k_c x,$$

and $\boldsymbol{C}$ and $\boldsymbol{D}$ are functions of T_i, $i = 1, 2, \ldots$. The last two terms of the right hand side of equation (3.16) contain terms of the form $\cos k_c x$ and $\sin k_c x$ and since these terms are solutions of the homogeneous problem

$$\mathcal{L}\begin{pmatrix} \theta_2 \\ n_2 \end{pmatrix} = \mathbf{0}, \tag{3.18}$$

the secular terms $x \cos k_c x$ and $x \sin k_c x$ would appear in the particular solution $(\theta_2^p, n_2^p)^T$. These secular terms do not satisfy our assumption that the solutions are periodic with period $2\pi/k_c$ and so we suppress them by assuming that $\gamma_1 = 0$ and $T_1 = 0$ in our series expansions (3.11) and (3.12) respectively. Our particular solution now becomes

$$\begin{pmatrix} \theta_2^p \\ n_2^p \end{pmatrix} = \boldsymbol{a} \cos 2k_c x + \boldsymbol{b} \sin 2k_c x, \tag{3.19}$$

where, from (3.16),

$$\begin{aligned} \boldsymbol{L}_{2k_c}\boldsymbol{a} &= \begin{pmatrix} 2k_c^2(p_3 + p_4 M + p_5 M^2) \\ 0 \end{pmatrix} \left\{A^2(T_2) - B^2(T_2)\right\}, \\ \boldsymbol{L}_{2k_c}\boldsymbol{b} &= \begin{pmatrix} 2k_c^2(p_3 + p_4 M + p_5 M^2) \\ 0 \end{pmatrix} 2A(T_2)B(T_2). \end{aligned}$$

We know that

$$\boldsymbol{L}_{2k_c}^{-1} = \frac{1}{\det(\boldsymbol{L}_{2k_c})} \begin{pmatrix} -4q_1 k_c^2 & 4p_2 k_c^2 \\ 4q_2 k_c^2 & -4k_c^2 - 16\beta k_c^4 - \rho - 4p_1 k_c^2 \end{pmatrix},$$

and using the fact that $\det(\boldsymbol{L}_{k_c}) = 0$, it follows that

$$\det(\boldsymbol{L}_{2k_c}) = 12q_1 k_c^2 (4\beta k_c^4 - \rho),$$

and so

$$\begin{aligned} \begin{pmatrix} a^{(1)} \\ a^{(2)} \end{pmatrix} &= \begin{pmatrix} 1 \\ M \end{pmatrix} K\{A^2(T_2) - B^2(T_2)\}, \\ \begin{pmatrix} b^{(1)} \\ b^{(2)} \end{pmatrix} &= \begin{pmatrix} 1 \\ M \end{pmatrix} 2KA(T_2)B(T_2), \end{aligned}$$

where

$$K = \frac{-2k_c^2(p_3 + p_4 M + p_5 M)}{3(4\beta k_c^2 - \rho)}.$$

At $O(\epsilon^3)$,

$$\mathcal{L}\begin{pmatrix}\theta_3\\ n_3\end{pmatrix} = \boldsymbol{R}, \tag{3.20}$$

where

$$\begin{aligned}
R^{(1)} &= -\frac{\partial^2}{\partial x^2}\left(2p_3\theta_1\theta_2 + p_4\theta_2 n_1 + p_4\theta_1 n_2 + 2p_5 n_1 n_2\right.\\
&\quad \left. + p_6\theta_1^3 + p_7\theta_1^2 n_1 + p_8\theta_1 n_2 + p_9 n_1^3\right),\\
R^{(2)} &= \frac{\partial^2}{\partial x^2}\left(\gamma_2 q_3\theta_1 - \gamma_2 q_6 n_1 + 2q_4 n_1 n_2 - q_5 n_1^3\right.\\
&\quad \left. + q_1\theta_1 n_2 + q_1\theta_1 n_2 - q_4\theta_1 n_1^2\right)\\
&\quad + \frac{\partial}{\partial x}\left[n_1\frac{\partial}{\partial x}\left(-q_2\theta_2 - q_1 n_2 + q_4 n_1^2 + q_1\theta_1 n_1\right)\right]\\
&\quad - \frac{\partial}{\partial x}\left[n_2\frac{\partial}{\partial x}\left(q_2\theta_1 + q_1 n_1\right)\right] + \frac{\partial n_1}{\partial T_2}.
\end{aligned}$$

By substituting the expressions (3.15) for $(\theta_1, n_1)^T$ and (3.17) for $(\theta_2, n_2)^T$ into the above equations it is easy to see that $\boldsymbol{R}$ contains terms of the form $\cos k_c x$ and $\sin k_c x$ and, as before, since they are solutions of the homogeneous problem (3.18), the secular terms $x\cos k_c x$ and $x\sin k_c x$ would appear in the solution for $(\theta_3, n_3)^T$. To suppress these secular terms we now make use of the Fredholm Alternative (see, for example, Keener 1988).

A solution $\boldsymbol{w} = (\theta_3, n_3)^T$ exists for (3.20) if and only if the Fredholm Alternative is satisfied, that is the inner product,

$$< \boldsymbol{w}^*, \boldsymbol{R} >= 0,$$

where $\boldsymbol{w}^*$ is a bounded solution of the adjoint problem

$$\mathcal{L}^*(\boldsymbol{w}^*) = \boldsymbol{0},$$

and $\mathcal{L}^*$ is the adjoint operator to $\mathcal{L}$. The inner product is defined as

$$< \boldsymbol{w}^*, \boldsymbol{R} >= \int_0^{\frac{2\pi}{k_c}} (\theta_3^* \bar{R}^{(1)} + n_3^* \bar{R}^{(2)})\, dx,$$

where the bar denotes the complex conjugate. In this case the adjoint of $\mathcal{L}$ is $\mathcal{L}^T$, so

$$\boldsymbol{w}^* = \begin{pmatrix}1\\ M^*\end{pmatrix}(A^*\cos k_c x + B^*\sin k_c x),$$

where A^* and B^* are real and M^* can be found from

$$\boldsymbol{L}_{k_c}^T \begin{pmatrix} 1 \\ M^* \end{pmatrix} = \mathbf{0}.$$

Hence

$$\begin{pmatrix} -\beta k_c^4 - (1+p_1)k_c^2 - \rho & -q_2 k_c^2 \\ -p_2 k_c^2 & -q_1 k_c^2 \end{pmatrix} \begin{pmatrix} 1 \\ M^* \end{pmatrix} = \mathbf{0},$$

so that

$$M^* = -\frac{p_2}{q_1}.$$

The integral becomes

$$\int_0^{\frac{2\pi}{k_c}} (R^{(1)} + M^* R^{(2)})(A^* \cos k_c x + B^* \sin k_c x)\, dx. \tag{3.21}$$

We now substitute $(\theta_1, n_1)^T$ and $(\theta_2, n_2)^T$ into $R^{(1)}$ and $R^{(2)}$. Since we can take any values for A^* and B^*, as long as one is non-zero, we set $A^* = 1$ and $B^* = 0$ and use the identities

$$\begin{aligned} \int_0^{\frac{2\pi}{k_c}} \sin^i k_c x \cos^j k_c x\, dx &= \frac{i-1}{i+j} \int_0^{\frac{2\pi}{k_c}} \sin^{i-2} k_c x \cos^j k_c x\, dx \\ &= \frac{j-1}{i+j} \int_0^{\frac{2\pi}{k_c}} \sin^i k_c x \cos^{j-2} k_c x\, dx \end{aligned}$$

to evaluate the integral (3.21). Setting this to zero leads to the governing Landau equation

$$\frac{dA(T_2)}{dT_2} = -\gamma_2 \Gamma A(T_2) + \Omega A(T_2)\{A^2(T_2) + B^2(T_2)\},$$

where

$$\Gamma = \frac{\alpha k_c^2}{(\gamma_c + 1)^3} > 0, \tag{3.22}$$

$$\begin{aligned} \Omega = \frac{\alpha k_c^2}{2p_2 M^2(1+\gamma_c)} \Big\{ & p_2 M(M+K) + K[2p_3 + p_4 M(1+M) + 2p_5 M^3] \\ & - \frac{3}{2}\left[p_6 + p_7 M + p_8 M^2 + p_9 M^3\right] \Big\} + \frac{3}{4} M k_c^2 (p_4 + p_5 M), \end{aligned} \tag{3.23}$$

By choosing $A^* = 0$ and $B^* = 1$ in the integral (3.21) we find a similar equation for $B(T_2)$, but with the roles of A and B reversed. Multiplying this equation by $B(T_2)$ and the above equation by $A(T_2)$ and adding gives

$$\frac{1}{2}\frac{d(A^2\{T_2) + B^2(T_2)\}}{dT_2} = -\gamma_2 \Gamma \{A^2(T_2) + B^2(T_2)\} + \Omega \{A^2(T_2) + B^2(T_2)\}^2. \tag{3.24}$$

	$\Omega < 0$	$\Omega > 0$
$\gamma_2 = -1$	$C^2 = 0$ unstable $C^2 = \frac{-\Gamma}{\Omega} > 0$ stable $C^2 \to \frac{-\Gamma}{\Omega}$	$C^2 = 0$ unstable $C^2 = \frac{-\Gamma}{\Omega} < 0$ stable $C^2 \to \infty$
$\gamma_2 = 1$	$C^2 = 0$ stable $C^2 = \frac{\Gamma}{\Omega} < 0$ unstable $C^2 \to 0$	$C^2 = 0$ stable $C^2 = \frac{\Gamma}{\Omega} > 0$ unstable Threshold in C^2 at $T_2 = 0$. $C^2_{T_2=0} < \frac{\Gamma}{\Omega} \Rightarrow C^2 \to 0$ $C^2_{T_2=0} > \frac{\Gamma}{\Omega} \Rightarrow C^2 \to \infty$

Table 3.1: Behaviour of the Landau equation (3.24) near the bifurcation point γ_c, $\gamma = \gamma_c + \epsilon^2\gamma_2$. The stability of the steady states and the solution behaviour as $T_2 \to \infty$ are shown. For convenience we denote the squared amplitude $A^2 + B^2$ by C^2.

This is the Landau equation for the amplitude of θ_1, namely $\{A^2(T_2)+B^2(T_2)\}^{\frac{1}{2}}$.

Note that a Taylor expansion of the dispersion relation $\lambda(k^2)$ about (k_c^2, γ_c) gives

$$\lambda(k_c^2, \gamma) = \lambda(k_c^2, \gamma_c) - \frac{\alpha k_c^2}{(1+\gamma_c)^3}\gamma_2\epsilon^2 + O(\epsilon^4).$$

Since the solution of the system (3.10) about the steady state is proportional to $\exp(ik_cx+\lambda(k_c^2)t)$, by substituting the Taylor series expansion for λ into this, the initial growth rate of the amplitude of the linear solution can be approximated by

$$\exp(-\frac{\alpha k_c^2}{(1+\gamma_c)^3}\gamma_2 T_2).$$

This values agrees with the initial growth rate predicted by the Landau equation, namely $-\gamma_2\Gamma$.

Clearly $\Gamma > 0$, but, since the signs of Ω and γ_2 can vary, we have four different types of behaviour as $T_2 \to \infty$, as summarized in Table 3.1. For simplicity we consider the cases where $\gamma_2 = \pm 1$.

If we are in the parameter space where $\Omega < 0$ and have subcritical bifurcation, thus $\gamma_2 = -1$, the solution evolves to a nonhomogeneous bounded steady

state solution of the form

$$\begin{pmatrix} \theta \\ n \end{pmatrix} = \begin{pmatrix} 0 \\ 1 \end{pmatrix} + \epsilon \begin{pmatrix} 1 \\ M \end{pmatrix} (A \cos k_c x + B \sin k_c x) + O(\epsilon^2) \text{ as } T_2 \to \infty, \quad (3.25)$$

where $A^2 + B^2 = -\Gamma/\Omega$. The final steady state amplitude of θ is $(-\Gamma/\Omega)^{\frac{1}{2}}$ and that of n is $M(-\Gamma/\Omega)^{\frac{1}{2}}$.

The next step in the analysis is to introduce the zero-flux boundary conditions (3.2), as required by biology considerations. With these boundary conditions the nonlinear analysis of system (3.10) is identical to the above, except that $k_c = j\pi/L$, for some positive integer j and $B = 0$ everywhere. So when we have subcritical bifurcation, say $\gamma_2 = -1$, the solution evolves to the steady state

$$\begin{pmatrix} \theta \\ n \end{pmatrix} = \begin{pmatrix} 0 \\ 1 \end{pmatrix} + \epsilon(-\frac{\Gamma}{\Omega})^{\frac{1}{2}} \begin{pmatrix} 1 \\ M \end{pmatrix} \cos k_c x + O(\epsilon^2) \text{ as } T_2 \to \infty, \quad (3.26)$$

which indeed satisfies the boundary conditions.

It is important to note that the amplitude of n is a factor $M = -(\gamma_c + 1)/\gamma_c$ larger than that of θ and that its value only depends on the bifurcation parameter γ_c. Since M is negative the patterns of n and θ are $\pi/2$ radians out of phase and so the solutions of the epithelial cell density $N(= 1 - \theta)$, and the dermal cell density n, are in phase as is intuitively expected from our model mechanism. Also, the fact that the amplitude of n is always equal to or larger than that of θ, is in accordance with our biological results — the aggregations in the dermis are larger than those in the epidermis. Note that the smaller the critical value of the bifurcation parameter γ_c, the larger the difference in the amplitudes of the solutions of θ and n.

3.4 Numerical Solutions

In this section we use numerical techniques to solve the small strain quasi-steady-state tissue interaction model (3.1) in one spatial dimension. We consider three examples. The parameters r, D and μ are set to zero in the first two cases

so that the numerical results can be compared with the analytical predictions (3.26) of the previous section. In the third example we solve the full small strain quasi-steady-state model.

Two different algorithms for solving the system of equations were employed. Initially we used NAG FORTRAN routine D03PGF which integrates a mixed system of nonlinear elliptic and parabolic equations in one space variable, using the method of lines and Gear's method. The method of lines involves a finite difference approximation in space to reduce the partial differential equations to a system of ordinary differential equations in time. This system was then solved with Gear's method which involves the implementation of a backward difference formula for the time derivative (Dew & Walsh 1981).

We also developed an implicit finite difference algorithm for solving the set of equations (3.10). The full details of this algorithm are discussed in the Appendix (see Section A.2). To test the accuracy of the two numerical algorithms we compared the results obtained from them.

The initial conditions for θ and n were taken to be random perturbation, with maximum and minimum values ± 0.001, about the uniform steady state $\theta = 0$, $n = 1$, thus simulating the natural inhomogeneties initially present in the biological tissue.

Example 3.4.1: In our first example we solve the nonlinear system (3.10) which we analysed in the previous section. For the homogeneous steady state to become unstable our dispersion relation (2.18) must have a positive real part for some eigenvalue, say, k_c^2, or in other words, there must be an unstable mode corresponding to the mode number $\tilde{k}_c$. To satisfy this condition we have to select appropriate values for the model parameters in (3.10).

We now derive a simple method from the linear results obtained in Section 2.6 for isolating such a mode with mode number $\tilde{k}_c$. Recall from equation (2.18) that

$$\lambda(k^2) = -\frac{c(k^2)}{b(k^2)},$$

where $b(k^2)$ is always positive and

$$c(k^2) = \beta Q_1 k^6 - (P_2 Q_2 - P_1 Q_1 - Q_1)k^4 + \rho Q_1 k^2.$$

As a first step, we shift the turning point of the function $c(k^2)$, which is a cubic in k^2, to the desired eigenvalue k_c^2. This implies that the parameters must be chosen so as to satisfy

$$\frac{(P_2 Q_2 - P_1 Q_1 - Q_1)}{2\beta Q_1} = k_c^2 = \left(\frac{\tilde{k}_c \pi}{L}\right)^2.$$

Since we are *isolating* the mode we also need the condition

$$c(k_c^2) = c((\tilde{k}_c \pi / L)^2) = 0 \text{ and } c(k^2) > 0 \text{ for every } k^2 \neq k_c^2,$$

The following two equations can be derived from these two conditions:

$$\beta k_c^4 - \rho = 0, \tag{3.27a}$$

$$(P_2 Q_2 - P_1 Q_1 - Q_1)k_c^2 - 2\rho Q_1 = 0. \tag{3.27b}$$

Therefore, to isolate the mode with mode number $\tilde{k}_c$, we select the parameters so that these two equations are satisfied. To make this mode unstable, the value of the bifurcation parameter γ_c, must be decreased marginally.

In this particular example, we select appropriate parameters for isolating the specific mode corresponding to $\tilde{k}_c = 3$ when $L = 1$. One parameter set that satisfies equations (3.27) after substituting $k_c^2 = (3\pi)^2$ is

$$\gamma_c = 1.0, \qquad c = 1.0, \qquad \hat{\nu} = 4.0, \qquad \alpha = 4.0,$$

$$\tau = 6.25, \qquad \beta = 0.011258, \qquad \rho = 88.826.$$

The resulting dispersion relation is shown in Figure 3.3(a).

To determine the analytical prediction for the solution we computed the values of the expressions Γ and Ω (see (3.22)) appearing in equation (3.26). Since we found that $\Omega < 0$ for this particular parameter range, a nonhomogeneous

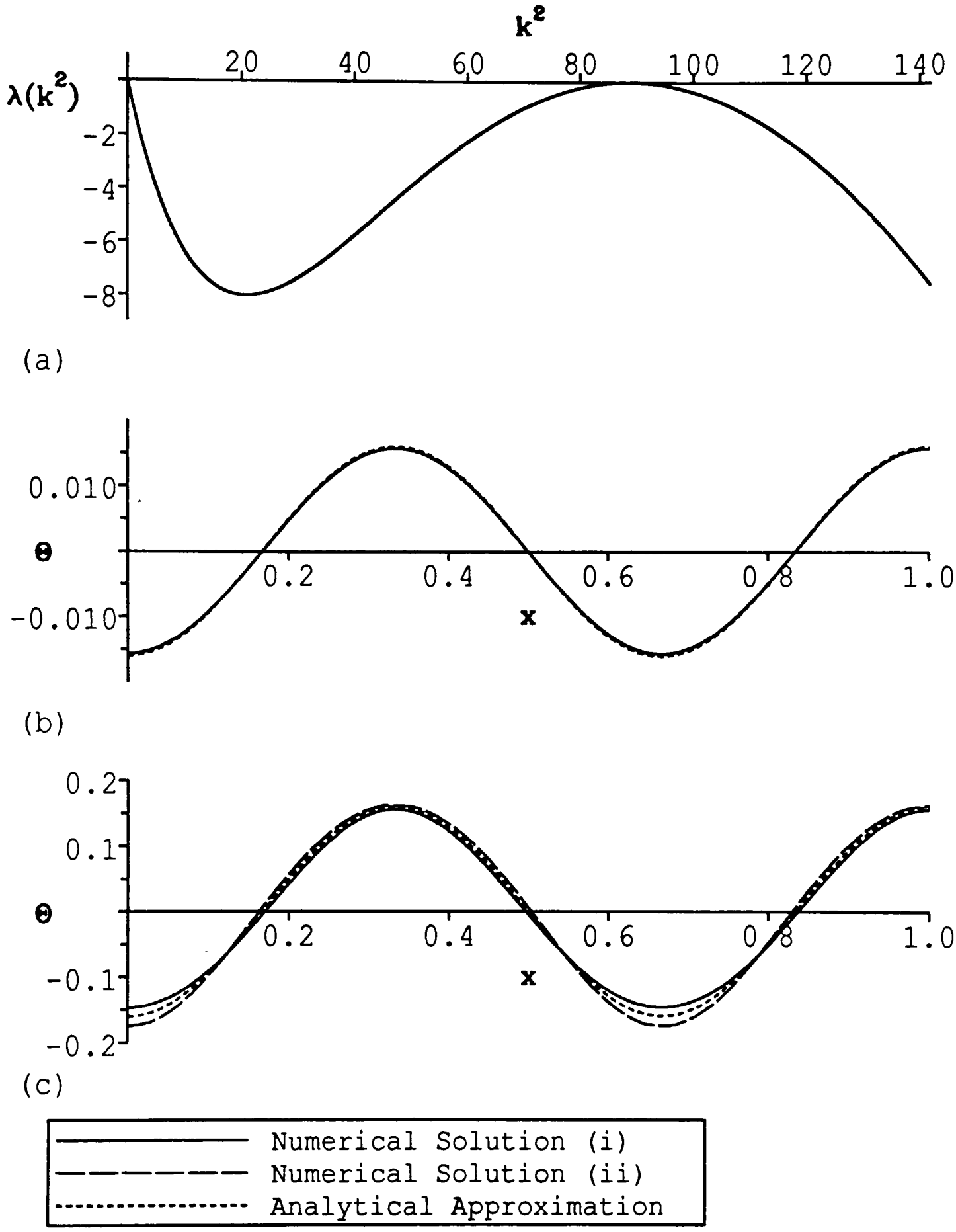

Figure 3.3: Solutions of system (3.10) with parameters as in Example 3.4.1, with unstable eigenvalue $k_c^2 = 9\pi^2$. The dispersion relation $\lambda(k^2)$ is shown in (a), while solutions for the epithelial dilation θ, are shown in (b) for $\epsilon = 0.01$ and in (c) for $\epsilon = 0.1$. Numerical solution (i) is obtained from the NAG algorithm while numerical solution (ii) is obtained from the finite difference algorithm.

steady state for large time exists if we have subcritical bifurcation, thus $\gamma_2 < 0$. More specifically, we chose $\gamma_2 = -1$ to predict analytically the solutions

$$\begin{aligned} \theta &\approx 1.6\epsilon \cos 3\pi x, \\ n &\approx 1.0 - 3.3\epsilon \cos 3\pi x. \end{aligned}$$

We performed numerical simulations of (3.10) for the cases $\epsilon = 0.01$ and $\epsilon = 0.1$ and compared the solutions to the above analytical predictions. Unfortunately the finite difference algorithm was only feasible for $\epsilon = 0.1$, since for smaller values of ϵ the growth rate of the solutions became too small to compute in real time. The results obtained from the NAG routine, however, compared very well with the approximate solutions predicted above for both values of ϵ as can be seen in Figures 3.3(b) and (c). The finite difference routine gave excellent results for $\epsilon = 0.1$, as can be seen in Figure 3.3(c). Since the solutions for the dermal cell density are similar to that of the dilation θ, we do not show them here.

Example 3.4.2: Here we consider the same set of equations as in Example 3.4.1, but isolate the mode with mode number $\tilde{k}_c = 6$. Again using the method described above we find the parameter range

$$\gamma_c = \frac{1}{3}, \qquad c = 2.0, \qquad \hat{\nu} = 1.0, \qquad \alpha = 5\frac{1}{2},$$

$$\tau = 9.0, \qquad \beta = 0.008443, \qquad \rho = 1065.92,$$

for which $\lambda(36\pi^2) = 0$ and $L = 1$. The dispersion relation for this parameter set is shown in Figure 3.4(a).

The expression Ω, see (3.22), is negative and so the nonlinear analysis predicts that we are in a parameter space that exhibits a nonhomogeneous steady state solution for large time if we have subcritical bifurcation. From (3.26), with $\gamma_2 = -1$, we find that

$$\begin{aligned} \theta &\approx 1.8\epsilon \cos 6\pi x, \\ n &\approx 1.0 - 7.1\epsilon \cos 6\pi x. \end{aligned}$$

As in the previous examples we performed numerical simulations for $\epsilon = 0.01$ and $\epsilon = 0.1$. Similarly we were only able to compute the finite difference solutions for the larger value of ϵ. The numerical results are compared with the analytical predicted solutions in Figure 3.4(b) and (c). Again they are in excellent agreement.

Example 3.4.3 In this example the more general system (3.1), where μ, D and r are non-zero, is considered. The dispersion relation is now as in (2.14) and thus to make $\lambda(k^2)$ positive for some $k^2 = k_c^2$ we must ensure that

$$\begin{aligned} c(k^2) &= \beta(D+Q_1)k^6 - (Q_2P_2 - r\beta - DP_1 - Q_1P_1 - D - Q_1)k^4 \\ &\quad +(r + rP_1 + \rho D + \rho P_1)k^2 + \rho r, \end{aligned}$$

is negative for $k^2 = k_c^2$.

Although finding a parameter space for isolating a specific mode with mode number $\tilde{k}_c$ is analytically feasible, it is extremely involved. We therefore investigate some alternative possibilities. Perelson *et al.* (1986) used an inverse technique by first choosing the desired form of the dispersion relation, followed by a curve fitting procedure for finding the parameter values. Bentil & Murray (1990) used Perelson's technique on a mechanochemical model and showed that it can indicate negative parameters which, of course, are biologically meaningless. We therefore choose the *Logical Parameter Search Method* of Bentil & Murray (1991) to find a parameter space for isolating, for example, mode number $\tilde{k}_c = 13$ when $L = 4$.

We begin by choosing biologically realistic ranges for the parameters appearing in the expression $c(k^2)$. A computer program is then used to search iteratively through these parameter ranges to select appropriate sets of values. For each set of possible parameter values the roots of our dispersion relation are found by Newton's Method. The procedure then checks whether the condition

$$c(13^2\pi^2/4^2) < 0 \text{ and } c(\tilde{k}_c^2\pi^2/4^2) > 0 \text{ when } \tilde{k}_c \neq 13,$$

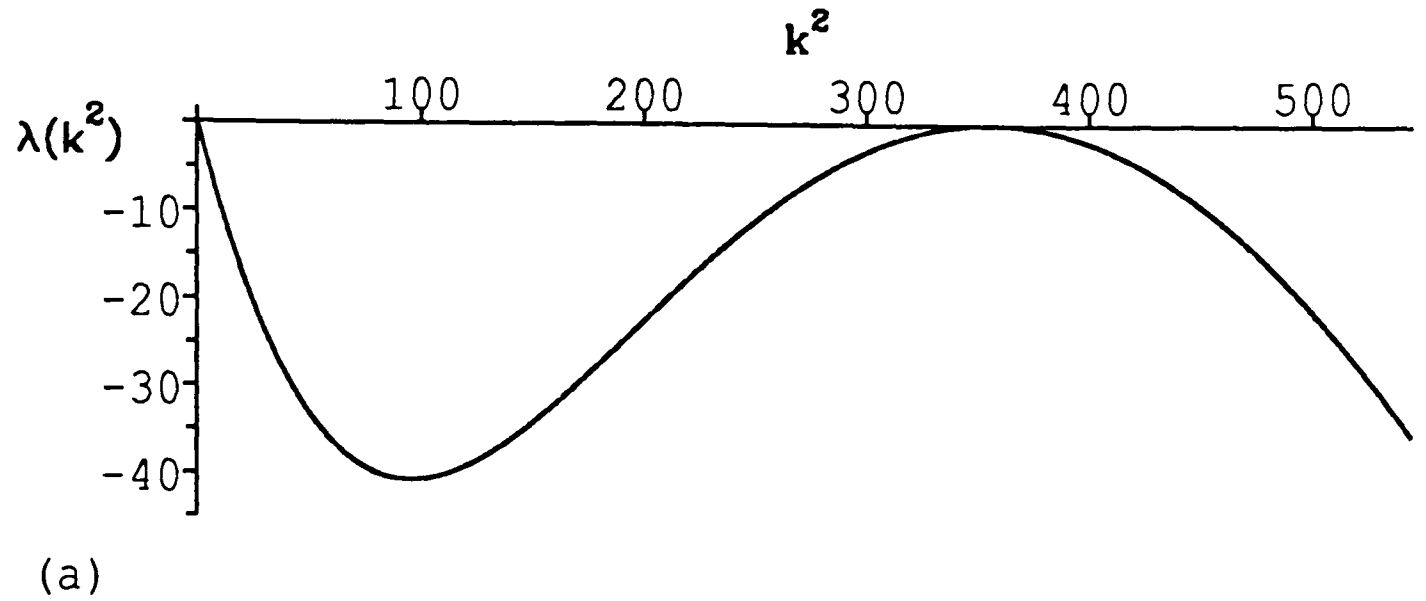

(a)

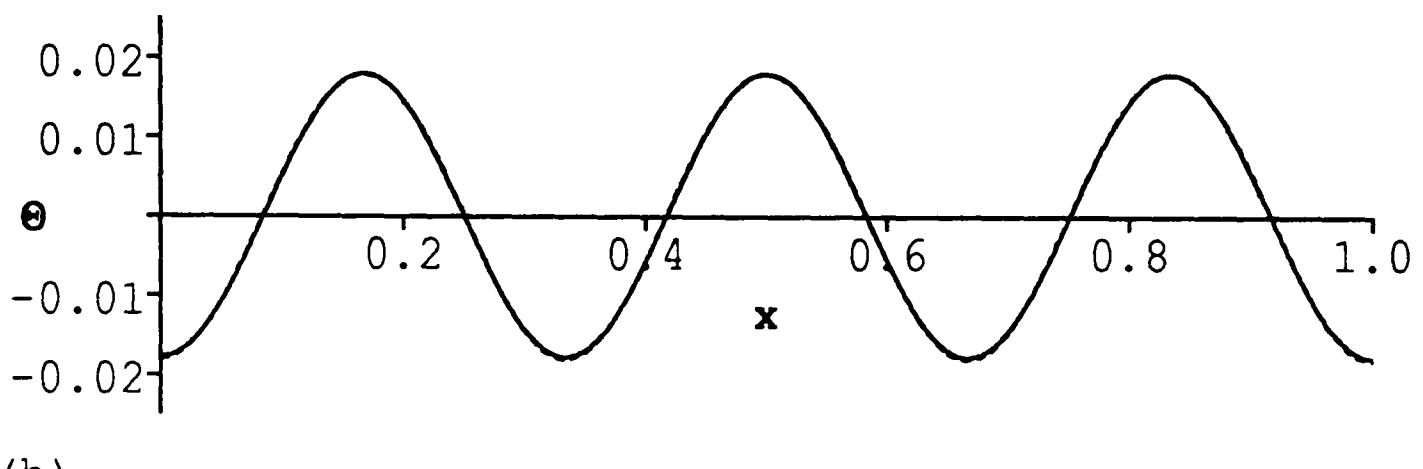

(b)

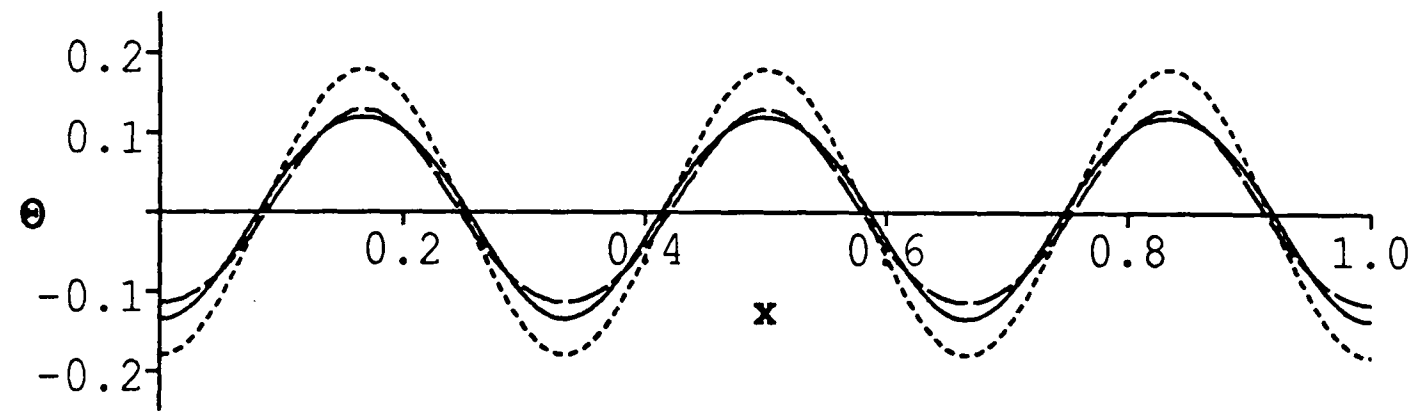

(c)

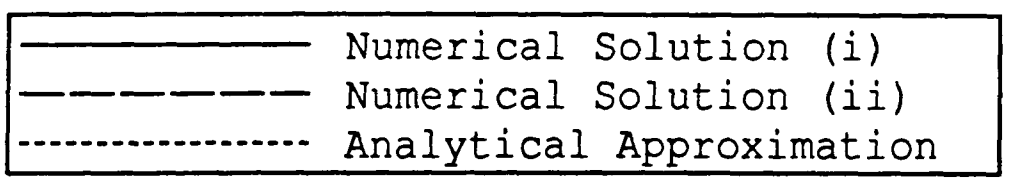

Figure 3.4: Solutions of system (3.10) with parameters as in Example 3.4.2, with unstable eigenvalue $k_c^2 = 36\pi^2$. The dispersion relation $\lambda(k^2)$ is shown in (a), while solutions for the epithelial dilation θ, are shown in (b) for $\epsilon = 0.01$ and in (c) for $\epsilon = 0.1$. Numerical solution (i) is obtained from the NAG algorithm while numerical solution (ii) is obtained from the finite difference algorithm.

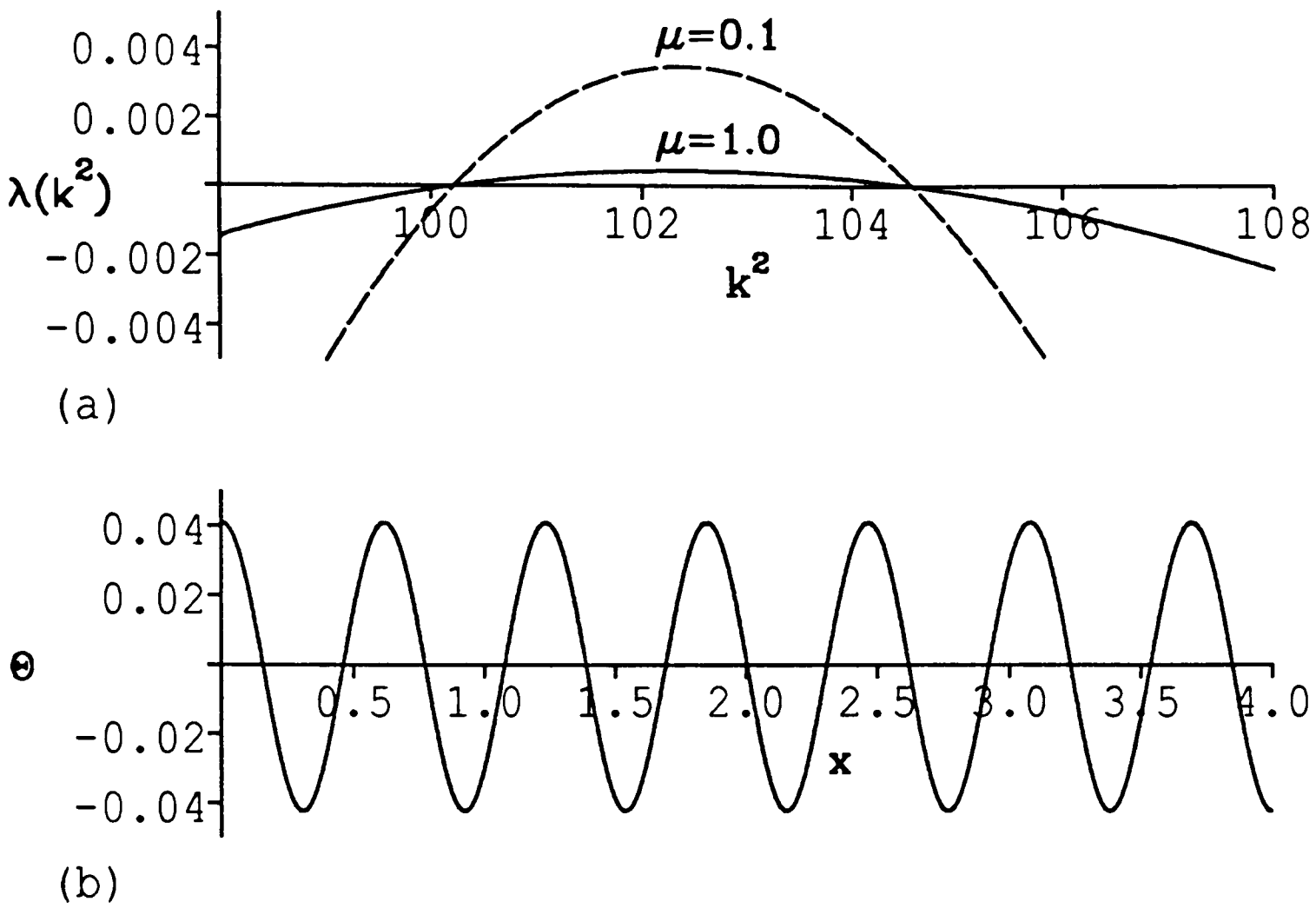

Figure 3.5: Solutions for (3.1) with parameters as in Example 3.4.3: In (a) we have the dispersion relations for $\mu = 0.1$ (broken line) and $\mu = 1.0$ (solid line). In both cases we get the same solutions for n and θ. The solution for θ is shown in (b).

is satisfied. The following parameter space was isolated by the program,

$$\beta = 0.01, \qquad r = 5.0, \qquad D = 0.1, \qquad \rho = 100.2, \qquad \hat{\nu} = 3.17,$$

$$c = 1.0, \qquad \tau = 9.73, \qquad \gamma = 0.29, \qquad \alpha = 5.0.$$

Note that parameter μ, reflecting the epithelial viscosity, does not appear in the expression $c(k^2)$ and is therefore not involved in the mode isolation. Since, from (2.12)

$$\lim_{\mu \to 0} \lambda(k^2) \to \infty,$$

it is clear that the magnitude of μ has a major influence on the linear growth rate of the evolving patterns. Compare the graphs of the dispersion relations in Figure 3.5(a).

To investigate the role of μ in the full nonlinear system, we solved two systems numerically, one where $\mu = 0.1$ and the other where $\mu = 1.0$. As before we used NAG routine D03PGF. In both cases the same solution resulted for large time (see Figure 3.5). This was expected since the term in which μ appears is zero in the steady state problem. More interesting, however, is that the solution evolved to the nonhomogeneous steady state much quicker when μ is small. For $\mu = 0.1$ the steady state solution is reached at $t \approx 70$, while for $\mu = 1.0$ the steady state solution is reached at $t \approx 600$. This agrees with what one would expect intuitively — at high viscosities the tissue responds more slowly to the applied forces and therefore takes longer to reach an equilibrium state.

We also considered several examples in which the long range effects were omitted, thus setting $\beta = 0$ in (3.1), so that we are left with a dispersion relation with an infinite number of allowable modes as was discussed in Section 2.6. Numerically, however, all these cases had unstable blow up solutions. We were also unable to establish any relationship between the initial conditions and the growing solutions, for example, the evolving solutions did not adhere to an initially specified unstable mode. It seemed as if a random combination of various unstable eigenvalues evolved, as permitted by the number of spatial grid points used in the numerical simulations. These results only further confirm the importance of the long range elastic forces as was discussed in Section 2.6. They also agree with the conclusions made by Plickert (1980) and Kolega (1986) from the experimental systems they examined.

With long range effects included, both analytical approximations as well as numerical solutions of our small strain quasi-steady-state system gave results similar in appearance to any one of the rows of feather germs observed on the back of the chick embryo. Our model mechanism can therefore explain chick feather pattern formation in one-dimension. Two-dimensional spatial feather formation will be considered in the following chapter. Note, however, that

in our model the one-dimensional aggregates develop simultaneously, whereas experiments suggest that they develop sequentially (Davidson 1983a, 1983b) as was discussed in Section 1.2. The ability of the model to simulate sequential pattern formation will be examined in Chapters 6 and 7.

Chapter 4

Two-Dimensional Solutions

4.1 Introduction

Although we have so far only considered the small strain quasi-steady-state system (2.11) in one spatial dimension the equations are also valid for higher dimensions. From a biological point of view it is, of course, much more realistic to consider the skin pattern formation problem as being specified on a two-dimensional domain. We can thus compare our model solution with the variety of patterns seen on vertebrate skin and especially feather germ patterns on the chick skin. Although the feather primordia are initiated sequentially we shall explore here only synchronous patterning. Sequential patterning in two-dimensional domains shall be investigated later on in Chapter 7.

The two-dimensional system bifurcates to spatial pattern at either a simple eigenvalue, as is the case in the one-dimensional problem, or at a multiple eigenvalue. Of particular mathematical interest is the bifurcation problem from a multiple eigenvalue, since, as far as we know, this has not been widely studied in pattern formation systems. The linear and nonlinear analysis of the equations in such cases are naturally much more involved. Instead of only single mode patterns evolving, various modes can interact to produce mixed mode patterns.

We begin our analysis in Section 4.2 by examining a range of possible solutions suggested by the linearized problem. In Section 4.3 a nonlinear bifurcation analysis is performed in the vicinity of a multiple eigenvalue. However, since the full small strain quasi-steady-state problem is extremely complicated, a reduced version of the model is used. In the analysis only the simple cases, where we have either one or two multiple eigenvalues at the bifurcation point, are considered in more detail.

Specific examples of the reduced small strain quasi-steady-state model are solved numerically in Section 4.4. The results are compared with the analytical predictions obtained from the perturbation analysis of Section 4.3. Corresponding bifurcation diagrams, as predicted by the nonlinear analysis, are also drawn for two examples.

4.2 Linear Analysis

In Chapter 3 we considered the linear patterned solutions that evolve on one-dimensional domains when zero-flux boundary conditions are imposed. Here we examine the two-dimensional tissue interaction problem linearized about the steady state $\theta = 0$, $n = 1$,

$$\mu \frac{\partial}{\partial t} \nabla^2 \theta = \rho\theta - \nabla^2\theta + \beta\nabla^4\theta - P_1\nabla^2\theta - P_2\nabla^2 n, \tag{4.1a}$$

$$\frac{\partial n}{\partial t} = D\nabla^2 n - rn + Q_1\nabla^2 n + Q_2\nabla^2\theta, \tag{4.1b}$$

as in (2.12). For simplicity we restrict our analysis to rectangular domains of dimensions $\boldsymbol{B} = (L_x, L_y)$, and we assume, as before, zero-flux boundary conditions

$$(\boldsymbol{\eta}\cdot\nabla)n = 0, \quad (\boldsymbol{\eta}\cdot\nabla)\theta = 0, \quad (\boldsymbol{\eta}\cdot\nabla^3)\theta = 0, \quad \text{for } \boldsymbol{B} \text{ on } \partial\boldsymbol{B}, \tag{4.2}$$

where $\boldsymbol{\eta}$ is the unit normal vector on the boundary $\partial\boldsymbol{B}$ of the domain $\boldsymbol{B}$. This ensures that the dermal and epidermal cell densities are conserved in the absence of the dermal logistic growth term. The dispersion relation $\lambda(k^2)$ for this problem is given in (2.14).

Solutions to the linear system (4.1), satisfying the boundary conditions (4.2) are

$$\boldsymbol{w}(\boldsymbol{x}, t) = \begin{pmatrix} \theta \\ n \end{pmatrix} = \sum_{\tilde{\phi},\tilde{\psi}} p_f(\tilde{\phi},\tilde{\psi}) \begin{pmatrix} 1 \\ M(k^2) \end{pmatrix} e^{\lambda(k^2)t} \cos\phi x \cos\psi y,$$

where the discrete wavevectors $\boldsymbol{k} = (\phi, \psi)^T$ are members of the sequence

$$\phi = \frac{\tilde{\phi}\pi}{L_x}, \quad \psi = \frac{\tilde{\psi}\pi}{L_y}, \qquad \tilde{\phi}, \tilde{\psi} = 0, 1, 2, \ldots, \tag{4.3}$$

and

$$M(k^2) = \frac{-Q_2 k^2}{\lambda(k^2) + (D + Q_1)k^2 + r}.$$

Each $p(\tilde{\phi}, \tilde{\psi})$ is determined by a Fourier transform of the initial conditions in terms of

$$\begin{pmatrix} 1 \\ M(k^2) \end{pmatrix} \cos \phi x \cos \psi y.$$

(Compare this solution with the linear solution on an infinite domain given in (2.15).)

As we have seen in the general linear analysis of Section 2.5, a range of unstable eigenvalues appear when we decrease the bifurcation parameter γ below the critical value γ_c. The spatially heterogeneous solution that emerges for large time, then, is the sum of the modes

$$p(\tilde{\phi}, \tilde{\psi}) \begin{pmatrix} 1 \\ M(k^2) \end{pmatrix} \cos \phi x \cos \psi y,$$

corresponding to the *mode pairs* $(\tilde{\phi}, \tilde{\psi})$ for which

$$\lambda \left(\left(\frac{\pi \tilde{\phi}}{L_x} \right)^2 + \left(\frac{\pi \tilde{\psi}}{L_y} \right)^2 \right) > 0.$$

In the remainder of this section we shall be concerned mainly with examples where only one of the discrete eigenvalues, say k_c^2, is unstable. Depending on the domain size, k_c^2 could be either a simple or a multiple eigenvalue. If k_c^2 is a multiple eigenvalue one or more of the mode pairs $(\tilde{\phi}, \tilde{\psi})$ from the above sequence (4.3) satisfy the expression

$$k_c^2 = \left(\frac{\tilde{\phi} \pi}{L_x} \right)^2 + \left(\frac{\tilde{\psi} \pi}{L_y} \right)^2.$$

For the square domain, $L_x = L_y$, some examples of mode pairs corresponding to a simple eigenvalue are

$$\{(1,1)\}, \{(2,2)\}, \{(3,3)\}.$$

Double eigenvalues correspond to the sets of mode pairs

$$\{(0,1),(1,0)\}, \{(0,2),(2,0)\}, \{(1,2),(2,1)\},$$

while a triple eigenvalue would, for example, correspond to

$$\{(5,5),(1,7),(7,1)\}.$$

The eigenvalue k_c^2, corresponding to the set of mode pairs

$$\{(0,5),(5,0),(3,4),(4,3)\},$$

is a quadruple eigenvalue and so on.

A large variety of linear patterns could develop from these various sets of allowable modes. Since the dermal cell density solution n, differs from the epithelial dilation θ, only by the constant factor $M(k_c^2)$, its solution is qualitatively similar. For simplicity we shall therefore only examine the dilation solutions θ, of the linear problem (4.1).

In general, single mode pair solutions give rise to rhombic spatial patterns, since the linear time independent solution which emerges is of the form

$$\theta(\boldsymbol{x}) = \cos\phi x \cos\psi y, \tag{4.4}$$

where $\boldsymbol{k}_c = (\phi,\psi)^T$ is the discrete wavevector satisfying the zero-flux boundary conditions (4.2). Note that the solution (4.4) has been scaled so that $\theta(0,0) = 1$.

Expression (4.4) can be rewritten as

$$\theta(\boldsymbol{x}) = \frac{\cos(\phi x + \psi y) + \cos(\phi x - \psi y)}{2},$$

which, in terms of polar coordinates (r,ϑ), is

$$\theta(r,\vartheta) = \frac{\cos\{r(\phi\cos\vartheta + \psi\sin\vartheta)\} + \cos\{r(\phi\cos\vartheta - \psi\sin\vartheta)\}}{2}. \tag{4.5}$$

Furthermore, by considering (ϕ,ψ) as variables and transforming them to polar coordinates $(\kappa,\varphi/2)$, expression (4.5) simplifies to

$$\theta(r,\vartheta) = \frac{\cos\{\kappa r\cos(\vartheta - \frac{1}{2}\varphi)\} + \cos\{\kappa r\cos(\vartheta + \frac{1}{2}\varphi)\}}{2}, \tag{4.6}$$

where

$$\kappa = \sqrt{\phi^2 + \psi^2} = \sqrt{k_c^2}, \qquad \varphi = 2\arccos\left(\phi/\sqrt{k_c^2}\right). \tag{4.7}$$

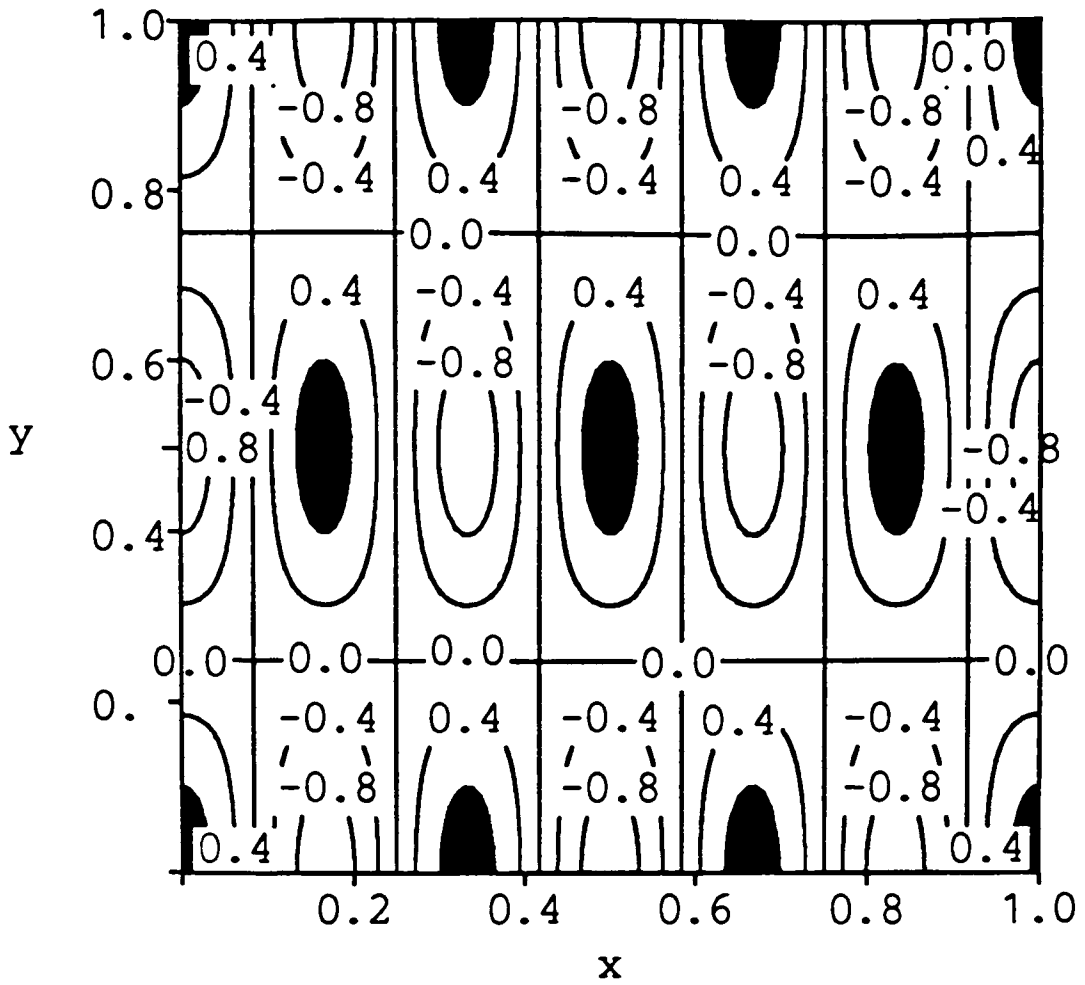

Figure 4.1: Contour graph of the linear mode solution corresponding to the mode pair (6,2) plotted on the square domain (1,1), see expression (4.4). Regions where the solution is larger than 0.8 are shaded. The rhombic angle is $\pi/6$.

It is now easy to see that φ represents the rhombic angle of the solution and that the solution is indeed invariant under a rhombic rotation, that is

$$\theta(r,\vartheta) = \theta(r,\vartheta+\pi) = \mathcal{R}\theta(r,\vartheta) = \theta(r,\vartheta),$$

where $\mathcal{R}$ is the rhombic operator.

A example of a rhombic pattern is illustrated in Figure 4.1. The unstable eigenvalue $k_c^2 = 40\pi^2$, on the square domain $(1,1)$, is a simple eigenvalue with corresponding mode pair $(6,2)$. Since the corresponding wavevector $\boldsymbol{k}_c = (\phi,\psi)^T = (6\pi, 2\pi)^T$, the rhombic angle of the pattern is $\varphi = \pi/6$.

If $\varphi = \pi/2$ or $\varphi = 3\pi/2$, then $\phi = \psi$ and so a square- or chessboard-type pattern results which is a special case of the rhombic pattern. It this case

$$\begin{aligned}\theta(\boldsymbol{x}) &= \cos\phi x \cos\phi y \\ &= \frac{\cos\{\phi(x+y)\} + \cos\{\phi(x-y)\}}{2}.\end{aligned}$$

As before by transforming (x, y) to the polar coordinates (r, ϑ), and (ϕ, ψ) to the polar coordinates $(\kappa, \varphi/2)$, we find

$$\theta(r, \vartheta) = \frac{\cos(r\kappa \cos \vartheta) + \cos(r\kappa \sin \vartheta)}{2},$$

with κ as in (4.7). This solution is square rotationally invariant, since

$$\theta(r, \vartheta) = \theta(r, \vartheta + \frac{\pi}{2}) = \mathcal{S}\theta(r, \vartheta) = \theta(r, \vartheta),$$

where $\mathcal{S}$ is the square rotational operator.

The simplest nonhomogeneous pattern possible on the two-dimensional rectangular domain is the roll, which occurs when either $\phi = 0$ or $\psi = 0$ in the rhombic solution (4.4). The roll is invariant under a rotation of π.

All the linear patterned solutions arising from a simple eigenvalue, as discussed above, tessellate the plane, since they satisfy

$$\boldsymbol{\Gamma}(\boldsymbol{x} + j\boldsymbol{\omega}_1 + l\boldsymbol{\omega}_2) = \boldsymbol{\Gamma}(\boldsymbol{x}),$$

where $\boldsymbol{\Gamma} = (n, \theta)^T$ is the solution of the system, j, l are integers and $\boldsymbol{\omega}_1$, $\boldsymbol{\omega}_2$ are appropriately chosen independent vectors. Patterns corresponding to multiple eigenvalues are not usually tessellations of the plane.

A much richer class of mixed mode patterns does, however, exist. For example, when we have a double eigenvalue k_c^2, with the two corresponding wavevectors, say $(\phi_1, \psi_1)^T$ and $(\phi_2, \psi_2)^T$, satisfying the zero-flux boundary conditions (4.2), two rhombic patterns interact, thus

$$\theta(\boldsymbol{x}) = \alpha \cos \phi_1 x \cos \psi_1 y + \beta \cos \phi_2 x \cos \psi_2, \tag{4.8}$$

where α and β are real numbers so that $\alpha + \beta = 1$. (This scales the time independent solution so that $\theta(0,0) = 1$.) Specifically, if we consider a square domain of dimensions $(3, 3)$ and isolate the unstable eigenvalue $k_c^2 = 40\pi^2/9$, then the corresponding unstable mode pairs are $(2, 6)$ and $(6, 2)$. The time independent solution to the linear problem, where $\alpha = \beta = 1/2$, is as illustrated in Figure 4.2.

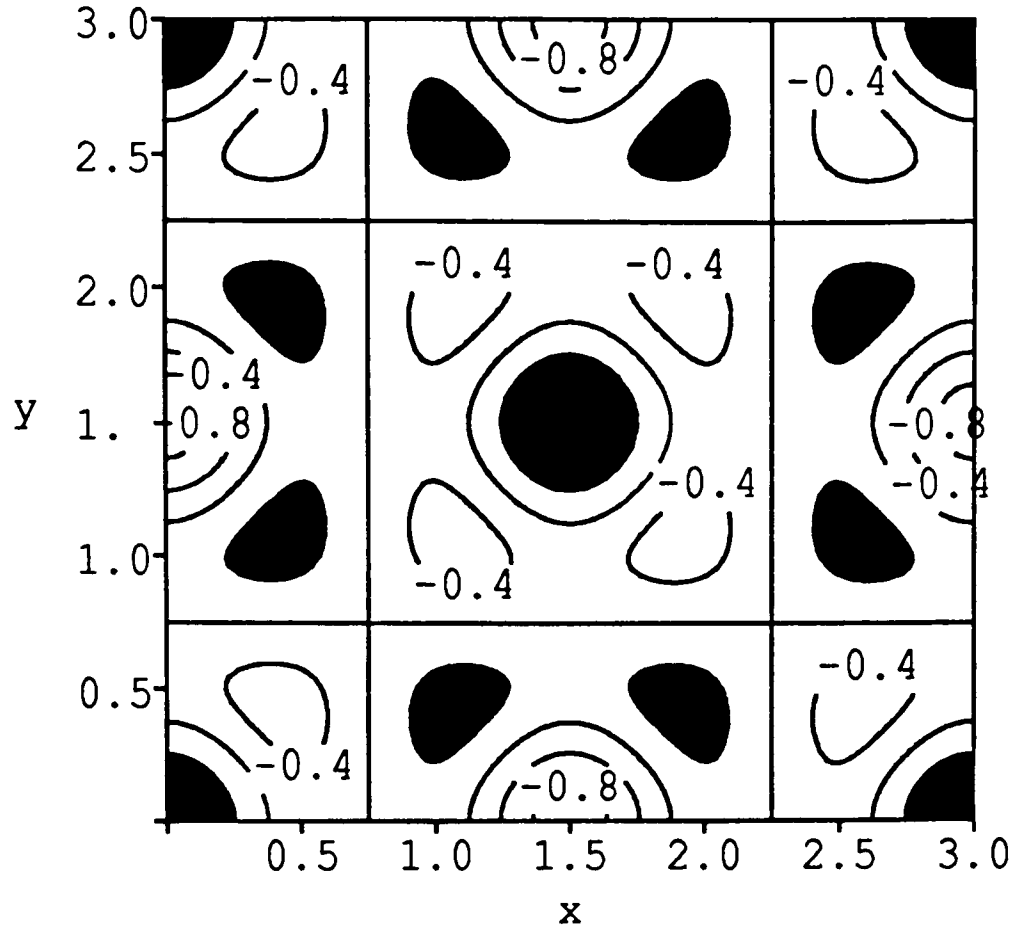

Figure 4.2: The linear double mode solution corresponding to the mode pairs $(2,6)$ and $(6,2)$ plotted on the square domain $(3,3)$, see expression (4.4). Here $\alpha = \beta = \frac{1}{2}$. Regions where the solution is larger than 0.8 are shaded.

Mixed mode patterns can vary considerably depending on the modes interacting. There is, however, a simple pattern tessellating the plane that can be generated by two interacting modes. When the two wavevectors are

$$\begin{pmatrix} \phi_1 \\ \psi_1 \end{pmatrix} = \begin{pmatrix} \kappa \\ \sqrt{3}\kappa \end{pmatrix}, \qquad \begin{pmatrix} \phi_2 \\ \psi_2 \end{pmatrix} = \begin{pmatrix} 2\kappa \\ 0 \end{pmatrix}, \tag{4.9}$$

or

$$\begin{pmatrix} \phi_1 \\ \psi_1 \end{pmatrix} = \begin{pmatrix} \sqrt{3}\kappa \\ \kappa \end{pmatrix}, \qquad \begin{pmatrix} \phi_2 \\ \psi_2 \end{pmatrix} = \begin{pmatrix} 0 \\ 2\kappa \end{pmatrix}, \tag{4.10}$$

and $\alpha = 2/3$, $\beta = 1/3$ then a hexagonal pattern results. With wavevectors as in (4.9) the solution can be written as

$$\theta(\boldsymbol{x}) = \frac{\cos\kappa(\sqrt{3}y + x) + \cos\kappa(\sqrt{3}y - x) + \cos 2\kappa x}{3}, \tag{4.11}$$

which, in terms of polar coordinates (r, ϑ), is

$$\theta(\boldsymbol{x}) = \frac{\cos\{2\kappa r \sin(\vartheta + \frac{\pi}{6})\} + \cos\{2\kappa r \sin(\vartheta - \frac{\pi}{6})\} + \cos\{2\kappa r \sin(\vartheta - \frac{\pi}{2})\}}{3}.$$

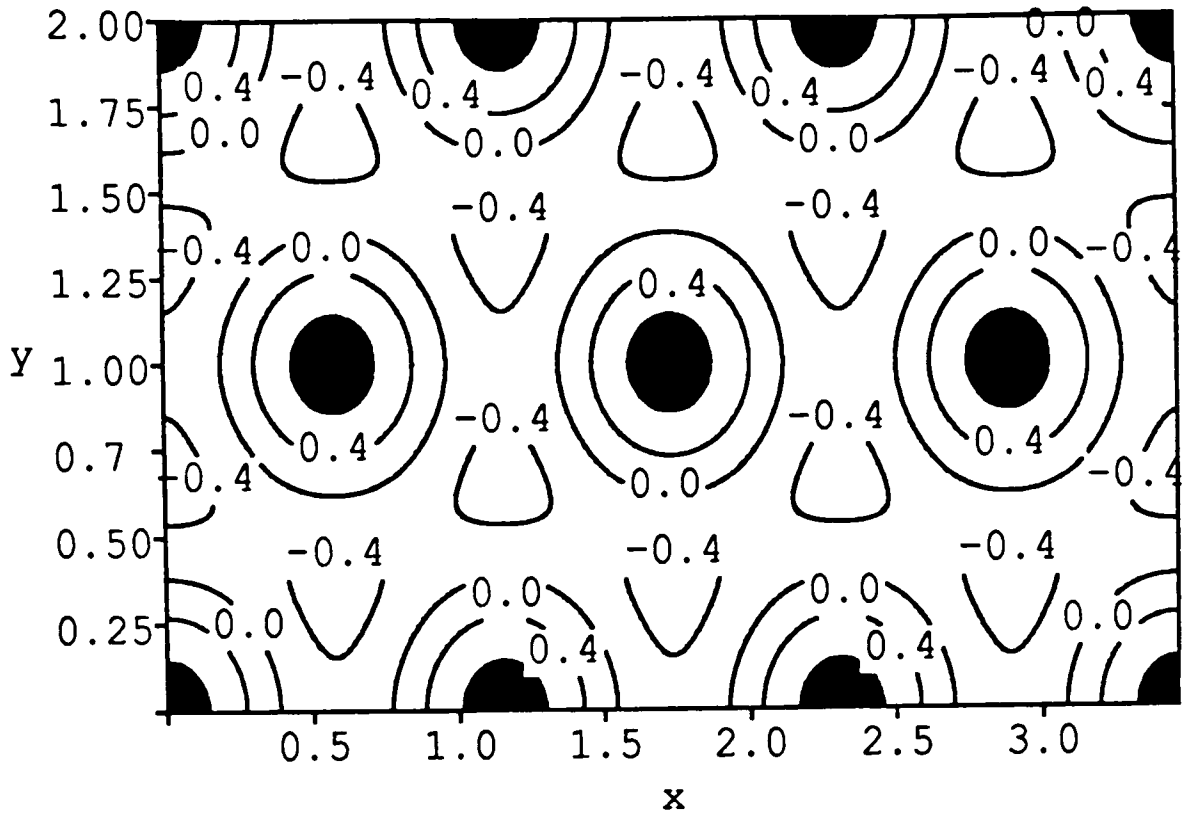

Figure 4.3: Contour graph of the linear hexagonal pattern corresponding to the mode pairs $(6,2)$ and $(0,4)$ plotted on the rectangular domain $(2\sqrt{3},2)$, see expression (4.10). Regions where the solution is larger than 0.8 are shaded.

The polar coordinate form shows the invariance under a hexagonal rotation, that is invariance to rotation by $\pi/3$, thus

$$\theta(r,\vartheta) = \theta(r,\vartheta+\frac{\pi}{3}) = \mathcal{H}\theta(r,\vartheta) = \theta(r,\vartheta),$$

where $\mathcal{H}$ is the hexagonal rotation operator.

As an illustrative example we assume the unstable eigenvalue $k_c^2 = 4\pi^2$ on the domain $(2\sqrt{3},2)$. The corresponding mode pairs are $(6,2)$ and $(0,4)$ so that the two wavevectors have the required form (4.10), where $\kappa = \pi$. The resulting pattern is shown in Figure 4.3. Note that hexagonal solutions not only satisfy zero-flux conditions on the boundaries of a rectangular domain, but do so also on all the hexagonal symmetry boundaries.

Naturally, where we have a triple or higher multiple eigenvalue, a much richer and more complex range of linear patterns is possible.

We have only considered linear solutions in this section. It is, however, important to realize that linear analysis gives only an approximated guide as to

the patterns we should expect from nonlinear systems. To fully investigate our nonlinear tissue interaction problem (2.9) a weakly nonlinear analysis as well as numerical simulations are necessary.

4.3 Nonlinear Bifurcation Analysis

In Section 3.3 we performed a weakly nonlinear bifurcation analysis on the nonlinear small strain quasi-steady-state problem in one spatial dimension. In this section we extend our analysis to a two-dimensional version of the model. A two-dimensional nonlinear analysis was performed by Maini & Murray (1988) on a mechanochemical equation for epithelial morphogenesis when bifurcation to patterns is from simple eigenvalues. Here we extend their work by considering bifurcations from multiple eigenvalues. Moreover, a system of two equations, rather than a single equation is considered.

The nonlinear analysis on the full two-dimensional problem is extremely involved. To make the system more manageable, yet still retain the essential features, we set some selected parameters equal to zero. Even though we are therefore looking at a simpler problem we can still get an idea of the vast range of possible patterns involved. The nonlinear analysis will help, as before, in selecting appropriate parameter spaces for solving our problem numerically.

We consider here a sub-problem by setting the variables γ and $\hat{\nu}$ equal to zero. This changes the tissue interaction mechanism described in Section 2.3, since we are ignoring the dermal and epidermal metabolism of the signal chemicals. Nevertheless, although the actual interaction mechanism is changed, the basic features remain similar: a high dermal cell density causes epithelial contraction while epithelial contraction, in turn, induces dermal cell chemotaxis.

As in the previous chapter we neglect viscous effects by setting $\mu = 0$ and logistic growth by setting $r = 0$. By using a steady state analysis similar to that of Section 3.2 on the one-dimensional version of this caricature system when the dermal diffusion D is set to zero as before, it is easy to demonstrate that

the nonhomogeneous solutions blow up. One- and two-dimensional nonhomogeneous steady state solutions are, however, possible if the dermal cell diffusion is not ignored as we shall demonstrate in this and in the next sections.

The tissue interaction model now becomes the two-dimensional caricature system

$$\nabla^2\theta - \beta\nabla^4\theta + \nabla^2\left\{\frac{\tau n^2}{1+cn^2}\right\} = \rho\theta, \tag{4.12a}$$

$$\frac{\partial n}{\partial t} = D\nabla^2 n - \nabla\cdot(n\nabla\alpha(1-\theta))\,. \tag{4.12b}$$

The general linear stability analysis of this system is as in Section 2.5. The linearization about the steady state $\theta = 0$, $n = 1$, is as in (2.12), but with the relevant parameters set to zero, which implies that the linear interaction parameters are

$$P_1 = Q_1 = 0, \qquad P_2 = \frac{2\tau}{1+c^2}, \qquad Q_2 = \alpha.$$

The dispersion relation reduces to

$$\lambda(k^2) = -\frac{c(k^2)}{b(k^2)},$$

where

$$\begin{aligned} b(k^2) &= \beta k^4 + k^2 + \rho, \\ c(k^2) &= \beta D k^6 - (\alpha P_2 - D)k^4 + \rho D k^2. \end{aligned}$$

As in the last example of Section 2.6 we can determine the conditions under which $c(k^2) < 0$, and hence the parameter space in which the linear analysis predicts spatially inhomogeneous solutions. Firstly, we require that

$$\alpha P_2 - D > 0,$$

and secondly that

$$(\alpha P_2 - D)^2 > 4\beta\rho D^2.$$

As bifurcation parameter we use the chemotactic factor α, and assume that α_c is the critical value at which the linear homogeneous steady state loses stability. For $\alpha > \alpha_c$ we have a range of unstable eigenvalues (k_-^2, k_+^2) where

$$k_\pm^2 = \frac{(\alpha P_2 - D) \pm \sqrt{(\alpha P_2 - D)^2 - 4\beta\rho D^2}}{2\beta D}.$$

At the critical point where $\alpha = \alpha_c$,

$$(\alpha_c P_2 - D)^2 = 4\beta\rho D^2,$$

while the critical eigenvalue

$$k_c^2 = \frac{\alpha_c P_2 - D}{2\beta D}.$$

In the one-dimensional case we carried out the nonlinear analysis in general on an infinite domain. However, for algebraic simplicity we consider, as mentioned above, the two-dimensional system on the rectangular domain $\boldsymbol{B} = (L_x, L_y)$ and assume the zero-flux boundary conditions as given in (4.2).

We further choose the dimensions L_x and L_y of our rectangular domain so that stability is lost at an isolated multiple eigenvalue k^2. We perform a perturbation analysis in the neighbourhood of this eigenvalue by setting

$$\alpha = \alpha_c + \alpha_1\epsilon + \alpha_2\epsilon^2 + \alpha_3\epsilon^3 + \ldots \quad \text{where } 0 < \epsilon \ll 1. \tag{4.13}$$

and also

$$t = T_1/\epsilon + T_2/\epsilon^2 + T_3/\epsilon^3 + \ldots, \tag{4.14}$$

thus introducing the multiple time scales

$$T_1 = \epsilon t, \qquad T_2 = \epsilon^2 t, \qquad T_3 = \epsilon^3 t,$$

and so on.

We assume a power series expansion for θ and n of the form

$$\theta(\boldsymbol{x}, \epsilon, T_1, \ldots) = \epsilon\theta_1(\boldsymbol{x}, T_1, \ldots) + \epsilon^2\theta_2(\boldsymbol{x}, T_1, \ldots) + \ldots, \tag{4.15a}$$

$$n(\boldsymbol{x}, \epsilon, T_1, \ldots) = 1 + \epsilon n_1(\boldsymbol{x}, T_1, \ldots) + \epsilon^2 n_2(\boldsymbol{x}, T_1, \ldots) + \ldots, \tag{4.15b}$$

where the variables θ and n are considered as functions of $\boldsymbol{x}$, ϵ and T_i, $i = 1, 2, 3, \ldots$.

For algebraic simplicity we initially set

$$\tilde{n}(\boldsymbol{x}, \epsilon, T_1, \ldots) = 1 - n(\boldsymbol{x}, \epsilon, T_1, \ldots),$$

and substitute this into the interaction term of equation (4.12a). The interaction term is then expanded in its Taylor series about $\tilde{n} = 0$,

$$\frac{\tau(1+\tilde{n})^2}{1+c(1+\tilde{n})^2} = p_0 + p_1\tilde{n} + p_2\tilde{n}^2 + p_3\tilde{n}^3 + O(\epsilon^4),$$

where

$$p_0 = \frac{\tau}{1+c}, \qquad p_2 = \frac{\tau(1-3c)}{(1+c)^3},$$
$$p_1 = \frac{2\tau}{(1+c)^2}, \qquad p_3 = \frac{4\tau c(c-1)}{(1+c)^4}.$$

As in the one-dimensional case our system can be written in the form

$$\mathcal{L}\begin{pmatrix} \theta \\ \tilde{n} \end{pmatrix} = \boldsymbol{G} + \boldsymbol{E}, \tag{4.16}$$

where $\mathcal{L}$ is the linear operator, $\boldsymbol{G}$ is the function arising from the nonlinear terms and $\boldsymbol{E}$ is the function arising from the dependence of α on ϵ and the time derivatives. We have

$$\mathcal{L} \equiv \begin{pmatrix} -\beta\nabla^4 + \nabla^2 - \rho & p_1\nabla^2 \\ \alpha_c\nabla^2 & D\nabla^2 \end{pmatrix}.$$

As before we denote the components of a two-dimensional vector by the superscripts (1) and (2), so

$$\begin{aligned} G^{(1)} &= -\nabla^2(p_2\tilde{n}^2 + p_3\tilde{n}^3) + O(\epsilon^4), \\ G^{(2)} &= -\alpha_c\nabla\cdot(\tilde{n}\nabla\theta) + O(\epsilon^4), \end{aligned}$$

and

$$\begin{aligned} E^{(1)} &= 0, \\ E^{(2)} &= -\nabla\cdot\{(\tilde{n}+1)\nabla(\alpha_1 + \epsilon\alpha_2)\epsilon\theta\} + \epsilon\frac{\partial\tilde{n}}{\partial T_1} + \epsilon^2\frac{\partial\tilde{n}}{\partial T_2} + O(\epsilon^4). \end{aligned}$$

The matrix $\boldsymbol{L}_{(\phi,\psi)}$, arising from applying the operator $\mathcal{L}$ on terms of the form $e^{i(\phi,\psi)\cdot\mathbf{x}}$, is defined as

$$\boldsymbol{L}_{(\phi,\psi)} = \begin{pmatrix} -\beta(\phi^2+\psi^2)^2 - (\phi^2+\psi^2) - \rho & -p_1(\phi^2+\psi^2) \\ -\alpha_c(\phi^2+\psi^2) & -D(\phi^2+\psi^2) \end{pmatrix}.$$

By substituting the series expansions (4.15) into (4.16) and equating coefficients of $O(\epsilon)$, $O(\epsilon^2)$ and so on, the system of nonlinear equations is reduced to a hierarchy of linear equations.

Equating coefficients of $O(\epsilon)$ gives

$$\mathcal{L}\begin{pmatrix} \theta_1 \\ n_1 \end{pmatrix} = \mathbf{0}.$$

We assume that k_c^2 is the only unstable eigenvalue with corresponding modes growing on the long time scale. Solving the $O(\epsilon)$ equation gives

$$\begin{pmatrix} \theta_1 \\ n_1 \end{pmatrix} = \sum_{i=1}^{\Delta} \begin{pmatrix} 1 \\ M_i \end{pmatrix} A_i(T_1,T_2)\cos\phi_i x \cos\psi_i y, \tag{4.17}$$

where Δ is the multiplicity of the eigenvalue the functions $A_i(T_1,T_2)$ are the slow-time dependent amplitudes. As before, for notational convenience we only consider the A_i as functions of T_1 and T_2. Since $\boldsymbol{k}_c = (\phi_i,\psi_i)^T$ the unstable eigenvalue satisfies

$$k_c^2 = \phi_i^2 + \psi_i^2,$$

where

$$\phi_i = \frac{\tilde{\phi}_i\pi}{L_x}, \qquad \psi_i = \frac{\tilde{\psi}_i\pi}{L_y}, \qquad i = 1,2,\ldots,\Delta,$$

and $\tilde{\phi}_i$, $\tilde{\psi}_i$ can only take on non-negative integer values. Since

$$\boldsymbol{L}_{(\phi_i,\psi_i)}\begin{pmatrix} 1 \\ M_i \end{pmatrix} = \mathbf{0},$$

we find that

$$M = M_i = -\frac{\alpha_c}{D}.$$

At $O(\epsilon^2)$,

$$\mathcal{L}\begin{pmatrix} \theta_2 \\ n_2 \end{pmatrix} = \boldsymbol{S},$$

where

$$\begin{aligned} S^{(1)} &= -p_2 \nabla n_1^2, \\ S^{(2)} &= -\alpha_c \nabla \cdot (n_1 \nabla \theta_1) - \alpha_1 \nabla^2 \theta_1 + \frac{\partial n_1}{\partial T_1}. \end{aligned}$$

Substituting θ_1 and n_1 into the above equations gives

$$\begin{aligned} \mathcal{L}\begin{pmatrix} \theta_2 \\ n_2 \end{pmatrix} &= \frac{1}{2} M \begin{pmatrix} 2p_2 M \\ \alpha_c \end{pmatrix} \sum_{i=1}^{\Delta} A_i^2(T_1, T_2) \left[\phi_i^2 \cos 2\phi_i x + \psi_i^2 \cos 2\psi_i y \right. \\ &\quad \left. + \left(\phi_i^2 + \psi_i^2 \right) \cos 2\phi_i x \cos 2\psi_i y \right] \\ &\quad + \frac{1}{4} M \begin{pmatrix} 2p_2 M \\ \alpha_c \end{pmatrix} \sum_{i=1}^{\Delta-1} \sum_{j=i+1}^{\Delta} A_i(T_1, T_2) A_j(T_1, T_2) \\ &\quad \left[\left\{ (\phi_i + \phi_j)^2 + (\psi_i + \psi_j)^2 \right\} \cos(\phi_i + \phi_j) x \cos(\psi_i + \psi_j) y \right. \\ &\quad + \left\{ (\phi_i + \phi_j)^2 + (\psi_i - \psi_j)^2 \right\} \cos(\phi_i + \phi_j) x \cos(\psi_i - \psi_j) y \\ &\quad + \left\{ (\phi_i - \phi_j)^2 + (\psi_i + \psi_j)^2 \right\} \cos(\phi_i - \phi_j) x \cos(\psi_i + \psi_j) y \\ &\quad \left. + \left\{ (\phi_i - \phi_j)^2 + (\psi_i - \psi_j)^2 \right\} \cos(\phi_i - \phi_j) x \cos(\psi_i - \psi_j) y \right] \\ &\quad + \begin{pmatrix} 0 \\ \alpha_1 \end{pmatrix} \sum_{i=1}^{\Delta} A_i(T_1, T_2) \left(\phi_i^2 + \psi_i^2 \right) \cos \phi_i x \cos \psi_i y \\ &\quad + \begin{pmatrix} 0 \\ M \end{pmatrix} \sum_{i=1}^{\Delta} \frac{\partial A_i(T_1, T_2)}{\partial T_1} \cos \phi_i x \cos \psi_i y. \end{aligned} \tag{4.18}$$

Terms of the form $\cos \phi_i x \cos \psi_i y$ appear in the right hand side of this equation if integers i, j and k exist, where $1 \leq i, j, k \leq \Delta$ and $i \neq j$, so that

$$\phi_i + \phi_j = \phi_k \quad \text{and} \quad \psi_i - \psi_j = \psi_k.$$

or

$$\phi_i - \phi_j = \phi_k \quad \text{and} \quad \psi_i + \psi_j = \psi_k. \tag{4.19}$$

Since these terms are solutions of the homogeneous problem

$$\mathcal{L}\begin{pmatrix} \theta_2 \\ n_2 \end{pmatrix} = \mathbf{0},$$

secular terms arise in the particular solution for $(\theta_2, n_2)^T$. If these secular terms do appear we suppress them, as in Section 3.3, by making use of the Fredholm Alternative. The full details are discussed below.

Even if conditions (4.19) are not satisfied secular terms still appear in the $O(\epsilon^2)$ solution because of the last two terms in expression (4.18). Similar to the one-dimensional nonlinear analysis we suppress these secular terms by setting $\alpha_1 = 0$ and $T_1 = 0$ in our power series expansions (4.13) and (4.14) so that the amplitudes A_i are now only dependent on T_2.

The solution of (4.18) consists of a complimentary function and a particular integral and so we write

$$\begin{pmatrix} \theta_2 \\ n_2 \end{pmatrix} = \begin{pmatrix} \theta_2^h \\ n_2^h \end{pmatrix} + \begin{pmatrix} \theta_2^p \\ n_2^p \end{pmatrix}, \tag{4.20}$$

where the complimentary solution

$$\begin{pmatrix} \theta_2^h \\ n_2^h \end{pmatrix} = \sum_{i=1}^{\Delta} \boldsymbol{C}_i \cos\phi_i x \cos\psi_i y,$$

with $\boldsymbol{C}_i$ a vector function of T_i, $i = 2, 3, \ldots$. The particular solution

$$\begin{aligned} \begin{pmatrix} \theta_2^p \\ n_2^p \end{pmatrix} &= \sum_{i=1}^{\Delta} A_i(T_1, T_2)[\boldsymbol{a}_i \cos 2\phi_i x + \boldsymbol{b}_i \cos 2\psi_i y \\ &\quad + \boldsymbol{d}_i \cos 2\phi_i x \cos 2\psi_i y] \\ &\quad + \sum_{i=1}^{\Delta-1} \sum_{j=i+1}^{\Delta} A_i(T_1, T_2) A_j(T_1, T_2) \\ &\quad [\, \boldsymbol{a}_{i,j} \cos(\phi_i + \phi_j) x \cos(\psi_i + \psi_j) y \\ &\quad + \boldsymbol{b}_{i,j} \cos(\phi_i + \phi_j) x \cos(\psi_i - \psi_j) y \\ &\quad + \boldsymbol{d}_{i,j} \cos(\phi_i - \phi_j) x \cos(\psi_i + \psi_j) y \\ &\quad + \boldsymbol{e}_{i,j} \cos(\phi_i - \phi_j) x \cos(\psi_i - \psi_j) y]. \end{aligned}$$

By substituting the particular solution into the left hand side of equation (4.18) and balancing the harmonics we find that

$$\begin{aligned} \boldsymbol{a}_i &= \begin{cases} \dfrac{\mathrm{adj}(\boldsymbol{L}_{(2\phi_i,0)})}{\det(\boldsymbol{L}_{(2\phi_i,0)})} \dfrac{1}{2} M \phi_i^2 \begin{pmatrix} 2p_2 M \\ \alpha_c \end{pmatrix} & \text{if } \phi_i > 0 \\ \boldsymbol{0} & \text{if } \phi_i = 0 \end{cases}, \\ \boldsymbol{b}_i &= \begin{cases} \dfrac{\mathrm{adj}(\boldsymbol{L}_{(0,2\psi_i)})}{\det(\boldsymbol{L}_{(0,2\psi_i)})} \dfrac{1}{2} M \psi_i^2 \begin{pmatrix} 2p_2 M \\ \alpha_c \end{pmatrix} & \text{if } \psi_i > 0 \\ \boldsymbol{0} & \text{if } \psi_i = 0 \end{cases}, \\ \boldsymbol{d}_i &= \frac{\mathrm{adj}(\boldsymbol{L}_{(2\phi_i,2\psi_i)})}{\det(\boldsymbol{L}_{(2\phi_i,2\psi_i)})} \frac{1}{2} M \left(\phi_i^2 + \psi^2\right) \begin{pmatrix} 2p_2 M \\ \alpha_c \end{pmatrix}, \end{aligned}$$

and also

$$\boldsymbol{a}_{i,j} = \frac{\mathrm{adj}(\boldsymbol{L}_{(\phi_i+\phi_j,\psi_i+\psi_j)})}{\det(\boldsymbol{L}_{(\phi_i+\phi_j,\psi_i+\psi_j)})}[(\phi_i+\phi_j)^2+(\psi_i+\psi_j)^2]\frac{1}{4}M\begin{pmatrix} 2p_2M \\ \alpha_c \end{pmatrix}, \quad (4.21a)$$

$$\boldsymbol{b}_{i,j} = \frac{\mathrm{adj}(\boldsymbol{L}_{(\phi_i+\phi_j,\psi_i-\psi_j)})}{\det(\boldsymbol{L}_{(\phi_i+\phi_j,\psi_i-\psi_j)})}[(\phi_i+\phi_j)^2+(\psi_i-\psi_j)^2]\frac{1}{4}M\begin{pmatrix} 2p_2M \\ \alpha_c \end{pmatrix}, \quad (4.21b)$$

$$\boldsymbol{d}_{i,j} = \frac{\mathrm{adj}(\boldsymbol{L}_{(\phi_i-\phi_j,\psi_i+\psi_j)})}{\det(\boldsymbol{L}_{(\phi_i-\phi_j,\psi_i+\psi_j)})}[(\phi_i-\phi_j)^2+(\psi_i+\psi_j)^2]\frac{1}{4}M\begin{pmatrix} 2p_2M \\ \alpha_c \end{pmatrix}, \quad (4.21c)$$

$$\boldsymbol{e}_{i,j} = \frac{\mathrm{adj}(\boldsymbol{L}_{(\phi_i-\phi_j,\psi_i-\psi_j)})}{\det(\boldsymbol{L}_{(\phi_i-\phi_j,\psi_i-\psi_j)})}[(\phi_i-\phi_j)^2+(\psi_i-\psi_j)^2]\frac{1}{4}M\begin{pmatrix} 2p_2M \\ \alpha_c \end{pmatrix}, \quad (4.21d)$$

where the operators det and adj indicate the determinant and adjoint respectively of the corresponding matrices. Calculating $\boldsymbol{a}_i$, for example, we find that

$$\begin{aligned} a_i^{(1)} &= \frac{2M\phi_i^2(\alpha_c p_1 - 2p_2DM)}{64D\beta\phi_i^4 + 16(D-\alpha_c p_1)\phi_i^2 + 4D\rho}, \\ a_i^{(2)} &= \frac{-16\alpha_c\beta M\phi_i^4 + 4\alpha_c M(2p_2M-1)\phi_i^2 - \alpha_c\rho M}{128D\beta\phi_i^4 + 32(D-\alpha_c p_1)\phi_i^2 + 8D\rho}. \end{aligned}$$

Similar forms can be found for $b_{i,j}$, $d_{i,j}$ and $e_{i,j}$.

At $O(\epsilon^3)$,

$$\mathcal{L}\begin{pmatrix} \theta_3 \\ n_3 \end{pmatrix} = \boldsymbol{R}, \quad (4.22)$$

where

$$\begin{aligned} R^{(1)} &= -\nabla^2(2p_2n_1n_2 + p_3n_1^3), \\ R^{(2)} &= -\nabla\alpha_c\cdot(n_1\nabla\theta_2) - \nabla\alpha_c\cdot(n_2\nabla\theta_1) - \alpha_2\nabla^2\theta_1 + \frac{\partial n_1}{\partial T_2} \end{aligned}$$

We write $\boldsymbol{R}$ in the following form

$$\begin{aligned} \boldsymbol{R} &= \boldsymbol{R}_0(\cos\phi_i x, \cos\psi_i y) + \boldsymbol{R}_1(\cos(\phi_i \pm 2\phi_j)x, \cos\psi_i y) \\ &\quad + \boldsymbol{R}_2(\cos\phi_i x, \cos(\psi_i \pm 2\psi_j)y) + \boldsymbol{R}_3(\cos 3\phi_i x, \cos\psi_i y) \\ &\quad + \boldsymbol{R}_4(\cos\phi_i x, \cos 3\psi_i y) + \boldsymbol{R}_5. \end{aligned} \quad (4.23)$$

Since it is easy to show, from (4.21), that

$$\boldsymbol{a}_{i,j} = \boldsymbol{a}_{j,i}, \qquad \boldsymbol{b}_{i,j} = \boldsymbol{b}_{j,i}, \qquad \boldsymbol{d}_{i,j} = \boldsymbol{d}_{j,i}, \qquad \boldsymbol{e}_{i,j} = \boldsymbol{e}_{j,i},$$

we find that

$$
\begin{aligned}
R_0^{(1)} &= \sum_{i=1}^{\Delta} \Big[M A_i^3(T_2) \left(\phi_i^2 + \psi_i^2\right) \left(a_i^{(2)} p_2 + b_i^{(2)} p_2 \right. \\
&\quad \left. + \frac{1}{2} d_i^{(2)} p_2 + \frac{9}{16} p_3 M^2 \right) \cos\phi_i x \cos\psi_i y \Big] \\
&\quad + \left(\sum_{i=1}^{\Delta-1} \sum_{j=i+1}^{\Delta} + \sum_{i=2}^{\Delta} \sum_{j=1}^{i-1} \right) \Big[\frac{1}{4} M A_i^2(T_2) A_j(T_2) \left(\phi_j^2 + \psi_j^2\right) \\
&\quad \left(2p_2 a_{i,j}^{(2)} + 2p_2 b_{i,j}^{(2)} + 2p_2 d_{i,j}^{(2)} + 2p_2 e_{i,j}^{(2)} + 3p_3 M^2\right) \Big] \cos\phi_j x \cos\psi_j y,
\end{aligned}
$$

and

$$
\begin{aligned}
R_0^{(2)} &= \sum_{i=1}^{\Delta} \Big[\alpha_2 A_i(T_2) \left(\phi_i^2 + \psi_i^2\right) + \alpha_c A_i^3(T_2) \Big\{ a_i^{(1)} M \phi_i^2 + b_i^{(1)} M \psi_i^2 \\
&\quad + \frac{1}{2} \left(\phi_i^2 + \psi_i^2\right) \left(d_i^{(1)} M - \frac{1}{2} d_i^{(2)} \right) \Big\} \Big] \cos\phi_i x \cos\psi_i y \\
&\quad + \left(\sum_{i=1}^{\Delta-1} \sum_{j=i+1}^{\Delta} + \sum_{i=2}^{\Delta} \sum_{j=1}^{i-1} \right) \Big[\frac{1}{4} \alpha_c A_i^2(T_2) A_j(T_2) \\
&\quad \Big\{ M \left(a_{i,j}^{(1)} + b_{i,j}^{(1)} + d_{i,j}^{(1)} + e_{i,j}^{(1)} \right) \left(\phi_j^2 + \psi_j^2\right) \\
&\quad + \left(a_{i,j}^{(1)} M - a_{i,j}^{(2)} \right) \left(\phi_i \phi_j + \psi_i \psi_j\right) \\
&\quad + \left(b_{i,j}^{(1)} M - b_{i,j}^{(2)} \right) \left(\phi_i \phi_j - \psi_i \psi_j\right) \\
&\quad + \left(d_{i,j}^{(1)} M - d_{i,j}^{(2)} \right) \left(-\phi_i \phi_j + \psi_i \psi_j\right) \\
&\quad + \left(e_{i,j}^{(1)} M - e_{i,j}^{(2)} \right) \left(-\phi_i \phi_j - \psi_i \psi_j\right) \Big\} \Big] \cos\phi_j x \cos\psi_j y \\
&\quad + M \sum_{i=1}^{\Delta} \frac{\partial A_i(T_2)}{\partial T_2} \cos\phi_i x \cos\psi_i y,
\end{aligned}
$$

where we have substituted the expressions (4.17) and (4.20) for $(\theta_1, n_1)^T$ and $(\theta_2, n_2)^T$ respectively. Also

$$
\begin{aligned}
R_1^{(1)} &= \left(\sum_{i=1}^{\Delta-1} \sum_{j=i+1}^{\Delta} + \sum_{i=2}^{\Delta} \sum_{j=1}^{i-1} \right) \Big\{ A_i(T_2) A_j^2(T_2) M \left(a_j^{(2)} p_2 + \frac{3}{8} p_3 M^2 \right) \\
&\quad \Big[\left(\phi_i^2 + \psi_i^2 + 4\phi_j^2 + 4\phi_i \phi_j\right) \cos(\phi_i - 2\phi_j) x \cos\psi_i y \\
&\quad + \left(\phi_j^2 + \psi_j^2 + 4\phi_j^2 - 4\phi_i \phi_j\right) \cos(2\phi_j + \phi_i) x \cos\psi_i y \Big] \\
&\quad + \frac{1}{2} p_2 M A_i^2(T_2) A_j(T_2) \Big[\left(a_{i,j}^{(2)} + b_{i,j}^{(2)} \right) \\
&\quad \left(\phi_i^2 + \psi_i^2 + 4\phi_i^2 + 4\phi_i \phi_j\right) \cos(\phi_j + 2\phi_i) x \cos\psi_j y \\
&\quad + \left(d_{i,j}^{(2)} + e_{i,j}^{(2)} \right) \left(\phi_j^2 + \psi_j^2 + 4\phi_i^2 - 4\phi_i \phi_j\right) \cos(\phi_j - 2\phi_i) x \cos\psi_j y \Big] \Big\},
\end{aligned}
$$

and

$$
\begin{aligned}
R_1^{(2)} \;=\; & \left(\sum_{i=1}^{\Delta-1}\sum_{j=i+1}^{\Delta}+\sum_{i=2}^{\Delta}\sum_{j=1}^{i-1}\right)\Big\{\alpha_c A_i A_j^2\Big\{\Big[Ma_j^{(1)}\left(2\phi_j^2+\phi_i\phi_j\right)\\
& +\frac{1}{2}a_j^{(2)}\left(\phi_i^2+\psi_i^2+2\phi_i\phi_j\right)\Big]\cos(\phi_i+2\phi_j)x\cos\psi_i y\\
& +\Big[Ma_j^{(1)}\left(2\phi_j^2-\phi_i\phi_j\right)\\
& +\frac{1}{2}a_j^{(2)}\left(\phi_i^2+\psi_i^2-2\phi_i\phi_j\right)\Big]\cos(\phi_i-2\phi_j)x\cos\psi_i y\Big\}\\
& +\frac{1}{4}\alpha_c A_i^2 A_j\Big\{\Big[Ma_{i,j}^{(1)}\left(\phi_j^2+\psi_j^2+2\phi_i^2+3\phi_i\phi_j+\psi_i\psi_j\right)\\
& +a_{i,j}^{(2)}\left(2\phi_i^2-\psi_i\psi_j+\phi_i\phi_j\right)+Mb_{i,j}^{(1)}\left(\phi_j^2+\psi_j^2+2\phi_i^2+3\phi_i\phi_j-\psi_i\psi_j\right)\\
& +b_{i,j}^{(2)}\left(2\phi_i^2+\psi_i\psi_j+\phi_i\phi_j\right)\Big]\cos(\phi_j+2\phi_i)x\cos\psi_j y\\
& +\Big[Md_{i,j}^{(1)}\left(\phi_j^2+\psi_j^2+2\phi_i^2-3\phi_i\phi_j+\psi_i\psi_j\right)\\
& +d_{i,j}^{(2)}\left(2\phi_i^2-\psi_i\psi_j-\phi_i\phi_j\right)+Me_{i,j}^{(1)}\left(\phi_j^2+\psi_j^2+2\phi_i^2-3\phi_i\phi_j-\psi_i\psi_j\right)\\
& +e_{i,j}^{(2)}\left(2\phi_i^2+\psi_i\psi_j-\phi_i\phi_j\right)\Big]\cos(\phi_j-2\phi_i)x\cos\psi_j y\Big\}\Big\},
\end{aligned}
$$

while

$$
R_3^{(1)}=\sum_{i=1}^{\Delta}MA_i^3(T_2)\left[p_2\left(a_i^{(2)}+\frac{1}{2}d_i^{(2)}\right)+\frac{3}{16}p_3M^2\right]\left(9\phi_i^2+\psi_i^2\right)\cos 3\phi_i x\cos\psi_i y,
$$

and

$$
\begin{aligned}
R_3^{(2)} \;=\; & \sum_{i=1}^{\Delta}\frac{1}{2}\alpha_c A_i^3(T_2)\left[6Ma_i^{(1)}\phi_i^2+\left(d_i^{(1)}M+a_i^{(2)}\right)\left(3\phi_i^2+\psi_i^2\right)\right.\\
& \left.+d_i^{(2)}\left(3\phi_i^2-\psi_i^2\right)\right]\cos 3\phi_i x\cos\psi_i y.
\end{aligned}
$$

We can similarly calculate $\boldsymbol{R}_2$ and $\boldsymbol{R}_4$. The expression $\boldsymbol{R}_5$ consists of terms of the form

$$
\cos 3\phi_i x\cos 3\psi_i y,\qquad \cos(\phi_i\pm 2\phi_j)x\cos(\psi_i\pm 2\psi_j)y,
$$
$$
\cos(\phi_i\pm\phi_j\pm\phi_l)x\cos(\phi_i\pm\phi_j\pm\phi_l)y,
$$

where $i\neq j\neq l$, $1\leq i,j,l\leq\Delta$ and each $\pm$-operator should be considered as being independent of preceding $\pm$-operators. As we shall see below, the actual expression for $\boldsymbol{R}_5$ is not required in our subsequent analysis.

The vector $\boldsymbol{R}$ contains terms of the form $\cos\phi_i x \cos\psi_i y$, which are solutions of the homogeneous problem

$$\mathcal{L}\begin{pmatrix}\theta_3\\ n_3\end{pmatrix} = \mathbf{0}, \tag{4.24}$$

so that they give rise to secular terms in the solution for $(\theta_3, n_3)^T$. Again we use the Fredholm Alternative to suppress these secular terms as we shall show below. As in the one-dimensional analysis of Section 3.3 this leads to the typical Landau-type amplitude equations. To determine the amplitude equations when the multiplicity of the eigenvalue is higher than two involves highly complex algebraic manipulations. We therefore restrict our analysis to the simpler cases where $\Delta = 1$ and $\Delta = 2$. There are three main cases to consider.

$\Delta = 1$

If $\Delta = 1$ then $\phi_1 = \psi_1 = \phi$ and secular terms appear in the $O(\epsilon^3)$ solution. Using the Fredholm Alternative we suppress these secular terms by determining the conditions under which

$$< \boldsymbol{w}^*, \boldsymbol{R} >= 0,$$

where $\boldsymbol{w}^*$ is the bounded solution of the adjoint problem to (4.24) and the inner product is defined as

$$< \boldsymbol{v}, \boldsymbol{w} >= \lim_{T_2\to\infty} \frac{1}{T_2 L_x L_y} \int_0^{T_2}\int_0^{L_x}\int_0^{L_y} \left(v^{(1)}\overline{w}^{(1)} + v^{(2)}\overline{w}^{(2)}\right)\, dy\, dx\, dT_2,$$

where the bar denotes the complex conjugate. (Refer to Section 3.3 for a full explanation of the theorem.)

As in the one-dimensional problem (see Section 3.3) it is simple to show that the adjoint operator to $\mathcal{L}$ is $\mathcal{L}^T$. The solution of the adjoint homogeneous problem is therefore

$$\boldsymbol{w}^* = \begin{pmatrix}1\\ M^*\end{pmatrix} A^* \cos\phi x \cos\psi y, \tag{4.25}$$

where A^* is real and

$$M^* = -\frac{p_1}{D}.$$

We find the Landau equation

$$\frac{dA_1(T_2)}{dT_2} = \alpha_2 \Gamma A_1(T_2) + \Omega A_1^3(T_2), \tag{4.26}$$

where

$$\begin{aligned}
\Gamma &= -\frac{2\phi^2}{M} > 0, \\
\Omega &= -\alpha_c \left(a_1^{(1)} + b_1^{(1)} + d_1^{(1)} - \frac{d_1^{(2)}}{2M} \right) \phi^2 \\
&\quad + \frac{D}{p_1} \left(2p_2 a_1^{(2)} + 2p_2 b_1^{(2)} + p_2 d_1^{(2)} + \frac{9}{8} p_3 M^2 \right) \phi^2.
\end{aligned}$$

This Landau equation is similar to the one obtained in the one-dimensional nonlinear analysis, see equation (3.24). Here, A_1, is the amplitude, to $O(\epsilon)$, of the epithelial dilation solution θ. Note that Γ is the initial exponential growth rate of the solution and that $\Gamma > 0$, since $M < 0$. Since the signs of Ω and α_2 can vary, we have four different types of behaviour when $T_2 \to \infty$ as was discussed in detail in Section 3.3, and summarized in Table 3.1. The solution of (4.26) only evolves to a nonhomogeneous bounded steady state if we are in the parameter space where $\Omega < 0$ and have supercritical bifurcation, thus $\alpha_2 > 0$.

We can assume, without loss of generality, that $\alpha_2 = 1$. The amplitude of θ is then $(-\Gamma/\Omega)^{\frac{1}{2}}$ while that of n is $M(-\Omega/\Gamma)^{\frac{1}{2}}$. With zero-flux boundary conditions the steady state solution that emerges is

$$\begin{pmatrix} \theta \\ n \end{pmatrix} = \begin{pmatrix} 0 \\ 1 \end{pmatrix} + \epsilon(-\frac{\Omega}{\Gamma})^{\frac{1}{2}} \begin{pmatrix} 1 \\ M \end{pmatrix} \cos\phi x \cos\phi y + O(\epsilon^2) \text{ as } T_2 \to \infty \tag{4.27}$$

We examine some specific numerical examples in the next section to test the accuracy of this analytical solution.

$\Delta = 2$ and Secular Terms Appear at $O(\epsilon^2)$

From (4.19) we know that for $\Delta = 2$, secular terms already appear in the $O(\epsilon^2)$ solution (4.20) when, for $i, j = 1, 2$ and $i \neq j$,

$$\phi_i + \phi_j = \phi_j \text{ and } \psi_i - \psi_j = \psi_j.$$

or

$$\phi_i - \phi_j = \phi_j \text{ and } \psi_i + \psi_j = \psi_j. \tag{4.28}$$

This is true if, for example,

$$\phi_1 = \phi, \quad \psi_1 = \sqrt{3}\phi, \quad \phi_2 = 2\phi, \quad \psi_2 = 0. \tag{4.29}$$

for any ϕ. Since our system of equations (4.12) is translation invariant in x and y and the analysis is not affected by a translation of wavevectors, it is sufficient to consider only this case. As we have seen in the linear analysis of the previous section, see (4.9) and (4.10), hexagonal patterns fall within this class of solutions.

At $O(\epsilon^2)$ the right hand side of our equation (4.18) now is

$$\begin{aligned}
\boldsymbol{S} \;=\; & \frac{1}{2}M\begin{pmatrix} 2p_2M \\ \alpha_c \end{pmatrix}\Big\{\phi^2 A_1^2(T_1)(\cos 2\phi x + 3\cos 2\sqrt{3}\phi y \\
& + 4\cos 2\phi x \cos 2\sqrt{3}\phi y) + 8\phi^2 A_2^2(T_1)\cos 4\phi x\Big\} \\
& + \begin{pmatrix} 4p_2M \\ 2\alpha_c \end{pmatrix}\phi^2 M A_1(T_1)A_2(T_1)(\cos\phi x\cos\sqrt{3}\phi y + 3\cos 3\phi x\cos\sqrt{3}\phi y) \\
& + \begin{pmatrix} 0 \\ 1 \end{pmatrix}\left(4\alpha_1\phi^2 A_1(T_2) + M\frac{dA_1(T_1)}{dT_1}\right)\cos\phi x\cos\sqrt{3}\phi y \\
& + \begin{pmatrix} 0 \\ 1 \end{pmatrix}\left(4\alpha_1\phi^2 A_2(T_2) + M\frac{dA_2(T_1)}{dT_1}\right)\cos 2\phi x.
\end{aligned}$$

Here the inner product is defined as

$$< \boldsymbol{v}, \boldsymbol{w} >= \lim_{T_1\to\infty}\frac{1}{T_1 L_x L_y}\int_0^{T_1}\int_0^{L_x}\int_0^{L_y}(v^{(1)}\overline{w}^{(1)} + v^{(2)}\overline{w}^{(2)})\,dy\,dx\,dT_1. \tag{4.30}$$

It is easy to show that the solutions of the adjoint problem to

$$\mathcal{L}\begin{pmatrix} \theta_2 \\ n_2 \end{pmatrix} = \mathbf{0}$$

are

$$\boldsymbol{w}_1^* = A_1^*\begin{pmatrix} 1 \\ M^* \end{pmatrix}\cos\phi x\cos\sqrt{3}\phi y, \qquad \boldsymbol{w}_2^* = A_2^*\begin{pmatrix} 1 \\ M^* \end{pmatrix}\cos 2\phi x,$$

where A_1^* and A_2^* are arbitrary real constants and as before $M^* = -p_1/D$.

Now calculating $< \boldsymbol{w}_1^*, \boldsymbol{S} >= 0$ and similarly for $\boldsymbol{w}_2^*$, we find the two amplitude equations

$$\frac{dA_1}{dT_1} = \alpha_1 \Gamma A_1 + \Omega A_1 A_2, \tag{4.31a}$$

$$\frac{dA_2}{dT_1} = \alpha_1 \Gamma A_2 + \frac{1}{4}\Omega A_1^2, \tag{4.31b}$$

where

$$\Gamma = -\frac{4\phi^2}{M} > 0, \qquad \Omega = -2\phi^2 \left(\alpha_c - \frac{2Dp_2M}{p_1} \right).$$

From the linear analysis we know that the homogeneous steady state loses stability when we have supercritical bifurcation, thus $\alpha_1 > 0$.

The time independent solutions for system (4.31) are

$$A_1^{(s_0)} = 0, \qquad A_2^{(s_0)} = 0,$$

and

$$A_1^{(s_1)} = \pm \frac{4\alpha_1 p_1}{M(2MDp_2 - \alpha_c p_1)}, \qquad A_2^{(s_1)} = \frac{2\alpha_1 p_1}{M(2MDp_2 - \alpha_c p_1)},$$

so $A_1^{(s_1)} = \pm 2A_2^{(s_1)}$. The different solutions $A_1^{(s_1)} = 2A_2^{(s_2)}$ and $A_1^{(s_1)} = -2A_2^{(s_2)}$ merely give patterns of different phases. Without loss of generality we only consider the case $A_1^{(s_1)} = 2A_2^{(s_1)}$.

The stability of each solution $(A_1^{(s_i)}, A_2^{(s_i)})^T$, $i = 0, 1$, is determined from a linear stability analysis of equations (4.31) about the steady state. Thus, in the usual way, we substitute

$$A_1 = A_1^{(s_i)} + \tilde{A}_1, \qquad A_2 = A_2^{(s_i)} + \tilde{A}_2, \qquad i = 0, 1,$$

into (4.31), where $|\tilde{A}_1| \ll 1$ and $|\tilde{A}_2| \ll 1$. Now the stability of the perturbations about the solutions $(A_1^{(s_i)}, A_2^{(s_i)})^T$ is determined by the eigenvalues of the matrix $\mathcal{M}$ where

$$\mathcal{M} = \begin{pmatrix} m_{1,1} & m_{1,2} \\ m_{2,1} & m_{2,2} \end{pmatrix}, \tag{4.32}$$

and

$$m_{1,1} = 0, \qquad m_{1,2} = -\frac{8\alpha_1\phi^2}{M} > 0,$$

$$m_{2,1} = \frac{4\alpha_1\phi^2}{M} > 0, \qquad m_{2,2} = -\frac{4\alpha_1\phi^2}{M} > 0.$$

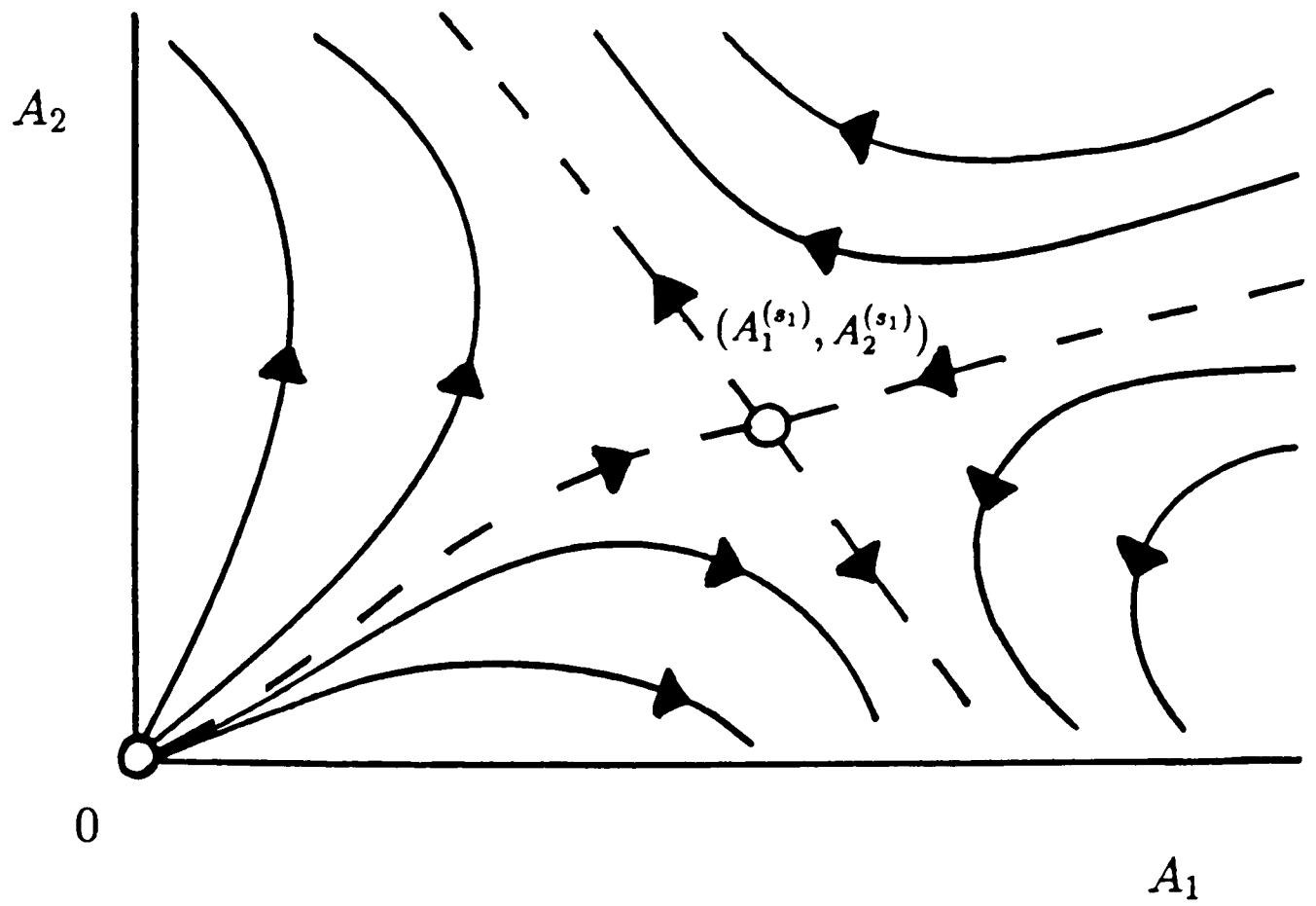

Figure 4.4: The qualitative (A_1, A_2)-phase plane for the Landau equation (4.31). The steady state $(0,0)$ is an unstable node while the steady state $(A_1^{(s_1)}, A_2^{(s_1)})$ is a saddle point.

since $M < 0$ and $\alpha_1 > 0$. The eigenvalues of this system are

$$\lambda = \frac{1}{2} m_{2,2} \pm \frac{1}{2} \sqrt{m_{2,2}^2 + 4 m_{1,2} m_{2,1}},$$

and since $m_{2,2} > 0$ and $m_{1,2} m_{2,1} > 0$, they are always positive. Thus no stable steady state pattern is possible for this specific mode combination. The qualitative (A_1, A_2)-phase plane for equations (4.31) is shown in Figure 4.4.

Since hexagonal patterns fall within the class of patterns considered here, the nonlinear analysis therefore predicts that our small strain quasi-steady-state tissue interaction system does *not* have steady state hexagonal patterned solutions. Interestingly hexagonal patterns are usually thought to be the stable two-dimensional patterns. In the next section we shall use numerical simulations to examine the correctness of this prediction in further detail.

$\Delta = 2$ and Secular Terms Appear at $O(\epsilon^3)$

For $\Delta = 2$ secular terms appear in the $O(\epsilon^3)$ solution when our unstable eigenvalue is such that the two corresponding allowable wavevectors do not satisfy conditions (4.28).

Suppressing the secular terms as in the previous two cases leads to the system of Landau equations

$$\frac{dA_1}{dT_2} = \alpha_2 \Gamma A_1 + \Omega_1 A_1^3 + \Upsilon_1 A_1 A_2^2, \tag{4.33a}$$

$$\frac{dA_2}{dT_2} = \alpha_2 \Gamma A_2 + \Omega_2 A_2^3 + \Upsilon_2 A_1^2 A_2, \tag{4.33b}$$

where

$$\Gamma = -\frac{\phi_1^2 + \psi_1^2}{M} > 0.$$

The expressions for Ω_1, Ω_2, Υ_1 and Υ_2 depend on the specific wavevectors involved as we shall see below.

The four time independent solutions of this system and the conditions for their existence are

$$\begin{aligned}
A_1^{(s_0)} &= 0, & A_2^{(s_0)} &= 0, \\
(A_1^{(s_1)})^2 &= -\tfrac{\alpha_2 \Gamma}{\Omega_1} > 0, & A_2^{(s_1)} &= 0, \\
A_1^{(s_2)} &= 0, & (A_2^{(s_2)})^2 &= -\tfrac{\alpha_2 \Gamma}{\Omega_2} > 0, \\
(A_1^{(s_3)})^2 &= \tfrac{\alpha_2 \Gamma (\Upsilon_1 - \Omega_2)}{\Omega_1 \Omega_2 - \Upsilon_1 \Upsilon_2} > 0, & (A_2^{(s_3)})^2 &= \tfrac{\alpha_2 \Gamma (\Upsilon_2 - \Omega_1)}{\Omega_1 \Omega_2 - \Upsilon_1 \Upsilon_2} > 0,
\end{aligned} \tag{4.34}$$

Again a linear stability analysis of the equations (4.33) is performed. We linearize about the steady states by substituting

$$A_1 = A_1^{(s_i)} + \tilde{A}_1, \qquad A_2 = A_2^{(s_i)} + \tilde{A}_2, \qquad i = 0, 1, \ldots, 3,$$

where $|\tilde{A}_1| \ll 1$ and $|\tilde{A}_2| \ll 1$. As before the stability of the steady states is determined by the eigenvalues of the matrix $\mathcal{M}$, see (4.32), where

$$\begin{aligned}
m_{1,1} &= \alpha_2 \Gamma + 3\Omega_1 \left(A_1^{(s_i)}\right)^2 + \left(\Upsilon_1 (A_2^{(s_i)})\right)^2, \\
m_{1,2} &= 2\Upsilon_1 A_1^{(s_i)} A_2^{(s)},
\end{aligned}$$

$$
\begin{aligned}
m_{2,1} &= 2\Upsilon_2 A_1^{(s_i)} A_2^{(s)}, \\
m_{2,2} &= \alpha_2\Gamma + 3\Omega_2 \left(A_2^{(s_i)}\right)^2 + \Upsilon_2 \left(A_1^{(s_i)})\right)^2 .
\end{aligned}
$$

The eigenvalues of this system are

$$
\lambda = \frac{1}{2}(m_{1,1} + m_{2,2}) \pm \frac{1}{2}\sqrt{(m_{1,1} - m_{2,2})^2 + 4m_{1,2}m_{2,1}}. \tag{4.35}
$$

The signs of the eigenvalues and thus the stability properties of the steady states are dependent on the parameter values. Phase planes similar to the one in Figure 4.4 could be constructed. Here, however, they would depend on the parameter values.

The linear analysis predicted that pattern formation would only be possible for (4.12) if we have supercritical bifurcation, that is $\alpha_2 > 0$. Without loss of generality we therefore assume that $\alpha_2 = 1$.

We have three nonhomogeneous steady state solutions for large time, two single mode steady states and also a mixed mode steady state. They are given by

$$
\begin{pmatrix} \theta \\ n \end{pmatrix} = \begin{pmatrix} 0 \\ 1 \end{pmatrix} + \epsilon A_1^{(s_1)} \begin{pmatrix} 1 \\ M \end{pmatrix} \cos\phi_1 x \cos\psi_1 y + O(\epsilon^2), \tag{4.36a}
$$

$$
\begin{pmatrix} \theta \\ n \end{pmatrix} = \begin{pmatrix} 0 \\ 1 \end{pmatrix} + \epsilon A_2^{(s_2)} \begin{pmatrix} 1 \\ M \end{pmatrix} \cos\phi_2 x \cos\psi_2 y + O(\epsilon^2), \tag{4.36b}
$$

$$
\begin{aligned}
\begin{pmatrix} \theta \\ n \end{pmatrix} &= \begin{pmatrix} 0 \\ 1 \end{pmatrix} + \epsilon A_1^{(s_3)} \begin{pmatrix} 1 \\ M \end{pmatrix} \cos\phi_1 x \cos\psi_1 y \\
&\quad + \epsilon A_2^{(s_3)} \begin{pmatrix} 1 \\ M \end{pmatrix} \cos\phi_2 x \cos\psi_2 y + O(\epsilon^2),
\end{aligned} \tag{4.36c}
$$

where the different $A_1^{(s_i)}$ and $A_2^{(s_i)}$ are the steady states (4.36) of the Landau equations (4.33) respectively.

We next discuss the forms which the expressions Ω_1, Ω_2, Υ_1 and Υ_2 take on. There are three cases to consider.

Case 1: If $\phi_i \neq 0$ and $\psi_i \neq 0$, $i = 1, 2$, then terms of the form $\cos\phi_i x \cos\psi_i y$ appear only in the expression for $\boldsymbol{R}_0$ in equation (4.23). After using the Fredholm

Alternative we find that

$$\begin{aligned}
\Omega_1 &= -\alpha_c\left(a_1^{(1)}\phi_1^2 + b_1^{(1)}\psi_1^2\right) - \frac{1}{2}\alpha_c\left(d_1^{(1)} - \frac{d_1^{(2)}}{2M}\right)\left(\phi_1^2+\psi_1^2\right) \\
&\quad + \frac{D}{p_1}\left(p_2 a_1^{(2)} + p_2 b_1^{(2)} + \frac{1}{2}p_2 d_1^{(2)} + \frac{9}{16}p_3 M^2\right)\left(\phi_1^2+\psi_1^2\right), \\
\Omega_2 &= -\alpha_c\left(a_2^{(1)}\phi_2^2 + b_2^{(1)}\psi_2^2\right) - \frac{1}{2}\alpha_c\left(d_2^{(1)} - \frac{d_2^{(2)}}{2M}\right)\left(\phi_2^2+\psi_2^2\right) \\
&\quad + \frac{D}{p_1}\left(p_2 a_2^{(2)} + p_2 b_2^{(2)} + \frac{1}{2}p_2 d_2^{(2)} + \frac{9}{16}M^2 p_3\right)\left(\phi_2^2+\psi_2^2\right),
\end{aligned}$$

and $\Upsilon_1 = \Upsilon_2 = \Upsilon$, where

$$\begin{aligned}
\Upsilon &= \frac{D}{4p_1}\left(2p_2 a_{1,2}^{(2)} + 2p_2 b_{1,2}^{(2)} + 2p_2 d_{1,2}^{(2)} + 2p_2 e_{1,2}^{(2)} + 3p_3 M^2\right)\left(\phi_1^2+\psi_1^2\right) \\
&\quad - \frac{1}{4}\alpha_c\left(a_{1,2}^{(1)} + b_{1,2}^{(1)} + d_{1,2}^{(1)} + e_{1,2}^{(1)}\right)\left(\phi_1^2+\psi_1^2\right) \\
&\quad - \frac{\alpha_c}{4M}\left[\left(a_{1,2}^{(1)}M - a_{1,2}^{(2)}\right)\left(\phi_1\phi_2 + \psi_1\psi_2\right)\right. \\
&\quad + \left(b_{1,2}^{(1)}M - b_{1,2}^{(2)}\right)\left(\phi_1\phi_2 - \psi_1\psi_2\right) \\
&\quad + \left(d_{1,2}^{(1)}M - d_{1,2}^{(2)}\right)\left(-\phi_1\phi_2 + \psi_1\psi_2\right) \\
&\quad \left. + \left(e_{1,2}^{(1)}M - e_{1,2}^{(2)}\right)\left(-\phi_1\phi_2 - \psi_1\psi_2\right)\right].
\end{aligned}$$

Case 2: If one and only one of ϕ_i or ψ_i, $i = 1, 2$ is equal to zero, then terms of the form $\cos\phi_i x \cos\psi_i y$ not only appear in the expression for $\boldsymbol{R}_0$ but also in $\boldsymbol{R}_1$ or $\boldsymbol{R}_2$ and $\boldsymbol{R}_3$ or $\boldsymbol{R}_4$, see equation (4.23). As before it is sufficient to consider only one case, say

$$\phi_1 \neq 0, \quad \psi_1 \neq 0, \quad \phi_2 = 0, \quad \psi_2 \neq 0,$$

where $\phi_1^2 + \psi_1^2 = \psi_2^2$.

For this particular set of wavevectors, terms of the form $\cos\phi_i x \cos\psi_i y$ appear in $\boldsymbol{R}_0$, $\boldsymbol{R}_1$ and $\boldsymbol{R}_3$. Suppressing the secular terms results in the same expressions for Ω_1 and Υ_2 as in Case 1 above, though Υ_2 simplifies to

$$\begin{aligned}
\Upsilon_2 &= \frac{D}{4p_1}\left(2p_2 a_{1,2}^{(2)} + 2p_2 b_{1,2}^{(2)} + 2p_2 d_{1,2}^{(2)} + 2p_2 e_{1,2}^{(2)} + 3p_3 M^2\right)\psi_2^2 \\
&\quad - \frac{1}{4}\alpha_c\left(a_{1,2}^{(1)} + b_{1,2}^{(1)} + d_{1,2}^{(1)} + e_{1,2}^{(1)}\right)\psi_2^2
\end{aligned}$$

$$
\begin{aligned}
&- \frac{\alpha_c}{4M}\left[M\left(a_{1,2}^{(1)} - b_{1,2}^{(1)} + d_{1,2}^{(1)} - e_{1,2}^{(1)}\right)\right. \\
&\left. - a_{1,2}^{(2)} + b_{1,2}^{(2)} - d_{1,2}^{(2)} + e_{1,2}^{(2)}\right]\psi_1\psi_2.
\end{aligned}
$$

We find that

$$
\begin{aligned}
\Omega_2 \;=\; & -\alpha_c\left(b_2^{(1)} + \frac{1}{2}d_2^{(1)} - \frac{d_2^{(2)}}{4M}\right)\psi_2^2 - \frac{\alpha_c p_1}{2D}\left(d_2^{(1)}M + \frac{1}{2}d_2^{(2)}\right)\psi_2^2 \\
& + \frac{D}{p_1}\left(p_2 b_2^{(2)} + \frac{1}{2}p_2 d_2^{(2)} + \frac{9}{16}p_3 M^2\right)\psi_2^2 + \frac{M}{2}\left(p_2 d_2^{(2)} + \frac{3}{8}p_3 M^2\right)\psi_2^2,
\end{aligned}
$$

and

$$
\begin{aligned}
\Upsilon_1 \;=\; & \Upsilon_2 + \left[2p_2 M a_2^{(2)} + \frac{3}{4}p_3 M^3 + \frac{1}{2}p_2 M\left(a_{1,2}^{(2)} + b_{1,2}^{(2)} + d_{1,2}^{(2)} + e_{1,2}^{(2)}\right)\right]\psi_2^2 \\
& - \frac{p_1\alpha_c}{D}\left[a_2^{(2)}\psi_2^2 + \frac{1}{4}M\left(a_{1,2}^{(1)} + d_{1,2}^{(1)}\right)\left(\psi_1^2 + \psi_1\psi_2\right)\right. \\
& \left. + \frac{1}{4}M\left(b_{1,2}^{(1)} + e_{1,2}^{(1)}\right)\left(\psi_1^2 - \psi_1\psi_2\right) - \left(a_{1,2}^{(2)} - b_{1,2}^{(2)} + d_{1,2}^{(2)} - e_{1,2}^{(2)}\right)\psi_1\psi_2\right].
\end{aligned}
$$

Case 3: If one and only one of $\phi_1 = \psi_2 = 0$ or $\phi_2 = \psi_1 = 0$ is true then terms of the form $\cos\phi_i x \cos\psi_i y$ appear in the expression for $\boldsymbol{R}_0$, $\boldsymbol{R}_1$ or $\boldsymbol{R}_2$ and $\boldsymbol{R}_3$ or $\boldsymbol{R}_4$, see equation (4.23). Again it is sufficient to consider only one combination of wavevectors, say

$$
\phi_1 = \phi, \qquad \psi_1 = 0, \qquad \phi_2 = 0, \qquad \psi_2 = \phi.
$$

By using the Fredholm Alternative we have

$$
\begin{aligned}
\Omega_1 \;=\; & -\alpha_c\left(a_1^{(1)} + \frac{1}{2}d_1^{(1)} - \frac{d_1^{(2)}}{4M}\right)\phi^2 - \frac{\alpha_c p_1}{2D}\left(d_1^{(1)}M - \frac{1}{2}d_1^{(2)}\right)\phi^2 \\
& + \frac{1}{2}M\left(p_2 d_1^{(2)} + \frac{3}{8}p_3 M^2\right)\phi^2 + \frac{D}{p_1}\left(p_2 a_1^{(2)} + \frac{1}{2}p_2 d_1^{(2)} + \frac{9}{16}M^2 p_3\right)\phi^2.
\end{aligned}
$$

and

$$
\begin{aligned}
\Omega_2 \;=\; & -\alpha_c\left(b_2^{(1)} + \frac{1}{2}d_2^{(1)} - \frac{d_2^{(2)}}{4M}\right)\phi^2 - \frac{\alpha_c p_1}{2D}\left(d_2^{(1)}M - \frac{1}{2}d_2^{(2)}\right)\phi^2 \\
& + \frac{1}{2}M\left(p_2 d_2^{(2)} + \frac{3}{8}p_3 M^2\right)\phi^2 + \frac{D}{p_1}\left(p_2 b_2^{(2)} + \frac{1}{2}p_2 d_2^{(2)} + \frac{9}{16}M^2 p_3\right)\phi^2.
\end{aligned}
$$

Also $\Upsilon_1 = \Upsilon_2 = \Upsilon$ where

$$\begin{aligned}\Upsilon &= p_2\left(\frac{D}{2p_1}+\frac{1}{M}\right)\phi^2\left(a_{1,2}^{(2)}+b_{1,2}^{(2)}+d_{1,2}^{(2)}+e_{1,2}^{(2)}\right)\\ &\quad -\frac{1}{4}\alpha_c\left(1+\frac{p_1M}{D}\right)\left(a_{1,2}^{(1)}+b_{1,2}^{(1)}+d_{1,2}^{(1)}+e_{1,2}^{(1)}\right)\phi^2\\ &\quad +\frac{3}{4}p_3M^2\left(\frac{D}{p_1}+M\right)\phi^2.\end{aligned}$$

The weakly nonlinear analysis performed in this section is very complicated and it is therefore impossible to relate the model parameters in any meaningful way directly to the stability and amplitudes of the predicted solutions. However, the analysis does give a good indication of what type of patterns to expect as well as parameter ranges for which various steady state patterns would exist. Numerical simulations for specific examples are considered in the next section.

4.4 Numerical Simulations

In this section we use numerical methods to solve the reduced small strain quasi-steady-state system (4.12) on rectangular domains. We select the parameters so that we are in the region of the bifurcation point to spatial patterns. The numerical results can then be compared with those predicted by the bifurcation analysis of the previous section.

An implicit finite difference approach is used to solve the nonlinear equations (4.12). The full details of the method are given in the Appendix, Section A.2. For examples where the small parameter $\epsilon = 0.1$, the computation took on average about 15 to 20 hours CPU time to reach a steady state solution on a DEC5500 Risc Ultrix computer. For smaller values of ϵ, for example $\epsilon = 0.01$, the growth rate of the patterns are even slower (see the discussion in Section 3.4) so that it becomes impractical to solve the model equations in real time.

In the first example we solved a system which has only one linearly unstable mode. The rest of the examples consider systems which have two linearly

unstable modes. As initial conditions we used random perturbations with minimum and maximum values ± 0.001, about the homogeneous steady state $\theta = 0$, $n = 1$, to simulate the natural inhomogeneties present in skin tissue.

To ensure that the numerical method employed is stable and convergent we solved the equations using different mesh sizes in both time and space. Because of computer time constraints we never used more than a 1000 mesh points for discretizing the rectangle $\boldsymbol{B}$.

Example 4.4.1: We consider system (4.12) and isolate the eigenvalue $k_c^2 = 4\pi^2$. For determining the parameter values we used the same method as in Example 3.4.1. Similarly we can show that for isolating an eigenvalue, say k_c^2, the following two equations must be satisfied

$$\beta k_c^4 - \rho = 0, \tag{4.37a}$$

$$(\alpha_c P_2 - D)k_c^2 - 2\rho D = 0. \tag{4.37b}$$

For linear instability, the value of the bifurcation parameter, α in this case, must be increased marginally beyond the critical value, α_c. (Compare these equations with (3.27).)

One set of parameter values that satisfies the above equations when $k_c = 4\pi^2$ is

$$\beta = 0.0126651, \quad \rho = 19.7369, \quad \tau = 4.0, \quad c = 1.0, \quad D = 2.0, \quad \alpha_c = 2.0.$$

If we consider the square domain $(\sqrt{2}, \sqrt{2})$, then only one linearly unstable mode exists, that is $(2, 2)$.

The analytical prediction for the steady state pattern, as obtained in the nonlinear analysis of the previous section, is therefore given in (4.27). We evaluated the expressions for Ω and Γ by computer, see equation (4.26), for the above parameter set. With $\epsilon = 0.1$ the predicted solution for large time is

$$\begin{aligned} \theta(x, y, t) &\approx 0.16 \cos\left(\frac{2\pi x}{\sqrt{2}}\right) \cos\left(\frac{2\pi y}{\sqrt{2}}\right) \\ n(x, y, t) &\approx 1 - 0.16 \cos\left(\frac{2\pi x}{\sqrt{2}}\right) \cos\left(\frac{2\pi y}{\sqrt{2}}\right). \end{aligned}$$

This is in excellent agreement with the numerically computed solutions for θ and n which reach maximum and minimum amplitudes for large time of 0.16 and -0.16 respectively. Both the predicted and computed steady state dilation patterns are shown in Figure 4.5.

Example 4.4.2: In this example the model parameters are selected so as to isolate the eigenvalue $k_c^2 = 6.5\pi^2$. By using equations (4.37) we find the parameter set

$$\beta = 0.00779393, \quad \rho = 32.0762, \quad \tau = 4.0, \quad c = 1.0, \quad D = 2.0, \quad \alpha_c = 2.0.$$

As in the first example we consider the problem on the domain $(\sqrt{2}, \sqrt{2})$; however, instead of only one unstable mode, there are now two linearly unstable modes, namely $(2,3)$ and $(3,2)$

We can now use expressions (4.34) for determining the steady states and (4.35) for determining their stability.

Note that the values of Ω_i and Υ_i are as in Case 1. There are three nonhomogeneous steady states — two single mode steady states which are stable and a mixed mode steady state which is unstable. We can now construct the bifurcation diagram as predicted by the nonlinear analysis. So as to separate the two single mode steady states on the bifurcation diagram when they have the same value, we plot the bifurcation parameter α_c, against the value $\sqrt{A_1^{(s_i)} + 2A_1^{(s_i)}}$ (see Figure 4.6).

The amplitudes of the steady state solutions were computed from (4.34) and the predicted solutions (see (4.36)) are

$$\begin{aligned} \theta(x,y,t) &\approx 0.16 \cos\left(\frac{2\pi x}{\sqrt{2}}\right) \cos\left(\frac{3\pi y}{\sqrt{2}}\right) \\ n(x,y,t) &\approx 1.0 - 0.16 \cos\left(\frac{2\pi x}{\sqrt{2}}\right) \cos\left(\frac{3\pi y}{\sqrt{2}}\right). \end{aligned}$$

or

$$\theta(x,y,t) \approx 0.16 \cos\left(\frac{3\pi x}{\sqrt{2}}\right) \cos\left(\frac{2\pi y}{\sqrt{2}}\right)$$

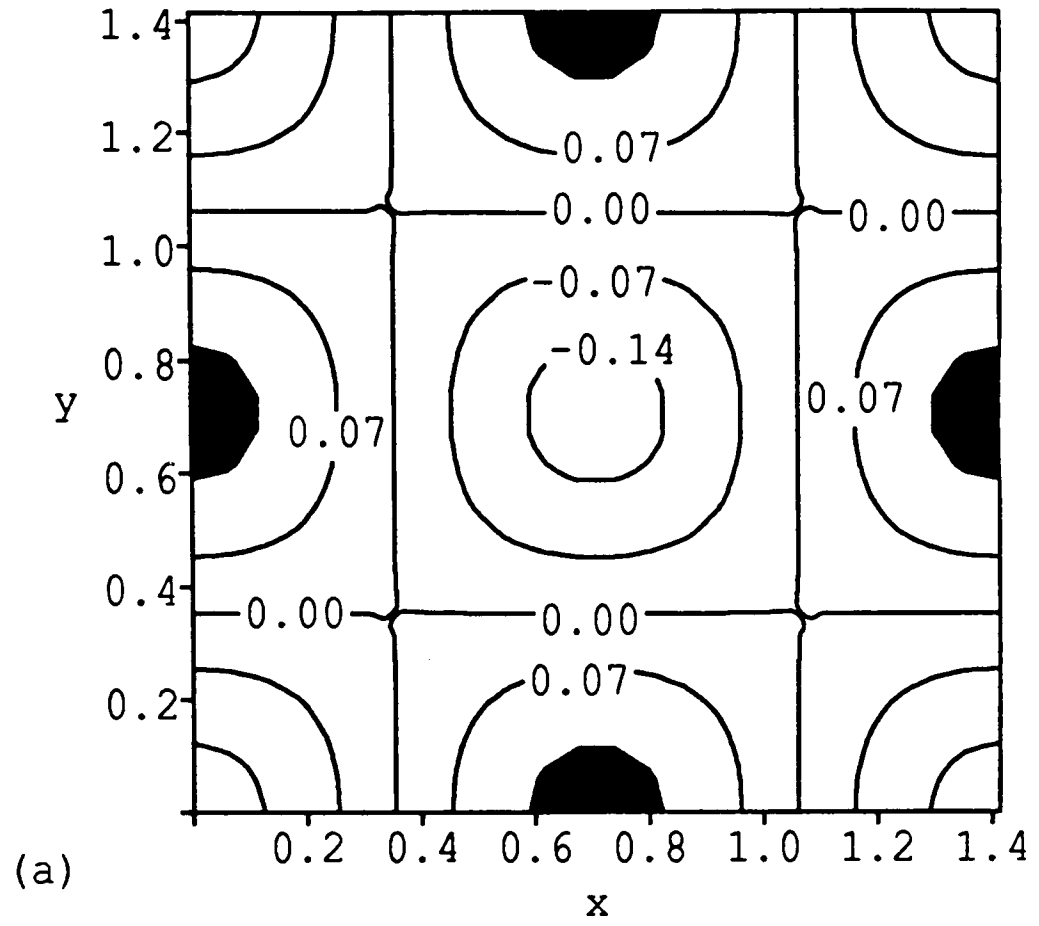

(a)

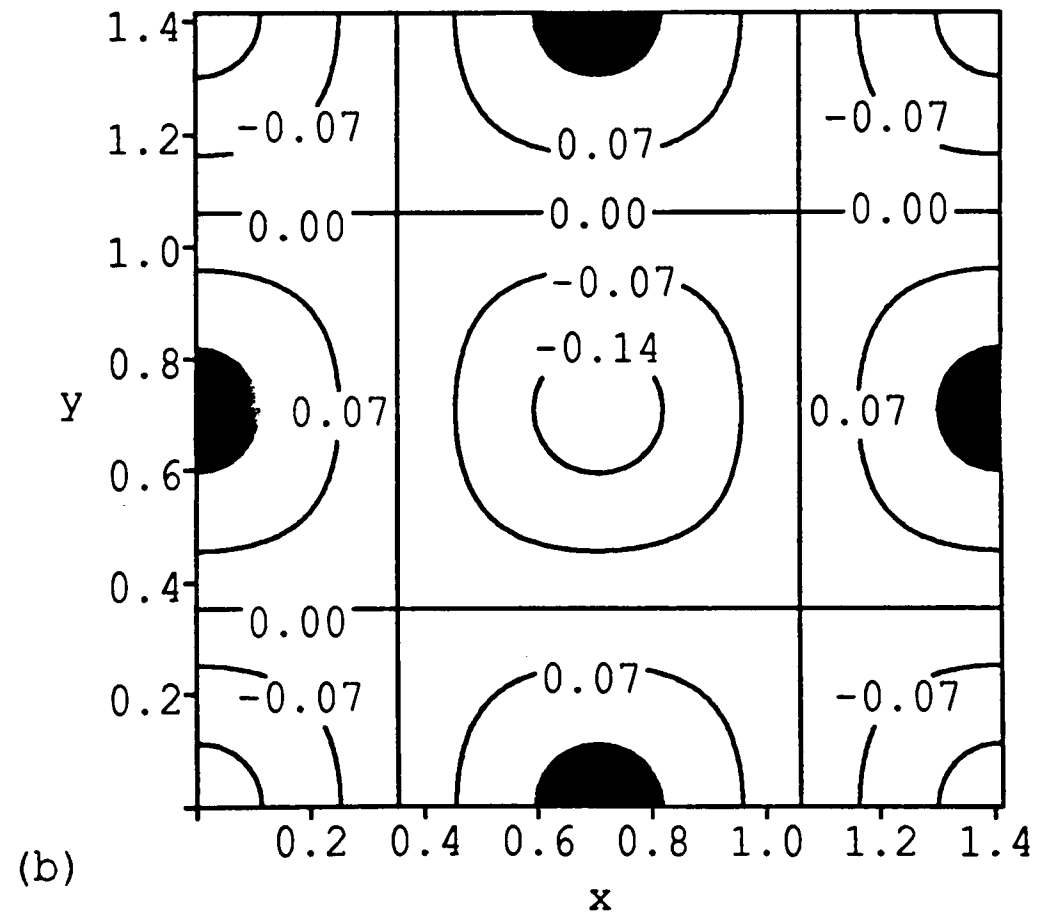

(b)

Figure 4.5: In (a) we show the contour graph of the computed steady state solution for the dilation θ, with the parameter set as in Example 4.4.1. Compare this with the predicted steady state solution in (b): the solutions are indistinguishable for $\epsilon = 0.1$. Regions where $\theta > 0.14$ are shaded.

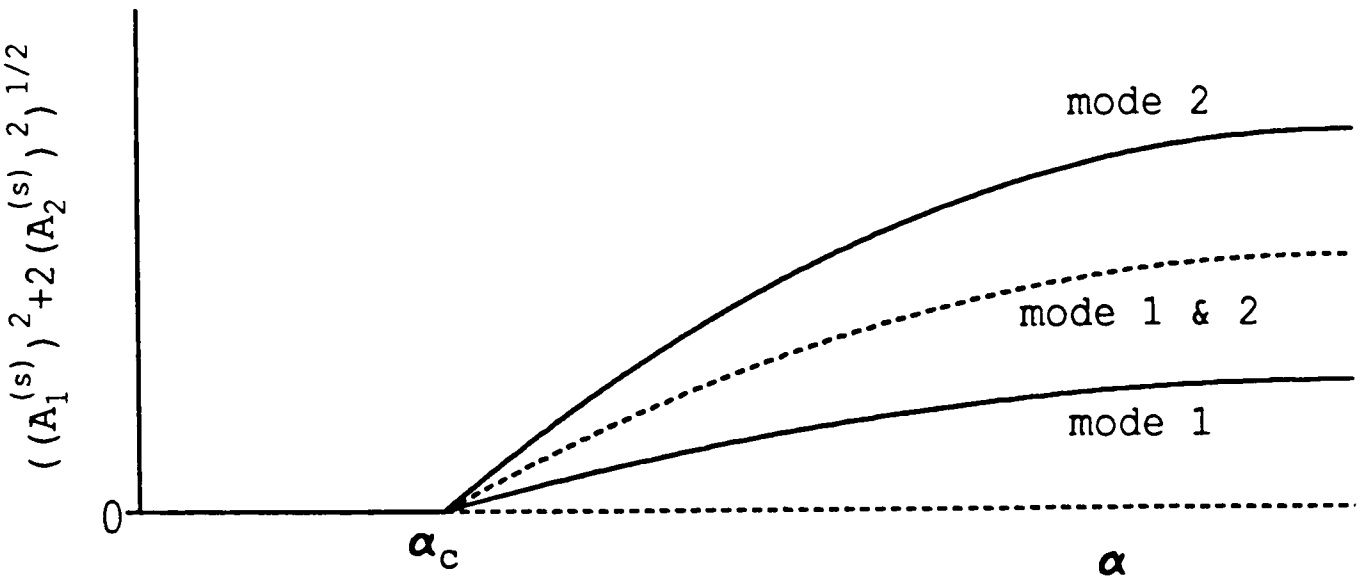

Figure 4.6: The qualitative bifurcation diagram for the steady state solutions, associated with various mode pairs, of system (4.31) when the parameter values are as in Example 4.4.2. The two mode pairs are $(2,3)$ and $(3,2)$. Solid lines indicate stable steady states while broken lines indicate unstable steady states.

$$n(x,y,t) \approx 1.0 - 0.16\cos\left(\frac{3\pi x}{\sqrt{2}}\right)\cos\left(\frac{2\pi y}{\sqrt{2}}\right).$$

Since we are dealing with a square domain and the problem is invariant under a change of x and y, the above two solutions are equivalent. Our numerical solutions have maximum and minimum values of 0.17 and -0.17 respectively which compare very well with our analytical predictions as shown in Figure 4.7.

Example 4.4.3: By selecting the parameter set

$$\beta = 0.005960, \quad \rho = 41.9458, \quad \tau = 4.2025, \quad c = 1.05, \quad D = 2.0, \quad \alpha = 2.0,$$

we isolate the unstable eigenvalue $k_c^2 = 8.5\pi^2$. On the square domain $(\sqrt{2}, \sqrt{2})$ the system has two linearly unstable modes $(1,4)$ and $(4,1)$. The bifurcation diagram, calculated from our nonlinear analysis, is similar to that in Figure 4.6. Here, however, the mixed mode solution is stable, while the two single mode solutions are unstable. So the expected solution is

$$\theta(x,y,t) \approx 0.14\cos\left(\frac{\pi x}{\sqrt{2}}\right)\cos\left(\frac{4\pi y}{\sqrt{2}}\right) + 0.14\cos\left(\frac{4\pi x}{\sqrt{2}}\right)\cos\left(\frac{\pi y}{\sqrt{2}}\right),$$

$$n(x,y,t) \approx 1.0 - 0.14\cos\left(\frac{\pi x}{\sqrt{2}}\right)\cos\left(\frac{4\pi y}{\sqrt{2}}\right) + 0.14\cos\left(\frac{4\pi x}{\sqrt{2}}\right)\cos\left(\frac{\pi y}{\sqrt{2}}\right).$$

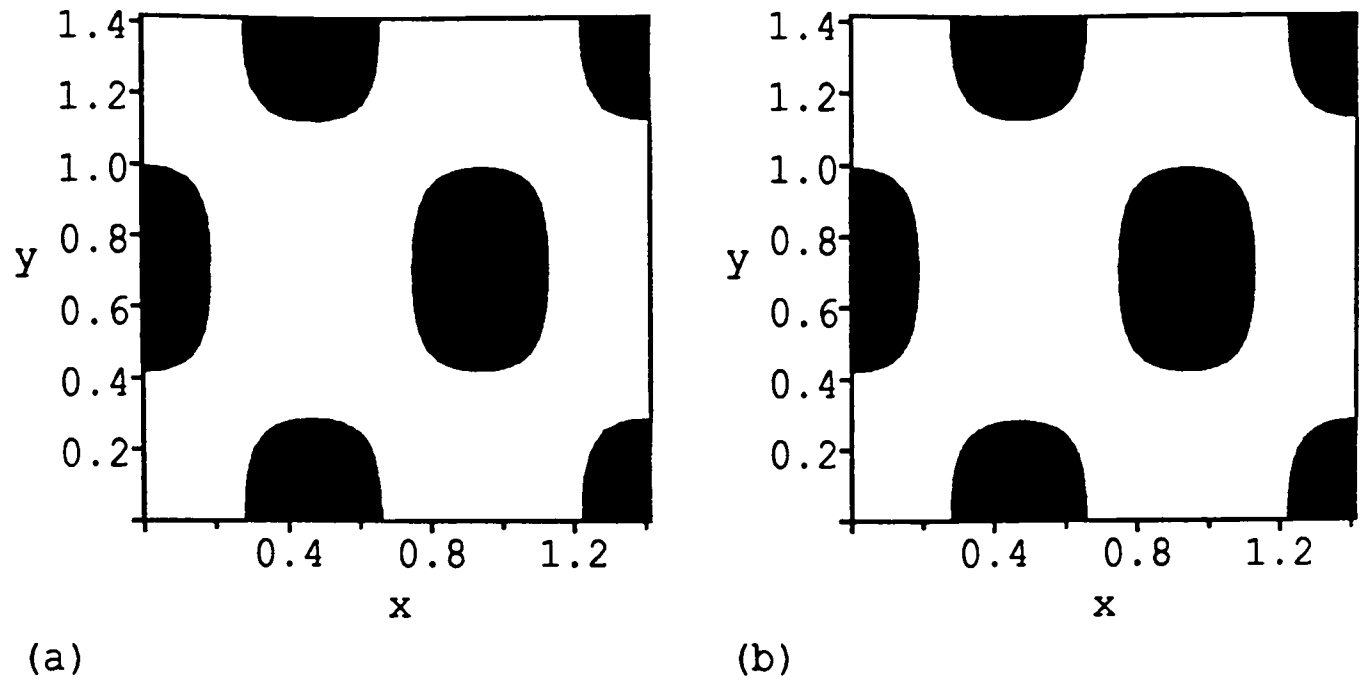

Figure 4.7: The computed dilation solution θ for parameter values as in Example 4.4.2 is shown in the the contour graph (a), while the predicted solution is shown in (b). Regions where $\theta \geq 0.05$ are shaded in both graphs.

The numerical simulations of the nonlinear system does indeed evolve to a mixed mode solution, as seen in Figure 4.8. Although the peaks in our numerical solution are not as high as those in our predicted solution, the troughs are almost of equal depth and the two solutions share similar characteristics. Hence the solutions are qualitatively similar.

Example 4.4.4: Here we select the parameters

$$\beta = 0.00405285, \quad \rho = 61.6850, \quad \tau = 4.5, \quad c = 1.12132, \quad D = 2.0, \quad \alpha = 2.0,$$

so that we are isolating the unstable eigenvalue $k_c^2 = 12.5\pi^2$. If we consider the system of equations on the rectangular domain $(\sqrt{2}, \sqrt{2}/2)$ the two linearly unstable modes are $(5,0)$ and $(3,2)$. Our bifurcation diagram allows for only the two single mode steady states — one is stable and the other unstable (see Figure 4.9).

The expressions for Ω_i and Υ_i, $i = 1,2$, are as in Case 2. The predicted steady state solution is

$$\theta(x,y,t) \approx 0.23 \cos\left(\frac{3}{\sqrt{2}}\pi x\right) \cos\left(\frac{4\pi y}{\sqrt{2}}\right)$$

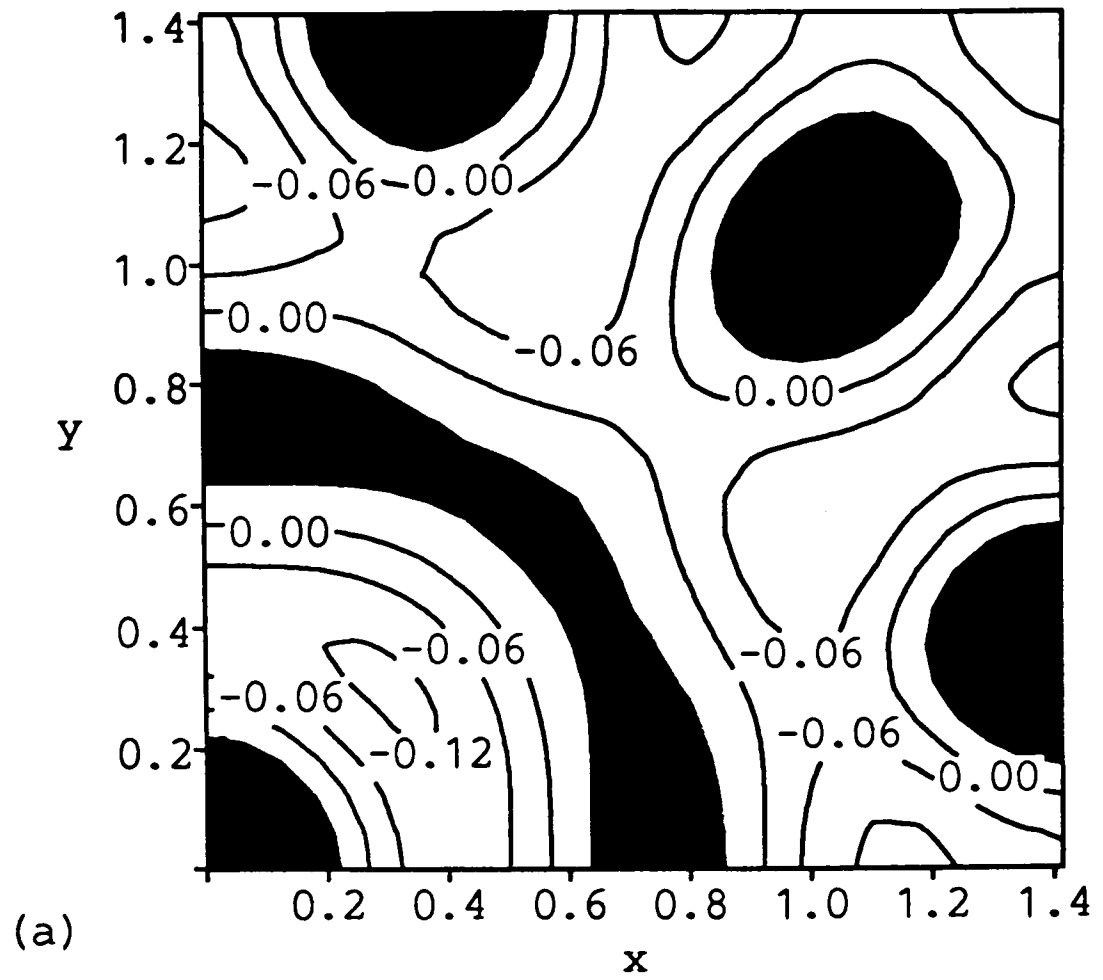

(a)

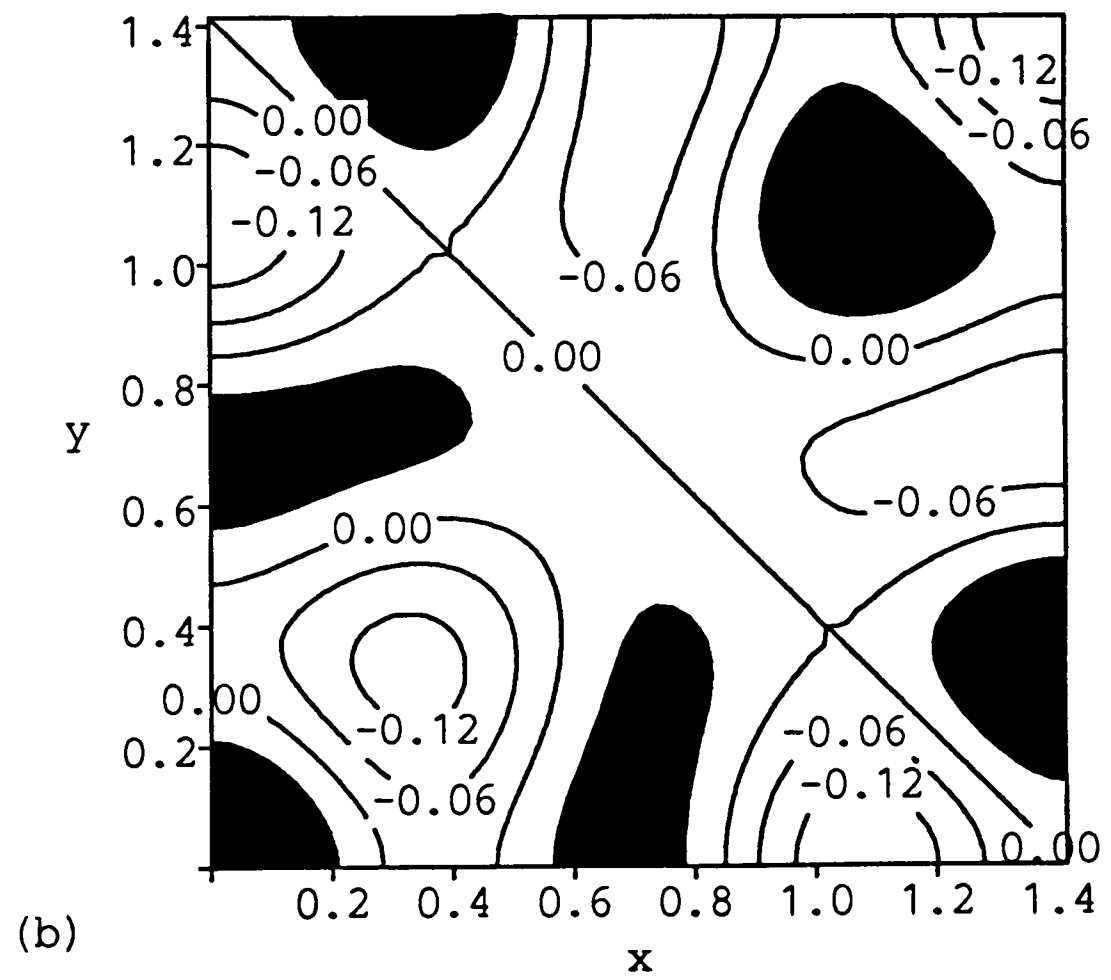

(b)

Figure 4.8: The numerically computed contour graph of the dilation θ when the parameter values are as in Example 4.4.3. The solution predicted by the nonlinear analysis is shown in (b). Note that we have a mixed mode steady state here. Regions where $\theta > 0.07$ are shaded in both graphs.

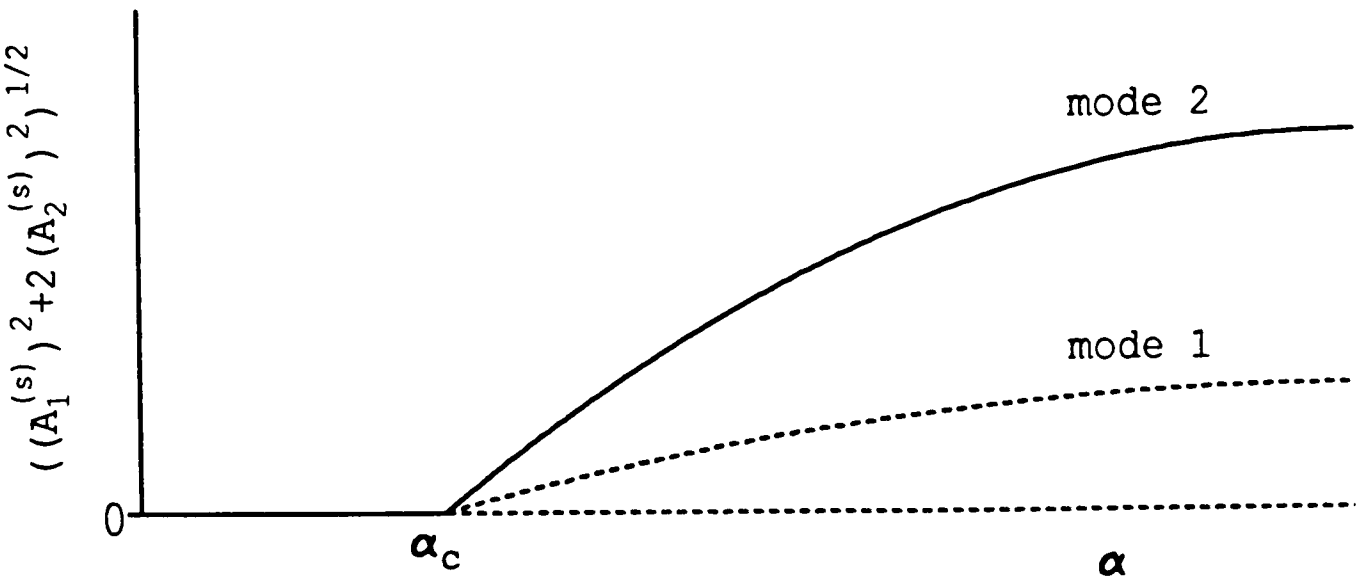

Figure 4.9: The qualitative bifurcation diagram for the steady state solutions of system (4.31) when the parameter values are as in Example 4.4.4. The steady state associated with the first mode pair $(5,0)$, is unstable and that associated with the second $(3,2)$, is stable.

$$n(x,y,t) \approx 1.0 - 0.23\cos\left(\frac{3}{\sqrt{2}}\pi x\right)\cos\left(\frac{4\pi y}{\sqrt{2}}\right).$$

For both random initial conditions and stripe-like initial conditions resembling the mode $(5,0)$ we found a steady state solution resembling the predicted mode. The troughs of the computed pattern have minimum values -0.23 while the peaks have a maximum of 0.28. The error is therefore $O(\epsilon^2)$ as expected.

Example 4.4.5: In this example we isolate the unstable eigenvalue satisfying $k_c^2 = 9\pi^2$. To do this we choose the parameters

$$\beta = 0.00562895, \quad \rho = 44.4132, \quad \tau = 4.8, \quad c = 1.19089, \quad D = 2.0, \quad \alpha = 2.0.$$

We consider the problem on the square domain $(1,1)$ so that we have the two linearly unstable modes $(2,0)$ and $(0,2)$. The bifurcation diagram is similar to that in the previous example, see Figure 4.9, except for the fact that both the nonhomogeneous steady states are now stable. The expressions for Ω_i and Υ_i are now as in Case 3. The nonlinear analysis predicts either

$$\begin{aligned} \theta(x,y,t) &\approx 0.30\cos(3\pi x), \\ n(x,y,t) &\approx 1.0 - 0.30\cos(3\pi x), \end{aligned}$$

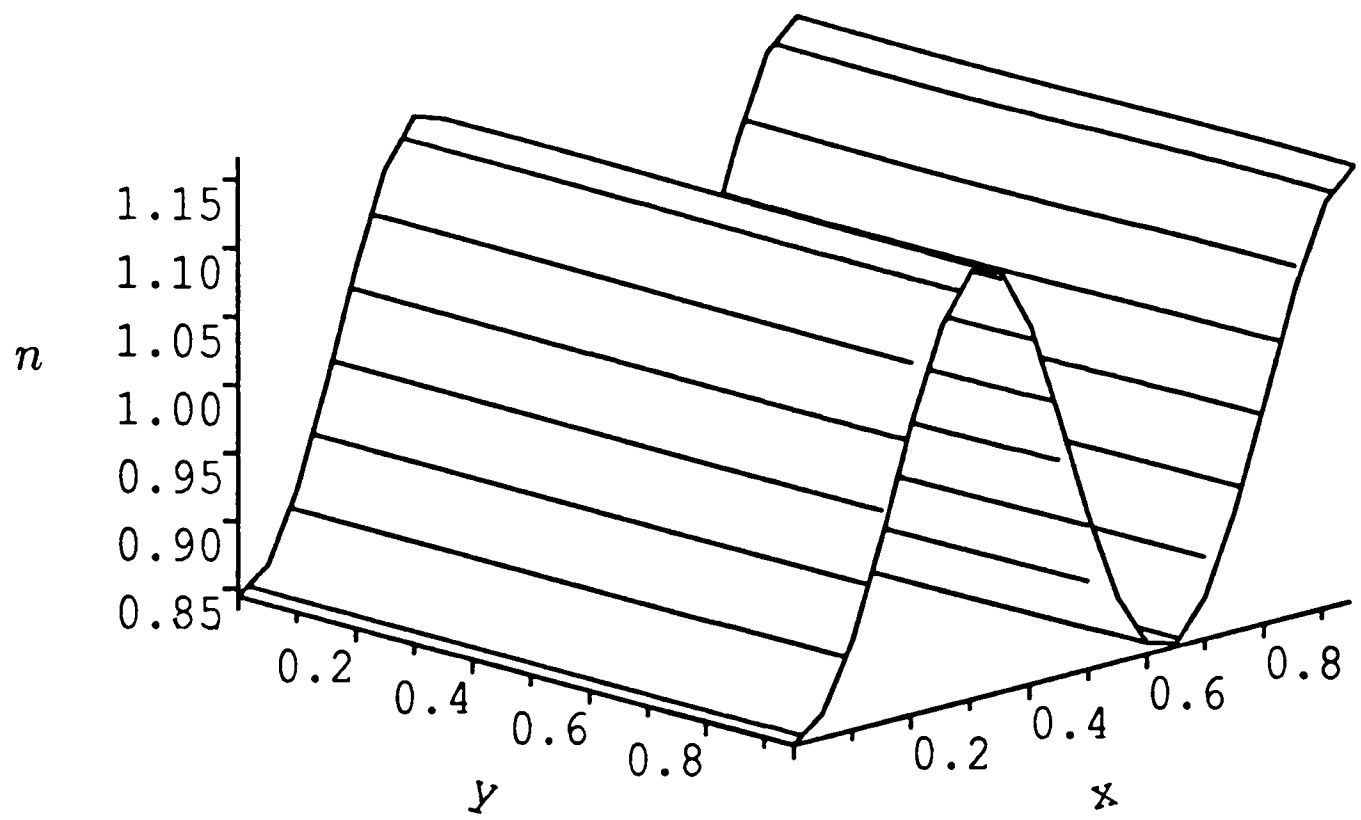

Figure 4.10: Isometric graph of the computed dilation solution θ, when the model parameters are as in Example 4.4.5.

or

$$\begin{aligned} \theta(x,y,t) &\approx 0.30\cos(3\pi y), \\ n(x,y,t) &\approx 1.0 - 0.30\cos(3\pi y), \end{aligned}$$

as the steady state solutions. The numerical solutions have amplitudes of ± 0.17, see Figure 4.10. This is much smaller than predicted, so the nonlinear analysis does not give such accurate results for this case. Qualitatively however, the solutions are identical.

Example 4.4.6: By isolating the eigenvalue $k_c^2 = 4\pi^2$ and considering the domain $(\sqrt{3}, 1)$ we have the degenerate case where secular terms appear at $O(\epsilon^2)$ in the nonlinear bifurcation analysis, since the two corresponding wavevectors are $(0,2)^T$ and $(\sqrt{3},1)^T$.

According to our nonlinear analysis (refer to the phase plane in Figure 4.4) no steady state pattern is possible. Numerically we did, however, find that a

steady state, resembling mode $(0,2)$, developed. Our parameter choice was

$$\beta = 0.0126651, \quad \rho = 19.7392, \quad \tau = 4.0, \quad c = 1.0, \quad D = 2.0, \quad \alpha = 2.0.$$

It seems therefore that a secondary bifurcation has occured here. Our nonlinear analysis, however, cannot predict this since it only applies to primary bifurcation points.

Example 4.4.7: We show another example in which a secondary bifurcation occurs. We isolate the same eigenvalue as in Example 4.4.2 and use the same parameters except for

$$\tau = 3.0625, \qquad c = 0.75.$$

Our bifurcation diagram is similar to that in Example 4.4.3, so that we expect the mixed mode solution, made up of the mode pairs $(2,3)$ and $(3,2)$ to develop. Numerical simulations, however, show that the mixed steady state is only a transient and that a hexagonal-type steady state pattern eventually develops — each peak is closest to its six nearest neighbours (see Figure 4.11).

Therefore, although our weakly nonlinear analysis indicates that hexagonal patterns are not possible, such steady patterns could still evolve due to secondary bifurcations.

In the majority of examples considered the numerical results agreed well with the nonlinear analysis. Even better agreement could have been achieved by using smaller values of ϵ in the numerical simulations. Furthermore, the mesh size used in the finite difference approximations was rather crude and a finer mesh would also contribute towards more accurate solutions. However, due to computing time constraints it was impractical to incorporate these factors into our simulations.

The above examples emphasize the limitations of a multi-scale asymptotic nonlinear analysis. For instance, in Example 4.4.6 the numerical simulations demonstrated the existence of a stable steady state, the bifurcation analysis,

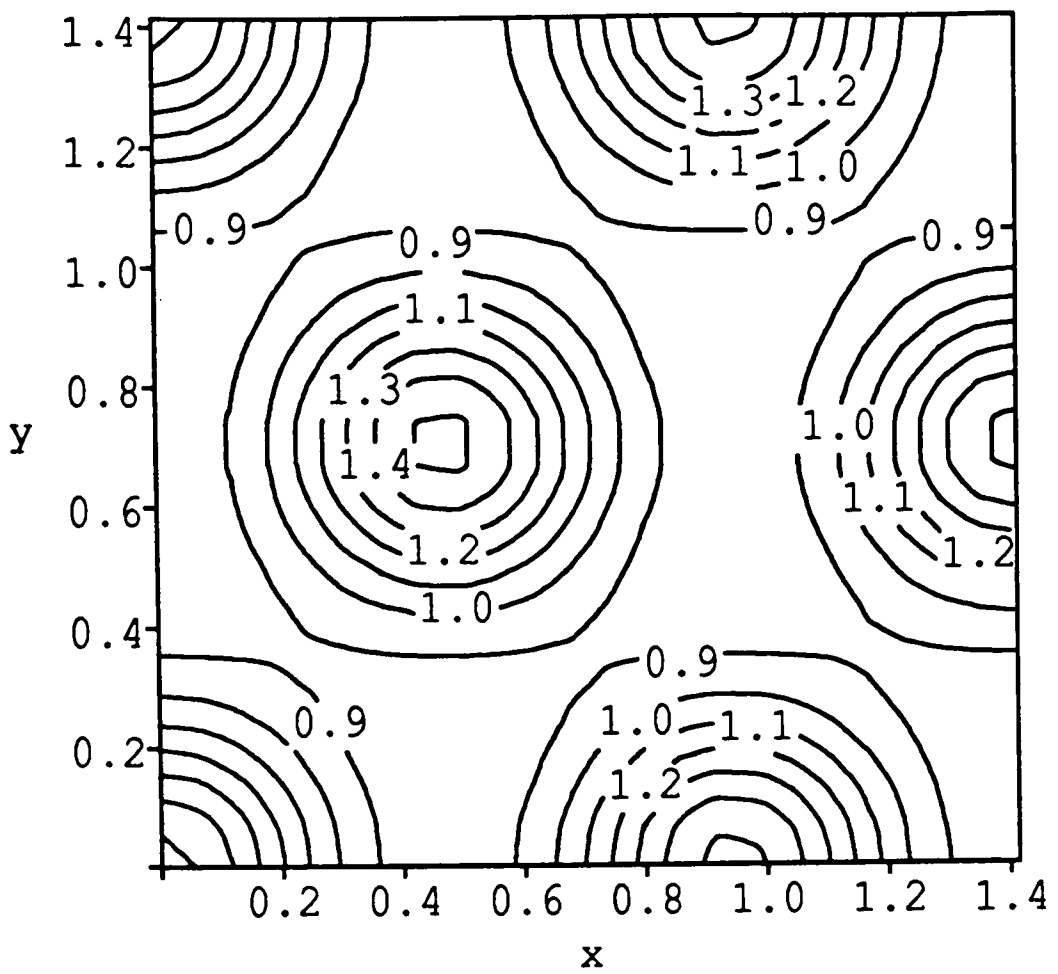

Figure 4.11: Contour graph of the numerically computed dilation θ, steady state solution when parameters are as in Example 4.4.7. A hexagonal-type pattern arises due to a secondary bifurcation.

however, indicated blow up. Also, in Example 4.4.7 the nonlinear analysis predicted that a stable steady state would emerge from primary bifurcation, however, the numerical simulations revealed that this steady state was only a transient and a very different steady state resulted. These anomalies are probably due to secondary bifurcations which take over relatively quickly. The nonlinear analysis does not address such secondary bifurcations. Furthermore, when more than one mode is unstable, as in Example 4.4.2, the domain of attraction of initial conditions for each of the modes cannot be predicted by the bifurcation analysis.

The above examples demonstrate the great variety of patterns which our reduced small strain quasi-steady state system (4.12) exhibits. The model clearly has even greater pattern formation potential than predicted by the nonlinear analysis, since not only primary, but higher order bifurcations occur. A large variety of vertebrate skin patterns seen in nature could therefore be explained in

terms of our tissue interaction model. The chessboard-like pattern of Example 4.4.1, for example, resembles that of feather germs on chicken skin (compare this result with the Figure 1.2). The stripe-like pigment patterns seen on alligators, are similar to the pattern of Example 4.4.5 (see Murray *et al.* (1990)). The more complex patterns seen on some vertebrates, especially reptiles, can also be explained by our model via mode interaction as we have shown in Example 4.4.3. Extremely involved coupled pattern generators giving rise to multiple unstable eigenvalues, as were considered by Shaw & Murray (1989), are therefore not necessary to explain complex patterns. Simple models with parabolic-type dispersion relations, can also serve the purpose.

We are in particular concerned with simple patterns and especially those of feather germs on the chick back. The sequential formation of such patterns is examined in the following chapters. We shall relate our tissue interaction model in fuller detail to the biology of chick skin patterning in Chapter 7.

Chapter 5

Travelling Wave Solutions

5.1 Introduction

Travelling wavefronts are the precursors to a vast range of developmental processes seen in embryonic tissue. For example, both chemical and mechanical waves propagate on the surface of many vertebrate eggs just after fertilization. Also, as we shall discuss in the next two chapters, travelling wave mechanisms are frequently involved in embryonic pattern formation.

Although some models have been proposed to explain such phenomena, there is still much work to be done. Cheer *et al.* (1987) proposed a reaction-diffusion system to model the progression of calcium waves over the egg of the teleost fish *Medaka*. This model was extended by Lane *et al.* (1987) to account for cortical contraction waves which accompany the calcium waves. They coupled the mechanochemical system for epithelial cell movements as proposed by Murray & Oster (1984b) (see Section 1.4.1 for a discussion) to a calcium conservation equation.

We show here that our tissue interaction model can also produce a contraction wave propagating through the epithelial layer. Although we do not account for the simultaneous propagation of a calcium wave, it is believed that the signal sent by the dermal layer to the epidermal layer stimulates epithelial calcium release (see Sections 1.4 and 2.2). Since we model the concentration of the chemical involved in dermal to epidermal signalling to be proportional to the dermal cell density, such a calcium wave will have the same shape as the dermal cell density wave.

For simplicity we only consider the one-dimensional version of the small strain quasi-steady-state system (3.1). Note that the dermal cell conservation

equation which appears in this system is the Fisher equation with an additional chemotactic interaction term. It is well known that the Fisher equation exhibits travelling wave solutions, see, for example, Murray (1977, 1989). In the light of this result we examine in this chapter whether our tissue interaction system can also give rise to travelling wave solutions.

In Section 5.2 we convert our system of partial differential equations to a system of ordinary differential equations. We then show that one of the equations in our system can be reduced to the Fisher equation. To find the conditions under which a travelling wave solution would be possible, a phase plane analysis is performed in Section 5.3. In Section 5.4 we find a regular perturbation approximation to the travelling wave solutions. In Section 5.5 these perturbation solutions are compared to the numerical solutions of the system of ordinary differential equations. From the perturbation analysis and numerical results we are able to make some biological interpretations and predictions. The system of partial differential equations is solved in Section 5.6 so as to examine the time evolution of the travelling fronts. In the last example of this section we show that the travelling waves can in fact act as precursors to pattern formation processes.

5.2 The System of Ordinary Differential Equations

By converting our system of partial differential equations to a system of ordinary differential equations, we can examine the equations for wave solutions travelling at constant speed. However, we first introduce a few simplifying assumptions which will reduce the subsequent analysis considerably.

In previous chapters we modelled the epidermal traction with a nonlinear switch function τ, depending on the dermal to epidermal signalling morphogen $\hat{s}$ (see Sections 1.4.1 and 2.3). For simplicity, as the nonlinear form of the traction function is not needed to keep patterned solutions bounded as in previous

chapters, we assume here a linear form,

$$\tau(\hat{s}) = \tau\hat{s}.$$

Furthermore, in the nondimensionalization (see Section 2.3) we can choose the representative time and length scales as $T_0 = 1/(r\bar{n})$ and $L_0 = \sqrt{(DT_0)}$ respectively. With this choice, and after rescaling α to αD, the dermal diffusion parameter D, and the dermal logistic growth rate parameter r, are incorporated into the other parameters, so that the number of parameters in the nondimensional system is reduced by two.

The one-dimensional version of the small strain quasi-steady-state system (3.1) now becomes

$$\mu\frac{\partial^3\theta}{\partial t\partial x^2} + \frac{\partial^2\theta}{\partial x^2} - \beta\frac{\partial^4\theta}{\partial x^4} + \frac{\partial^2}{\partial x^2}\left\{\frac{\tau n}{1+\hat{\nu}(1-\theta)}\right\} = \rho\theta, \tag{5.1a}$$

$$\frac{\partial n}{\partial t} = \frac{\partial^2 n}{\partial x^2} - \alpha\frac{\partial}{\partial x}\left\{n\frac{\partial}{\partial x}\left(\frac{1-\theta}{1+\gamma n}\right)\right\} + n(1-n). \tag{5.1b}$$

We look for travelling wave solutions in the usual way by setting $z = x + vt$, where the constant v is the positive wavespeed. We are thus concerned with waves moving in the negative z-direction. With this change of variables (5.1) converts to the following system of ordinary differential equations in z, where n and θ are now functions of z,

$$\mu v\frac{d^3\theta}{dz^3} + \frac{d^2\theta}{dz^2} - \beta\frac{d^4\theta}{dz^4} + \tau\frac{d^2}{dz^2}\left\{\frac{n}{1+\hat{\nu}(1-\theta)}\right\} = \rho\theta, \tag{5.2a}$$

$$v\frac{dn}{dz} = \frac{d^2 n}{dz^2} - \alpha\frac{d}{dz}\left\{n\frac{d}{dz}\left(\frac{1-\theta}{1+\gamma n}\right)\right\} + n(1-n). \tag{5.2b}$$

We begin our analysis by considering a simplified version of this system where the epidermal to dermal interaction is ignored. This is achieved by setting $\alpha = 0$, thus decoupling the dermal cell conservation equation (5.2b) from the epidermal dilation equation (5.2a) so that it becomes the well studied Fisher equation (see, for example, Murray 1977, 1989). Now only the dermal to epidermal interaction remains.

If we set

$$n_0 = n, \qquad n_1 = \frac{dn}{dz},$$

we can write the Fisher equation as a pair of first order ordinary differential equations, namely

$$n_0' = n_1 \tag{5.3a}$$

$$n_1' = vn_1 - n_0(1 - n_0), \tag{5.3b}$$

where the prime denotes differentiation with respect to z. This system has the two steady states $(0,0)$ and $(1,0)$.

The trivial steady state $(0,0)$, with eigenvalues

$$\lambda_{0\pm} = \frac{v \pm \sqrt{v^2 - 4}}{2},$$

is linearly unstable, since for $v > 0$ the real part of the eigenvalues will always be positive. If $0 < v < 2$ the steady state $(0,0)$ is an unstable spiral, which means that n_0 oscillates about zero in the vicinity of the origin. If $v \geq 2$ then $(0,0)$ is an unstable node. Note that the origin is a degenerate node when $v = 2$.

The other steady state $(1,0)$ has the eigenvalues

$$\lambda_{1\pm} = \frac{v \pm \sqrt{v^2 + 4}}{2},$$

which are of opposite signs, hence it is a saddle point.

From this analysis we see that a trajectory in the (n_0, n_1)-phase plane, connecting $(0,0)$ to $(1,0)$, could exist and it would correspond to a travelling wave in the negative z-direction. Note that for biologically realistic waves the value of the cell density, n, cannot become negative and therefore the eigenvalues $\lambda_{0\pm}$ must be real. To satisfy this the wavespeed $v \geq 2$. That such a trajectory indeed exists has been proven (see, for example, Fife 1979). The phase plane and corresponding travelling wave are shown in Fig. 5.1.

Next we investigate how the dermal Fisher wave affects the epidermal sheet equation (5.2a) through the coupling parameter τ. Since

$$\lim_{z\to\infty} n(z) = 1, \qquad \lim_{z\to-\infty} n(z) = 0,$$

we have from (5.3) that

$$\lim_{z\to\pm\infty} n'(z) = 0, \qquad \lim_{z\to\pm\infty} n''(z) = 0.$$

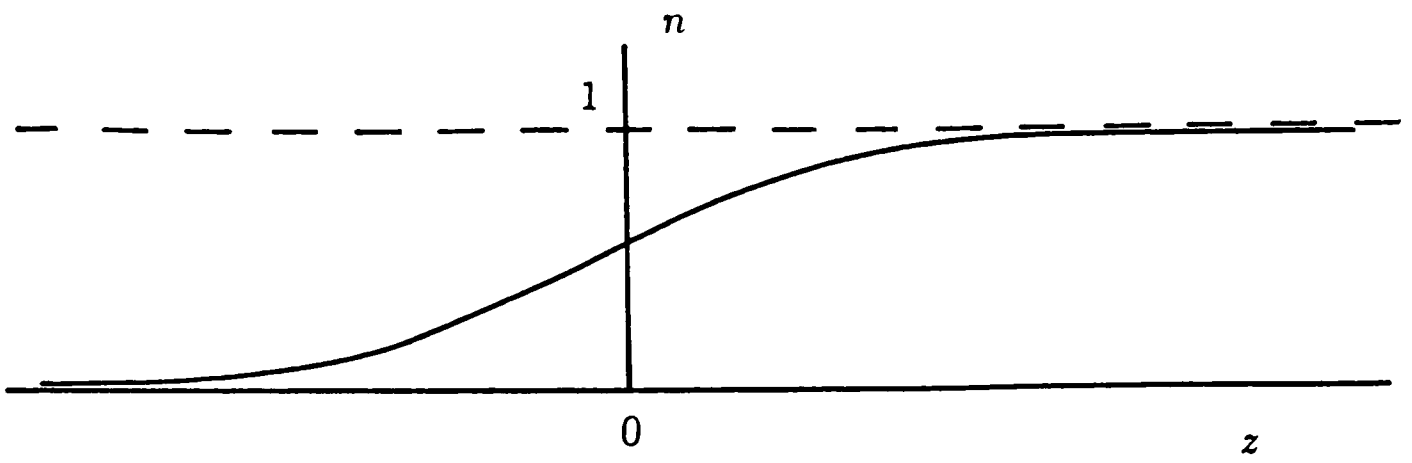

(a)

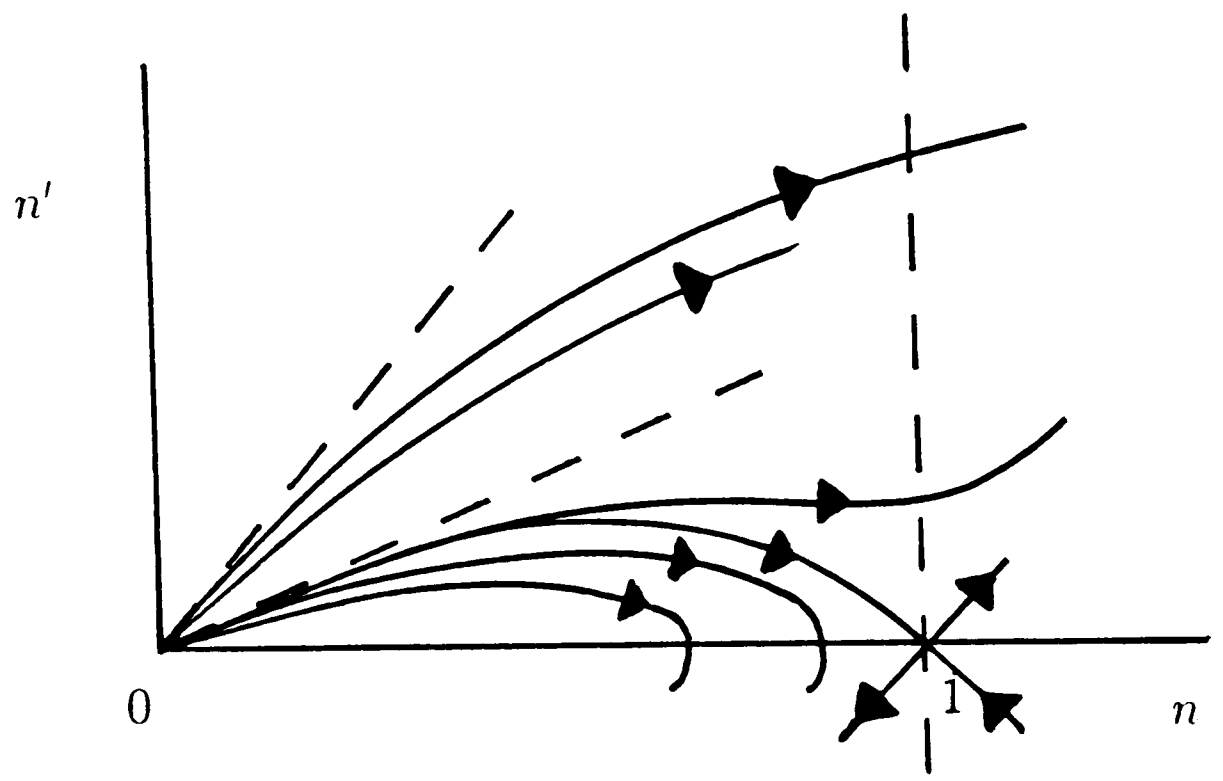

(b)

Figure 5.1: In (a) we show the typical travelling wave solution of the Fisher equation (5.3). The phase plane is shown in (b). Redrawn from Murray (1977).

It follows that the boundary conditions for (5.2a) are

$$\mu v\frac{d^3\theta}{dz^3}+\frac{d^2\theta}{dz^2}-\beta\frac{d^4\theta}{dz^4}+\left(\frac{\tau\hat{\nu}}{[1+\hat{\nu}(1-\theta)]^2}\right)\frac{\partial^2\theta}{\partial z^2}$$
$$+\left(\frac{2\tau\hat{\nu}^2}{[1+\hat{\nu}(1-\theta)]^3}\right)\left(\frac{\partial\theta}{\partial z}\right)^2=\rho\theta \quad \text{as} \quad z\to\infty.$$

and

$$\mu v\frac{d^3\theta}{dz^3}+\frac{d^2\theta}{dz^2}-\beta\frac{d^4\theta}{dz^4}=\rho\theta \quad \text{as} \quad z\to-\infty.$$

The simplest solution satisfying this has

$$\lim_{z\to\pm\infty}\theta(z)=\lim_{z\to\pm\infty}\theta'(z)=\lim_{z\to\pm\infty}\theta''(z)=\lim_{z\to\pm\infty}\theta'''(z)=\lim_{z\to\pm\infty}\theta''''(z)=0.$$

The form of our equations suggests that the dermal Fisher wave will cause a disturbance wave in the epithelial layer which will also propagate at the same velocity as the dermal wave.

In the following sections we use this intuitive idea on the behaviour of the reduced system to examine the two-way interaction system (5.2) for travelling wave solutions.

5.3 Linear Analysis

As mentioned in the previous section, for the Fisher equation one can prove that a trajectory corresponding to the travelling wave solution exists in the phase plane. To prove the existence of travelling wave solutions for the two-way tissue interaction system (5.2), if at all possible, is not a trivial task, since one has to deal with a six-dimensional phase space. However, using a linear analysis about the steady states, as for the Fisher equation, we can conjecture under which conditions a trajectory corresponding to a travelling wave solution will be possible.

The tissue interaction system (5.2) has the steady states $\theta = 0$, $n = 0$ and $\theta = 0$, $n = 1$. Realistic waves require a heteroclinic orbit in n, connecting the steady state $n = 0$ to $n = 1$, and a homoclinic orbit in θ, connecting the steady state $\theta = 0$ to itself. By setting

$$\theta_0 = \theta, \quad \theta_1 = \theta', \quad \theta_2 = \theta'', \quad \theta_3 = \theta''', \quad n_0 = n, \quad n_1 = n',$$

we can rewrite the coupled pair of ordinary differential equations (5.2) as a sixth order system, namely

$$\theta_0' = \theta_1, \tag{5.4a}$$

$$\theta_1' = \theta_2, \tag{5.4b}$$

$$\theta_2' = \theta_3, \tag{5.4c}$$

$$
\begin{aligned}
\theta_3' &= \frac{1}{\beta}\left\{\mu v\theta_3 + \theta_2 - \rho\theta_0 + \frac{\tau}{\sigma^3}\left[\sigma\left(\sigma n_1' + \hat{\nu} n_0\theta_2\right)\right.\right. \\
&\quad \left.\left. + 2\tau\hat{\nu}\theta_1\left(\sigma n_1 + \hat{\nu} n_0\theta_1\right)\right]\right\}, \qquad (5.4d) \\
n_0' &= n_1, \qquad (5.4e) \\
n_1' &= \frac{1}{\zeta^2 + \alpha\gamma n_0(1-\theta_0)}\left\{\zeta^2[vn_1 + n_0(n_0-1)]\right. \\
&\quad - \alpha\gamma n_1(1-\theta_0) - \alpha\zeta(\theta_1 n_1 + n_0\theta_2) \\
&\quad \left. + \frac{2\alpha\gamma n_0 n_1}{\zeta}\left[\zeta\theta_1 + \gamma n_1(1-\theta_0)\right]\right\}, \qquad (5.4f)
\end{aligned}
$$

where

$$
\sigma = 1 + \hat{\nu}(1-\theta_0), \qquad \zeta = 1 + \gamma n_0,
$$

and the expression (5.4f) for n_1' must be substituted into (5.4d).

We now investigate whether a trajectory connecting the steady state $S_0 = (0,0,0,0,0,0)$ to the steady state $S_1 = (0,0,0,0,1,0)$ is possible. As in the simple Fisher case, we show that the steady state S_0 has an unstable manifold and the steady state S_1 has a stable manifold.

Linearizing about the trivial steady state S_0 yields

$$
\begin{aligned}
\theta_0' &= \theta_1, \\
\theta_1' &= \theta_2, \\
\theta_2' &= \theta_3, \\
\theta_3' &= \frac{1}{\beta}\left\{\mu v\theta_3 + \theta_2 - \rho\theta_0 + \frac{\tau}{1+\hat{\nu}}\left(vn_1 - n_0\right)\right\}, \\
n_0' &= n_1, \\
n_1' &= vn_1 - n_0.
\end{aligned}
$$

We analyse the stability of this system in the usual way by looking for solutions of the form $\boldsymbol{A}e^{\lambda z}$, where the vector $\boldsymbol{A}$ is a constant and the sign of $\Re\lambda$ determines the stability of the steady state. Substituting this into the linearized system leads to a system of six simultaneous homogeneous equations. A non-trivial solution for this system exists only if λ satisfies the following solvability

condition

$$\det \begin{bmatrix} -\lambda & 1 & 0 & 0 & 0 & 0 \\ 0 & -\lambda & 1 & 0 & 0 & 0 \\ 0 & 0 & -\lambda & 1 & 0 & 0 \\ -\frac{\rho}{\beta} & 0 & \frac{1}{\beta} & \frac{\mu v}{\beta} - \lambda & -\frac{\tau}{\beta(1+\hat{\nu})} & \frac{\tau v}{\beta(1+\hat{\nu})} \\ 0 & 0 & 0 & 0 & -\lambda & 1 \\ 0 & 0 & 0 & 0 & -1 & v - \lambda \end{bmatrix} = 0.$$

This is a sixth order polynomial in λ which includes as solution, the complex conjugate pair

$$\lambda_{0\pm} = \frac{v \pm \sqrt{v^2 - 4}}{2}, \tag{5.5}$$

with eigenvectors of the form

$$[\kappa, \kappa\lambda_{0\pm}, \kappa\lambda_{0\pm}^2, \kappa\lambda_{0\pm}^3, 1, \lambda_{0\pm}] \tag{5.6}$$

where

$$\kappa = \frac{\tau(v\lambda_{0\pm} - 1)}{(1 + \hat{\nu})(\beta\lambda_{0\pm}^4 - \mu v\lambda_{0\pm}^3 - \lambda_{0\pm}^2 + \rho)}.$$

The four other eigenvalues λ_i, $i = 1, 2, 3, 4$, satisfy

$$\beta\lambda^4 - \mu v\lambda^3 - \lambda^2 + \rho = 0, \tag{5.7}$$

with eigenvectors of the form

$$[1, \lambda_i, \lambda_i^2, \lambda_i^3, 0, 0]. \tag{5.8}$$

Since $v > 0$ the steady state S_0 will always have a linearly unstable manifold spanned by the eigenvectors corresponding to the positive eigenvalues in (5.5) and (5.7).

From the biology it is, of course, impossible for the dermal cell density n_0, to be negative. Since the eigenvector (5.6) corresponding to the eigenvalue with the positive real part in (5.5) has an imaginary n_1-component if $v < 2$, such unrealistic trajectories are possible. However, if $v \geq 2$ then $n_0 \geq 0$ on all trajectories shooting out from S_0, since then the eigenvectors (5.6) have real n_1-components. Thus, similar to the Fisher equation, there is a lower bound on the speed of realistic travelling wave solutions for the reduced tissue interaction system.

We can also derive a linearly valid condition on the model parameters for determining when the epithelial cell dilation solution will exhibit oscillatory behaviour in the vicinity of S_0. Using Descarte's rule of signs, since all the model parameters, as well as the wavespeed v, are positive, it follows that the polynomial (5.7) has either two or zero positive and either two or zero negative roots. To determine the three turning points (5.7) we set its first derivative equal to zero and solve for λ to find

$$\lambda_{\pm}^{*} = \frac{3\mu v + \sqrt{9\mu^2 v^2 - 32\beta}}{8\beta} \quad \text{and} \quad \lambda^{*} = 0.$$

By substituting λ_{+}^{*} into the polynomial (5.7), we find the condition under which it will have two real positive roots, that is

$$512\rho\beta^3 - 27\mu^4 v^4 - 144\beta\mu^2 v^2 - 16\beta - \mu v(9\mu^2 v^2 + 32\beta)^{\frac{3}{2}} < 0. \tag{5.9}$$

Under this condition the θ_1-components of the eigenvectors (5.8) corresponding to the positive eigenvalues in (5.7) are real, thus the span of the unstable manifold at S_0 is made up real vectors and therefore oscillatory behaviour in the model variables about S_0 will not occur. However, if condition (5.9) is not satisfied imaginary values appear in the θ_1-components of the eigenvectors (5.8) corresponding to the eigenvalues in (5.7) with positive real parts. In this case oscillatory trajectories in θ could shoot from the steady state S_0.

We next conduct a similar linear analysis at the steady state S_1. Linearizing about S_1 yields the system

$$\begin{aligned}
\theta_0' &= \theta_1, \\
\theta_1' &= \theta_2, \\
\theta_2' &= \theta_3, \\
\theta_3' &= \frac{1}{\beta}\left\{\mu v\theta_3 + \theta_2 - \rho\theta_0 + \frac{\tau w}{1+\hat{\nu}}[(1+\gamma)(vn_1 + n_0) - \alpha\theta_2] + \frac{\tau\hat{\nu}\theta_2}{(1+\hat{\nu})^2}\right\}, \\
n_0' &= n_1, \\
n_1' &= w[(1+\gamma)(vn_1 + n_0) - \alpha\theta_2],
\end{aligned}$$

where

$$w = \frac{1+\gamma}{(1+\gamma)^2 + \alpha\gamma} > 0.$$

Again we look for solutions of the form $Ae^{\lambda z}$. The eigenvalues for this system are

$$\lambda_{\pm} = \frac{(1+\gamma)vw \pm \sqrt{(1+\gamma)^2 v^2 w^2 + 4(1+\gamma)w}}{2}, \tag{5.10}$$

as well as the four roots satisfying

$$\beta\lambda^4 - \mu v\lambda^3 - \varsigma\lambda^2 + \rho = 0, \tag{5.11}$$

where

$$\varsigma = 1 + \frac{\tau\hat{\nu}}{(1+\hat{\nu})^2}.$$

It is easy to see from (5.10) that S_1 always has a stable manifold for positive values of v. Here since the eigenvalues (5.5) have no imaginary part there will be no oscillation in cell density n, in the vicinity of the steady state.

Since the polynomial (5.11), according to Descarte's rule of signs, has two or zero negative roots we can again find a linearly valid condition under which the dilation solution θ, would not approach the zero steady state solution in an oscillatory manner. Using a similar method as before we can find the condition as

$$512\rho\beta^3 - 27\mu^4 v^4 - 144\beta\varsigma\mu^2 v^2 - 16\beta\varsigma^2 + \mu v(9\mu^2 v^2 + 32\varsigma\beta)^{\frac{3}{2}} \leq 0. \tag{5.12}$$

If this condition is violated oscillatory trajectories in θ in the vicinity of S_1 are possible.

From the above analysis we conjecture that a biologically realistic travelling wave, connecting the steady states S_0 and S_1 for all parameter ranges could exist if $v \geq 2$. In the following sections we shall examine by analytical and numerical means whether such travelling wave solutions actually do exist.

5.4 Regular Perturbation Solution

In this section we attempt to find a regular perturbation solution for the travelling wave solutions of the tissue interaction system (5.2). Such a solution would

assist us in understanding the roles which the various model parameters play in determining the solution. Moreover, by using a regular perturbation solution we could confirm the correctness of the numerically computed solutions shown in the next section.

For the purpose of our perturbation method we assume that there does indeed exist a travelling wave solution for (5.2) satisfying the boundary conditions

$$\lim_{z\to\infty} n(z) = 1, \qquad \lim_{z\to-\infty} n(z) = 0,$$
$$\lim_{z\to\pm\infty} \theta(z) = 0, \qquad \lim_{z\to\pm\infty} \theta'(z) = 0. \tag{5.13}$$

We begin by rescaling the system of ordinary differential equations (5.2). To find the appropriate scalings we rescale the dependent and independent variables in (5.2) by setting

$$\Theta = \pi^{-1}\theta, \qquad N = \phi n, \qquad \xi = \delta z, \tag{5.14}$$

where Θ, N and ξ are the rescaled variables, δ is an appropriate scale to the independent variable and π and ϕ are appropriate scales for the dependent variables.

Since we have no *a priori* reason for favouring one term above another we therefore try to employ a scaling which simplifies the equations (5.13) the least, that is, which makes as many terms as possible in the relevant differential equation have the same order of magnitude. This principle is sometimes referred to as Kruskal's principle of minimum simplification, see Segel & Slemrod (1989).

Using (5.14) gives for (5.2a), after multiplying by π,

$$\mu v\delta^3\pi\frac{d^3\Theta}{d\xi^3} + \delta^2\pi\frac{d^2\Theta}{d\xi^2} - \beta\delta^4\pi\frac{d^4\Theta}{d\xi^4} + \tau\delta^2\phi\frac{d^2}{d\xi^2}\left\{\frac{N}{1+\hat{\nu}(1-\pi\Theta)}\right\} = \rho\pi\Theta. \tag{5.15}$$

We find here that it is impossible to make all the terms the same order of magnitude and we are forced to favour some terms above others.

To ensure that we have a non-zero solution for this equation at the lowest order we must assume that the interaction term, in which $n(z)$ appears, is in the lowest order equations. As mentioned earlier the viscous and long range elastic

terms, the first and third terms in (5.15) respectively, are not as important as the short range elastic term and the epithelial tethering term, the second term and the term on the right hand side of equation (5.15) respectively.

We assume that the interaction and the tethering terms are of the same order of magnitude, thus setting $\delta^2\tau\phi = \rho\pi$, This determines a unique relationship between δ and π which would be violated if we assume other terms in the equation are also of the same order. Alternatively, one could assume that the elastic and the interaction terms are of the same order of magnitude. However, by using a similar procedure as below, exactly the same perturbation solutions for n and θ result.

By using the scaling (5.14), where $\phi = 1$, equation (5.2b) becomes

$$v\delta\frac{dN}{d\xi} = \delta^2\frac{d^2N}{d\xi^2} - \alpha\delta^2\frac{d}{d\xi}\left\{N\frac{d}{d\xi}\left(\frac{1-\pi\Theta}{1+\gamma\phi N}\right)\right\} + N(1-\phi N),$$

which is the Fisher equation with an interaction term included. Here again we have to favour some terms above others. Murray (1977) gives a perturbation solution for the normal Fisher equation in terms of the small parameter $1/v^2$, by assuming that $\phi = 1$ and furthermore that the term on the left hand side of the equation is the same order of magnitude as the logistic growth term on the right hand side. We make the same assumption for our interaction system, thus setting $v\delta = 1$. From now on we shall again use n instead of N.

So, if we assume that

$$\delta = \frac{1}{v}, \qquad \pi = \frac{\tau}{\rho v^2},$$

and set $\epsilon = \delta^2$ we obtain the rescaled system

$$\mu\epsilon\frac{d^3\Theta}{d\xi^3} + \epsilon\frac{d^2\Theta}{d\xi^2} - \epsilon^4\beta\frac{d^4\Theta}{d\xi^4} + \rho\frac{d^2}{d\xi^2}\left\{\frac{n}{1+\hat{\nu}(1-\epsilon\tau\Theta/\rho)}\right\} = \rho\Theta \qquad (5.16a)$$

$$\frac{dn}{d\xi} = \epsilon\frac{d^2n}{d\xi^2} - \epsilon\alpha\frac{d}{d\xi}\left\{n\frac{d}{d\xi}\left(\frac{1-\epsilon\tau\Theta/\rho}{1+\gamma n}\right)\right\} + n(1-n), \qquad (5.16b)$$

with boundary conditions

$$\lim_{\xi\to\infty} n(\xi) = 1, \qquad \lim_{\xi\to-\infty} n(\xi) = 0,$$
$$\lim_{\xi\to\pm\infty} \Theta(\xi) = 0, \qquad \lim_{\xi\to\pm\infty} \Theta'(\xi) = 0. \qquad (5.17)$$

These equations are translation-invariant in ξ, so for uniqueness we additionally fix one point,

$$n(0) = \frac{1}{2}. \tag{5.18}$$

The linear analysis of the previous section predicted that if the tissue interaction system has travelling wave solutions then their speed $v \geq 2$, so that $\epsilon \leq 0.25$. Hence, we use a regular perturbation method to obtain approximate solutions to this system with ϵ as our small parameter. Although ϵ is relatively large when the wavespeed has minimum value $v = 2$, a similar method gives very good perturbation solutions to the Fisher equation (see Murray 1977). We therefore assume that the solution of (5.16), satisfying the boundary conditions (5.17) and (5.18), can be written as a series expansion of the form

$$\Theta(\xi, \epsilon) = \Theta_0(\xi) + \epsilon\Theta_1(\xi) + \ldots \tag{5.19a}$$

$$n(\xi, \epsilon) = n_0(\xi) + \epsilon n_1(\xi) + \ldots. \tag{5.19b}$$

Substituting (5.19) into (5.16) reduces the system of nonlinear equations (5.16) to a hierarchy of linear equations. The boundary conditions at $\xi = \pm\infty$ and the choice of $n(0) = 1/2$, which requires that $n(0, \epsilon) = 1/2$ for all ϵ, lead to the following conditions on $\Theta_i(\xi)$ and $n_i(\xi)$,

$$\begin{aligned}
&\lim_{z\to\pm\infty} \Theta_i(z) = 0, \qquad \lim_{z\to\pm\infty} \Theta_i'(z) = 0, \quad \text{for } i = 0, 1, 2, \ldots \\
&\lim_{z\to-\infty} n_0(z) = 0, \qquad \lim_{z\to\infty} n_0(z) = 1, \qquad n_0(0) = 1/2, \\
&\lim_{z\to\pm\infty} n_i(z) = 0, \qquad n_i(0) = 0, \quad \text{for } i = 1, 2, 3, \ldots.
\end{aligned} \tag{5.20}$$

Before carrying out the perturbation procedure we must decide on the magnitude of the physical model parameters μ, β, τ, $\hat{\nu}$, ρ, α and γ. As these parameters are difficult to measure biologically, we scale them so that as many terms as are biologically and algebraically realistic, have the same order of magnitude in the relevant equations. This way we keep as much flexibility as possible and we are consistent with Kruskal's principle of minimum simplification.

We assume that ρ is $O(1)$. If we assume that α, γ or $\hat{\nu}$ is $O(1/\epsilon)$ or larger, to find perturbation solutions for the system becomes analytically intractable;

consequently we assume that they are all $O(1)$. Biologically we expect the long range elasticity, reflected by β, and the viscous effects, measured by the parameter μ, to be small and so, to insure that these effects do not dominate the short range elastic forces, we choose both β and μ to be $O(1)$ or smaller. We also do not expect the chemically induced traction force, measured by the parameter τ, to be larger than the restoring forces of the adhesion tethers, reflected by ρ, and we can safely assume that ρ/τ is $O(1)$ or larger. Later we shall discuss how the order of magnitude of these parameters may influence the solutions.

At $O(1)$ the equations are

$$\Theta_0 = \frac{1}{1+\hat{\nu}} \frac{d^2 n_0}{d\xi^2} \tag{5.21a}$$

$$\frac{dn_0}{d\xi} = n_0(1-n_0). \tag{5.21b}$$

By integrating the second equation and using the midpoint condition $n(0) = 1/2$ we find that

$$n_0 = \frac{e^\xi}{1+e^\xi}. \tag{5.22}$$

Substituting this into the first equation gives

$$\Theta_0 = \frac{e^\xi(1-e^\xi)}{(1+\hat{\nu})(1+e^\xi)^3}. \tag{5.23}$$

Note that Θ_0 satisfies the boundary conditions.

At $O(\epsilon)$ we have

$$\Theta_1 = \frac{\mu}{\rho}\frac{d^3\Theta_0}{d\xi^3} + \frac{1}{\rho}\frac{d^2\Theta_0}{d\xi^2} + \frac{1}{1+\hat{\nu}}\frac{d^2 n_1}{d\xi^2} + \frac{\nu}{(1+\nu)^2}\frac{d^2(n_0\Theta_0)}{d\xi^2} \tag{5.24a}$$

$$\frac{dn_1}{d\xi} + (2n_0 - 1)n_1 = \frac{d^2 n_0}{d\xi^2} - \alpha\frac{d}{d\xi}\left\{n_0\frac{d}{d\xi}\left(\frac{1}{1+\gamma n_0}\right)\right\} \tag{5.24b}$$

By substituting n_0 into (5.24b) we get

$$\frac{dn_1}{d\xi} + P(\xi)n_1 = Q(\xi), \tag{5.25}$$

where

$$P(\xi) = \frac{e^\xi - 1}{e^\xi + 1}$$

$$Q(\xi) = \frac{e^\xi(1-e^\xi)}{(1+e^\xi)^3} - \frac{\alpha\gamma e^{2\xi}[(1+\gamma)e^{2\xi} - e^\xi - 2}{[(\gamma+1)e^\xi + 1]^3(1+e^\xi)^2}.$$

The solution of (5.25) is

$$n_1(\xi) = f(\xi)[\xi - 2\ln(1+e^{\xi}) + k] - \frac{\alpha\gamma f(\xi)}{2(1+\gamma)^2 h^2(\xi)} \left\{3 + 2\gamma + 2h^2(\xi)\ln h(\xi) + h'(\xi)[2 - 2h(\xi) - h'(\xi)]\right\}, \quad (5.26)$$

where

$$f(\xi) = \frac{e^{\xi}}{(1+e^{\xi})^2}, \qquad h(\xi) = 1 + (1+\gamma)e^{\xi}, \qquad h'(\xi) = (1+\gamma)e^{\xi},$$

and k is the constant of integration. Using the midpoint condition $n_1(0) = 0$ we find that the integration constant is given by

$$k = 2\ln 2 + \frac{\alpha\gamma}{2(1+\gamma)^2(2+\gamma)^2}[2(2+\gamma)^2\ln(2+\gamma) - \gamma(3^2+4)].$$

Substituting n_0, n_1 and Θ_1 into (5.24b) we have

$$\Theta_1 = \frac{\mu}{\rho}\Theta_0''' + \Theta_0''\left(\frac{1}{\rho} + \frac{\hat{\nu}n_0}{(1+\hat{\nu})^2}\right) + \frac{n_1''}{1+\hat{\nu}}\left(1 + \frac{\nu\Theta_0}{1+\hat{\nu}}\right) + \frac{2\hat{\nu}\Theta_0' n_0'}{(1+\hat{\nu})^2}, \quad (5.27)$$

where

$$\begin{aligned}
\Theta_0'(\xi) &= \frac{f(\xi)(1 - 4e^{\xi} + e^{2\xi})}{(1+\hat{\nu})(1+e^{\xi})^2}, \\
\Theta_0''(\xi) &= \frac{f(\xi)(1 - 11e^{\xi} + 11e^{2\xi} - e^{3\xi})}{(1+\hat{\nu})(1+e^{\xi})^3}, \\
\Theta_0'''(\xi) &= \frac{f(\xi)(1 - 26e^{\xi} + 66e^{2\xi} - 26e^{3\xi} + e^{4\xi})}{(1+\hat{\nu})(1+e^{\xi})^4}, \\
n_0' &= f(\xi), \\
n_0'' &= f'(\xi), \\
n_1'' &= f''(\xi)[\xi - 2\ln(1+e^{\xi}) + k] + 2f(\xi)\left[\left(\frac{1-e^{\xi}}{1+e^{\xi}}\right)^2 - f(\xi)\right] \\
&\quad - \frac{\alpha\gamma}{2(1+\gamma)^2 h^4(\xi)}\left\{[f''(\xi)h^2(\xi) - 4f'(\xi)h(\xi)h'(\xi)\right. \\
&\quad + 6f(\xi)(h'(\xi))^2 - 2f(\xi)h(\xi)h''(\xi)][3 + 2\gamma + 2h^2(\xi)\ln h(\xi) \\
&\quad + h'(\xi)(2 - 2h(\xi) - h'(\xi))] + 2h(\xi)h'(\xi)[f'(\xi)h(\xi) - 2f(\xi)h'(\xi)] \\
&\quad [2 - 4h'(\xi) + 4h(\xi)\ln h(\xi)] + f(\xi)h^2(\xi)h'(\xi)[2 - 4h'(\xi) \\
&\quad \left. + 4(h(\xi) + h'(\xi)\ln h(\xi))]\right\},
\end{aligned}$$

and

$$\begin{aligned} f'(\xi) &= \frac{f(\xi)(1-e^{\xi})}{1+e^{\xi}}, \\ f''(\xi) &= f(\xi)\left[\left(\frac{1-e^{\xi}}{1+e^{\xi}}\right)^2 - 2f(\xi)\right]. \end{aligned}$$

We can continue with this process to find expressions for the higher order terms, however the expressions become algebraically too complicated to handle. Besides, the additional correction provided by, say, the $O(\epsilon^3)$ term, is too small to be significant.

Biologically it is very difficult to measure the dilation θ, of the epithelial layer. Since we know from our small strain approximation (2.8) that

$$\frac{\partial u(x,t)}{\partial x} = \theta(x,t),$$

we can find the perturbation solution in terms of the displacement u by integrating the dilation function. In terms of the variable ξ, we have that

$$\frac{du(\xi)}{d\xi} = \frac{\tau}{\rho v}\Theta(\xi).$$

The constant that arises on integration can be set to zero if we assume that the displacement at ∞ is zero. This automatically fixes the displacement at $-\infty$ as zero, since $\lim_{z\to\pm\infty}\Theta(z) = 0$. Assuming that we can integrate the perturbation solution for $\Theta(\xi)$ we find that

$$u(\xi) = \frac{\tau}{\rho}(\epsilon^{\frac{1}{2}}u_0(\xi) + \epsilon^{\frac{3}{2}}u_1(\xi) + \ldots), \tag{5.28}$$

where

$$\begin{aligned} u_0(\xi) &= \frac{e^{\xi}}{(1+\hat{\nu})(1+e^{\xi})^2}, \\ u_1(\xi) &= \frac{\mu}{\rho}\Theta_0'' + \Theta_0'\left[\frac{1}{\rho} + \frac{\hat{\nu}n_0(\xi)}{(1+\hat{\nu})^2}\right] + \frac{n_1'(\xi)}{1+\hat{\nu}} + + \frac{\hat{\nu}\Theta_0 n_0'(\xi)}{(1+\hat{\nu})^2}, \end{aligned}$$

and

$$\begin{aligned} n_1' &= \frac{1-e^{\xi}}{1+e^{\xi}}f'(\xi) + f(\xi)[\xi - 2\ln(1+e^{\xi}) + k] \\ &\quad - \frac{\alpha\gamma}{2(1+\gamma)^2h^3(\xi)}\{[f'(\xi)h(\xi) - 2f(\xi)h'(\xi)] \\ &\quad [3+2\gamma+2h^2(\xi)\ln h(\xi) + h'(\xi)(2-2h(\xi)-h'(\xi)] \\ &\quad + f(\xi)h(\xi)h'(\xi)[2-4h'(\xi)+4(h(\xi)\ln h(\xi)]\}. \end{aligned}$$

Hence we have found a regular perturbation solution for the system of ordinary differential equations (5.2) when all the parameters are $O(1)$. The solution, however, changes if the parameter values do not satisfy this condition. A discussion of this shall be given in the following section.

5.5 Numerical Solutions and Biological Interpretation

Here we solve our ordinary differential equation system (5.2) numerically. The results obtained can then be compared with the perturbation solutions of the previous section. In the light of the results of our numerical computations and perturbation analysis we can give an intuitive biological interpretation of these travelling waves. We also examine the contribution of the various parameters to the model solution.

To solve the (5.2) numerically we employed the NAG FORTRAN routine D02RAF which uses a finite difference technique for solving boundary value problems. An initial estimate is corrected using Newton iteration and deferred correction. We specified as initial solution the first order perturbation solutions (5.22) and (5.23) as obtained in the previous section.

The equations were solved on the spatial domain $[-20, 20]$ which is large in comparison with the part of the domain where the solution changes shape rapidly. To simulate the boundary conditions (5.13) we used the following set of boundary conditions

$$n(-20) + n(20) = 1, \qquad \theta(-20) + \theta(20) = 0, \qquad \theta'(-20) + \theta'(20) = 0.$$

So as to satisfy the uniqueness criteria used in the previous section, the numerical solutions were shifted so that $n(0) = 1/2$.

Some trial runs were performed for different parameter sets. We found that biologically realistic waves occur only when the wavespeed satisfied $v \geq 2.0$. In all the cases we computed with $v < 2$, the dermal cell density dropped below

zero in the region of the boundary $z = -20$. This confirms what the linear analysis of Section 4.2 predicted.

To find the displacement $u(z)$, we numerically solved $u'(z) = \theta(z)$ by using NAG FORTRAN routine D02CBF which integrates a first order ordinary differential equation over a given range by using a variable order, variable step, Adams routine. Since we require the displacement to be zero at $\pm\infty$ we assume as initial condition that $u(-20) = 0.0$ and integrated to $z = 20$. The numerical solution of $\theta(z)$ was calculated at discrete mesh points by the finite difference routine. Since the Adams routine requires the value for $\theta(z)$ at intermediate points we used NAG FORTRAN routine E01AAF to interpolate the value of $\theta(z)$ at the z-values required by the Adams routine, using the four closest mesh values of θ. This routine uses Aitken's technique of successive linear interpolations.

We illustrate our numerical results with two examples for different values of the wavespeed v.

Example 5.5.1: In the first example we assumed that all our parameters are $O(1)$ so that we can compare our numerical solution with the regular perturbation solution. We therefore set μ, β, τ, $\hat{\nu}$, ρ, α and γ all equal to 1.0. It was further assumed that the wave travels at minimum speed, $v = 2.0$, as predicted by the linear analysis of Section 5.2. For such a low value of the wavespeed v, the value of the small parameter ϵ in our perturbation expansions (5.19) is relatively large. We therefore did not expect the approximate perturbation solution to fit the numerical solution very closely.

The numerical solution is compared with the zero and first order analytical approximations in Figure 5.2. We see that the approximation for θ improves slightly by adding the $O(\epsilon)$ term. The bend appearing in the solution at $z = 0$ is due to the Θ'' and Θ''' terms in our perturbation solution (5.27) which are relatively large at the origin, see Figure 5.3. As seen in the previous section there is, however, no alternative scaling to rectify this problem.

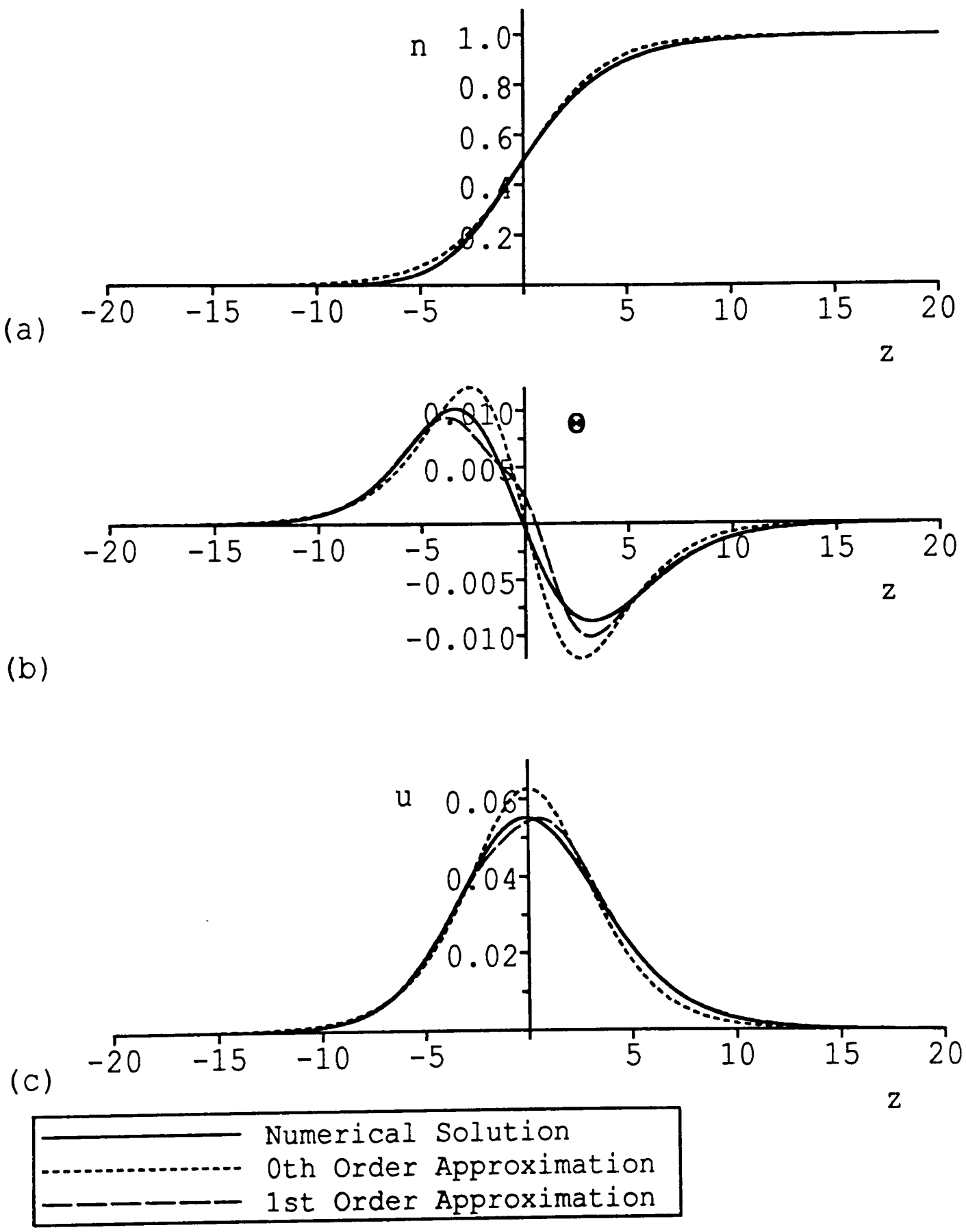

Figure 5.2: A comparison of the numerical solution with the regular perturbation solutions to $O(1)$ and $O(\epsilon)$ when $v = 2$ and thus $\epsilon = 1/4$. The parameters are as in Example 5.5.1.

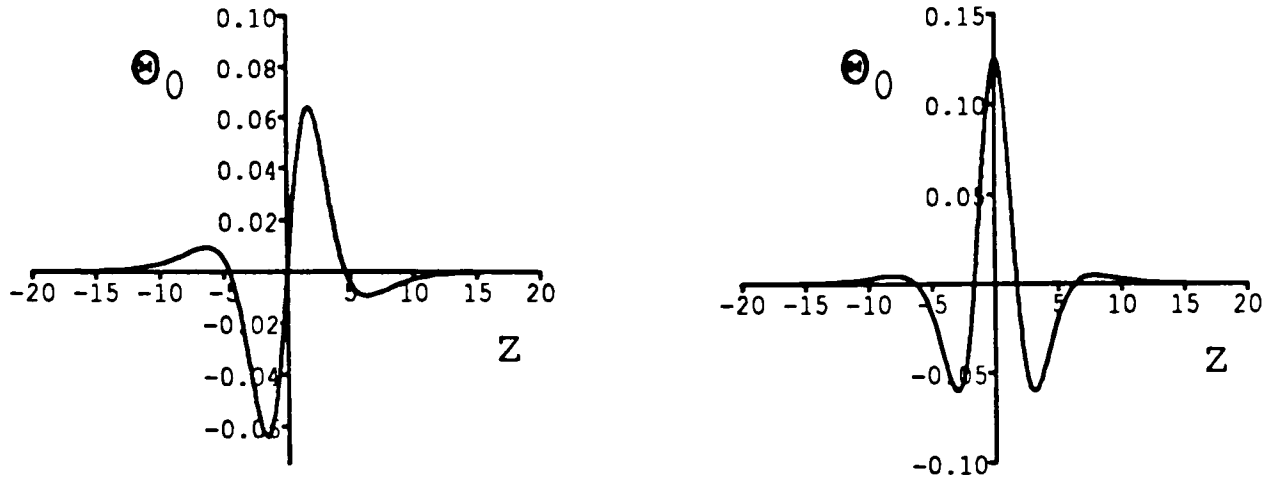

(a) (b)

Figure 5.3: The contributions of (a) the Θ_0'' and (b) the Θ_0''' terms in the regular perturbation solution when parameters are as in Example 5.5.1.

Example 5.5.2: For the second example we used the same parameter values as in Example 5.5.1, but we increased the wavespeed to $v = 3$, so as to see whether the perturbation solution approximation of the numerical solution improves as ϵ becomes smaller — in our previous example ϵ was $1/4$, in this example it is $1/9$. As can be seen in Figure 5.4 this is indeed the case. With the first order terms included the perturbation solution and numerical solution are almost identical. However, the increase in wavespeed has caused a considerable decrease in the amplitude of the epithelial disturbance wave.

In both examples considered above the linear non-oscillatory conditions on θ in the vicinity of the steady states, (5.9) and (5.12), were satisfied. As expected the dilation solution approached the steady states smoothly. However, we also considered some examples with parameter sets so that conditions (5.9) and (5.12) were violated. In these cases the dilation solution θ changed sign as it approached the steady states, suggesting a possible oscillatory behaviour.

The form of the epithelial displacement wave agrees with our physical understanding of the interaction mechanism and can be explained as follows. Initially we have a small clump of dermal cells at $x = \infty$ and the epithelial sheet is fixed

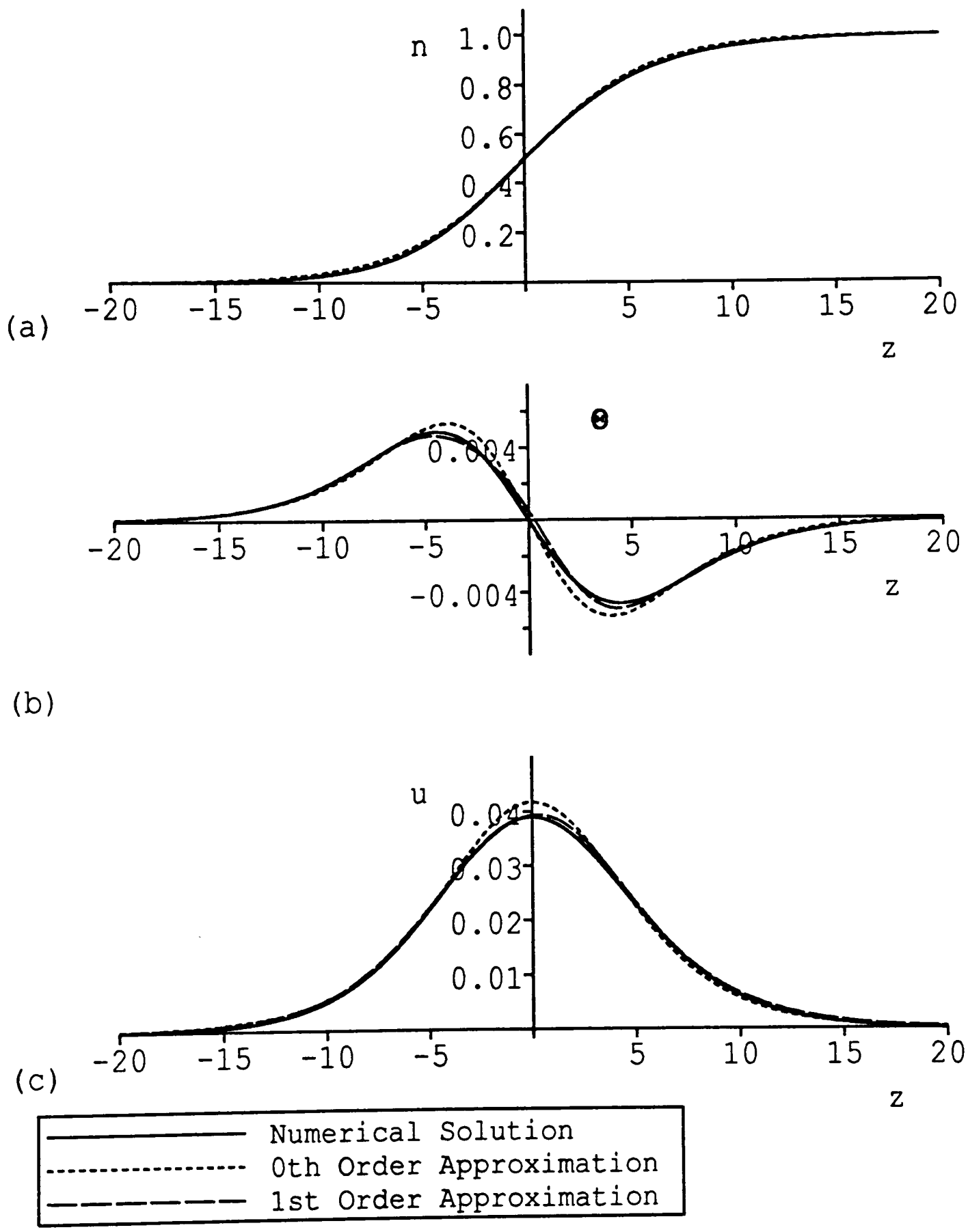

Figure 5.4: A comparison of the numerical solution with the regular perturbation solutions to $O(1)$ and $O(\epsilon)$ when $v = 3$ and thus $\epsilon = 1/9$. The parameters are as in Example 5.5.2.

at this point, that is $u(\infty, t) = 0$. Since the production of the dermal-to-epidermal signal chemical is proportional to the dermal cell density, a stronger signal will be received by the epidermal layer at $x = \infty$ than anywhere else. The epithelial sheet contraction increases in this region, thus pulling the epithelial cells in the positive x-direction. So an epithelial point, say x_0, to the left of $x = \infty$, undergoes a positive displacement. As the dermal cell density increases towards $x = -\infty$ the point x_0 experiences traction in both the positive and negative x-directions, because the signals received and the resulting epithelial contraction experienced, differ to the left and right of this point. As the wave travels past x_0, this difference diminishes and the resulting force, pulling the material point x_0 to the right, decreases. The displacement $u(x_0)$, gradually decreases until, eventually when the dermal cell density wave has passed, it returns to zero.

From a biological point of view it is also important to examine the role which the various parameters play in determining the shape and size of the respective waves. The regular perturbation solution obtained in the previous section lends itself particularly well to such an exercise as it is possible to predict the qualitative role of some of the model parameters from the perturbation solution. It is also relatively easy to confirm these predictions by numerical studies.

We begin by investigating how the epidermal contraction wave is influenced by the adhesion tethers with which the epidermal sheet is connected through the basal lamina to the dermal layer. For large values of ρ, the sheet is firmly attached and the dermal travelling wave causes a very small disturbance in the epithelial layer. This is apparent from the scaling (5.14) we used, since by increasing ρ the value of π decreases. On the other hand decreasing the value of ρ has the opposite effect — the amplitude of the epithelial contraction wave increases.

It is interesting to note that when ρ is zero, two constants appear when we

integrate the epidermal equation, (5.1a),

$$\mu\frac{\partial\theta}{\partial t}+\theta+\frac{\tau}{1+\hat{\nu}(1-\theta))}=k_0(t)x+k_1(t).$$

This equation does not possess travelling wavefront solutions with constant speed and shape. Due to the terms on the right hand side, the equation does not convert into an ordinary differential equation in terms of z after the usual substitution $z=x+vt$.

Changing the traction parameter τ, has a similar effect as changing ρ. For example, by decreasing the epithelial traction parameter τ, the value of the scaling parameter π in (5.14) decreases and so does the size of the epithelial contraction wave.

The value of the viscosity parameter, μ, similarly influences the amplitude of the epithelial contraction wave. When μ is very large, say $O(1/\epsilon^2)$, the viscous nature of the epithelial sheet dominates the elastic properties. The size of the contraction wave decreases accordingly, since now our $O(1)$ perturbation solution is $\Theta_0=0$. On the other hand, by decreasing the viscous parameter, μ, to say $O(\epsilon)$, the $\mu\Theta_0'''$ term, see Figure 5.3(b), in our $O(\epsilon)$ solution (5.24) disappears. The disturbance in the leading edge of the dilation wave therefore increases while that in the trailing edge decreases. The change in the solution, however, would be very small, since decreasing μ only effects the first and higher order terms in our perturbation solution.

The results obtained in the last two sections lead to several interesting predictions. To summarize: a change in epithelial viscosity, traction and/or adhesion influence the amplitude of the contraction wave. Experimentally it would be very interesting to test these predictions. For example, by experimentally inducing a travelling wave in the dermal layer one could then examine the epidermal layer for a disturbance wave as seen in the solutions considered above. A dermal cell density wave could, for example, be initiated by injecting a mitotic promoter at one end of the developing skin. One could then investigate whether the amplitude of the epithelial wave increases if, say, the tethers, with

which the epithelial layer is attached to the dermal layer, are severed. Such an experiment could also indicate whether the dermal-epidermal interaction is chemical or mechanical.

In addition one could look at the effect of anti-L-CAM antibodies on the travelling waves. This might throw further light on the role of CAMs in pattern formation and tissue interaction in particular, as discussed in Section 2.2.

Biologically it is believed that the whole pattern formation process in morphogenesis is the result of a few simple mechanisms. We have now shown that our tissue interaction model mechanism can simulate several fundamental processes in the developing embryo. In particular, we have illustrated that tissue interaction models can exhibit travelling wave solutions. This lends additional support to the key role of tissue interaction in morphogenesis.

5.6 The Partial Differential Equation Problem

In this section the system of partial differential equations (5.1) is solved numerically so as to examine the time evolution of the travelling wavefronts. We discuss five different examples, each highlighting a different feature of the wave solutions.

In the first example considered the numerical solution of the system (5.1) is compared to that of the system of ordinary differential equations (5.2) as obtained in Example 5.5.1. The minimum wavespeed of $v = 2.0$ is obtained, which is consistent with the prediction made in the linear analysis of Section 5.2. That this also holds for a more realistic set of parameters is shown in the second example. However, by perturbing the leading edge of the dermal travelling wave, the wave solutions can travel at speeds higher than this minimum speed as is illustrated in the third example. By disturbing the homogeneous steady state in a small region in the centre of the domain two travelling fronts, moving in opposite directions, evolve, as can be seen in Example 5.6.4. In the last example

we investigate whether the travelling wave solutions discussed in this chapter can act as precursor to pattern formation.

To solve the system of partial differential equations (5.1) numerically NAG FORTRAN routine D03PGF was used. This is the same routine as was used in Section 3.4 for computing the one-dimensional spatially patterned solutions. The equations were considered on a very large domain so that the influence of the boundary conditions become negligible. As in Section 3.4 we imposed zero-flux boundary conditions, see (3.2), both for epithelial dilation and dermal cell density.

The velocity of the travelling wavefront for the classical Fisher equation (5.3) depends on the initial conditions. Kolgomoroff *et al.* (1937) proved that if the initial conditions satisfy

$$n(x,0) = \begin{cases} 1 \text{ if } x \geq x_2 \\ 0 \text{ if } x \leq x_1 \end{cases}, \tag{5.29}$$

where $x_1 < x_2$ and $n(x,0)$ is continuous in the domain (x_1, x_2), then the solution of the Fisher equation evolves to a travelling wavefront solution with minimum speed $v = 2.0$. We conjecture that this result also holds for our system.

It is also known that for initial data other than the above, the wavespeed of the Fisher equation depends critically on the behaviour of $n(x,0)$ as $x \to \pm\infty$. To find the dependence of our the wavespeed of our system on the initial conditions at infinity, analysis similar to that proposed by Mollison (1977) for the Fisher equation is used.

We consider the leading edge of the evolving wave. Here, since n and θ are small, we linearize the dermal cell equation to

$$\frac{\partial n}{\partial t} = \frac{\partial^2 n}{\partial x^2} + n, \tag{5.30}$$

which is similar to the linearized version of the Fisher equation at the leading edge. Assume that the initial condition in dermal cell density is

$$n(x,0) = Ae^{ax} \text{ as } x \to -\infty,$$

where A and a are positive arbitrary constants. We look for travelling wave solutions satisfying (5.30) and of the form

$$n(x,t) = Ae^{a(x+vt)},$$

which represents the leading edge of the wavefront solution of the nonlinear equation. Substituting this expression into the linear equation (5.30) gives the dispersion relation

$$v = a + \frac{1}{a}. \tag{5.31}$$

So, for $a = 1$, the wavespeed v takes the minimum value 2. For all other positive values of a, v is larger than 2.

Now consider $\min[e^{ax}, e^{x}]$ for x large and negative. If $a < 1$ then $e^{ax} > e^{x}$ for $x < 0$ and therefore the velocity of propagation will depend on the leading edge of the wave and the value of v is given by (5.31). On the other hand if $a > 1$ then e^{ax} is bounded from above by e^{x} and thus the wavefront with speed $v = 2$. So

$$v = \begin{cases} a + 1/a & \text{if} \quad 0 < a \leq 1 \\ 2 & \text{if} \quad a \geq 1. \end{cases} \tag{5.32}$$

We now use this result to construct initial conditions for the numerical simulations.

Example 5.6.1: We solved the system of partial differential equations (5.1) with parameter values as in Example 5.5.1, that is μ, β, τ, $\hat{\nu}$, ρ, α, γ all equal to 1.0. The initial conditions (5.29) were used. A comparison of the solution with that of the system of ordinary differential equations (5.2) in Example 5.4.1 gives excellent agreement, as is illustrated in Figure 5.5. As was expected we found that the wave solution did indeed travel at minimum speed $v = 2.0$.

Example 5.6.2: Here again we study the time evolution of the travelling wavefront, however, a more realistic parameter set is used,

$$\mu = 0.1, \qquad \beta = 0.01, \qquad \tau = 1.0, \qquad \hat{\nu} = \frac{1}{3},$$

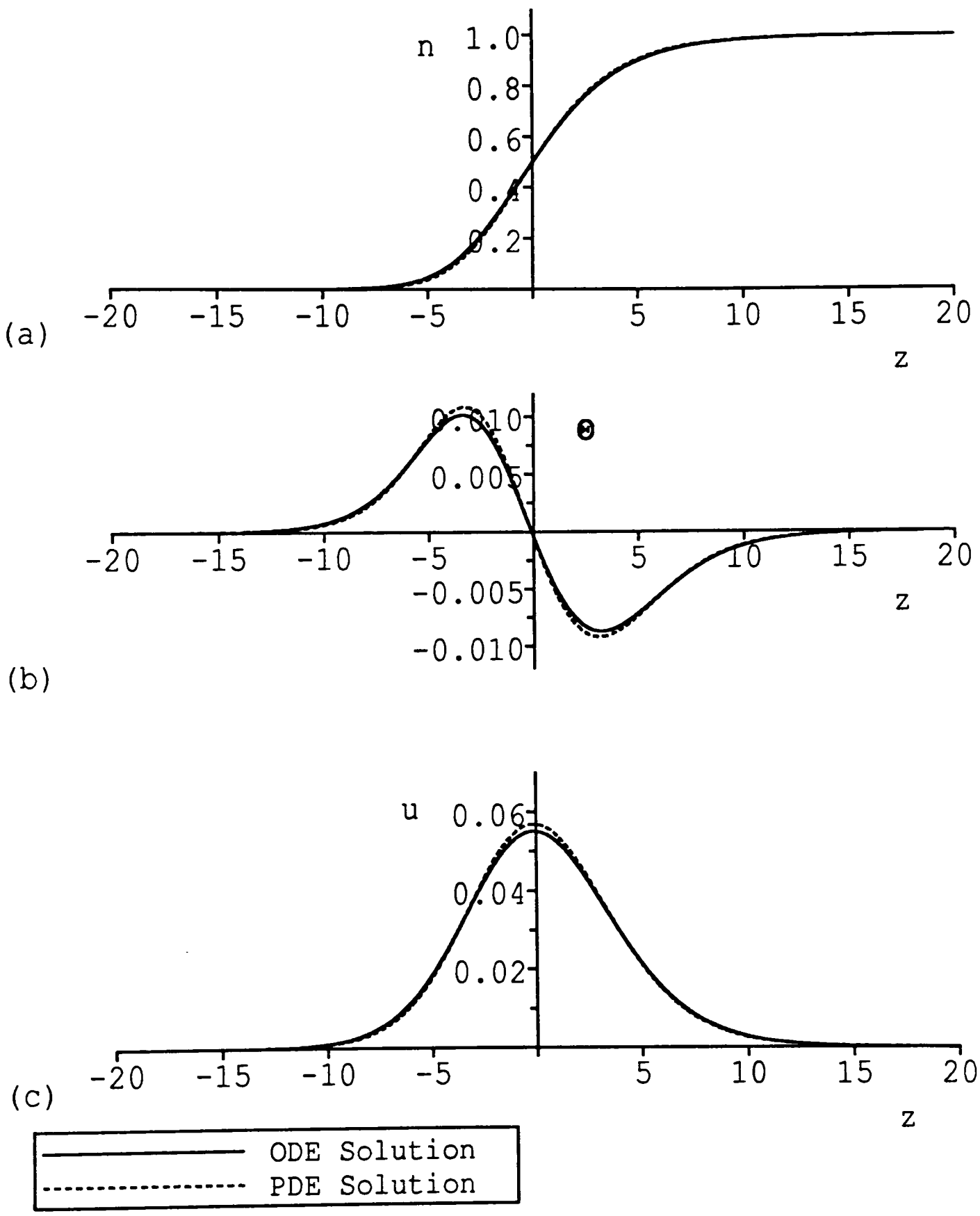

Figure 5.5: A comparison of the numerical solution of the system of ordinary differential equations (5.2), see Example 5.5.1, with the numerical solution of the system of partial differential equations (5.1), see Example 5.6.1. The wave travels at minimum speed, $v = 2$; all the parameters are equal to 1.

$$\rho = 15.0, \qquad \alpha = 1.0, \qquad \gamma = \frac{1}{3}.$$

As before we assumed that $n(x,0)$ satisfies (5.29). By following the progress of the midpoint, that is where $n(x,t) = 1/2$, a wavespeed $v = 2.0$, as expected, was obtained, see Figure 5.6. This provides further confirmation of the correctness of the predictions made in the linear analysis of Section 5.2 and also of the analysis done earlier in this section.

Example 5.6.3: We use the same parameter set as in the previous two examples, but set our initial conditions so that a wavespeed $v = 5.2$ is expected. According to (5.32) this means that the initial conditions at the leading edge must be of the form $n(x,0) = e^{5x}$. To simulate this numerically the dermal leading edge was perturbed accordingly after each numerical iteration. (We assumed the leading edge to be the region where the dermal cell density is less than 0.1.) A wavespeed $v = 5.2$ was indeed obtained as can be seen in Figure 5.7. The change in the nature of the solution at the leading edge, apparent in the figure, is due to our perturbation method.

Example 5.6.4: Since the system of partial differential equations (5.1) is invariant under a change of sign of x there also is a travelling wave solution of the form $n(x,t) = n(x - vt)$ and $\theta(x,t) = n(x - vt)$ with $v > 0$, where now

$$\lim_{z \to -\infty} n(z) = 1, \qquad \lim_{z \to \infty} n(z) = 0.$$

So, with initial condition such that $n(x,0)$ is zero outside a finite domain, two travelling wavefronts evolve, one moving to the left, the other moving to the right, both with speed $v = 2$. If $n(x,0) < 1$ the solution will grow until $n = 1$. We show a numerical example of this in Figure 5.8. Again all parameters were set to 1.0. As initial conditions we used

$$n(x,0) = 0.1\delta(x), \qquad \theta(x,0) = 0,$$

where $\delta(x)$ is the Dirac-delta.

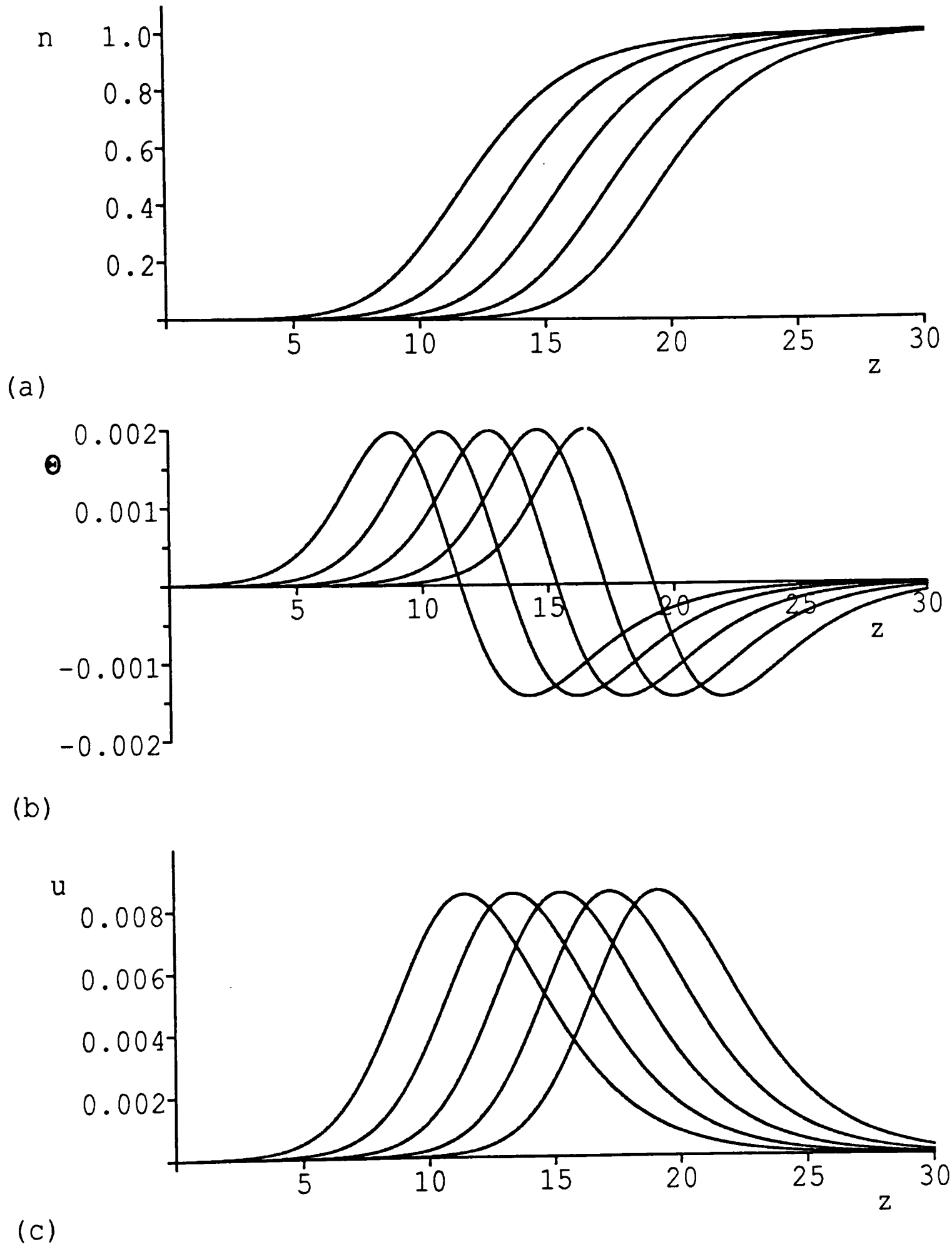

Figure 5.6: Time evolution of the travelling front at intervals of unit time when parameters are as in Example 5.6.2 and initial conditions as in (5.29). The wave velocity, $v = 2.0$, is as predicted by the linear analysis.

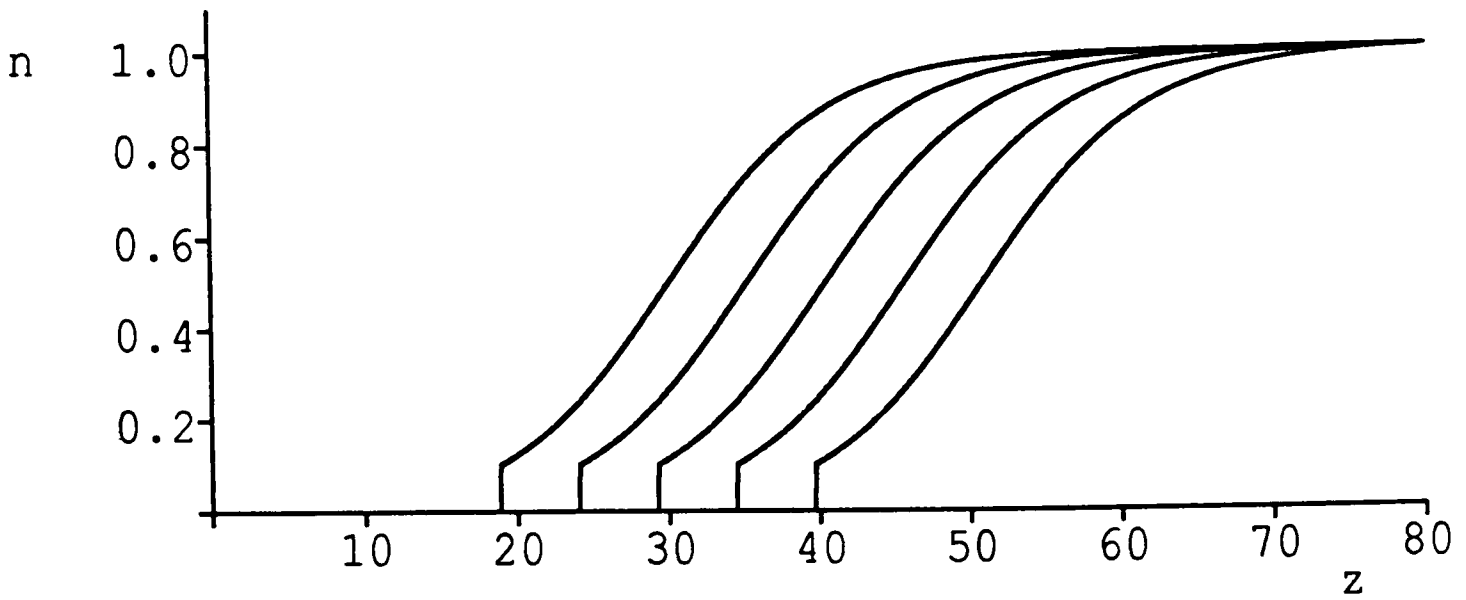

(a)

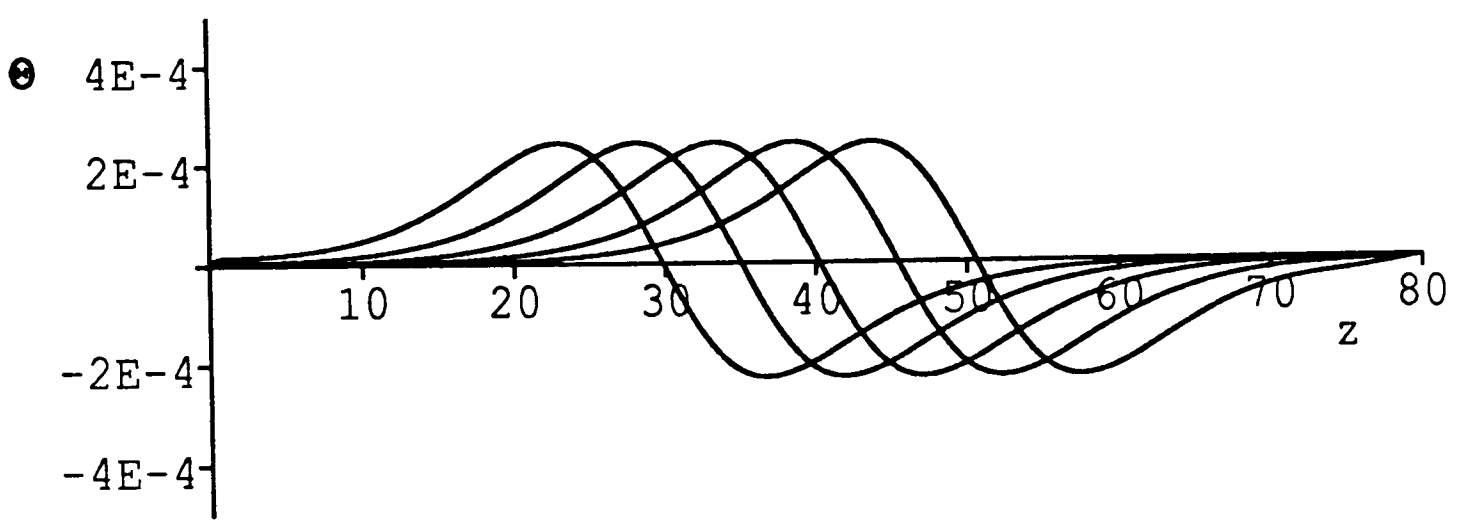

(b)

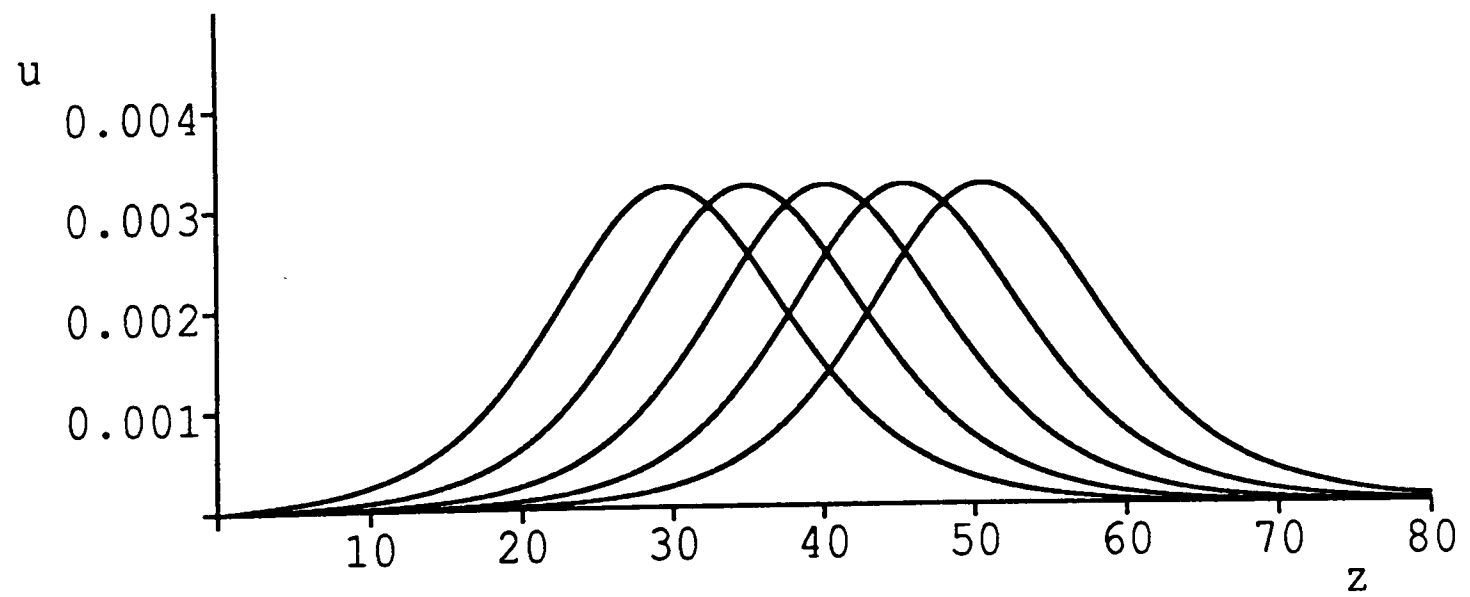

(c)

Figure 5.7: The time evolution of the travelling front at intervals of unit time when parameters are as in Example 5.6.3 and the leading edge of the dermal cell density wave is disturbed. The wave velocity, $v = 5.2$, is as predicted by the linear analysis.

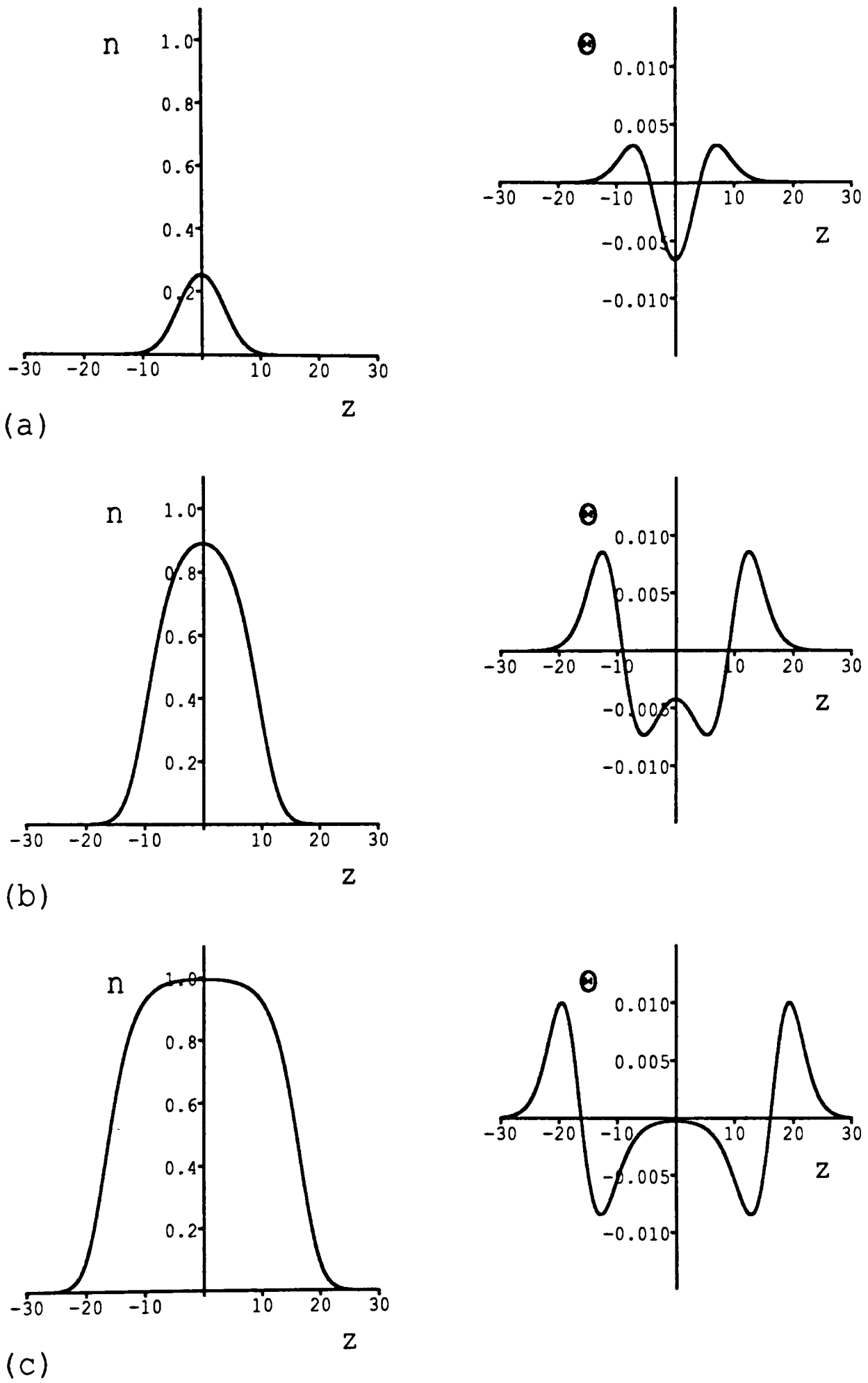

Figure 5.8: The time evolution of fronts travelling in opposite directions, and evolving from an initial hump in dermal cell density at the origin. In (a) $t = 6.0$, (b) $t = 9.5$ and (c) $t = 13.0$. Parameter values and initial conditions are given in Example 5.6.4.

The patterned solutions we have considered in Chapters 3 and 4 evolve synchronously over the relevant domain. However, as we shall explain in the next two chapters, the development of patterns in embryos, is often a *sequential* process. Initially patterns develop in a small localised area on the tissue. These patterns then start to propagate outwards over the rest of the tissue. We investigate here whether the travelling wave solutions considered in this chapter could be precursors to such sequential patterning.

It was demonstrated in Chapters 2 and 3 that, given certain parameters, the system of partial differential equations will evolve from the homogeneous steady state $\theta = 0$, $n = 1$ to steady state patterns. Since the travelling wave solutions connect the solutions from the steady state $\theta = 0$, $n = 0$ to the steady state $\theta = 0$, $n = 1$, under the right conditions, one would expect a bifurcation to spatially heterogeneous patterns as the solution is transformed into the new steady state.

In the last example of this section we show that, given the right circumstances, one-dimensional waves of pattern formation does indeed evolve in the wake of the travelling wave solutions as they progress through the dermal and epithelial layers.

Example 5.6.5: We solved the system (5.1), but so as to bound possible growing patterns we assumed the switch-like form for the epithelial traction function τ, as introduced in Section 1.4 and used in Chapters 3 and 4. We selected the parameter set such that the steady state $\theta = 0$, $n = 1$, is unstable and a bifurcation to spatial pattern occurs, that is

$$\mu = 0.001, \qquad D = 0.1 \qquad \beta = 0.01, \qquad \tau = 9.73, \qquad \hat{\nu} = 3.17,$$

$$\rho = 100.2, \qquad \alpha = 5.0, \qquad \gamma = 0.285, \qquad c = 1.0 \qquad r = 5.0,$$

which has the unstable eigenvalue $k_c^2 = 13^2\pi^2/4$. The parameter values are similar to those used in Example 3.3. Here, however, we have chosen μ slightly smaller so as to increase the growth rate of the patterns (see the discussion in

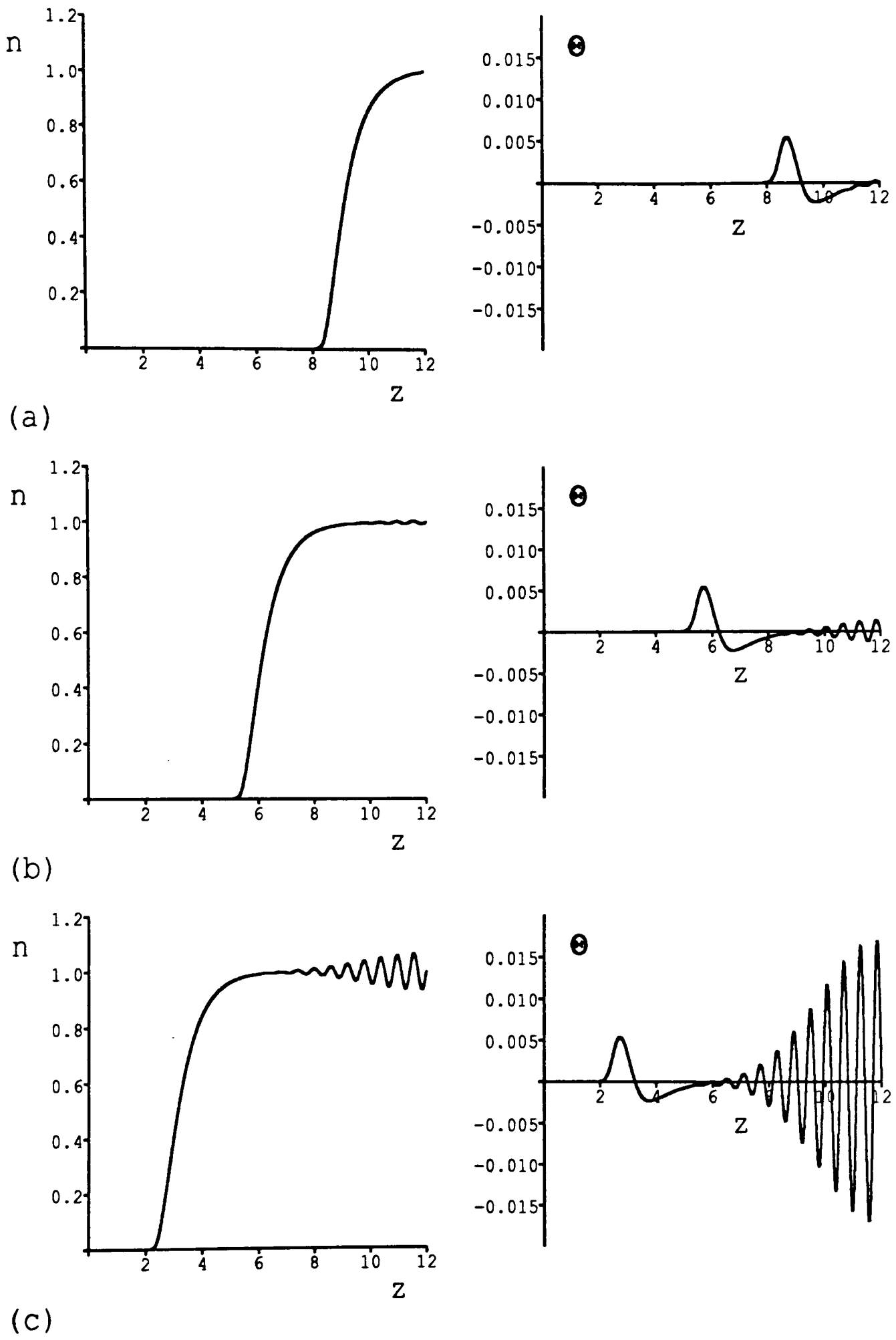

Figure 5.9: The time evolution of travelling wavefronts acting as precursors for pattern formation. In (a) $t = 1.5$, (b) $t = 3.0$ and (c) $t = 4.5$. Parameter values are given in Example 5.6.5.

Section 3.4) and we have decreased our bifurcation parameter γ, even further so as to increase the amplitudes of the resulting patterns.

We solved the equations on a domain $[0, 12]$ with initial conditions

$$n(x, 0) = 0.1\delta(12 - x), \qquad \theta(x, 0) = 0.$$

The results are shown in Figure 5.9. A travelling wave of patterns, with the expected wavenumber, followed behind the travelling wave solutions. When the wave has passed through the domain a steady state pattern similar to that in Figure 3.5, see Example 3.4.3, remains.

Since, as demonstrated in Example 5.5.4, our system can exhibit two travelling waves moving laterally outwards, a wave of pattern formation moving away from a central point can be simulated as well.

Travelling waves of pattern formation in both one- and two-dimensions will be discussed in further detail in Chapters 6 and 7.

Chapter 6

One-Dimensional Sequential Pattern Formation

6.1 Introduction

During morphogenesis, regular patterns of repeated units often develop at a frontier of pattern formation (Zeeman 1974) which moves across the prospective area to transform bland tissue into an array of patterned components. As we have described in Section 1.2 this is indeed the case for chick feather germ initiation. Similar waves of pattern formation also occur, for example, in the development of somites (Pearson & Elsdale 1979), reptilian teeth (Edmund 1969), scales (Maderson 1965a,1965b) and alligator skin patterns (Murray *et al.* 1990).

The various mathematical models for pattern formation in morphogenesis proposed so far (see the references in Chapter 1) are mainly concerned with synchronous patterning. As was demonstrated in Chapters 3 and 4 our tissue interaction model can also account for such synchronous patterning. Here, however, we examine whether sequential pattern formation, so often seen in morphogenesis, can be explained in terms of our tissue interaction model. We restrict ourselves to one-dimensional domains. In the next chapter we shall extend the analysis to two-dimensional domains.

In Section 6.2 we demonstrate that sequential pattern formation could be the result of a small localised disturbance in the tissue which develops into pattern and subsequently propagates through the domain to form a travelling wave of pattern formation.

In Section 6.3 the method of steepest descents is used to find an analytical

approximation for the speed of the spreading pattern in one-dimension when we are in the vicinity of the bifurcation point from homogeneous to patterned solutions. A new method, using *envelope* functions, is proposed in Section 6.4 for obtaining a bound on the speed of the wave of pattern formation. Both these methods give good analytical approximations for the wavespeed. In Section 6.5 we compare them and discuss their relative merits.

6.2 Propagating Patterns

To examine whether our reduced small strain quasi-steady-state tissue interaction model has propagating pattern solutions we extend the ideas recently proposed by Myerscough & Murray (1992) for analysing stripe pigmentation in alligators.

The stripe-like patterns seen on alligators are formed in the early embryonic stages of development. The first stripe to form is the one closest to the head; the rest are formed sequentially towards the tail (Murray *et al.* 1990). There is thus a travelling wave of stripe patterning propagating from the head towards the tail.

Myerscough & Murray (1992) proposed a reaction diffusion-chemotaxis mechanism for describing this sequential patterning in one-dimensional terms. They showed that a wave of pattern formation could be initiated by randomly perturbing the homogeneous linearly unstable steady state in a small localised region of the domain. In this way they were able to determine, by a combination of biological observation and mathematical analysis, the stage of the embryo at which the pattern could reasonably be laid down (in their case this occurs when the embryo is of the order of 9 cm long).

In Chapter 3 we solved our reduced tissue interaction system on an one-dimensional spatial domain. As initial conditions random perturbations about the homogeneous steady states for the dermal cell density n, and the epithelial dilation θ were used. This led to a pattern of peaks and troughs developing

simultaneously across the whole domain. If, however, a perturbation is made in, say, the dermal cell density n, in just one small region on a very large domain, the pattern is generated progressively. In effect the initial conditions as specified in this case give rise to a propagating wave of pattern.

To illustrate this phenomenon we look at two one-dimensional examples of the reduced tissue interaction problem (3.10), with zero-flux boundary conditions as defined in (3.2). To solve the system numerically we again, as in Chapter 3 and 5, made use of NAG FORTRAN routine D03PGF.

Example 6.2.1: Here we select the same parameter set as in Example 3.4.1, with $\epsilon = 0.1$ and consider the problem on the large domain $[0, 30]$. Initially n and θ are set to their homogeneous steady state solution, $\theta = 0$ and $n = 1$, on the whole domain except for a small region at the origin. Here we specify small random perturbations about the uniform steady states. As was expected these perturbations develop into coherent pattern which gradually spreads outwards into the rest of the domain. The result is a travelling wave of pattern formation propagating from the origin towards the other end of the domain. In Figure 6.1 we show how the pattern in dermal cell density progresses with time.

Example 6.2.2: The parameters used here are as in Example 3.4.2, and again $\epsilon = 0.1$. We consider the problem on the domain $[0, 12]$ and instead of perturbing the uniform steady state at the origin we perturb it in a small region in the middle of the domain at $x = 6.0$. Solving the system numerically gave two travelling waves of pattern formation propagating towards the edges of the domain. In Figure 6.2. we show how the waves spread in the epithelial layer.

The results of these two examples correspond to those of Myerscough & Murray's (1992) for a reaction diffusion-chemotaxis model thus confirming that our small strain quasi-steady-state tissue interaction can have propagating pattern solutions.

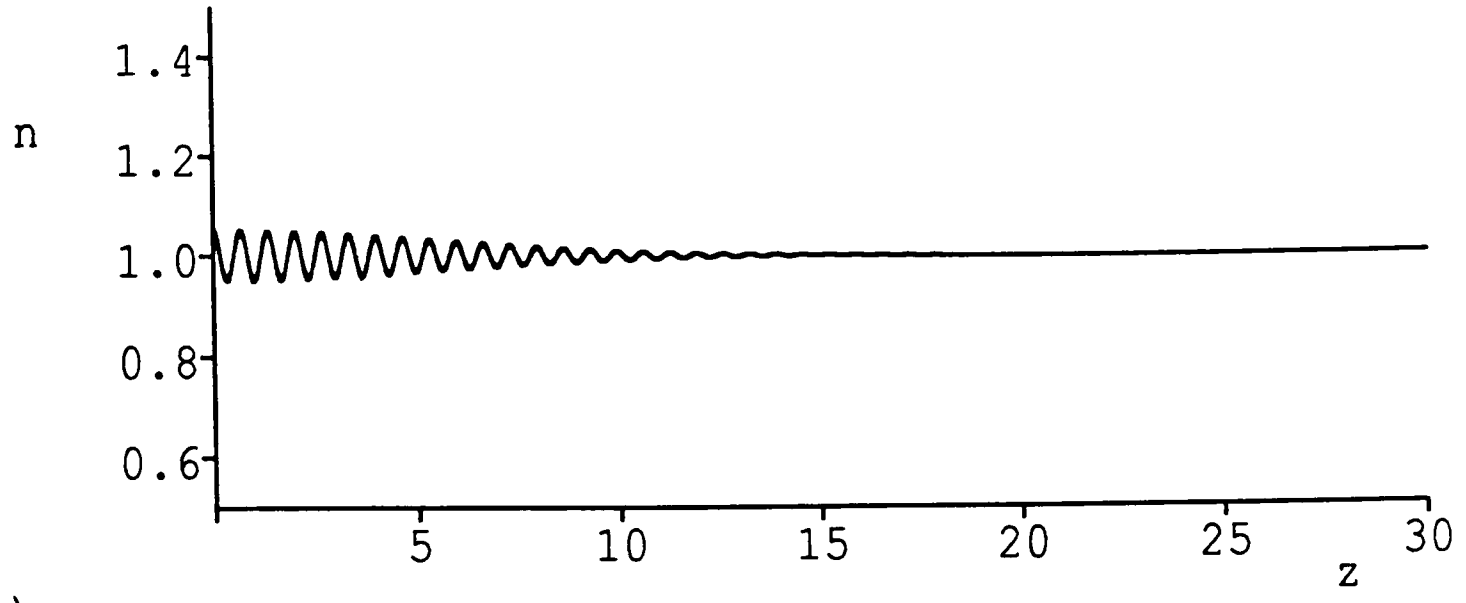

(a)

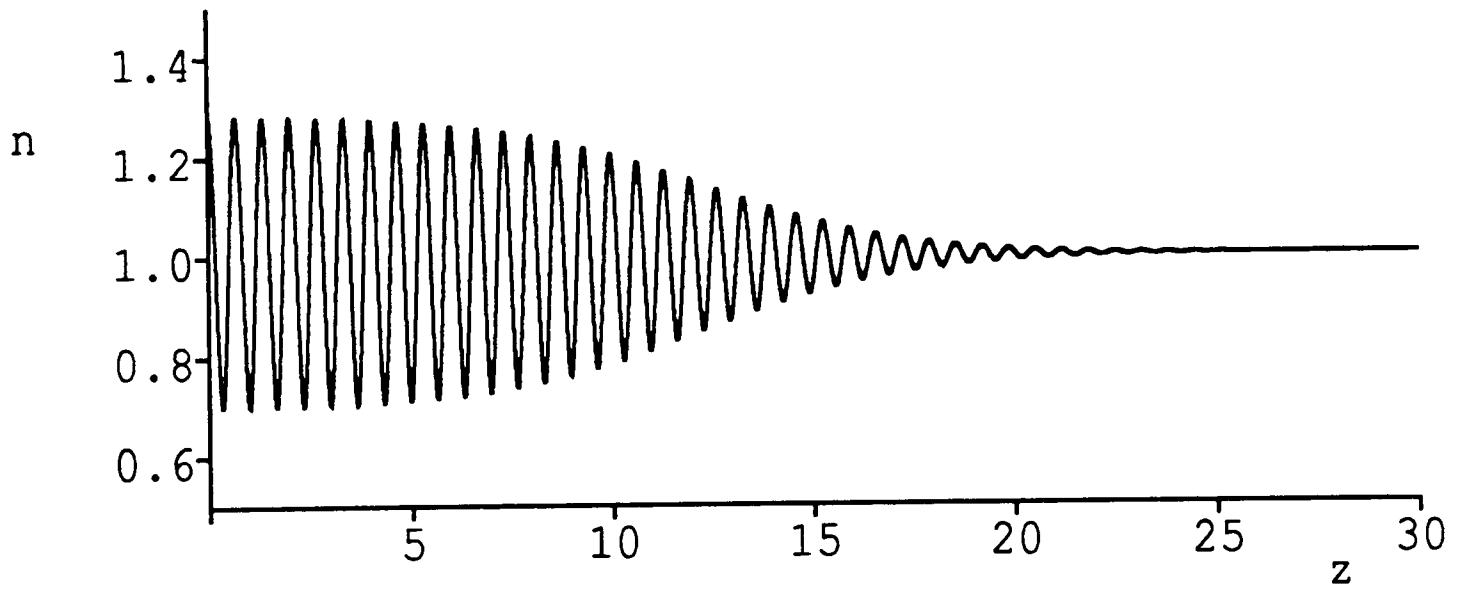

(b)

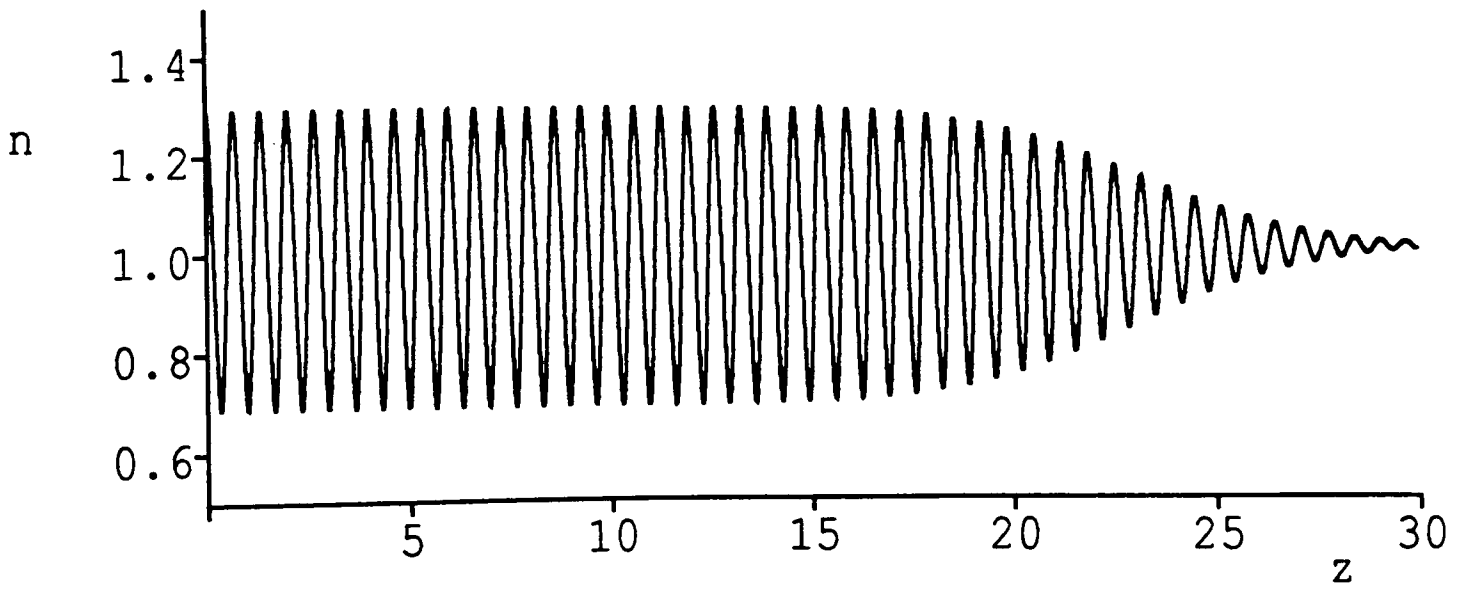

(c)

Figure 6.1: The time evolution of propagating patterns generated from random initial conditions at the origin by solving (3.10) with parameter values as in Example 6.2.1. In (a) $t = 15$, (b) $t = 22$ and (c) $t = 29$.

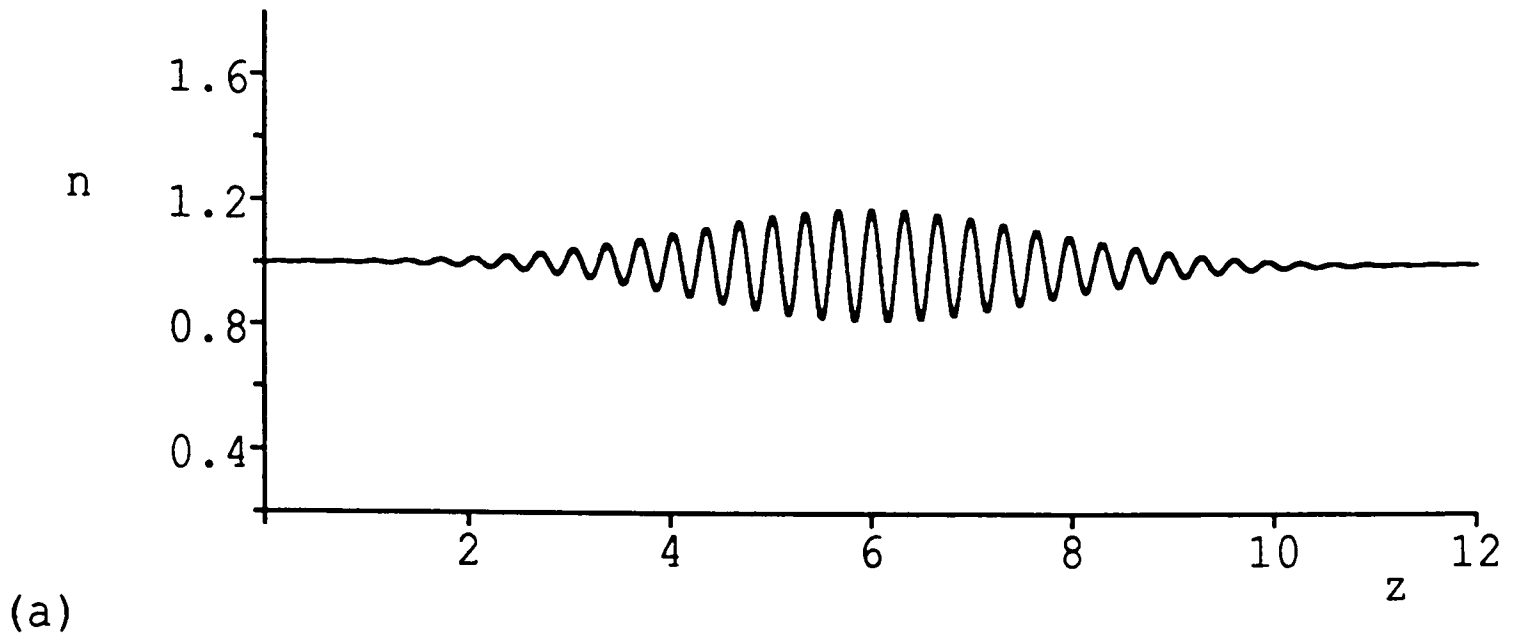

(a)

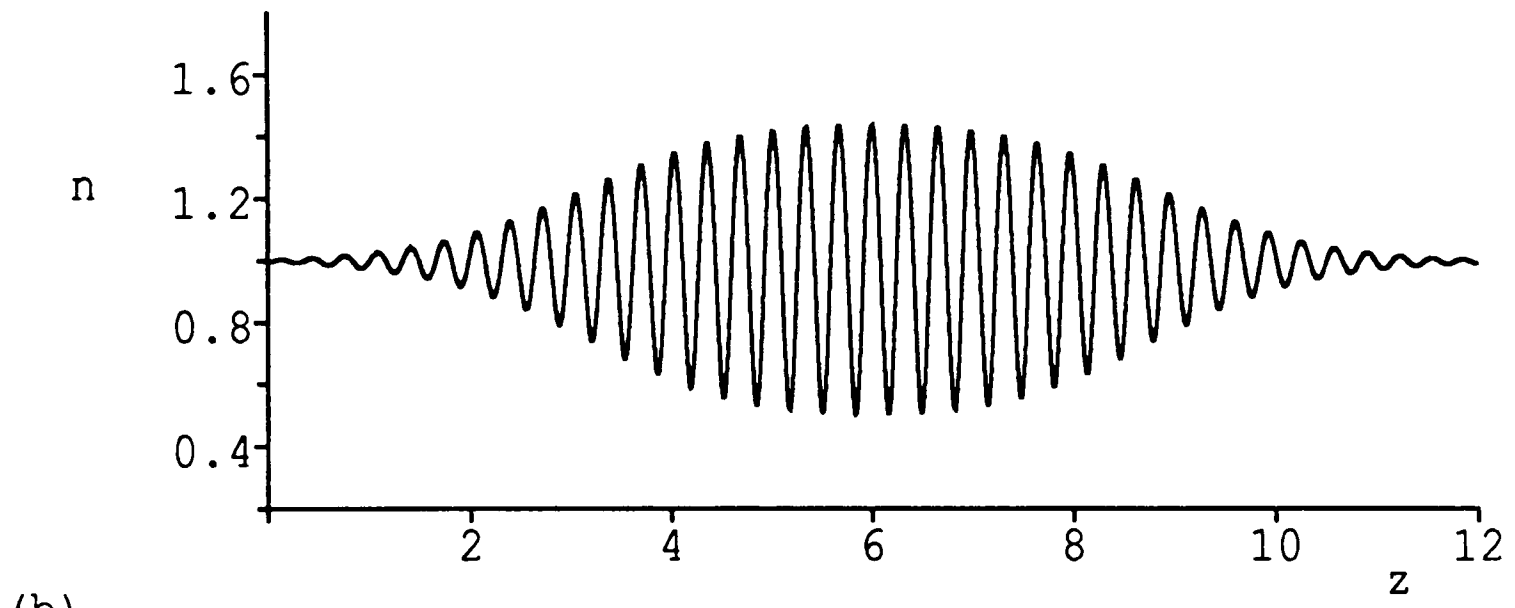

(b)

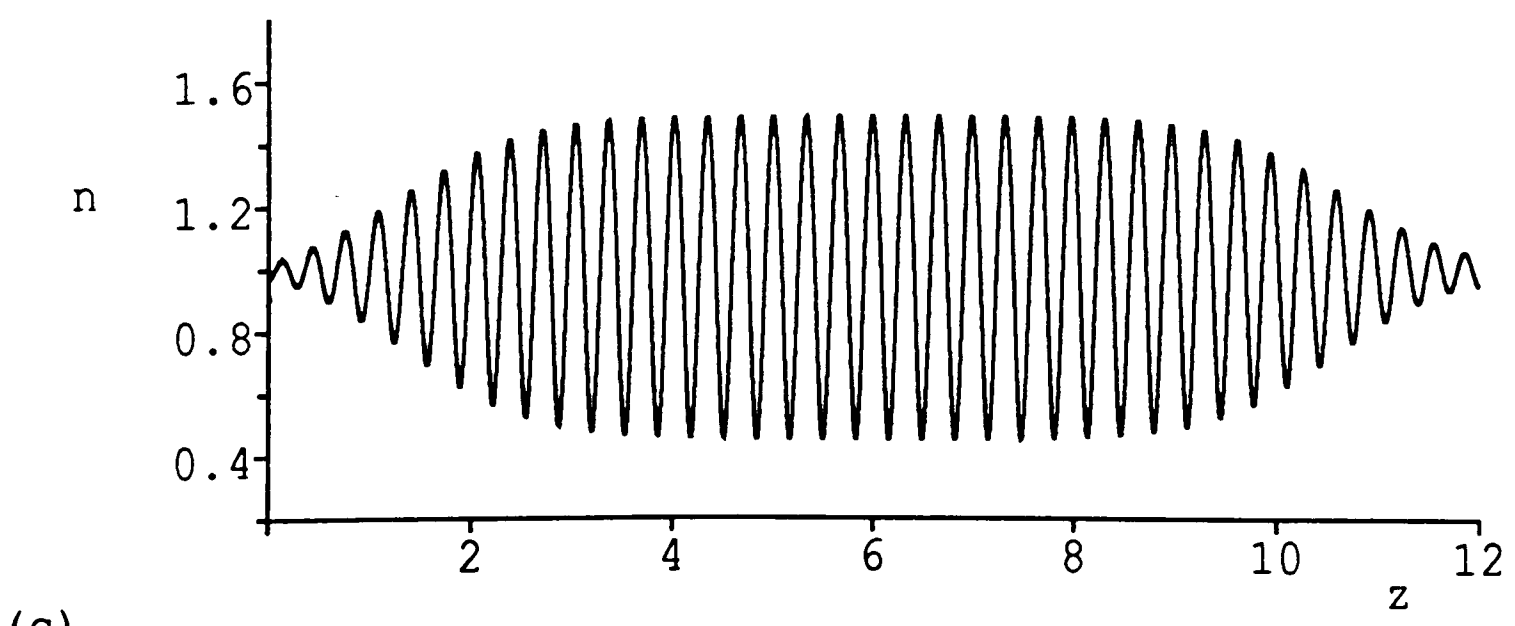

(c)

Figure 6.2: The time evolution of propagating patterns, generated from random initial conditions in a small region in the middle of the domain where $x = 6.0$, by solving (3.10) with parameter values as in Example 6.2.2. In (a) $t = 1.0$, (b) $t = 1.2$ and (c) $t = 1.4$.

6.3 Asymptotic Analysis for Propagating Patterns

In the numerical examples of the previous section we found that, far away from the initial disturbance, the wavelength of the standing pattern and the speed of propagation across the domain are constant and independent of the initial conditions. This motivates us to look for analytical methods to determine expressions for these quantities.

By using an asymptotic method we are able to find approximate analytical expressions for both the wavespeed and wavelength as will be shown in Section 6.3.1. How the wavespeed and wavenumber are related to the linear dispersion relation and some of the model variables is discussed in Section 6.3.2. In Section 6.3.3 numerical examples are given so as to evaluate the accuracy of the approximate results.

6.3.1 The Asymptotic Analysis

We use asymptotic techniques to investigate the spread of pattern across an infinite one-dimensional domain when we are in the vicinity of the bifurcation point to spatially patterned solutions. The method was first used by Dee & Langer (1983) and later used by Myerscough & Murray (1992) for their reaction diffusion-chemotaxis model for alligator stripe pigmentation.

For simplicity the analysis is performed on the reduced small strain quasi-steady-state tissue interaction system (3.10) as was used in the nonlinear bifurcation analysis and numerical simulations of Chapter 3. The analysis for the full small strain quasi-steady-state system is similar. We repeat the reduced system here for convenience,

$$\frac{\partial^2\theta}{\partial x^2} - \beta\frac{\partial^4\theta}{\partial x^4} + \tau\frac{\partial^2}{\partial x^2}\frac{n^2}{[1+\hat{\nu}(1-\theta)]^2 + cn^2} = \rho\theta, \tag{6.1a}$$

$$\frac{\partial n}{\partial t} = -\alpha\frac{\partial}{\partial x}\left\{n\frac{\partial}{\partial x}\left(\frac{1-\theta}{1+\gamma n}\right)\right\}, \tag{6.1b}$$

for which we have calculated the dispersion relation as

$$\lambda(k^2) = -\frac{\beta Q_1 k^6 - (P_2 Q_2 - P_1 Q_1 - Q_1)k^4 + \rho Q_1 k^2}{\beta k^4 + (P_1 + 1)k^2 + \rho}, \tag{6.2}$$

(see expression (2.18)).

We consider the behaviour of the propagating pattern close to its leading edge. Here the amplitude of the pattern is still small and we can therefore approximate its growth by the linear dispersion relation (6.2). Using this linear approximation the solution at the leading edge can be written as the integral of Fourier modes,

$$\begin{pmatrix} \theta(x,t) \\ n(x,t) \end{pmatrix} = \begin{pmatrix} 0 \\ 1 \end{pmatrix} + \int_{-\infty}^{\infty} p_f(k) \begin{pmatrix} 1 \\ M(k^2) \end{pmatrix} e^{ikx + \lambda(k^2)t} dk. \tag{6.3}$$

As we shall see, the specific form of the functions

$$M(k^2) = \frac{-Q_2 k^2}{\lambda(k^2) + Q_1 k^2},$$

determined from the linear analysis of Section 2.5, and $p_f(k)$, determined by a Fourier transform of the initial conditions at the leading edge, do not concern us here.

As one follows the leading edge of the disturbance as it propagates across the domain, the integral (6.3) remains valid. We therefore consider this integral at the leading edge by making the substitution $x = vt$, where v is the fixed positive propagation rate. Thus we are assuming that the developing pattern is sufficiently far away from the initial point of disturbance for v to be constant. We are concerned with patterns travelling in the positive x-direction.

The above equation (6.3) can now be written as

$$\begin{pmatrix} \theta(vt,t) \\ n(vt,t) \end{pmatrix} = \begin{pmatrix} 0 \\ 1 \end{pmatrix} + \int_{-\infty}^{\infty} p_f(k) \begin{pmatrix} 1 \\ M(k^2) \end{pmatrix} e^{tg(k)} dk \tag{6.4}$$

where

$$g(k) = ikv + \lambda(k^2).$$

To obtain an approximation for the wavespeed v, which we assume to be $O(1)$, we evaluate the integral (6.4) asymptotically for large t and hence large

x. We do this by using the method of steepest descents (see Murray 1984) in which (6.4) is considered as a contour integral in the complex k-plane. The method of steepest descents entails the deformation of the present contour, say C, to a contour C^*, so that it passes through the saddle points of $g(k)$, which are given by the solutions of

$$\frac{dg}{dk} = iv + \frac{d\lambda}{dk} = 0. \tag{6.5}$$

The complicated nature of our dispersion relation means that the procedure, as described in the rest of this section, gives rise to an extremely involved set of equations from which it is analytically impossible to extract the necessary information. Myerscough & Murray (1992) had similar difficulties with the dispersion relation obtained from their model. To circumvent this they used a simple caricature dispersion relation encapsulating the basic features of the full dispersion relation. As they were successful in obtaining some good results and insight into the pattern propagation, we employ a similar method here.

Generally the systems of partial differential equations which give rise to pattern formation have parabolic-type dispersion relations. As caricature dispersion relation we therefore use the simplest form that encapsulates this feature, namely the parabolic equation

$$\sigma(k^2) = -pk^4 + qk^2 - r, \tag{6.6}$$

where p, q and r are all positive. Although the dispersion relation of our tissue interaction model (6.2) is not purely of the *parabolic-type* and has two turning points instead of one (see Figure 2.4(b)) we show that the above caricature version can still be used with success. How we fit the caricature dispersion relation $\sigma(k^2)$, to the full one, $\lambda(k^2)$, shall be explained later.

Substituting (6.6) into our saddle point equation (6.5) we have

$$iv - 4pk^3 + 2qk = 0. \tag{6.7}$$

Solving for k, which is now complex, gives three saddle points

$$k_0 = iy_0, \qquad k_{\pm 1} = \pm x_1 + iy_1, \tag{6.8}$$

where

$$\begin{aligned} v + 4py_0^3 + 2qy_0 &= 0, && \text{(6.9a)} \\ \frac{q}{2p} - x_1^2 + 3y_1^2 &= 0, \qquad x_1 > 0, && \text{(6.9b)} \\ v - 32py_1^3 - 4qy_1 &= 0. && \text{(6.9c)} \end{aligned}$$

Since the cubic equations for y_0 and y_1 have no turning points (Descarte's rule of signs) each of the above equations (6.9) has only one real root.

Following the method of steepest descent, we must now deform the contour C, which runs along the positive real axis in the complex k-plane, to a contour C^*, which runs through a saddle point, along a path of steepest descent. The curves of steepest descent have constant imaginary parts and on these curves $e^{g(k)t}$ attains its maximum value at the saddle points. As we have three possible saddle points we must determine which will give the dominant contribution.

We first consider the saddle $k_0 = iy_0$. The curves of constant imaginary part which pass through this saddle are

$$x = 0, \qquad v + 4py^3 + 2qy - 4px^2y = 0. \tag{6.10}$$

On the curve $x = 0$,

$$\frac{d^2\Re g(k)}{dy^2} = -12py^2 - q < 0$$

and hence $\Re g(k)$ has a maximum on $x = 0$. So $x = 0$ is the curve of steepest descent.

Consider the saddles at $k_{\pm 1}$. The two curves of constant imaginary part at each saddle are solutions to

$$f_\pm(x, y) = \Im g(k) - \Im g(k_{\pm 1}) = 0. \tag{6.11}$$

So as to find the curves of steepest descent at these saddle points we also define

$$h_\pm(x, y) = \Re g(k) - \Re g(k_{\pm 1}). \tag{6.12}$$

To see the approximate position of the curves of constant imaginary part and to find which are the curves of steepest descent we expand $f_\pm$ and $g_\pm$ as Taylor

series about the saddle points $k_{\pm 1}$. We set $x = \pm x_1 + \delta x$ and $y = \pm y_1 + \delta y$, where $|\delta x| \ll 1$ and $|\delta y| \ll 1$. We know that $f_\pm$ and $h_\pm$ and their first derivatives are zero at the saddle point. Using this and the Cauchy-Riemann conditions our Taylor series expansions become

$$\begin{aligned} f_\pm(x,y) &= \frac{1}{2}\frac{\partial^2}{\partial x^2}\Im g(\pm x_1, y_1)\{(\delta x)^2 - (\delta y)^2\} \\ &\quad + \frac{\partial^2}{\partial x^2}\Re g(\pm x_1, y_1)\, \delta x\, \delta y + O((\delta x)^3, (\delta y)^3), \\ h_\pm(x,y) &= \frac{1}{2}\frac{\partial^2}{\partial x^2}\Re g(\pm x_1, y_1)\{(\delta x)^2 - (\delta y)^2\} \\ &\quad - \frac{\partial^2}{\partial x^2}\Im g(\pm x_1, y_1)\, \delta x\, \delta y + O((\delta x)^3, (\delta y)^3), \end{aligned}$$

where

$$\begin{aligned} \frac{\partial^2}{\partial x^2}\Im g(\pm x_1, y_1) &= \mp 24 p x_1 y_1, \\ \frac{\partial^2}{\partial x^2}\Re g(\pm x_1, y_1) &= -4q - 24 p y_1^2. \end{aligned}$$

To estimate how the curves of constant imaginary part approach the saddles $\pm x_1 + i y_1$, and to determine which are the curves of steepest descent, we examine the signs of $f_\pm(x,y)$ and $g_\pm(x,y)$ by setting δx and δy to various values. The three saddles, the contours of the surface generated by $\Re g(k)$ and the curves of steepest descent are illustrated in Figure 6.3.

The original contour C must now be deformed so that it passes through the saddle points of $g(k)$. However, we see that C cannot be deformed so that it passes through the saddle point $k = iy_0$, since the resulting contour cannot return to the real axis unless $\Re g(k) > \Re g(iy_0)$ for some k. This contradicts the basic assumption that the maximum of $\Re g(k)$, along the contour, is obtained at the saddle points. At the other two saddle points we have that $\Re g(k_{-1}) = \Re g(k_{+1})$. So, to obtain the new contour C^* as illustrated in Figure 6.3, we must deform the contour over both these saddle points

For deforming C to C^* we introduce the real variables φ and ϱ so that

$$\begin{aligned} g(k) - g(k_{+1}) &= -\varphi^2, \\ g(k) - g(k_{-1}) &= -\varrho^2 \end{aligned}$$

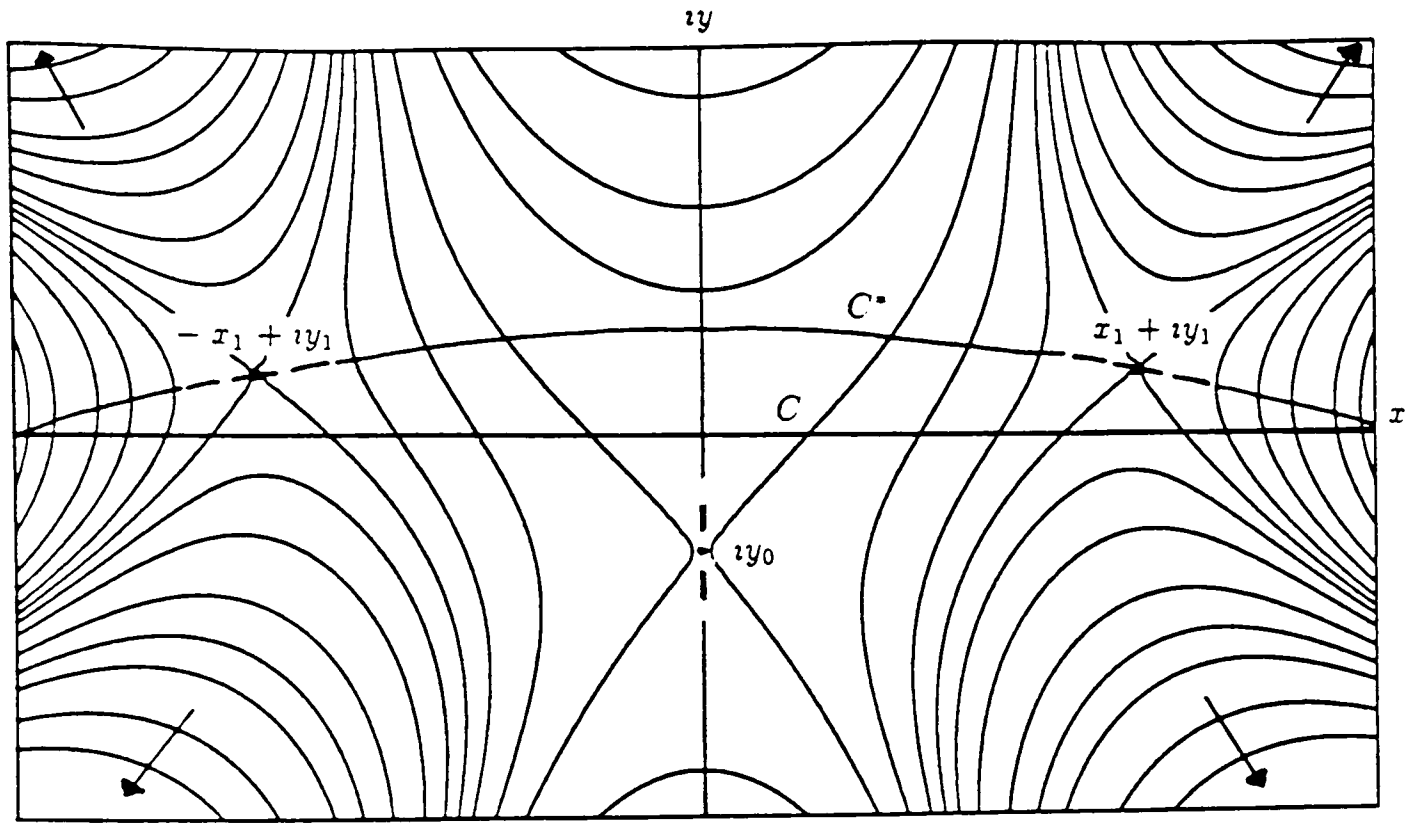

Figure 6.3: The contour map of the surface $\Re g(k)$ near the saddle points. The arrows show the direction of increasing $\Re g(k)$, the broken lines are the paths of steepest descent, C is the original contour and C^* is the new contour.

where k is close to either k_{+1} or k_{-1} and on C^*.

Our equation (6.4) now becomes

$$\begin{pmatrix} \theta(vt,t) \\ n(vt,t) \end{pmatrix} = \begin{pmatrix} 0 \\ 1 \end{pmatrix} + e^{tg(k_{+1})} \int_{\varphi_1}^{\varphi_2} p_f(k(\varphi)) \begin{pmatrix} 1 \\ M(k^2(\varphi)) \end{pmatrix} e^{-t\varphi^2} \frac{dk}{d\varphi} d\varphi + e^{tg(k_{-1})} \int_{\varrho_1}^{\varrho_2} p_f(k(\varphi)) \begin{pmatrix} 1 \\ M(k^2(\varphi)) \end{pmatrix} e^{-t\varrho^2} \frac{dk}{d\varrho} d\varrho,$$

with φ_1, φ_2, ϱ_1 and ϱ_2 the transformed endpoints. Using Watson's Lemma (Murray 1984) we evaluate the integrals asymptotically for large t to find

$$\begin{pmatrix} \theta(vt,t) \\ n(vt,t) \end{pmatrix} \approx \begin{pmatrix} 0 \\ 1 \end{pmatrix} + \boldsymbol{J}_\varphi e^{tg(k_{+1})} + \boldsymbol{J}_\varrho e^{tg(k_{-1})} + O(\frac{e^{tg(k_{+1})}}{t}, \frac{e^{tg(k_{-1})}}{t}), \quad (6.13)$$

where $\boldsymbol{J}_\varphi$ and $\boldsymbol{J}_\varrho$ are the approximations of the respective integrals to $O(1)$.

We observed in the numerical simulations of Section 6.2 that the amplitude of the pattern, viewed in the moving frame of the travelling wave, remains constant when we are sufficiently far away from the initial disturbance. The real value of the asymptotic solution (6.13) is therefore always constant for all

time, so that we can hypothesize a restriction on $g(k)$ of the form

$$\Re g(k_{\pm 1}) = 0.$$

Hence we obtain

$$-vy_1 - p(x_1^4 - 6x_1^2y_1^2 + y_1^4) + q(x_1^2 - y_1^2) - r = 0. \tag{6.14}$$

Using (6.9b), (6.9c) and (6.14) we find

$$x_1^2 = \frac{1}{8p}\left(3q + \sqrt{7q^2 - 24pr}\right), \tag{6.15a}$$

$$y_1^2 = \frac{1}{24p}\left(-q + \sqrt{7q^2 - 24pr}\right), \tag{6.15b}$$

$$v = \frac{4}{3}y_1\left(2q + \sqrt{7q^2 - 24pr}\right). \tag{6.15c}$$

The value of $x_1 = |\Re k_{\pm 1}|$ gives the wavenumber at the leading edge of the disturbance and v gives the rate of spread of the disturbance. For the caricature dispersion relation (6.6) to have unstable eigenvalues we require that

$$q^2 - 4pr > 0, \tag{6.16}$$

so that x_1^2, y_1^2 and v will therefore always be positive.

If we consider the pattern in the moving frame of the developing wave we observe that an oscillating pattern originates at the leading edge. The frequency at which this pattern oscillates is

$$\Omega = \Im g(k_{\pm 1}),$$

which is also the frequency at which new nodes are created at the front of the envelope. We assume that nodes are conserved so that Ω is also the frequency of oscillation far from the leading edge of the disturbance in the moving frame of the envelope.

Assume that k^* is the wavenumber of the pattern far from the leading edge so that $\Omega = k^*v$. Thus

$$k^* = x_1\left(1 - \frac{8py_1^3}{v}\right), \tag{6.17}$$

gives the wavenumber of the standing pattern far behind the leading edge of the disturbance.

6.3.2 The Dispersion Relation and Propagating Patterns

Above, we have found expressions for the wavespeed v, and wavenumbers k and k^* in terms of the parameters p, q and r of our caricature dispersion relation $\sigma(k^2)$. To get a qualitative understanding of how the actual parameters of the system are related to the wavespeed and wavenumber of the developing pattern we now examine how the shape and position of our caricature dispersion relation (6.6) affects the spreading pattern.

Since the caricature dispersion relation is a caricature for the dispersion relations of all pattern formation systems with parabolic-type dispersion relations, the information we gain here has therefore a much wider applicability than only our tissue interaction model — we obtain a better intuitive understanding of spreading pattern formation in general.

We begin by examining how the wavespeed of the propagating pattern is affected by increasing the magnitude of the positive function values of the caricature dispersion relation $\sigma(k^2)$ (see Figure 6.4(a)). We do this by multiplying each of the parameters p, q and r by a scaling factor s. As s becomes larger than one, the unstable eigenvalues *become even more unstable.* Using (6.15c) we find that

$$v(s) = s(4q_1y_1 + 32py_1^3),$$

and so, as s increases, the wavespeed v increases. This is what one would have expected, since as the dispersion relation becomes more positive, the initial growth rate increases and therefore the pattern is laid down quicker. However, from (6.15a) it follows that the wavenumber at the leading edge stays fixed.

Secondly, we decrease the range of unstable eigenvalues, while keeping both the turning point and the maximum value of $\sigma(k^2)$ constant (see Figure 6.4(b)). We do this by again multiplying q and p with a scaling factor s and by replacing r with $r + (s-1)q^2/(4p)$. By increasing s from 1 to ∞, the range of unstable

eigenvalues contracts. We now find that

$$v^2(s) = \frac{2}{27p}\left[\left(7q^2 - 24pr\right)\sqrt{s(sq^2 + 6q^2 - 24pr)} + 18sq(q^2 - 4pr) - s^2q^3\right],$$

so that

$$\begin{aligned}\frac{dv^2}{ds} &= \frac{2}{27p}\left\{18q(q^2 - 4pr) + \frac{9sq^2(q^2 - 4pr) + 18q(q^2 - 4pr)^2}{[s^2q^2 + 6s(q^2 - 4pr)]^{\frac{1}{2}}}\right. \\ &\quad \left. + 2q^2\{[s^2q^2 + 6s(q^2 - 4pr)]^{\frac{1}{2}} - sq\}\right\},\end{aligned}$$

which is positive for $s > 1$, because of inequality (6.16). Thus as the range of unstable eigenvalues contracts the wavespeed v increases. On the other hand one can easily show from (6.15a) that the wavenumber at the leading edge decreases as s increases.

Shifting the dispersion relation in the positive k^2 direction, without a shape change (see Figure 6.4(c)) not only influences the wavenumber of the spreading pattern, but also affects the wavespeed. We displace the graph by s units in the positive k^2 direction by substituting $2ps + q$ into q and $ps^2 + qs + r$ into r, so that

$$\begin{aligned}v^2(s) &= \frac{2}{27p}\left\{-8s^3p^3 - 12qp^2s^2 + 30q^2ps - 144p^2rs\right. \\ &\quad \left. + 17q^3 - 72qpr + (4s^2p^2 + 4pqs + 7q^2 - 24pr)^{\frac{3}{2}}\right\}.\end{aligned}$$

We now prove that $v^2(s)$ is monotonic increasing for $|s| \ll 1$. It is easy to calculate that

$$\frac{dv^2}{ds}|_{s=0} = \frac{2}{27p}\left\{36p(q^2 - 4pr) + 6pq[q^2 + 6(q^2 - 24pr)]^{\frac{1}{2}} - 6pq^2\right\},$$

which is always positive. Since, for any value of s there exist parameters p^*, q^* and r^* such that

$$v(p, q, r, s) = v(p^*, q^*, r^*, 0),$$

it follows that $v^2(s)$ is monotonic increasing in s. So the wavespeed becomes larger as the unstable eigenvalue, and thus the wavenumber, increases in value. As expected, the wavenumber at the leading edge also increases with increasing s, since

$$x_1^2 = \frac{1}{8p}\left[6ps + 3q + (4p^2s^2 + 4qps + 7q^2 - 24pr)^{\frac{1}{2}}\right].$$

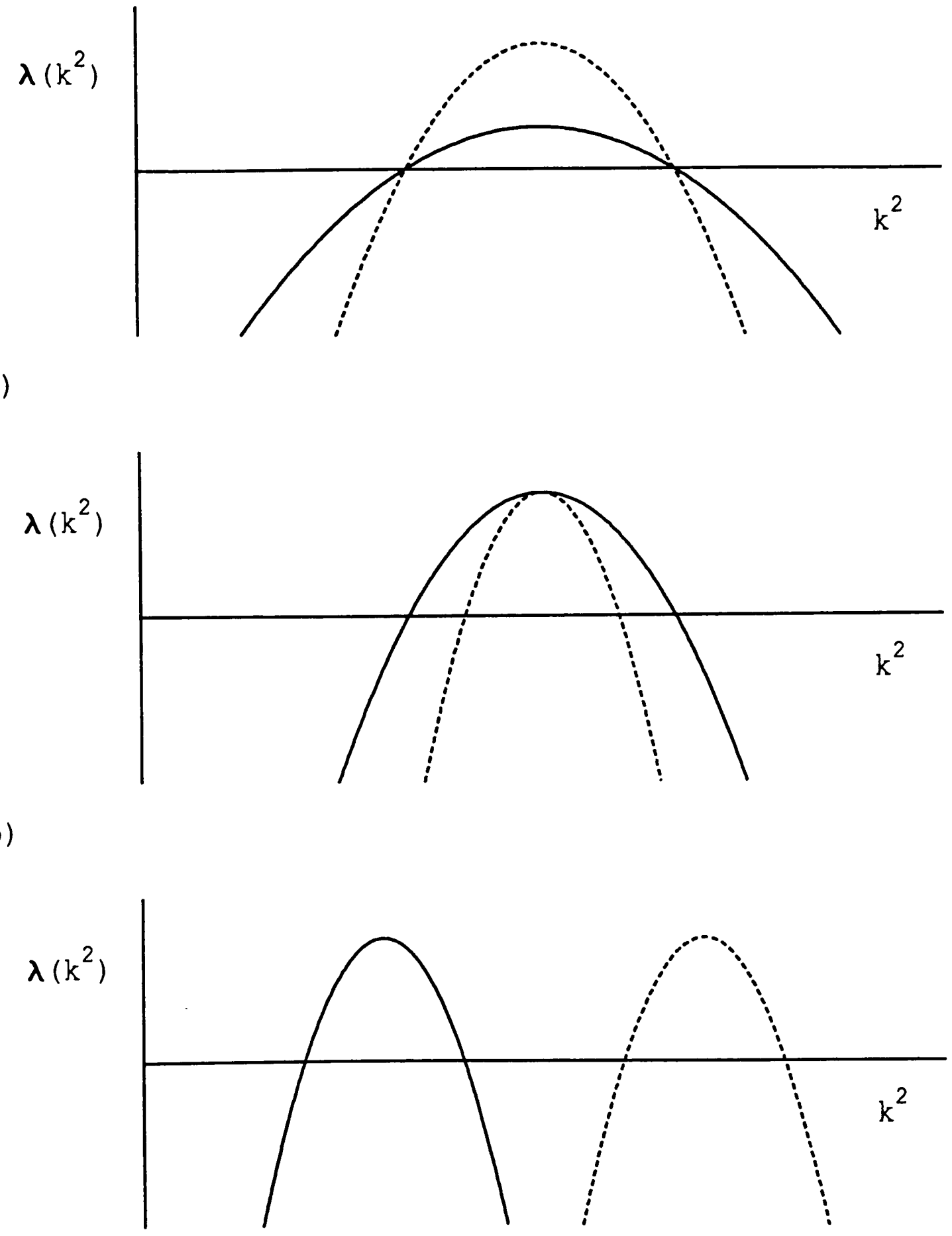

Figure 6.4: Transformations of a dispersion relation (solid line) to a new one (broken line). (a) The magnitude of the dispersion relation is increased in the region of the unstable eigenvalues, thus increasing the linear growth rate of the solution. (b) The range of unstable eigenvalues is decreased. (c) The dispersion relation is shifted in the positive k^2-direction.

We now have a qualitative idea of how the caricature dispersion relation relates to the wavespeed and wavenumber of the propagating pattern. More specifically, we would like to establish the qualitative dependence of the speed and wavenumber on the individual parameters appearing in the full dispersion relation (6.2) of the spreading pattern.

By referring to our linear expressions reflecting the tissue interaction mechanism, that is Q_1, Q_2, P_1 and P_2 as given in expressions (2.13), it is easy to see that both the chemotactic factor α, and the chemical production rate k_e, could act as scaling parameters. By increasing the value of either of these the linear growth rate of the solution is increased (see Figure 6.4(a)) and so, as shown in the above analysis, the wavespeed v increases. However, a similar change to any other model parameter leads to a combination of changes to the caricature dispersion relation so that it is difficult to relate such a parameter directly to the wavespeed and wavenumber of the propagating pattern.

6.3.3 Numerical Examples

We now look at some specific examples so as to evaluate the utility and accuracy of the asymptotic method. However, before we can do any calculations, we have to describe the method used for fitting our caricature dispersion relation $\sigma(k^2)$ to the actual dispersion relation $\lambda(k^2)$.

As we are approximating a relatively complicated function with a simple parabola, we do not expect a particularly close fit and some error will arise regardless of how the fitting is done. Myerscough & Murray (1992) showed in their work that the fitting method used is not crucial to the results obtained. We use here a Chebyshev least squares method (see, for example, Atkinson 1978) to approximate the function $\lambda(k^2)$.

Since only the positive values of the dispersion relation $\lambda(k^2)$ contribute to the integral in (6.4) when it is evaluated asymptotically for large t, we focus on the domain where $\lambda(k^2)$ is non-negative. The exact form of the caricature

dispersion relation is not so important in the regions where the dispersion relation is negative as long as it has the correct sign. We use NAG FORTRAN routine C05ADF to find the two roots of the dispersion relation $\lambda(k^2)$ so as to determine the region over which the function is non-negative. The routine combines the methods of bisection, linear interpolation and linear extrapolation to find a sufficiently small domain in which the root lies.

The full dispersion relation (6.2) is transformed from the domain on which it is non-negative (excluding the point $k = 0$) to the domain $[-1, 1]$, on which the Chebyshev polynomials are defined. On this domain it is denoted by $\tilde{\lambda}(k^2)$. The caricature dispersion relation transformed to $[-1, 1]$ is given by

$$\tilde{\sigma}(k^2) = -\tilde{p}k^4 + \tilde{q}k^2 - \tilde{r}.$$

To fit this transformed caricature dispersion relation $\tilde{\sigma}(k^2)$, to the full transformed dispersion relation $\tilde{\lambda}(k^2)$, via the Chebyshev least squares approximation, we calculate the values

$$\begin{aligned}
\tilde{r} &= -\frac{1}{\pi}\int_{-1}^{1} \frac{\tilde{\lambda}(k^2)}{\sqrt{1-k^4}}\, dk^2, \\
\tilde{q} &= \frac{2}{\pi}\int_{-1}^{1} \frac{\tilde{\lambda}(k^2)k^2}{\sqrt{1-k^4}}\, dk^2, \\
\tilde{p} &= -\frac{4}{\pi}\int_{-1}^{1} \frac{\tilde{\lambda}(k^2)(2k^4-1)}{\sqrt{1-k^4}}\, dk^2.
\end{aligned}$$

After making the substitution $k^2 = \cos\phi$ to get rid of the singularities at the end points, we evaluated the integrals numerically using NAG FORTRAN routine D01BDF which uses the Gaussian quadrature method. Subsequently the function $\tilde{\sigma}(k^2)$ is transformed back to its original domain to become $\sigma(k^2)$. Since $\sigma(k^2)$ will be negative everywhere $\lambda(k^2)$ is negative, we can use it on the whole real line as the caricature dispersion relation.

The asymptotic method we use for finding the wavespeed depends on the linear behaviour of the system close to the leading edge of the disturbance and the implicit assumption that our system is only weakly nonlinear in this region. This, and the fact that we are using a caricature dispersion relation rather than the actual one, will cause an error in the predicted values.

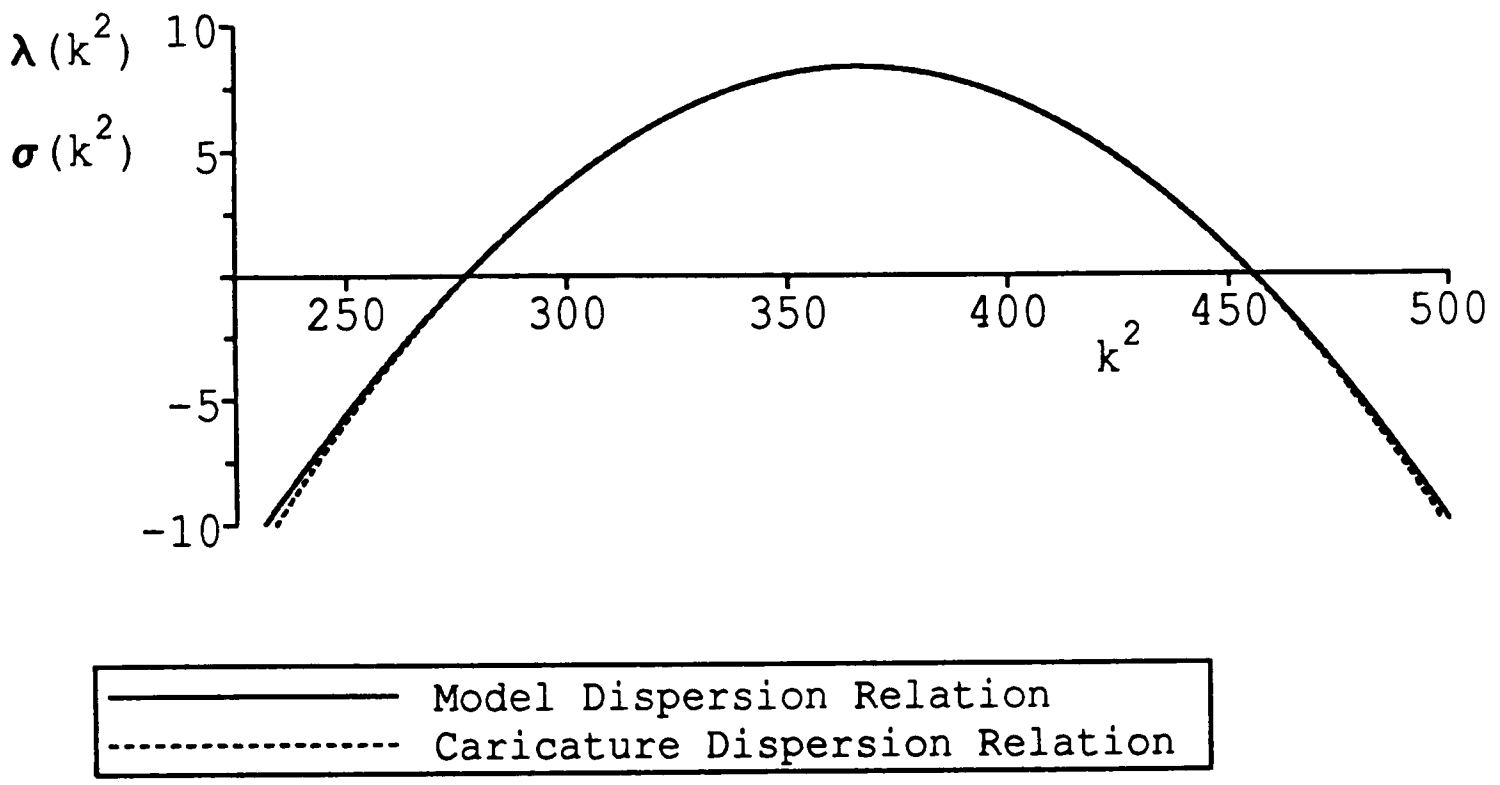

Figure 6.5: The caricature dispersion relation $\sigma(k^2)$, see (6.6), is fitted to the actual dispersion relation $\lambda(k^2)$, see (6.2). The parameters are as in Example 6.3.1.

In the asymptotic analysis it is also assumed that there is only one unstable eigenvalue. This would be a valid assumption when we are sufficiently close to the bifurcation point. However, as one moves away from the bifurcation point the range of unstable eigenvalues increases and so a combination of modes evolves instead of only one isolated mode.. The approximate results of the asymptotic method will therefore become less accurate.

We now show a specific example where we compare the predicted wavespeed and wavenumbers to those obtained numerically. As in the previous section NAG FORTRAN routine D03PGF was used.

Example 6.3.1: We used the same parameter set as in Example 6.2.2 and examined the problem for three different values of ϵ, $\epsilon = 0.01, 0.1, 0.25$. In each case we fitted our caricature dispersion relation to our full dispersion relation according to the method described above. In Figure 6.5 we show how close the fit is if $\epsilon = 0.1$. Using expressions (6.15c), (6.15a) and (6.17) respectively we

	Wavespeed, c	Wavenumber, k	Wavenumber, k^*
$\epsilon = 0.01$			
Numerical	0.70	6.0π	6.0π
Analytical	0.69	6.0π	6.0π
$\epsilon = 0.1$			
Numerical	7.12	6.1π	6.1π
Analytical	7.17	6.1π	6.2π
$\epsilon = 0.25$			
Numerical	21.5	6.7π	7.7π
Analytical	20.9	6.9π	7.2π

Table 6.1: The approximate wavespeed and wavenumbers as found by the asymptotic method is compared to the values obtained from the numerical simulations for different values of ϵ. The model parameters are as in Example 6.3.1.

calculated the analytical predictions for the wavespeed and wavenumber in each case. The results are summarized in Table 6.1. As was expected, the smaller the value of ϵ, or in other words the closer we are to the bifurcation point, the better the agreement between the analytical and the numerical results.

We also carried out these calculations with parameter values as in Example 6.2.1 and likewise obtained very good agreement between the approximate and numerical wavespeeds. (The results are shown in Table 6.2, see Section 6.5)

Thus the asymptotic method we presented above does give an useful estimate of the speed of propagation and the wavelength of the final pattern. We shall discuss the merits of this method in more detail in Section 6.5.

6.4 Envelope Technique for Propagating Pattern Analysis

We propose here a new and different method for determining the wavespeed of propagating patterns, valid in the vicinity of the bifurcation point from homogeneous steady state solutions to patterned steady state solutions. We again examine our system on an infinite spatial domain.

By connecting those peaks of the evolving cell density and cell dilation patterns which are above the homogeneous steady state solution, and then those below, one can construct *envelopes* which enclose the developing patterns (see Figure 6.6(a)). These envelopes travel at the same speed as the propagating patterns and encapsulate the average behaviour of the travelling wave of pattern. Here we use the properties of these envelopes to determine the approximate minimum wavespeed of the spreading pattern.

We introduce a coordinate system moving with the travelling pattern by the usual change of variables $z = x - vt$, where v is a positive constant. We are thus concerned with patterns propagating in the positive x-direction. The assumption that the patterns travel at a constant speed v is based on the results of the numerical solutions shown in Section 6.2. Using this change of variables our equations can now be written in terms of x and z as

$$\begin{aligned} -\mu v\left(\frac{\partial^3\theta}{\partial z^3}+2\frac{\partial^3\theta}{\partial z^2\partial x}+\frac{\partial^3\theta}{\partial z\partial x^2}\right)+\left(\frac{\partial^2\theta}{\partial z^2}+2\frac{\partial^2\theta}{\partial z\partial x}+\frac{\partial^2\theta}{\partial x^2}\right) \\ -\beta\left(\frac{\partial^4\theta}{\partial z^4}+4\frac{\partial^4\theta}{\partial z^3\partial x}+6\frac{\partial^4\theta}{\partial z^2\partial x^2}+4\frac{\partial^4\theta}{\partial z\partial x^3}+\frac{\partial^4\theta}{\partial x^4}\right) \\ +\tau\left(\frac{\partial^2}{\partial z^2}+\frac{\partial^2}{\partial z\partial x}+\frac{\partial^2}{\partial x^2}\right)\left(\frac{n^2}{[1+\hat{\nu}(1-\theta)]^2+cn^2}\right)=\rho\theta, \qquad (6.18a) \\ -v\frac{\partial n}{\partial z}=D\left(\frac{\partial^2 n}{\partial z^2}+2\frac{\partial^2 n}{\partial z\partial x}+\frac{\partial^2 n}{\partial x^2}\right)+rn(1-n) \\ -\alpha\left(\frac{\partial}{\partial z}+\frac{\partial}{\partial x}\right)\left\{n\left(\frac{\partial}{\partial z}+\frac{\partial}{\partial x}\right)\left(\frac{1-\theta}{1+\gamma n}\right)\right\}, \qquad (6.18b) \end{aligned}$$

where θ and n are now functions of x and z.

We introduce functions for describing the envelopes of the spreading pattern

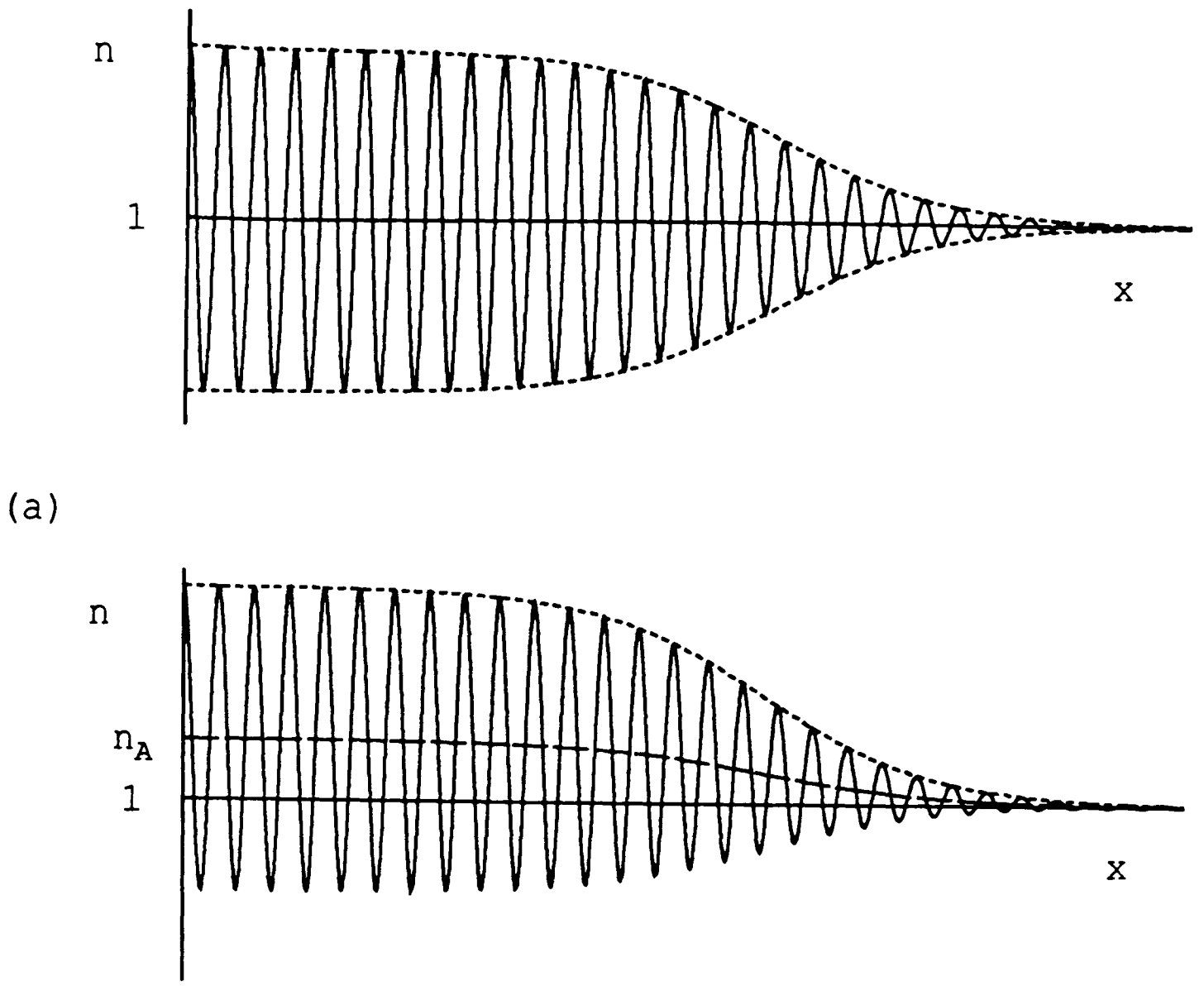

Figure 6.6: (a) An illustration of the *envelope* of the propagating wave of pattern formation in cell density. (b) An illustration of the envelope functions representing the change in the pattern's amplitude and the change in the average cell density.

as follows. There are three envelopes involved: the envelope of the pattern in epithelial dilation; the envelope of the pattern in dermal cell density; and the envelope to represent the change in the average dermal cell density (see Figure 6.6(b)). We represent them by the normalized curves $p(z)$, $q(z)$ and $s(z)$ respectively. The last function $s(z)$ is strictly speaking, not an envelope, but we shall describe it as such, for convenience. The envelope functions have the following properties,

$$\lim_{z\to\infty} p(z) = 0, \quad \lim_{z\to\infty} q(z) = 0, \quad \lim_{z\to\infty} s(z) = 0, \tag{6.19a}$$

$$\lim_{z\to-\infty} p(z) = 1, \quad \lim_{z\to-\infty} q(z) = 1, \quad \lim_{z\to-\infty} s(z) = 1. \tag{6.19b}$$

The solution of the system (6.18) can now be expressed as

$$\theta(x,z) = p(z)\theta_G(x,z), \tag{6.20a}$$

$$n(x,z) = q(z)[n_G(x,z) - n_A] + s(z)(n_A - 1) + 1. \tag{6.20b}$$

where θ_G and n_G are functions of x and z. The value n_A is the average dermal cell density as $z \to -\infty$,

$$n_A = \lim_{z\to-\infty} \frac{1}{P} \int_0^P n(x,z)dx,$$

where P is the period of the steady state spatial pattern at $z = -\infty$.

Note that a second envelope function $s(z)$ also appears in the expression for $n(x,z)$. This is because the average cell density, n_A, of the final solution is not equal to the initial average cell density $n = 1$, which is of course the homogeneous steady state value. So we have to track the change in average cell density, which is due to the logistic growth term in our dermal cell conservation equation, as well as the change in the developing pattern.

To explain the properties of the functions $n_G(x,z)$ and $\theta_G(x,z)$, we consider their behaviour in the limit as $z \to \pm\infty$. Far behind the leading edge of the disturbance, that is where $z \to -\infty$, the system is at a spatially periodic steady state, say S_1. We represent this steady state pattern by $S_1 = (\theta_{S_1}(x), n_{S_1}(x))^T$, which is also the solution of the z-independent nonlinear problem. So, from (6.19) and (6.20) it follows that

$$\lim_{z\to-\infty} \begin{pmatrix} \theta_G(x,z) \\ n_G(x,z) \end{pmatrix} = \begin{pmatrix} \theta_{S_1}(x) \\ n_{S_1}(x) \end{pmatrix},$$

and hence

$$\lim_{z\to-\infty} \begin{pmatrix} \theta(x,z) \\ n(x,z) \end{pmatrix} = \begin{pmatrix} \theta_{S_1}(x) \\ n_{S_1}(x) \end{pmatrix}.$$

On the other hand, far ahead of the leading edge of the disturbance, that is at $z \to \infty$, the system is at a homogeneous steady state, say S_0, where $S_0 = (0,0)$. As the disturbance propagates into the homogeneous region, in the direction

of positive z, the steady state is perturbed and a spatially periodic solution begins to evolve. We represent the form of this initial pattern in dilation and cell density by the functions $\theta_{S_0}(x)$ and $n_{S_0}(x)$ respectively. In terms of the above expressions (6.19) and (6.20) this means that

$$\lim_{z\to\infty}\begin{pmatrix}\theta_G(x,z)\\ n_G(x,z)\end{pmatrix}=\begin{pmatrix}\theta_{S_0}(x)\\ n_{S_0}(x)\end{pmatrix}.$$

Additionally we assume that the amplitudes of the periodic functions $\theta_{S_0}(x)$ and $n_{S_0}(x)$, representing the initial shape of the patterns, are the same as the amplitudes of the final pattern $\theta_{S_1}(x)$ and $n_{S_1}(x)$. The change in form of the initial pattern at S_0 into the final pattern at S_1 is thus tracked by the functions $\theta_G(x,z)$ and $n_G(x,z)$. As explained above the envelope functions $p(z)$, $q(z)$ and $s(z)$ track the amplitudes of these patterns. Note that the dependence of $\theta_G(x,z)$ and $n_G(x,z)$ on z is necessary since the initial shape and period of the pattern changes as the wave propagates through the domain, or in other words as z changes.

However, as is evident from Figures 6.1 and 6.2, the most significant changes in the patterns are in their amplitudes, while changes in their shapes are not really noticeable. Therefore, although the functions $\theta_G(x,z)$ and $n_G(x,z)$ are dependent on z, this dependence is very weak. For the purpose of our subsequent analysis we assume that this dependence is negligibly small. As we shall see below, this is a very reasonable assumption when we are in the vicinity of the bifurcation point to spatial patterns. This assumption implies that

$$\begin{pmatrix}\theta_G(x,z)\\ n_G(x,z)\end{pmatrix}=\begin{pmatrix}\theta_{S_0}(x)\\ n_{S_0}(x)\end{pmatrix}=\begin{pmatrix}\theta_{S_1}(x)\\ n_{S_1}(x)\end{pmatrix}, \tag{6.21}$$

and thus the final steady state pattern far behind the wave is the same as the initial evolving pattern at the leading edge of the wave. For notational convenience we shall write

$$\begin{pmatrix}\theta_S(x)\\ n_S(x)\end{pmatrix}=\begin{pmatrix}\theta_G(x,z)\\ n_G(x,z)\end{pmatrix}.$$

Also, before we proceed any further, we simplify our model equations as before by setting D, μ and r equal to zero. Since the logistic growth term has

been dropped, the average cell density stays fixed at $n_A(z) = 1$ and so the envelope function $s(z)$ in (6.20b) disappears.

We now study the phase space of the above system which has the two (z-independent) steady states $S_1 = (\theta_{S_1}(x), n_{S_1}(x))$ and $S_0 = (0,0)$. The system has a propagating pattern solution if and only if there exists a trajectory in the phase space connecting these two steady states. As in the previous chapter, by linearizing about these steady states, one can examine their stability to see whether such a trajectory is possible. In this way we will also get a bound on the wavespeed v as before.

We begin by linearizing about S_1, by setting

$$\theta(x,z) = \theta_S(x) + \tilde{p}(z)\theta_S(x), \tag{6.22a}$$

$$n(x,z) = n_S(x) + \tilde{q}(z)n_S(x), \tag{6.22b}$$

where

$$|\tilde{q}(z)| \ll 1 \quad \text{and} \quad |\tilde{p}(z)| \ll 1.$$

Because of our assumption that the form of the pattern stays fixed while the amplitudes of the propagating patterns change, only the amplitudes of the pattern are perturbed about the steady state.

By substituting (6.22) into equations (6.18) and dropping the tildes for algebraic convenience, we have the linear system

$$\begin{aligned} -\mu v\left(\frac{\partial^3}{\partial z^3} + 2\frac{\partial^3}{\partial z^2\partial x} + \frac{\partial^3}{\partial z\partial x^2}\right)(p\theta_S) + \left(\frac{\partial^2}{\partial z^2} + 2\frac{\partial^2}{\partial z\partial x} + \frac{\partial^2}{\partial x^2}\right)(p\theta_S) \\ -\beta\left(\frac{\partial^4}{\partial z^4} + 4\frac{\partial^4}{\partial z^3\partial x} + 6\frac{\partial^4}{\partial z^2\partial x^2} + 4\frac{\partial^4}{\partial z\partial x^3} + \frac{\partial^4 p\theta_S}{\partial x^4}\right)(p\theta_S) \\ + \left(\frac{\partial^2}{\partial z^2} + \frac{\partial^2}{\partial z\partial x} + \frac{\partial^2}{\partial x^2}\right)(U_1(x)p\theta_S + U_2(x)qn_S) = \rho p\theta_S, \end{aligned} \tag{6.23a}$$

$$\begin{aligned} -v\frac{\partial}{\partial z}(qn_S) = \left(\frac{\partial}{\partial z} + \frac{\partial}{\partial x}\right)\left\{qn_S\left(\frac{\partial}{\partial z} + \frac{\partial}{\partial x}\right)W_0(x)\right. \\ \left. + n_S\left(\frac{\partial}{\partial z} + \frac{\partial}{\partial x}\right)(W_1(x)qn_L + W_2(x)p\theta_L)\right\}, \end{aligned} \tag{6.23b}$$

where

$$U_1(x) = \frac{2\tau\hat{\nu}[1 + \hat{\nu} - \hat{\nu}\theta_S(x)]}{\{[1 + \hat{\nu} - \hat{\nu}\theta_S(x)]^2 + cn_S^2(x)\}^2}$$

$$U_2(x) = \frac{2\tau n_S(x)[1+\hat{\nu}-\hat{\nu}\theta_S(x)]^2}{\{[1+\hat{\nu}-\hat{\nu}\theta_S(x)]^2+cn_S^2(x)\}^2}$$

and

$$\begin{aligned} W_0(x) &= \frac{-\alpha[1-\theta_S(x)]}{1+\gamma n_S(x)} \\ W_1(x) &= \frac{\alpha\gamma[1-\theta_S(x)]}{[1+\gamma n_S(x)]^2} \\ W_2(x) &= \frac{\alpha}{1+\gamma n_S(x)}. \end{aligned}$$

Likewise, we linearize about the steady state S_0 by setting

$$\theta(x,z) = \tilde{p}(z)\theta_S(x), \tag{6.24a}$$

$$n(x,z) = 1+\tilde{q}(z)n_S(x), \tag{6.24b}$$

where

$$|\tilde{q}(z)| \ll 1 \quad \text{and} \quad |\tilde{p}(z)| \ll 1.$$

Substituting this into (6.18) and dropping the tildes give

$$-\mu v\left(\frac{\partial^3}{\partial z^3}+2\frac{\partial^3}{\partial z^2\partial x}+\frac{\partial^3}{\partial z\partial x^2}\right)(p\theta_S)+\left(\frac{\partial^2}{\partial z^2}+2\frac{\partial^2}{\partial z\partial x}+\frac{\partial^2}{\partial x^2}\right)(p\theta_S)$$
$$-\beta\left(\frac{\partial^4}{\partial z^4}+4\frac{\partial^4}{\partial z^3\partial x}+6\frac{\partial^4}{\partial z^2\partial x^2}+4\frac{\partial^4}{\partial z\partial x^3}+\frac{\partial^4 p\theta_L}{\partial x^4}\right)(p\theta_S)$$
$$+\left(\frac{\partial^2}{\partial z^2}+\frac{\partial^2}{\partial z\partial x}+\frac{\partial^2}{\partial x^2}\right)(P_1 p\theta_L+P_2 qn_L)=\rho p\theta_L, \tag{6.25a}$$

$$-v\frac{\partial}{\partial z}(qn_L)=\left(\frac{\partial^2}{\partial z^2}+2\frac{\partial^2}{\partial z\partial x}+\frac{\partial^2}{\partial x^2}\right)(Q_1 qn_L+Q_2 p\theta_L), \tag{6.25b}$$

where P_1, P_2, Q_1 and Q_2 are as in (2.13).

These linear systems are extremely complicated and it is very difficult to carry out a stability analysis. However, by assuming that we are in the vicinity of the point where the stability of the steady state solution S_0 changes, one can actually find a perturbation solution for the nonhomogeneous steady state solution S_1 as was demonstrated in Section 3.3. This perturbation solution can then be used for simplifying the above linear systems.

For the purpose of our explanation below we briefly refer back to system (3.10) which is the above set of equations (6.18) written in terms of the space

and time coordinates x and t. In Section 2.6 we have shown that this system bifurcates from the homogeneous steady state S_0 if the dispersion relation (see equation (2.18)) becomes positive for some critical eigenvalue k_c^2. This happens, for example, if the bifurcation parameter γ, becomes marginally smaller than the critical value γ_c. By setting $\gamma = \gamma_c - \epsilon^2$, where ϵ is the small perturbation parameter, an approximate nonhomogeneous steady state solution for large time (see (3.25)) was found in Section 3.3 by a multiple time scale analysis.

The perturbation solution is valid for the travelling coordinate system (6.18) in the region where $z \to -\infty$ and is in fact the steady state solution S_1. Hence, from (3.25), we have that

$$\begin{pmatrix} \theta_{S_1}(x) \\ n_{S_1}(x) \end{pmatrix} = \Lambda \begin{pmatrix} 1 \\ M \end{pmatrix} (A \cos k_c x + B \sin k_c x) + O(\epsilon^2), \tag{6.26}$$

where the amplitude is given by Λ, $M = -(\gamma_c + 1)/\gamma_c$ and $A^2 + B^2$ is as in the nonlinear analysis of Section 3.3.

Next we look at the steady state S_0, as $z \to \infty$ and more specifically at the functions θ_{S_0} and n_{S_0}. Initially, for t very small, the solution of (3.10) is evolving from the homogeneous steady state $\theta = 0$, $n = 0$. The variables are still close to their steady state values so that we can approximate our nonlinear system by a linearized version about the steady state. The linear solution of (3.10), obtained for large time, can be written as

$$\begin{pmatrix} \theta(x,t) \\ n(x,t) \end{pmatrix} \approx \begin{pmatrix} 0 \\ 1 \end{pmatrix} + \int_{k_L}^{k_R} p_f(k) \begin{pmatrix} 1 \\ M(k^2) \end{pmatrix} e^{\lambda(k^2)t} (A \cos kx + B \sin kx) dk,$$

where $p_f(k)$ is determined by a Fourier transform of the initial conditions, A and B are arbitrary constants, the function

$$M(k^2) = \frac{-Q_2 k^2}{\lambda(k^2) + Q_1 k^2},$$

is determined from the analysis of Section 2.5, and $[k_L, k_R]$ is the range of unstable wavenumbers.

When performing the weakly nonlinear analysis (see Section 3.3) it is assumed that, since one is in the vicinity of the bifurcation point, the linear solution with the critical eigenvalue k_c^2, is the dominant one and, for small enough

ϵ, the only one that evolves initially. So, using expression (6.19) and (6.20) we can write

$$\begin{pmatrix} \theta_{S_0}(x) \\ n_{S_0}(x) \end{pmatrix} = \Lambda \begin{pmatrix} 1 \\ M \end{pmatrix} (A \cos k_c x + B \sin k_c x), \tag{6.27}$$

where we have multiplied the solution by Λ so that the amplitudes of $\theta_{S_0}(x)$ and $n_{S_0}(x)$ are rescaled to be the same as the amplitudes of the final steady state solution (6.26).

Our initial pattern $(\theta_{S_0}(x,z), n_{S_0}(x,z))^T$, far ahead of the leading edge of the travelling wave, is to $O(\epsilon)$ the same as the final pattern, $(\theta_{S_1}(x), n_{S_1}(x))^T$, far behind. This means that our solution $(\theta(x,z), n(x,z))^T$ is to $O(\epsilon)$ separable in a x-independent part $(p,q)^T$ and a z-independent part $(n_G, \theta_G)^T$ and that for small enough values of ϵ the assumption (6.21) is correct. To $O(\epsilon)$ we thus have

$$\begin{pmatrix} \theta_S \\ n_S \end{pmatrix} = \Lambda \begin{pmatrix} 1 \\ M \end{pmatrix} (A \cos k_c x + B \sin k_c x). \tag{6.28}$$

We substitute this into the linearized system (6.23). Ignoring terms of $O(\epsilon^2)$ and equating coefficients of $\cos k_c x$ we get the following two equations

$$\begin{aligned} &\beta A p'''' + 4\beta B p''' - (1 + 6\beta k_c^2 + P_1) A p'' - (2k_c + 4\beta k_c^3 + P_1 k_c) B p' \\ &+ (k_c^2 + \beta k_c^4 + P_1 k_c^2 + \rho) A p = M P_2 (A q'' + k_c B q' - k_c^2 A q), \end{aligned} \tag{6.29a}$$

$$\begin{aligned} &Q_2 A p'' + 2 Q_2 k_c B p' - Q_2 A k_c^2 p = -M Q_1 A q'' \\ &- (vAM + 2MQ_1 k_c B) q' + M Q_1 k_c^2 A q, \end{aligned} \tag{6.29b}$$

where the prime indicates differentiation with respect to z.

Likewise, by equating coefficients of $\sin k_c x$ we get

$$\begin{aligned} &\beta B p'''' - 4\beta A p''' - (1 + 6\beta k_c^2 + P_1) B p'' + (2k_c + 4\beta k_c^3 + P_1 k_c) A p' \\ &+ (k_c^2 - \beta k_c^4 + P_1 k_c^2 - \rho) B p = M P_2 (B q'' - k_c A q' - k_c^2 B q), \end{aligned} \tag{6.30a}$$

$$\begin{aligned} &Q_2 B p'' - 2 Q_2 k_c A p' - Q_2 B k_c^2 p = -M Q_1 B q'' \\ &+ (vMB + 2MQ_1 k_c A) q' + M Q_1 k_c^2 B q. \end{aligned} \tag{6.30b}$$

We add equations (6.29a) to (6.30a) and (6.29b) to (6.30b) after multiplying equations (6.29) by A and equations (6.30) by B. After dividing the two resulting

equations by $(A^2 + B^2)$ we are left with

$$\beta p'''' - (1 + 6\beta k_c^2 + P_1)p''$$

$$+(k_c^2 + \beta k_c^4 + P_1 k_c^2 + \rho)p = MP_2(q' - k_c^2 Bq), \tag{6.31a}$$

$$Q_2 p'' - Q_2 B k_c^2 p = -MQ_1 q'' + vMq' + MQ_1 k_c^2 q, \tag{6.31b}$$

which is the linearized system about the steady state S_1 to $O(\epsilon)$.

The linearized system to $O(\epsilon)$ about the steady state S_0 can be found in a similar fashion. Substitute (6.28) and (6.27) into equation (6.25) and follow the same procedure as above to derive exactly the same equations as (6.31). The two original linear systems have now been reduced considerably — they are only dependent on the variable z and are written in terms of the envelope functions p and q.

By setting

$$p_0 = p, \qquad p_1 = p', \qquad p_2 = p'', \qquad p_3 = p''', \qquad q_0 = q, \qquad q_1 = q',$$

the coupled pair of ordinary differential equations (6.31) can be written as a sixth order system, namely

$$\begin{aligned}
p_0' &= p_1, \\
p_1' &= p_2, \\
p_2' &= p_3, \\
p_3' &= \frac{1}{\beta}\left[\left(-\beta k_c^4 - (P_1 + 1 - \frac{P_2 Q_2}{Q_1})k_c^2 - \rho\right) p_0 \right. \\
&\qquad \left. + \left(6\beta k_c^2 + P_1 + 1 - \frac{P_2 Q_2}{Q_1}\right) p_2 + \frac{P_2 Q_2 v}{Q_1^2} q_1\right], \\
q_0' &= q_1, \\
q_1' &= p_2 - k_c^2 - \frac{v}{Q_1} q_1 + k_c^2 q_0.
\end{aligned}$$

We examine the stability of this system in the usual way by looking for solutions

$$(p_0, p_1, p_2, p_3, q_0, q_1)^T = \boldsymbol{W} e^{\eta z}, \tag{6.32}$$

where the vector $\boldsymbol{W}$ is a constant and the sign of $\Re\eta$ determines the stability of the steady state. For example the steady states S_0 and S_1 have an unstable manifold if η has a positive value.

Substituting (6.32) into the linearized system of equations leads to a system of six homogeneous equations. A non-trivial solution exists for this system if and only if η satisfies the following solvability condition,

$$\Delta(\eta) = \eta^6 + \frac{v}{Q_1}\eta^5 - \left(k_c + \frac{\chi}{\beta}\right)\eta^4 - \frac{v}{\beta Q_1}\left(6\beta k_c^2 + P_1 + 1\right)\eta^3$$
$$+\frac{1}{\beta}\left(k_c^2\chi - \omega\right)\eta^2 + \frac{1}{\beta Q_1}\left(\beta k_c^4 + k_c^2 + P_1 k_c^2 + \rho\right)\eta + \frac{k_c^2\omega}{\beta} = 0, \quad (6.33)$$

where

$$\begin{aligned}\chi &= 6\beta k_c^2 + P_1 + 1 - \frac{P_2 Q_2}{Q_1},\\ \omega &= -\beta k_c^4 - P_1 k_c^2 + \frac{P_2 Q_2 k_c^2}{Q_1} - k_c^2 - \rho.\end{aligned}$$

This is a sixth order polynomial in η, and so Descarte's rule of signs can be used to determine the number and signs of the roots. It follows from the linear analysis of Section 2.6 that

$$\beta Q_1(\gamma)k_c^6 - [P_2Q_2(\gamma) - P_1Q_1(\gamma) - Q_1(\gamma)]k_c^4 + \rho Q_1(\gamma)k_c^2 < 0 \quad \text{if} \quad \gamma < \gamma_c,$$

and so

$$\omega(\gamma) > 0 \quad \text{if} \quad \gamma < \gamma_c,$$

which implies that the last term of the polynomial (6.33) is positive. We also know from equation (2.19) that

$$P_2Q_2(\gamma) - P_1Q_1(\gamma) - Q_1(\gamma) > 0 \quad \text{if} \quad \gamma < \gamma_c,$$

and thus

$$\chi(\gamma) - 4\beta k_c^2 > 0 \quad \text{if} \quad \gamma < \gamma_c.$$

Using this we have that

$$k_c^2\chi - \omega = 3\beta k_c^2 + \rho + 2k_c^2(\chi - 4\beta k_c^2) > 0 \quad \text{if} \quad \gamma < \gamma_c,$$

and so the polynomial (6.33) has only two sign changes in the sequence of coefficients. This implies that there are either 2 or 0 positive roots. By substituting

$-\eta$ for η into (6.33) we see that the resulting polynomial has 4 sign changes and it therefore has either 4, 2 or 0 negative roots.

As z changes from $-\infty$ to ∞ we move along the trajectory from S_1 to S_0. As necessary conditions for a trajectory to exist in the phase space an unstable manifold at S_1 and a stable manifold at S_0 are required. Notice that these are not sufficient conditions; whether there indeed exists a trajectory connecting the steady state S_1 to S_0 cannot be proven.

Our solvability condition (6.33), which is valid to $O(\epsilon)$ at both steady states, allows for both stable and unstable manifolds. However, we must substitute the parameters to confirm that the polynomial (6.33) indeed has positive and negative roots and we therefore examine a specific example.

Example 6.4.1: We choose our parameter set as in Example 6.2.1 and set $\epsilon = 0.01$, so that we are in the vicinity of the bifurcation point. The linear stability of the steady states to $O(\epsilon)$ is examined by substituting our parameters into the polynomial (6.33). As in the analysis of the travelling wave solutions in Section 5.3, we aim to get a bound on v for which the steady state S_0 is stable and S_1 is unstable.

Initially we set $v = 0$. The polynomial has two positive and two negative roots and therefore we have two stable and two unstable manifolds. In fact for $v \geq 0$ we find that these 4 roots persist so that we always have two stable and two unstable manifolds. If these are the actual manifolds from and into which the trajectories shoot, at S_1 and S_0 respectively, we cannot obtain a bound on the wavespeed v and any wavespeed is in principle possible. However, from our numerical results of Section 6.2 we know that a travelling wave solution can only exist for certain wavespeeds. Clearly a wavespeed of $v = 0$ is impossible, since that would indicate a standing wave. A trajectory connecting the above mentioned manifolds could therefore not exist.

However, by increasing the value of v from zero, one can add another two negative eigenvalues. If we hypothesize that the stable manifold at S_0 into

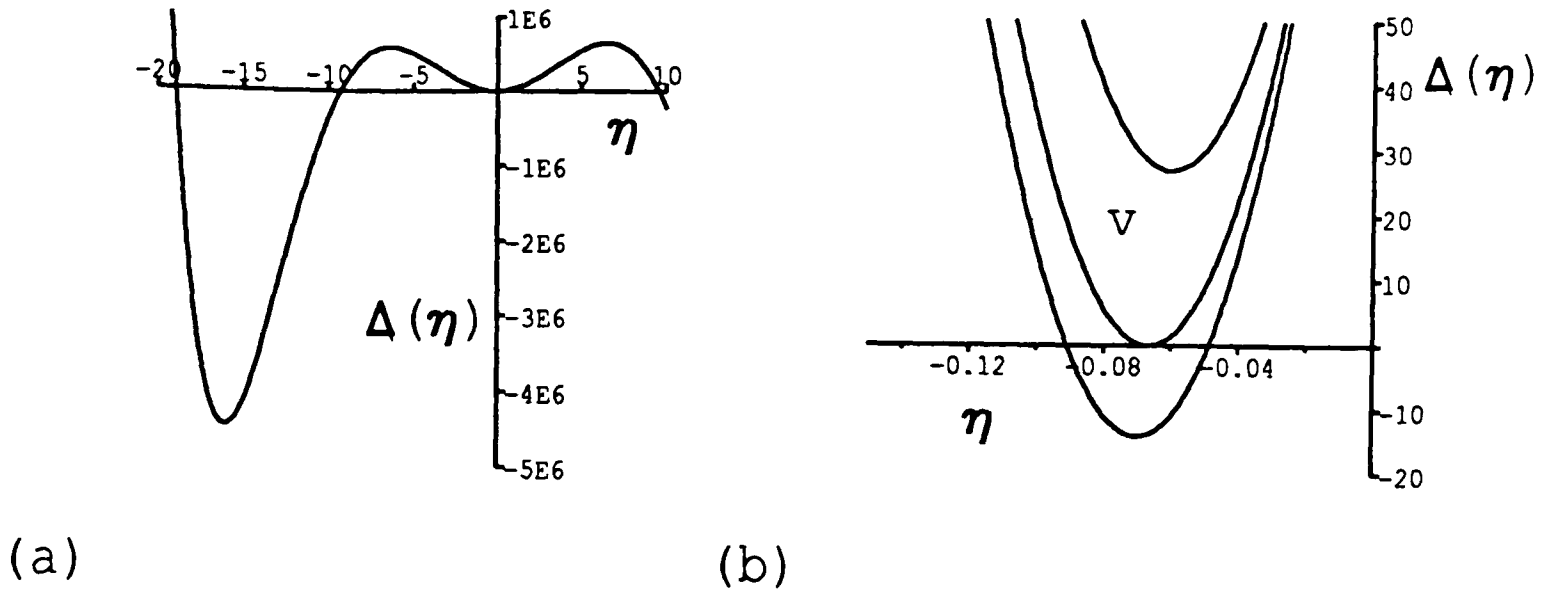

(a) (b)

Figure 6.7: The solvability polynomial (6.33) with parameter values as in Example 6.4.1 and $\epsilon = 0.01$. (a) All the roots of the polynomial are shown. (b) The double root that appears as the wavespeed v increases through 0.13.

However, by increasing the value of v from zero, one can add another two negative eigenvalues. If we hypothesize that the stable manifold at S_0 into which the connecting trajectory shoots is represented by these two roots, we can indeed get a bound on v. One can find the minimum value v, for which these two new roots appear as a double negative root. This value of v would then represent a lower bound on the wavespeed of the travelling pattern. The arguments used here are similar to those of Section 5.3 and, as before, although we cannot prove the existence of a trajectory connecting the steady states S_0 and S_1 such a trajectory seems highly likely in the light of the numerical experiments performed below.

Numerically we found that the double negative root appeared at a minimum value $v = 0.13$, see Figure 6.7. The actual speed at which the pattern propagates, as was found from the numerical simulations, agrees exactly with this prediction. As is the case for the Fisher wave we see that our wave of pattern formation indeed travels at, or very close to, the minimum speed, since it agrees well with the analytical approximation for the minimum speed.

We repeated this analysis when we were slightly further away from the bifur-

ever, the further we move away from the bifurcation point, the worse we expect our prediction to become since the above analysis is really only valid in the limit as we approach the bifurcation point. For example, for $\epsilon = 0.5$ the shape of our solvability polynomial (6.33) changes completely and the above argument does not hold any more.

We carried out similar comparisons for several different parameter sets, and got similar results (see, for example, Table 6.2 in Section 6.5).

Since our solvability condition is very complicated it remains a difficult task to relate the individual parameters to the behaviour of the polynomial. Given a set of parameters one must therefore examine numerically how changing a certain value would change the polynomial and thus the wavespeed.

We know from the analysis carried out in Section 5.6 on regular travelling waves that the speed of propagation increases if the leading edge of the wave is perturbed. In the next example we show that similar results are also obtained for travelling waves of pattern formation.

Example 6.4.2: We use the same parameter set as in the previous example and select $\epsilon = 0.1$. As in the Example 6.2.1, we again start from a random initial perturbation at one end of the domain and then track the progression of the wave of pattern as it propagates towards the other end. We perturb the leading edge of the epithelial dilation pattern by random perturbations about the steady state equal to or less than 0.001 in the range where the leading edge has amplitudes [0.0001,0.001]. The wave progression is shown in Figure 6.8. Because of the changing conditions specified at the leading edge, the wavespeed is not constant as in the other examples, but differs from time-step to time-step. We calculated the average wavespeed numerically and found it as $v = 1.44$, which is higher than the minimum of $v = 1.35$. This result lends further credibility to our hypothesis that the stable manifold at S_0, into which the connecting trajectory shoots, is represented by an eigenvector space arising from increasing the value of v from zero.

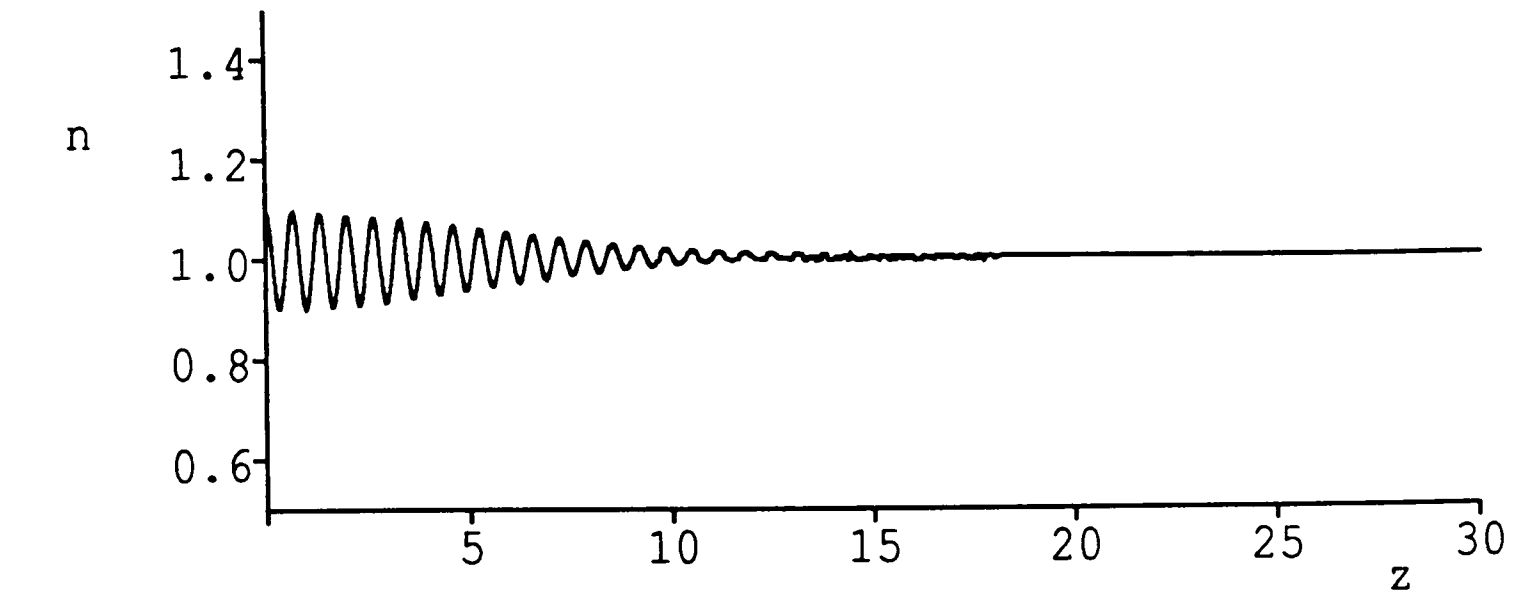

(a)

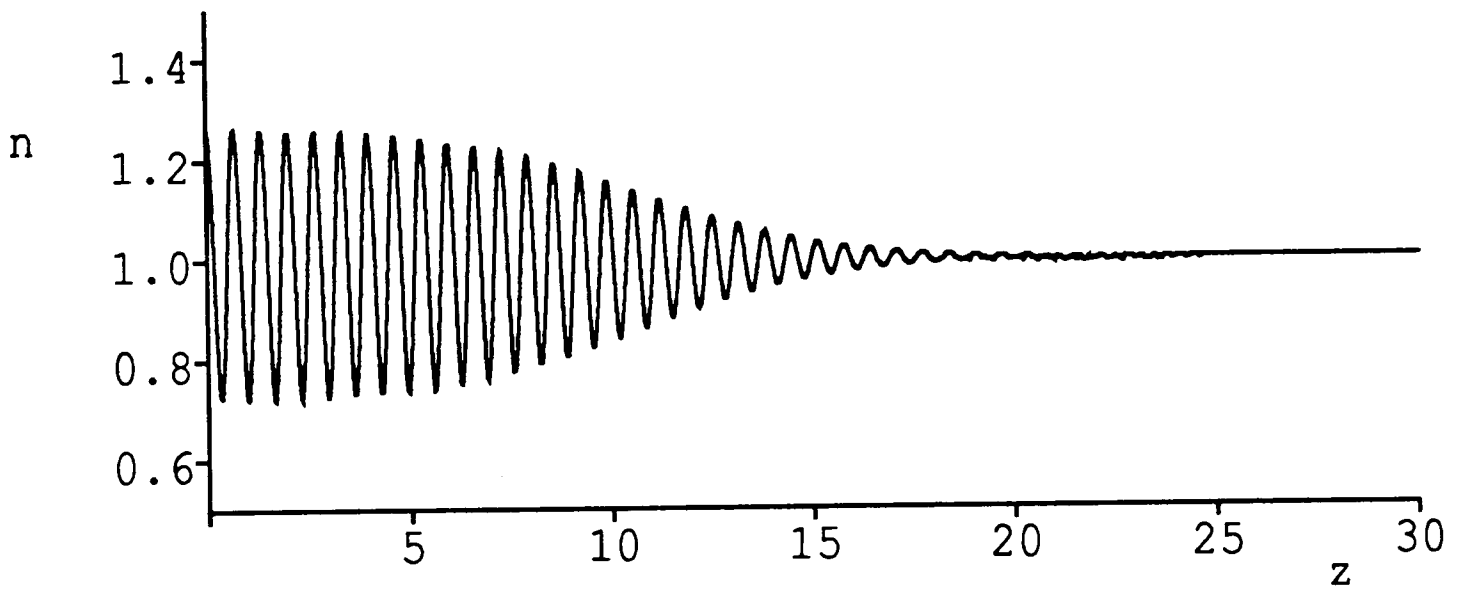

(b)

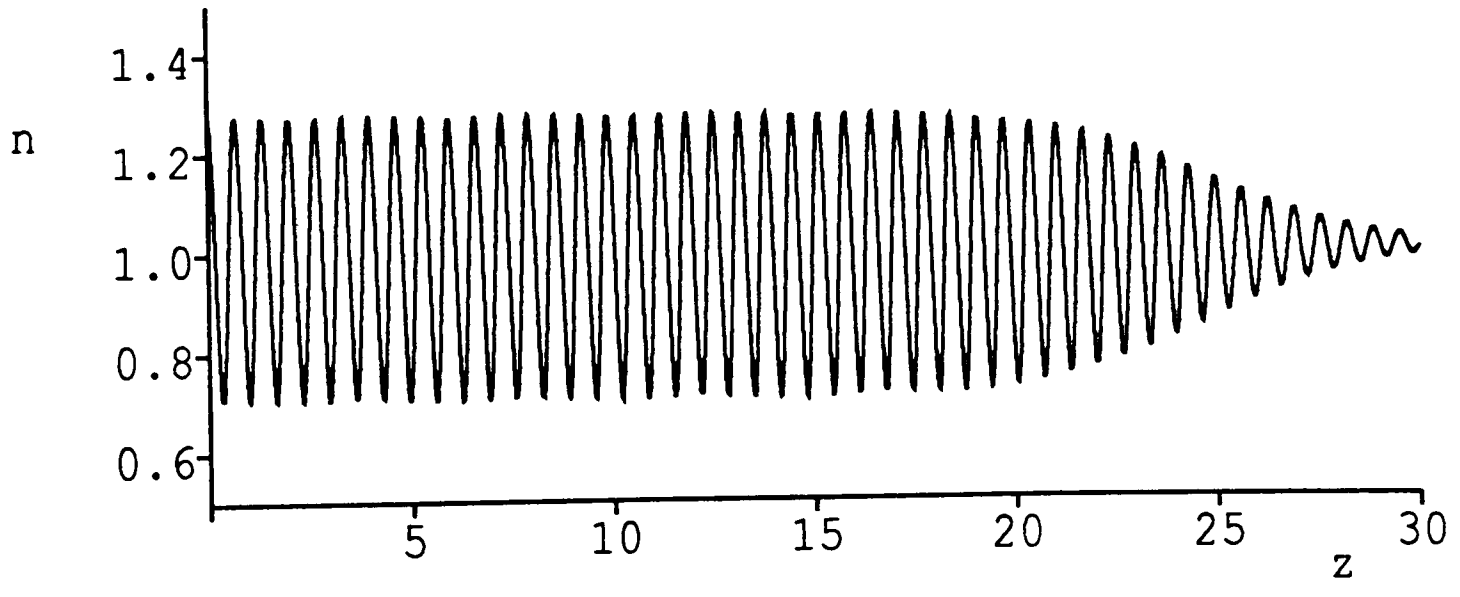

(c)

Figure 6.8: The time evolution of dermal cell density patterns generated by an initial small random perturbation at the origin followed by a continual random disturbance at the leading edge of the wave of patterning. See Example 6.4.2 for the parameter values and a more detailed explanation. In (a) $t = 16$, (b) $t = 21$ and (c) $t = 26$.

To test the general applicability of this envelope method for determining the minimum wavespeed at which waves of pattern formation travel we applied the method to a reaction-diffusion system. For the purpose of our analysis we chose the Schnakenberg system, one of the simplest reaction-diffusion systems (see Murray 1990). Instead of a sixth order polynomial we found a fourth order polynomial as the stability condition for the two steady states. As we varied the wavespeed we got either zero or two stable manifolds at these steady states. Therefore if a trajectory connecting the two steady states does exist we do get a bound on the wavespeed. The results of the numerically computed travelling wave also compared favourably with the minimum wavespeed predicted analytically. Also, since we only have a polynomial of the fourth order, it is easier to relate the parameters to the wavespeed than it is in the tissue interaction model.

6.5 Comparison of the Envelope and Asymptotic Methods

Here we compare the asymptotic method for determining the wavespeed of the propagating pattern as described in Section 6.3 with the envelope method as described in Section 6.4. Each method has its particular advantages and both gave reasonably good results in the vicinity of the bifurcation point.

We used both methods to compute approximate wavespeeds for the tissue interaction system with parameter values as in Examples 6.2.1 and 6.2.2. We did the computations for when we are very close to the bifurcation point by choosing $\epsilon = 0.01$, as well as slightly further away from this critical point by choosing $\epsilon = 0.1$. Examples for even larger values of ϵ were also considered. The results are shown in Table 6.2.

When we are close to the bifurcation point, $\epsilon = 0.01$, both methods have the same degree of accuracy. However, as we move away from the bifurcation point, the envelope method seems to give wavespeeds slower than the actual

ϵ	Numerical Result	Asymptotic Method	Envelope Method
Example 6.2.1			
0.01	0.13	0.13	0.13
0.1	1.35	1.36	1.33
0.5	9.4	9.9	-
Example 6.2.2			
0.01	0.70	0.69	0.69
0.1	7.13	7.17	6.87
0.25	21.5	20.9	-

Table 6.2: A comparison of the wavespeeds obtained for the propagating pattern from the asymptotic method, the envelope method and the numerical simulations.

wavespeed, while the asymptotic method gives wavespeeds faster than the actual wavespeed. So, for accurate predictions close to the bifurcation point any of these two methods could be used. However, although both methods become less accurate further away from the bifurcation point, it seems though that the asymptotic method gives better results. When ϵ is too large the envelope method completely fails and for such cases the asymptotic method is preferred.

The accuracy with which the caricature dispersion relation approximates the full dispersion relation could have an important effect on the accuracy of the wavespeed predicted by the asymptotic method. We got a particularly good fit in our tissue interaction model (see Figure 6.5). For other systems this may not always be the case. Using polynomials of degree higher than three for approximating the full dispersion relation is not feasible, as was discussed in Section 6.3, and one has to be satisfied with a simple polynomial approximation of degree less than three. For example, Murray & Myerscough (1992) did not get as close a fit and so their predicted wavespeed is not as good as it is in our case. When the fit is particularly bad the envelope method is to be preferred.

The asymptotic method could still be useful even when it does not give very

good results. A major feature of this method is that it gives an intuitive idea of how the dispersion relation relates to the wavespeed. This could help in determining the effect of some of the model parameters on the speed at which the patterns are laid down. The asymptotic method also gives approximate wavenumbers both for the leading edge of the pattern as well as for the standing pattern. In the envelope method one assumes a fixed wavenumber and there is no distinction between the wavenumber at the leading edge and that of the standing pattern.

The major disadvantage of using the asymptotic method is the amount of computation involved in finding an approximate polynomial to fit the full dispersion relation. Depending on the method used it involves the numerical calculation of definite integrals.

We saw here that in both methods it is difficult to relate the parameters to the actual wavespeed. However, we believe that for less complicated systems the envelope method would lend itself better to this. By changing one parameter one could examine the result on the polynomial calculated from the solvability condition. In the asymptotic method one has the problem, because of the caricature approach, that all the parameters appearing in the model are represented by the three appearing in the caricature dispersion relation which makes it particularly difficult to relate the actual parameters to the wavespeed. Also, by changing a certain parameter slightly, it is necessary to recalculate the whole approximate dispersion relation. This is a much more involved task than only substituting a new value for the parameter into the solvability polynomial obtained from the envelope method.

More extensive comparisons need to be carried out on other systems to get a clearer idea of the advantages and the disadvantages of each method.

Chapter 7

Two-Dimensional Sequential Pattern Formation

7.1 Introduction

In the previous chapter we have discussed sequential pattern formation on one-dimensional domains. We showed there that an initial disturbance in a small region of the domain develops into a travelling wave of pattern formation. In this chapter we examine whether similar propagating waves of patterning can also occur on two-dimensional domains. Since a two-dimensional spatial domain is a more realistic representation of the skin we are able to relate the model results obtained directly to the biology. Furthermore, by using a mathematical model mechanism for explaining sequential patterning we are able to provide a better evaluation of the possible mechanisms that could drive such a process.

As we have discussed in the introduction of Chapter 6, sequential patterning occurs in a large variety of morphogenetic processes. However, as our model is mainly constructed from experimental evidence of chick skin pattern formation, we especially relate it to the sequential feather bud initiation on the chick back as was described in detail in Section 1.2. We refer briefly though to other examples as well, such as alligator stripe formation and lizard scale formation.

In Section 7.2 we consider two-dimensional sequential pattern formation which evolves from an initial pattern specified in a small localised region of a rectangular domain. This is an extension of the ideas presented in the previous chapter. In Section 7.3 we discuss the results of various experiments concerned with the sequential feather bud morphogenesis on the chicken skin. From the biological evidence it seems that a temporal mechanism plays a crucial role

in this process. We therefore introduce the concept of a switch mechanism in Section 7.4 and relate our model predictions to experimental results.

7.2 Sequential Pattern Formation From Initial Pattern

In this section we consider the two-dimensional analogue of the problem we examined in Section 6.2. We show here that the sequential pattern formation problem becomes very different on two-dimensional domains and that the one-dimensional results cannot be carried over directly. Unlike the one-dimensional case the initial pattern from which the propagating wave evolves is crucial to the actual pattern that develops. As was discussed in the previous chapter Myerscough & Murray (1992) modelled sequential alligator stripe formation on a one-dimensional domain. The results obtained in this section demonstrate however, that since alligator skin is actually two-dimensional, a two-dimensional version of their model should really have been used.

As we have explained in Section 4.2, the linearized two-dimensional problem (4.1), with zero-flux boundary conditions (4.2), only admits a discrete set of unstable mode pairs. As before, we assume here that we are close enough to the bifurcation point to spatial patterns so that k_c^2 is the only unstable eigenvalue.

Since the wavevectors corresponding to the unstable eigenvalue

$$k_c^2 = \phi^2 + \psi^2 \tag{7.1}$$

are of the form $\boldsymbol{k}_c = (\phi, \psi)^T$, each wavevector has in fact two degrees of freedom. On an infinite domain any combination $(\phi, \psi)^T$ satisfying (7.1) could be selected, depending on the initial conditions. However, on a finite domain the values which ϕ and ψ can take are determined by the size and shape of the domain as well as the boundary conditions.

As in Chapter 4, we again consider rectangular domains, since they are reasonable approximations to the biological tissue with which we are concerned.

We solve the system on the rectangular domain $\boldsymbol{B} = (L_x, L_y)$ with $L_y \ll L_x$, so that the rectangle is much larger in the x- than in the y-direction. Initially it is assumed that the system is at the homogeneous steady state, $\theta = 0$, $n = 1$, everywhere except for a small subdomain at one end,

$$\boldsymbol{B}^* = (L_x^*, L_y) \quad \text{where} \quad L_x^* \ll L_x.$$

We specify an initial pattern in $\boldsymbol{B}^*$ and examine its propagation across the rest of the domain. How this initial pattern would be set up in the tissue does not concern us for the moment.

Because of the zero-flux boundary conditions at $y = 0$ and $y = L_y$ the y-component, ψ, of the wavevector $\boldsymbol{k}_c$, associated with the developing pattern, is necessarily fixed by the initial pattern. The x-component, ϕ, is thus forced to take on a certain value so as to satisfy (7.1).

We now show two numerical examples to illustrate the different types of travelling waves of pattern formation that can arise. In both examples a rectangular domain of dimensions $\boldsymbol{B} = (6\sqrt{2}, 3\sqrt{2}/2)$ is considered, thus $L_y \ll L_x$. We use the same parameter set as in Example 4.4.1 so that the unstable eigenvalue is $k_c^2 = 4\pi^2$.

Example 7.2.1: As initial conditions we specify a pattern satisfying the zero-flux boundary conditions (4.2), corresponding to the wavevector $\mathbf{k}_c = (2\pi, 0)^T$ on the subdomain $\boldsymbol{B}^*$ with $L_x^* = 3/4$. The homogeneous steady state is specified everywhere else, see Figure 7.1(a). As one might expect, this stripe-like pattern propagates along the length of the domain as can be seen in Figures 7.1(b) and (c).

Example 7.2.2: Next we set as initial conditions a pattern resembling the wavevector $\boldsymbol{k}_c = (2\pi/\sqrt{2}, 2\pi/\sqrt{2})^T$ on the subdomain $\boldsymbol{B}^*$, where $L_x^* = \sqrt{2}/4$. Thus the first half row of pattern in the x-direction is specified, see Figure 7.2(a). As was the case with the stripe pattern in the previous example, we see that new rows are added progressively in the x-direction, which leads, in this

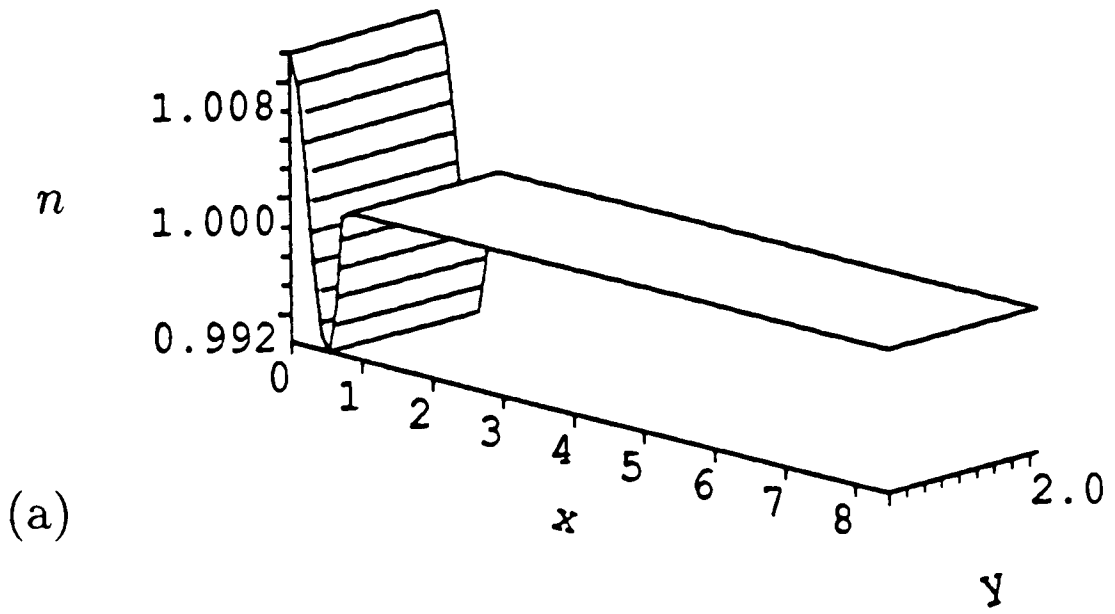

(a)

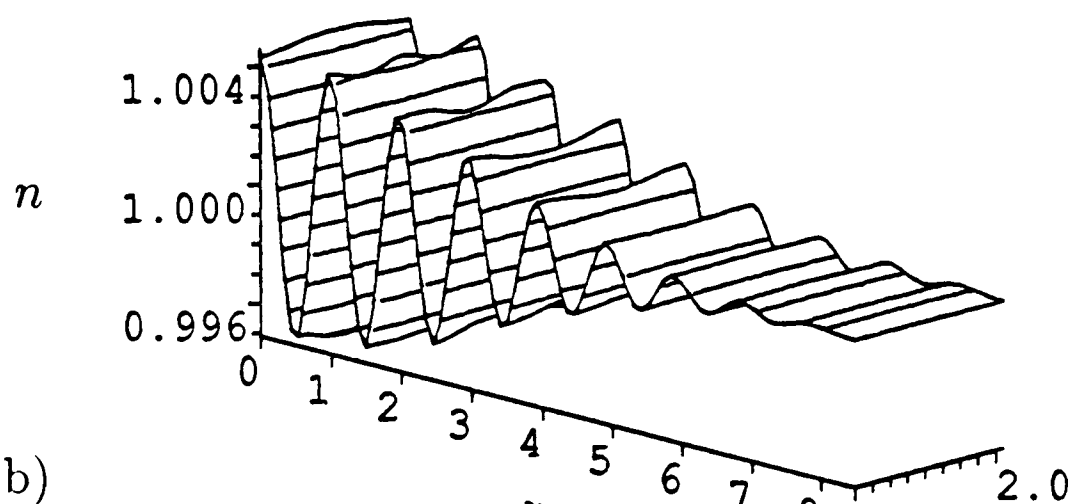

(b)

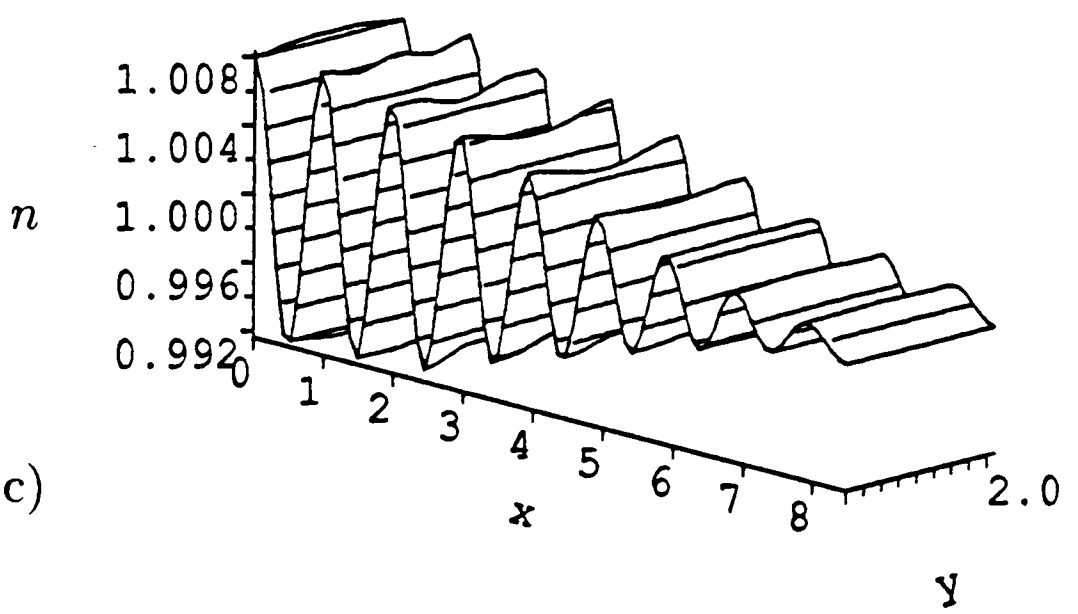

(c)

Figure 7.1: An initial stripe in dermal cell density given at time $t = 0$ in a small region at one end of a rectangular domain (a), propagates through the domain as can be seen in (b) when $t = 5.0$ and (c) when $t = 10.0$. The model parameters are as in Example 7.2.1.

case, to a rhombic pattern (see Figure 7.2(b) and (c)).

An important point, illustrated by these numerical simulations, is that an initial pattern specified on a small subdomain determines the form of the evolving propagating pattern. Also, a simple quasi-one-dimensional initial pattern is all that is required to specify the complicated pattern over the whole two-dimensional domain.

Both the above examples resemble real pattern formation processes seen in embryology. The first simulation is similar to the stripe pattern which is laid down sequentially on the alligator embryo (see Section 6.2). The second simulation mimics the sequential row-by-row feather bud formation on the chick back. Note that we are only concerned here with transient states and that when the pattern reaches the boundary $x = L_x$ it may rearrange to form a final steady state pattern. However, in biological tissue such a rearrangement is irrelevant since cells only have a small window of time in which they can respond to their environment before the pattern is *locked in.*

Depending on the basin of attraction of each pattern, random initial perturbations could develop into any of these two propagating patterns and so a specific pattern cannot be set up by the natural inhomogeneties present in the embryonic tissue. For the above propagating mechanism to operate, the initial pattern has to be specified independently of the model mechanism. Whether this is biologically reasonable shall be discussed after the next section in which we consider the available experimental evidence on sequential chick feather bud formation in detail.

7.3 The Biology of Sequential Pattern Formation

Various biological explanations for the temporal development of patterns across tissue have been proposed. That the actual mechanisms causing the travelling

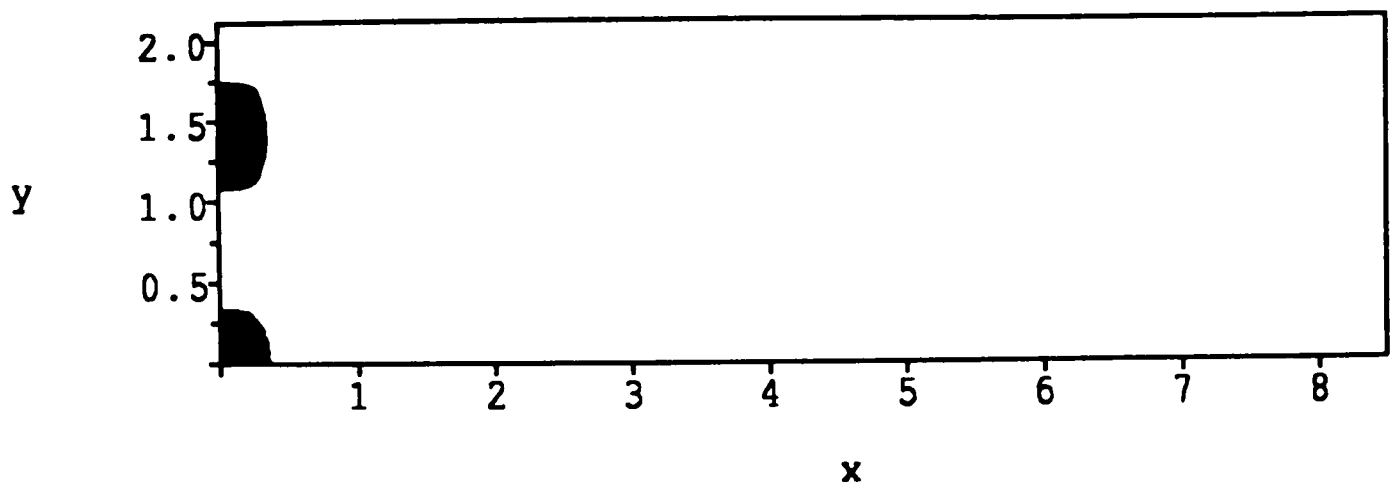

(a)

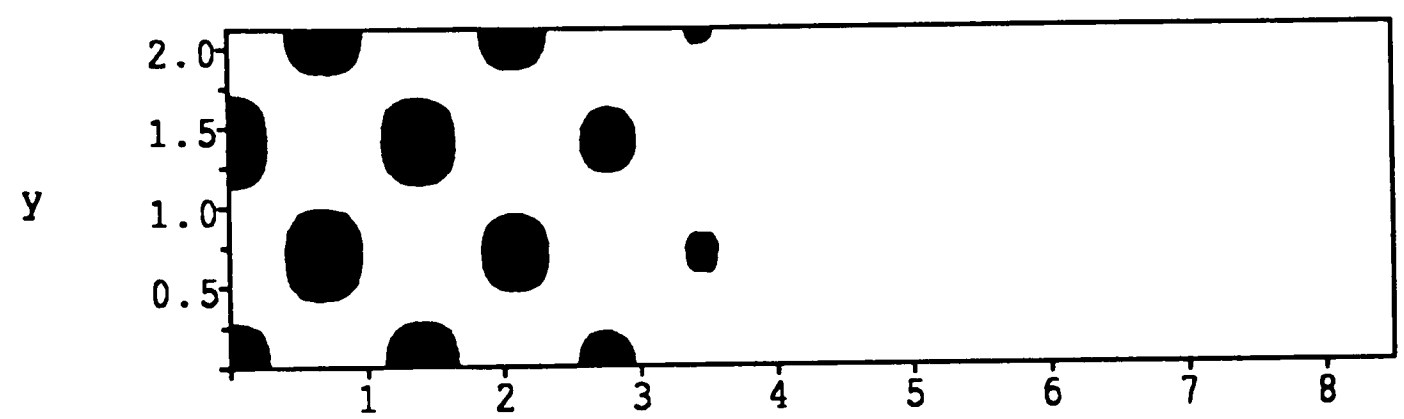

(b)

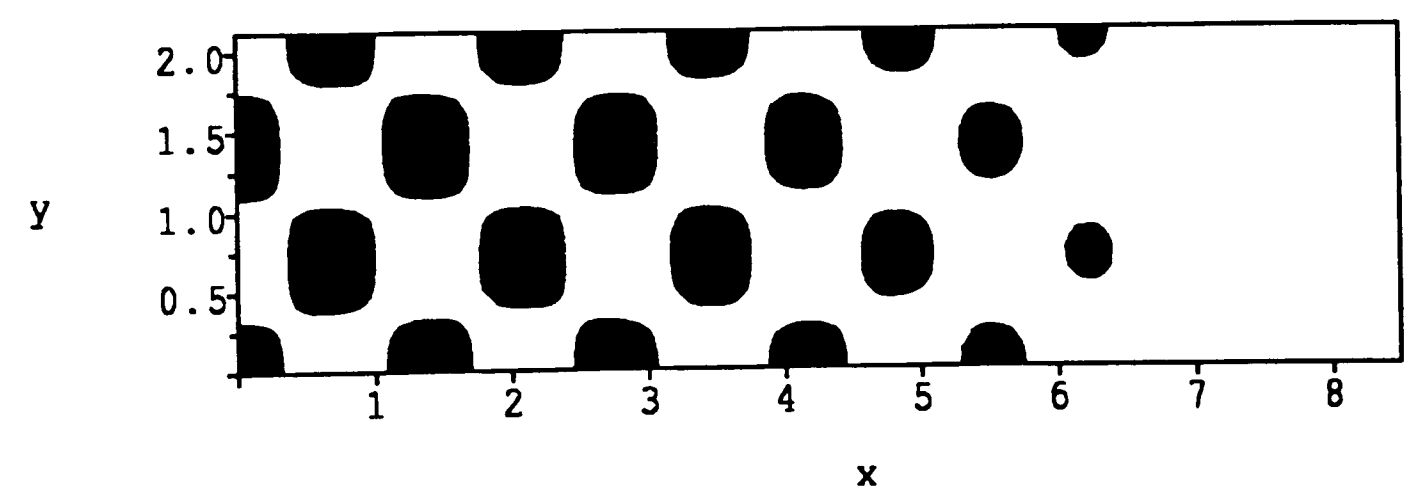

(c)

Figure 7.2: An initial half-row pattern in dermal cell density given at time $t = 0$ in a small region at one end of a rectangular domain (a), propagates through the domain as can be seen in (b) when $t = 3.0$ and (c) when $t = 6.0$ to form a regular chessboard pattern. Regions where the dermal cell density $n > 1.0$ are shade. The model parameters are as in Example 7.2.2.

wave of pattern formation might also differ from animal to animal complicates the matter even further. Here we focus on mechanisms for the sequential formation of feather buds on the chick back.

One could easily argue that the position of the feather buds are predefined and that their temporal initiation is due to the natural course of development as the skin grows. Davidson (1983a) demonstrated, however, that this is not the case. He cut two equivalent pieces of chick skin just beyond the most recently formed row of primordia. One of the pieces was stretched anteroposteriorly, while the other piece served as a control. Several of these experiments were performed at various stages of the pattern morphogenesis and different stretch factors were used. When the experiment was done where the first five rows or less had developed, the increase in the number of primordia per row was roughly proportional to the increase in the length of skin (see Figure 7.3). However, when more rows were present, stretching the skin did not have such a dramatic affect on the number of primordia which developed subsequently. Typical results of these experiments are shown in Table 7.1. Experimental results obtained earlier by McLachlan (1980) also confirms Davidson's (1983a) findings.

Since the positions of the primordia in the first five rows depend intricately on the local geometry of the skin, it is unlikely that they are predetermined. An invisible wave of determination at which the cells become committed to form primordia or interplumary skin, preceding the visible wave of morphogenetic activity, is thus indicated. Davidson's experiments suggest that, for the initial five rows, the wave of determination is almost immediately followed by feather primordia morphogenesis. However, this gap seems to widen as the waves progress.

Sengel (1976) (see, also Ede 1972 and Novel 1973) proposed that this wave of feather determination could in fact be a physical wave propagating immediately ahead of the visible primordia formation. Pattern propagation would then be the result of the transmission of a stimulus, either chemical or mechanical, that

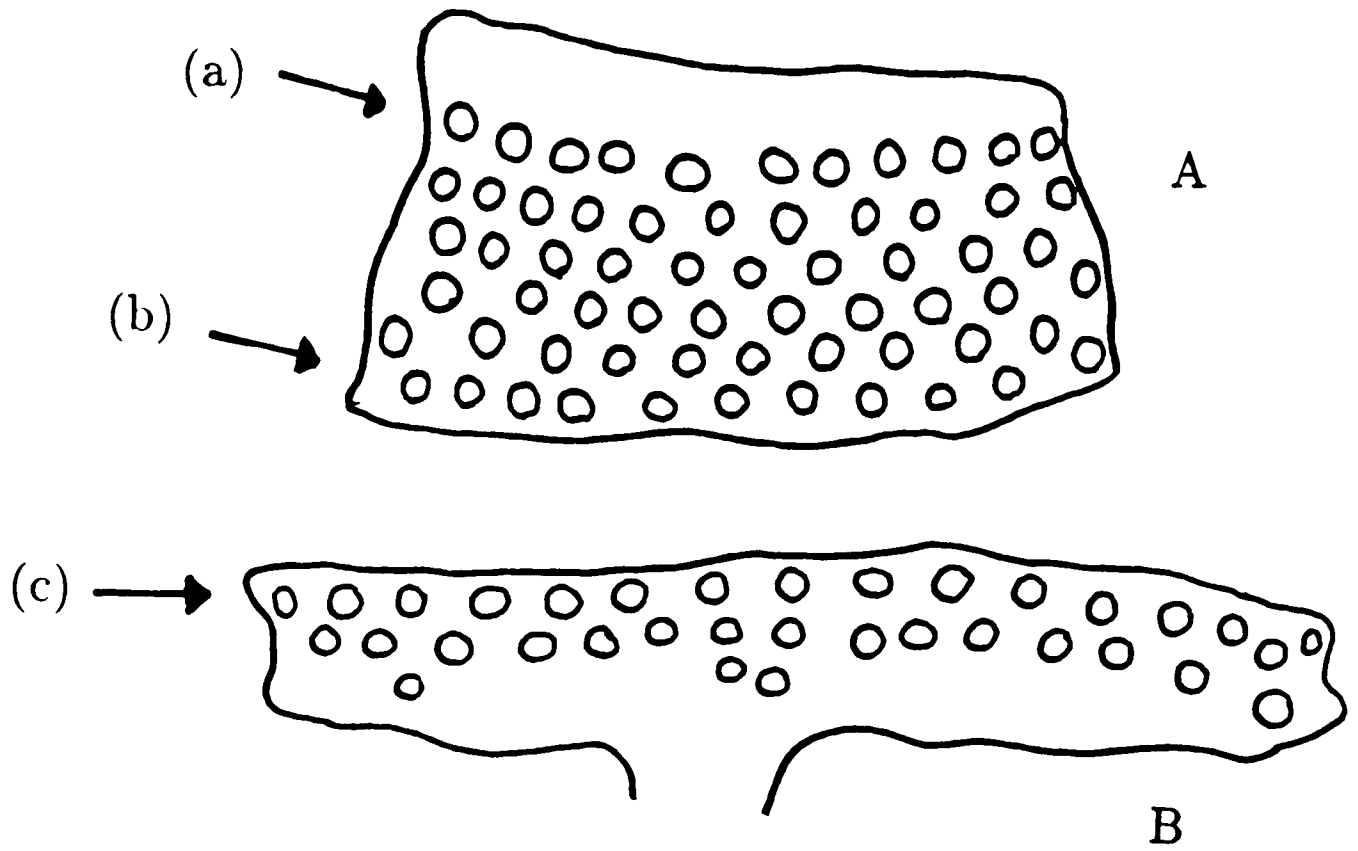

Figure 7.3: Tracings of feather primordia redrawn from the results of Davidson (1983a) in his investigation of the effect of stretched skin on the number of primordia per row. Chick skin from the dorsal back was cut immediately lateral to the most recently formed row (b) before explanted. The control piece (A) was explanted without stretching, while the other piece (B) was stretched. After two days in culture the first row in B, (c), comprises 16 primordia while the equivalent row in A, (a), comprises 11 primordia.

is passed along the cells so that each row of primordia induces the next one.

The experimental findings of Davidson (1983b), however, question this scenario. He cut chicken skin (*in vivo* and *in vitro*) parallel, and at angles to the dorsal midline, at various distances ahead of the developing patterns. This did not influence the time course of the developing primordia. (In his experimental work he considered a primordia as a visible dermal condensation combined with a visible epithelial placode.) The pattern on the operated skin was laid down at the same time as on the control skin and in the same well-defined rows as can, for example, be seen in Figure 7.4. In fact, even when the cut was so far away from the dorsal midline that the first primordia formed 48 hours after the

SPECIMEN	TREATMENT		RESULT	
	No. of rows at time of operation	Stretch factor as percentage	Primordia per stretched row	Primordia per control row
1	0	46	13	9
2	1	28	15	11
3	3	34	15	12
4	5	26	15	12
5	7	54	16	12
6	9	44	13	13
7	11	30	16	15

Table 7.1: Extract from the experimental results of Davidson (1983a). The number of primordia formed in the first row of the stretched skin is compared with the control. A second row usually also formed in the stretched skin with approximately the same number of primordia as in the first row. The stretch factor is the increase in the length of the stretched skin as percentage of the length of the control skin.

operation, the results were identical on the operated and control tissue. (As a new row forms every 6 hours this means the cut was made eight rows away from the developing pattern.) Very similar results were obtained by Lisenmayer (1972), although he only cut the skin a day in advance of the expected primordia formation, rather than at various distances as Davidson did.

In the light of his experimental observations, Davidson (1983b) argues that if the sequential pattern formation was caused by a physical propagating wave, the time course of the process would naturally have been interrupted by cutting the tissue. As this was not the case, the temporal development of primordia must therefore have been pre-programmed before the pattern developed.

This idea is common to several developmental phenomena. For example, a temporal gradient exists in amphibian somitogenesis where the sequence of pattern development is governed by an anteroposterior gradient in the time of somite formation. Both experiment (Elsdale & Pearson 1979) and theory (Cooke & Zeeman 1976) suggest that this temporal organization is crucial for

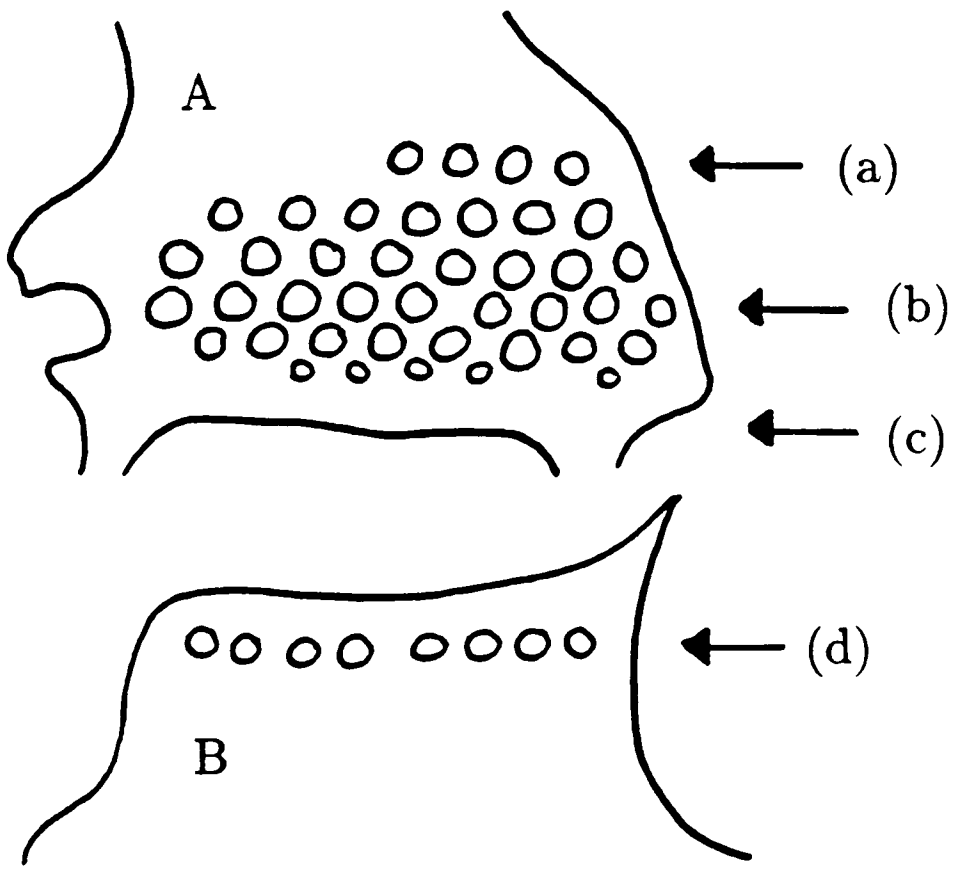

Figure 7.4: Tracings of feather primordia redrawn from the results of Davidson (1983b) in his investigation of the time course of primordia formation in transected skin. Skin from the dorsal back of a chick was cut along line (c) and explanted before the mid-dorsal line was visible. The tracings show the control piece (A) incorporating the mid-dorsal line (b) as well as the skin lateral to the cut (B) after 2 days in culture. Note that both the first row of primordia, (d), lateral to the cut as well as the equivalent row, (a) in the control skin, is in the process of forming. The row in the skin lateral to the cut is slightly advanced due to the cut.

development of regular somite pattern. A similar scenario in chick skin pattern formation is therefore a very attractive possibility.

It is unknown how these temporal gradients are established — they could possibly be a reflection of the way the tissue has become organized earlier in development. Lisenmayer (1972), for example, demonstrated that the direction of the morphogenetic wave is governed by the orientation of the dermis. Using this result Davidson (1983b) postulated that, by combining dermal tissue reconstituted from dissociated dermal cells with intact epidermis, it might be

possible to get *composite skin* in which feather primordia will develop. The primordia would form all at once, or in no particular order and on the present hypothesis an irregular pattern with roughly normal spacing will result. Such irregular patterns did indeed develop in the anti-L-CAM experiments of Gallin *et al* (1986) (see Section 2.2) which suggests a link between the cell adhesion molecules and the temporal wave of development.

From the experimental results it is possible to get some information on how such a temporal wave or gradient of determination could operate. For instance, although the periodicity of spatial pattern suggests that the spatiotemporal organization of the skin is a discontinuous row-by-row step-like event, the experiments of Davidson (1983b) indicate otherwise. The exact positions of the primordial rows were sensitive to spatial constraints at the cut boundary. The row immediately adjacent to the cut was slightly shifted (away from the dorsal midline) according to the position of the cut, see Figure 7.4. The following rows, however, did develop in their correct positions in relation to the first row beyond the cut. The time delay in the development of the first row beyond the cut differed by less than the interval between the development of successive rows. The time interval between the formation of subsequent rows, however, was as in the control skin, but temporally and spatially out of phase due to this initial shift. This suggests a continuous, rather than a row-by-row step-like, temporal gradient.

To summarize, the experiments of Davidson and others not only suggest the existence of a temporal wave of feather determination but also show that the feathers do not develop in predefined positions. By stretching the skin or cutting the skin one can influence the positions in which the buds develop. The wave of feather determination is therefore not a pre-pattern wave which determines the positions of the feather buds, it merely makes the skin continuously competent for primordia formation.

Moreover, the fact that the pattern is strongly dependent on the geometrical details of the tissue and the local position of neighbouring primordia correlates

well with the results obtained from our model. In the model, as we have seen in Chapter 4, the number of condensations that develops in the x- and y-directions on a given rectangular domain is directly proportional to the respective lengths of the domain.

One can conclude that skin pattern formation is not the result of gene expression alone, but is a process where the mechanical and chemical properties of the skin combined with geometrical aspects play a crucial role.

In the next section we examine whether our mathematical model could explain sequential pattern formation in a manner consistent with the experimental results discussed above.

7.4 A Switch Mechanism in Sequential Pattern Formation

The experimental evidence discussed in the previous section clearly indicates that feather bud patterns on the chick skin are not laid down by the natural propagating mechanism that was presented in Section 7.2. Such a mechanism resembles the physical wave of pattern determination as hypothesized by Sengel (1976). Apart from the experimental evidence against physical propagating mechanisms the results of the numerical simulations of Section 7.2 also contradicts the experimental findings discussed in the previous section.

Firstly, in the numerical solutions of Example 7.2.2 (see Figure 7.2), a gradual decrease in the pattern amplitude towards the leading edge of the travelling wave is evident. In feather bud formation however, this gradual change is not present — no feather primordia are observed more than one row lateral to the most recently developed row (Davidson 1983a).

Secondly, as was discussed in Section 7.2, the particular pattern that propagates across a domain is determined by the pattern specified initially, by an additional mechanism different from the model mechanism, at one end of the domain. Since the pattern that develops beyond a cut in the skin is laid down

in the same manner as the pattern that propagates initially from the dorsal midline, not only the initial row at the dorsal midline, but also the initial row which develops directly beyond a cut in the skin must be specified by this separate mechanism. The existence of such a mechanism, operating only under special circumstances in small specified domains, seems very unlikely.

In the light of the above experimental and numerical results the alternative theory, based on a temporal gradient of feather determination across the tissue, seems therefore to be more plausible than the mechanical propagating wave approach. Such a temporal wave or gradient may be thought of as *switching on* tissue to pattern formation. Nagorcka (1986) first introduced the concept of a temporal wave of determination in a reaction-diffusion based tissue interaction model for pattern formation.

His model, which was mentioned in Section 2.3, consists of a dermal switch mechanism controlling the epidermal morphogenesis. At any time during the pattern formation process a line, which Nagorcka (1986) calls a *switch boundary*, could be drawn dividing a region of tissue where the pattern has developed, from where it still has to develop. He introduced such a switch boundary in his model by assuming that the dermal switch mechanism has switched on the epidermal pattern formation process inside the boundary, while outside the boundary pattern formation remains switched off. We introduce a similar switch boundary to our model.

The addition of feather buds in the longitudinal direction is about five to ten times quicker than the addition of rows in the lateral direction (according to the observation made by Nagorcka (1986) of Gerber's (1937) work). Sequential pattern formation therefore continues laterally long after it has ended in the longitudinal direction. Since we would also like to explain sequential pattern formation beyond an experimental cut (see previous section) when the antero-posterior addition of feather buds have ceased, we therefore only concentrate on the lateral addition of new rows. Nagorcka (1986) however, experimented with various switch boundaries, for example ellipses, to account for the initial

longitudinal spread.

We use as switch boundary a line satisfying the parametric equation $x = vt$, where v is the speed of propagation. We assume v is positive so that the switch boundary moves in the positive x-direction away from $x = 0$ as time increases from $t = 0$. As before the zero-flux boundary conditions (4.2) are used.

We further assume that the switch mechanism resides in the dermis. It could, for example, be due to a change in production of the dermally produced chemical morphogen. In terms of our nondimensional parameters this would be reflected by a switch in τ. Alternatively, it may be due to a change in the chemotactic response of the dermal cells to the signal chemical received from the epidermis, which would be reflected by a switch in the parameter α. Since a decrease in the strength of the tethering of the epithelial layer through the basal lamina into the dermal layer causes pattern formation, one could also use the tethering parameter ρ as a switch. Presently, there is no good biological evidence for favouring any particular switch mechanism. Note that any of the parameters in the reduced small strain quasi-steady-state tissue interaction model can be used as a switch or bifurcation parameter.

For illustrative purposes we select ρ as bifurcation parameter and set

$$\rho(x,t) = \begin{cases} \rho_1 & \text{if } x \leq vt \\ \rho_2 & \text{if } x > vt \end{cases} \quad \text{where} \quad \rho_1 < \rho_c < \rho_2,$$

in which ρ_c is the critical value where the system bifurcates from a homogeneous steady state to patterned solutions. So, the uniform steady state is linearly unstable behind the switch boundary, but linearly stable beyond it. For notational convenience we shall denote the switch boundary by $\tilde{L}_x$ and the domain inside the switch boundary by $\tilde{\boldsymbol{B}} = (\tilde{L}_x, L_y)$. We assume that ρ_1 is such that there is only one unstable eigenvalue, say k_c^2. This distinguishes our work from that of Nagorcka (1986) who had a range of unstable eigenvalues. As initial conditions we specify small random perturbations about the homogeneous steady state across the whole domain.

So as to get an intuitive understanding of the problem we assume that our

developing solution in the domain $\tilde{\boldsymbol{B}}$ can be expressed in the linear form

$$\begin{pmatrix} \theta \\ n \end{pmatrix} = \begin{pmatrix} 0 \\ 1 \end{pmatrix} + \begin{pmatrix} 1 \\ M(k_c) \end{pmatrix} e^{\lambda(k_c^2)t} f(x, \tilde{L}_x) \cos \psi y, \tag{7.2}$$

where $M(k_c)$ is as in the linear analysis of Section 4.2, λ is the dispersion relation (2.14) and

$$\psi = \frac{\tilde{\psi}\pi}{L_y} \leq k_c^2 \quad \text{where} \quad \tilde{\psi} = 0, 1, 2, \ldots.$$

Note that this expression satisfies the zero-flux boundary conditions (4.2) at $y = 0$ and $y = L_y$. We assume that the function $f(x, \tilde{L}_x)$ is such that it satisfies the zero-flux boundary conditions at $x = 0$ and also at L_x when $\tilde{L}_x$ eventually reaches L_x.

Two numerical examples are now considered and in both we use the same parameters as in Example 4.4.1, but instead of α we consider ρ as bifurcation parameter. The unstable eigenvalue is $k_c^2 = 4\pi^2$ and we choose the switch parameter values as

$$\rho_1 = 18.239, \qquad \rho_2 = 21.239.$$

Example 7.4.1: In the first example the width of the domain is chosen as $L_y = 2.0$, while the length $L_x = 6\sqrt{2}$ so that $L_y \ll L_x$. Various values for the speed, v, of the travelling switch boundary were used. In all the cases its value was taken to be very small relative to the rate of pattern formation.

As the switch boundary moves away from $x = 0$ a stripe pattern perpendicular to the switch boundary is laid down, as can be seen in Figure 7.5. The developing solution adheres to the form of the expression (7.2) and in this case the value of $\tilde{\psi} = 4$, which is the maximum value that it can assume. Also when $\tilde{L}_x$ hits the boundary L_x, the value of $f(x, \tilde{L}_x) = 1$, which would be the solution predicted by a linear analysis on the whole domain $\boldsymbol{B}$.

It is important to note here that as the switch boundary moves out it selects, in terms of our approximate expression (7.2), the pattern with the highest integral mode number possible that can fit into the y-direction, that is, a value $\tilde{\psi} = 4$, rather than say 3, 2, 1 or even zero.

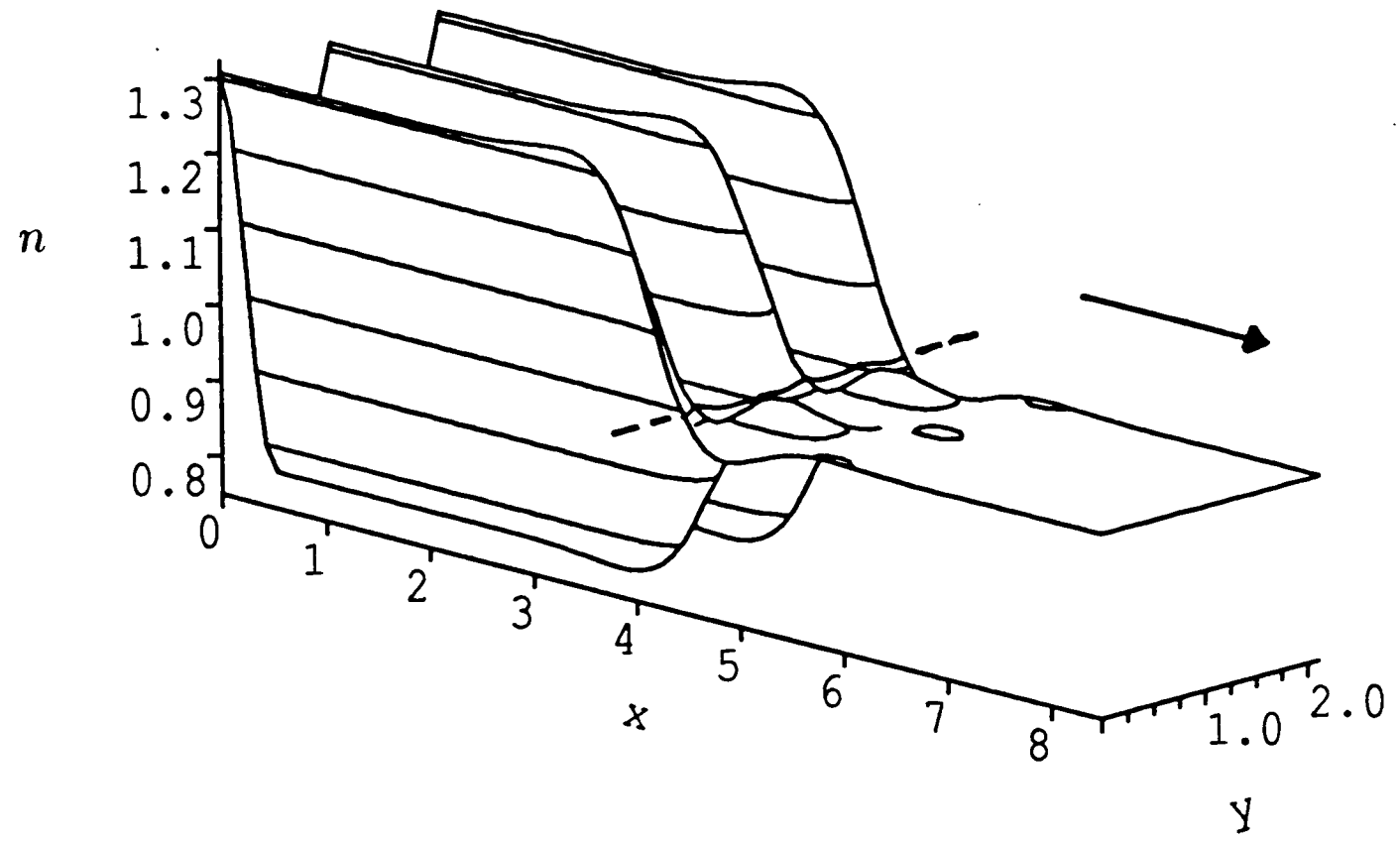

Figure 7.5: The isometric plot of the longitudinal stripes that develop in dermal cell density when a switch boundary, indicated by the broken line, moves away from $x = 0$. Here $L_x = 2.0$, ρ is used as switch function and the values of the parameters are as in Example 7.4.1.

We now examine a second example where the pattern that develops is such that $f(x, \tilde{L}_x) \neq 1$ for any $\tilde{L}_x = L_x$.

Example 7.4.2: Here we choose our domain length as before, but now choose the width as $L_y = 1.2\sqrt{2}$ so that the largest integral mode that can fit into the y-direction has mode number 3. Similar to Example 7.4.1, as the switch moves away from $x = 0$, stripes perpendicular to the switch boundary develop, but now $\tilde{\psi} = 3$ instead of 4. However, these stripes do not persist, and as the switch continues across the domain, they break up to form a rhombic pattern as can be observed in Figure 7.6. Again the system of equations was solved for different speeds of the moving switch boundary, but the same qualitative result was obtained in each case.

Why do the stripes break up into a rhombic pattern, whereas in the previous

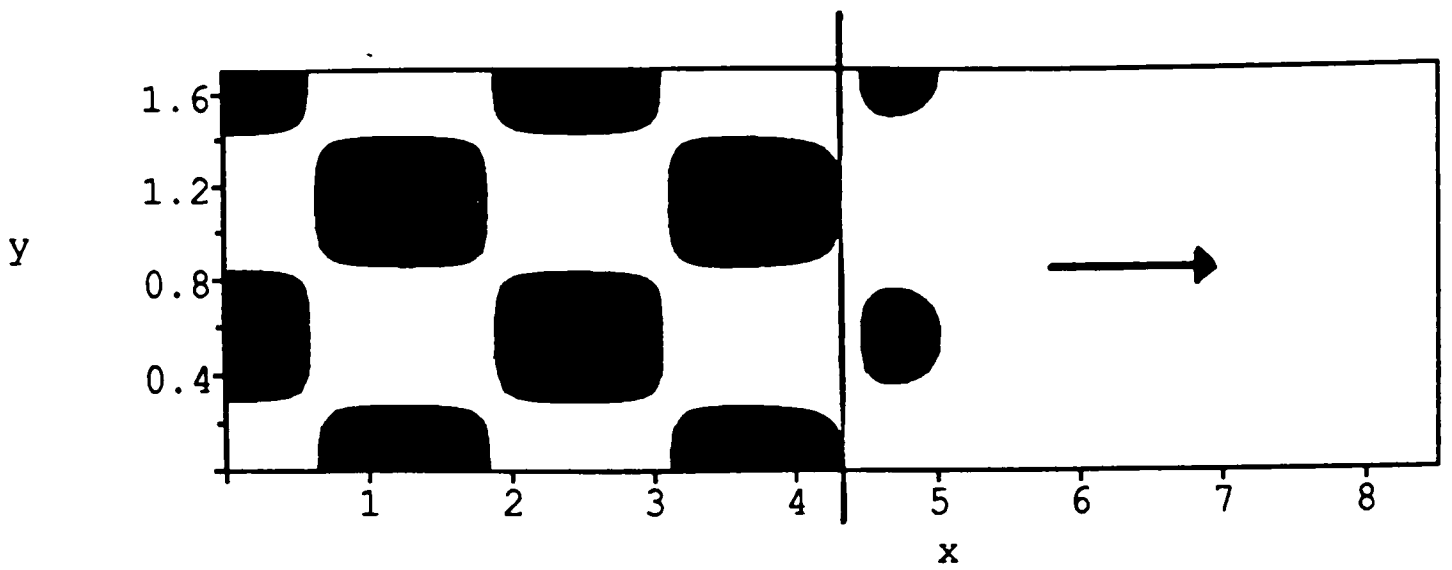

Figure 7.6: The contour plot of the rhombic pattern that develops in dermal cell density when a switch boundary, indicated by the heavy line, moves away from $x = 0$. Regions where $n > 1$ are shaded. Here $L_x = 1.2\sqrt{2}$, ρ is used as switch function and the values of the parameters are as in Example 7.4.1.

example they persisted? This is because, in terms of our linear approximation (7.2), the value of the y-component, ψ, of the wavevector $\boldsymbol{k}_c = (\phi, \psi)^T$ corresponding to the developing pattern is such that the x-component, ϕ, is forced to be non-zero so as to satisfy expression (7.1).

For the purpose of our explanation, we assume that $L_x = 4\sqrt{2}$. Thus when $\tilde{L}_x$ reaches L_x, to satisfy expression (7.1), $\tilde{\phi}$ must take the value 3. Thus the pattern which develops on this rectangular domain has the wavevector $\boldsymbol{k}_c = (3\pi/L_x, 3\pi/L_y)^T$, which is also the wavevector that the linear analysis on this domain would predict.

We computed several examples with different domain sizes and parameter values and found in all the cases that as the switch boundary travels away from the origin, the pattern that forms is such that $\tilde{\psi}$ takes the highest integer value that satisfies the constraint (7.1). So it seems that the pattern, corresponding to the wavevector with the largest possible y-component, always develops.

To simulate the typical chessboard-type pattern of primordia, as observed on the chick back, we must therefore choose our domain width L_y appropriately. When $\tilde{L}_x$ hits L_x we require the unstable wavevector $\boldsymbol{k}_c = (\phi, \psi)^T$ to be such

that it specifies a square pattern.

Without loss of generality we can assume that $L_x = L_y$. Hence,

$$\phi = \frac{\tilde{\phi}\pi}{L_y}, \qquad \psi = \frac{\tilde{\psi}\pi}{L_y} \quad \text{where} \quad \tilde{\phi}, \tilde{\psi} = 0, 1, 2, 3, \ldots.$$

We now calculate for which value of L_y the developing pattern's wavevector is such that $\tilde{\phi} = \tilde{\psi}$, which is the condition for a square pattern on a square domain.

As we have discussed above, the pattern which develops is the one with the highest possible integral mode that can fit into the y-direction. So that a pattern corresponding to the wavevector with the y-component $(\tilde{\psi} + 1)\pi/L_y$ cannot fit into the specified domain, we require that

$$\frac{(\tilde{\psi} + 1)^2\pi^2}{L_y^2} > k_c^2. \tag{7.3}$$

Also, from (7.1) it follows that

$$L_y^2 = \frac{(\tilde{\phi}^2 + \tilde{\psi}^2)\pi^2}{k_c^2}. \tag{7.4}$$

Combining (7.3) and (7.4) we get the inequality

$$2\tilde{\psi} + 1 - \tilde{\phi}^2 > 0. \tag{7.5}$$

Thus the required condition for square patterns, namely $\tilde{\psi} = \tilde{\phi}$, is satisfied only if $\tilde{\psi} = 1, 2$. So only chessboard patterns corresponding to the mode pairs $(1, 1)$ and $(2, 2)$ are possible. If $\tilde{\psi} > 2$ we are forced to choose $\tilde{\phi}$ much smaller than $\tilde{\psi}$ so as to satisfy inequality (7.5). In such cases rhombic patterns, as were shown in the previous example, will develop.

From the discussion above we saw that the chessboard arrangement of primordia, as seen on the chick back, can develop only for extremely narrow domains, that is, if the length of the initial row is less than or equal to two primordia. For larger domains, as in Example 7.4.2, a rhombic pattern will develop with the long sides of the rhombi perpendicular to the switch line. The anteroposterior rows on the chick back has initially about 9 and eventually about

16 primordia per row, thus, if the temporal gradient mechanism is to operate, a rhombic pattern, rather than a square pattern, should develop on the chick back.

Although Nagorcka (1986) did not isolate one particular eigenvalue in his work as we have done here, he nevertheless came to a similar conclusion. When the switch mechanism moved out slowly, stripes perpendicular to the switch boundary, developed. For high values of the speed v, rhombic patterns were selected. Nagorcka proposed a possible explanation for this phenomena, based on skin growth, which we can also be used to justify our model mechanism.

The longitudinal growth of the embryo is very rapid — Nagorcka (1986) observed from the experiments of Gerber (1939) that the length of the embryo increases from 8 mm to 20 mm from day $6\frac{1}{2}$ to day 8, which is the time span during which the primordia initiate. So he suggested that if this longitudinal growth is sufficiently fast the rhombic pattern could be stretched into the required square pattern.

That this longitudinal growth could indeed be sufficient to correct the pattern is not difficult to show. If we set $\tilde{\psi} = 18$, so as to represent the initial 9 feather germs, then, according to (7.5), $\tilde{\phi}$ can take on a maximum value of 6 so that rectangular patterns are laid down with the lateral side of a condensation three times the length of the anteroposterior side. Since the length of the embryo almost increases three times during the period of primordia initiation, the first few rows of the rhombic pattern could thus be stretched into a square pattern.

The switch boundary combined with our model equations could thus explain at least the first few rows of patterning. However, very fine tuning is required for the correct rhombic pattern to develop, since as we saw in the above examples, different domain widths give rise to completely different patterns.

The type of laterally stretched patterns obtained in Example 7.4.2 is also reminiscent of the observed arrangement of scales in a number of lizard species (see Cogger 1975). Since the temporal formation of scales in lizards is similar

to that of feather buds in the chicken (Maderson 1965a), a similar travelling switch boundary could therefore operate in lizard scale formation. Also, the patterns obtained in Example 7.4.1 agrees very well with the stripe formation on alligator skin as was discussed earlier. These examples suggest that our model mechanism could have a much wider applicability than only to chick feather bud formation.

Conclusion

The most intriguing feature of morphogenesis is the ability of organisms, tissues and cells to organize themselves into functional entities. This self organization occurs from the microscopic up to the macroscopic level. No single mechanism could explain the wide range of pattern and form that results. Even the very simple pattern formation processes are still beyond the understanding of today's scientists. However, by a combination of experimental and theoretical investigations we are gradually improving our understanding of certain aspects of pattern formation.

By using a theoretical modelling approach we examined here pattern formation on vertebrate skin. Although a large variety of models have been proposed for skin morphogenesis (see Chapter 1) we are still unable to explain this phenomenon satisfactorily. As new experimental evidence comes to light, previous models become obsolete and new improved versions have to be considered.

The aspect of tissue interaction (see Chapter 2), which forms the cornerstone of our model mechanism, has not been widely addressed before. Recent experimental evidence, however, emphasizes that interaction between various tissues plays a crucial role in skin morphogenesis. We used a mechanochemical approach in our modelling, rather than a reaction-diffusion pre-pattern approach, which allows us to relate the model mechanism much more closely to experimental facts. As far as we know, a mechanochemical based tissue interaction model has never been used before for examining pattern formation. In this sense our mechanism is a new and more accurate description of pattern formation processes in vertebrate skin.

We found that our mechanochemical tissue interaction system can explain synchronous patterning on both one-dimensional as well as two-dimensional spatial domains (see Chapters 3 and 4). A large variety of patterns, such as rolls, squares, rhombi and hexagons, all seen in nature, can be simulated.

Travelling fronts of morphogenetic activity are one of the most common ways in which development occurs. Contraction waves and waves of cell migration can both be simulated by our model mechanism (see Chapter 5). However, even more significant, is the ability of the tissue interaction system to generate sequential waves of patterning in both one- and two-dimensional spatial domains (see Chapters 6 and 7), in a manner consistent with experimental observation of many skin patterning processes.

It is evident that our mechanochemical tissue interaction model can simulate a large variety of the fundamental processes seen in pattern formation. Since it is believed that morphogenesis is driven by a few simple mechanisms only, this gives strong support for the mechanism we have proposed.

A large variety of mathematical and numerical techniques, including simple linear analyses, ordinary perturbation methods and multiple time-scale bifurcation techniques were used to examine the synchronous and sequential patterned solutions which the nonlinear model exhibits. Of particular interest is a new envelope method (Section 6.4) that was developed to measure the speed of propagating patterns. Also of significance is the two-dimensional nonlinear bifurcation analysis (Section 4.3) which generalizes previous analyses to more complex cases.

By a combination of mathematical and numerical analyses we have complimented the available experimental results to improve our understanding of one of the most interesting aspects of developmental biology. Using these analytical techniques we were able to examine the role of various subprocesses on the ultimate pattern formation. In this way new theoretical ideas were introduced and we also hope that novel experimental routes have been opened.

Some of the work presented in this thesis have already been published in Cruywagen & Murray (1992a), Cruywagen & Murray (1992b), Murray *et al.* (1992) and Cruywagen *et al.* (1992). Several other articles are still in preparation.

Appendix A

Numerical Methods

A.1 Introduction

We outline here the numerical method used for solving the small strain quasi-steady-state tissue interaction model both on one- and two-dimensional domains. Initially in Section A.2 a FORTRAN 77 computer programme, based on a finite difference scheme, is developed for the one-dimensional problem. To test the accuracy of this programme we can compare its results with those produced by NAG ROUTINE D03PGF (see Section 3.4) which uses Gear's method to solve a mixed system of parabolic and elliptic equations on one-dimensional domains. This programme is then adapted in Section A.3 for solving the reduced tissue interaction system on two-dimensional rectangular domains.

A.2 The One-Dimensional System

Recall that the one-dimensional reduced small strain quasi-steady-state system (3.10) is

$$\frac{\partial^2\theta}{\partial x^2} - \beta\frac{\partial^4\theta}{\partial x^4} + \tau\frac{\partial^2}{\partial x^2}\left\{\frac{n^2}{[1+\hat{\nu}(1-\theta)]^2+cn^2}\right\} = \rho\theta, \tag{A.1a}$$

$$\frac{\partial n}{\partial t} = -\alpha\frac{\partial}{\partial x}\left\{n\frac{\partial}{\partial x}\left(\frac{1-\theta}{1+\gamma n}\right)\right\}, \tag{A.1b}$$

with the zero-flux boundary conditions (3.2)

$$\frac{\partial n(0,t)}{\partial x} = 0, \qquad \frac{\partial n(L_x,t)}{\partial x} = 0, \tag{A.2a}$$

$$\frac{\partial \theta(0,t)}{\partial x} = 0, \qquad \frac{\partial \theta(L_x,t)}{\partial x} = 0, \tag{A.2b}$$

$$\frac{\partial^3 \theta(0,t)}{\partial x^3} = 0, \qquad \frac{\partial^3 \theta(L_x,t)}{\partial x^3} = 0, \tag{A.2c}$$

where L_x is the length of the domain. Note that the epithelial viscosity, the dermal logistic growth and the dermal diffusion terms are omitted, which means that μ, r and D are respectively equal to zero in (3.10). For the full system the methods described below must be adapted since it consists of two parabolic-type equations, instead of an elliptic and a parabolic-type equation.

Finite Difference Approximation

The system (A.1) consists of an ordinary fourth order differential equation in epithelial dilation coupled to a parabolic-type equation in dermal cell density. To solve the set of equations, we divide the spatial-time domain into discrete units. We solve the parabolic-type cell density equation by using a simple updating scheme in time. At each time level we then solve the ordinary differential equation for epithelial dilation.

We begin by presenting a generalized scheme for the parabolic-type equation (A.1b). We use the integer index i, $-2 \leq i \leq l_x + 2$, to discretize x into equal increments of size δx. The integer index k, $0 \leq k \leq l_t$, is used for discretizing time into equal increments of size δt. For a general variable $u(x,t)$, the value at the mesh point i, at time-step k, is denoted by

$$u(i\delta x, k\delta t) = u_i^k \quad \text{where} \quad -2 \leq i \leq l_x + 2 \quad \text{and} \quad 0 \leq k \leq l_t,$$

so that $u(0,t) = u(0,k\delta t)$ and $u(L_x,t) = u(l_x\delta x, k\delta t)$. We use the normal notation for finite difference equations where δ_x, the central difference operator, is defined as

$$\delta_x u_i^k = u_{i+\frac{1}{2}}^k - u_{i-\frac{1}{2}}^k,$$

and $i + \frac{1}{2}$ is a point halfway between the mesh points i and $i+1$ (Richtmeyer & Morton 1967). It is easy to show that

$$\begin{aligned}
\delta_x(\delta_x u_i^k) \equiv \delta_x^2 u_i^k &= u_{i+1}^k - 2u_i^k + u_{i-1}^k, \\
\delta_x(\delta_x^2 u_i^k) \equiv \delta_x^3 u_i^k &= u_{i+\frac{3}{2}}^k - 3u_{i+\frac{1}{2}}^k + 3u_{i-\frac{1}{2}}^k - u_{i-\frac{3}{2}}^k, \\
\delta_x(\delta_x^3 u_i^k) \equiv \delta_x^4 u_i^k &= u_{i+2}^k - 4u_{i+1}^k + 6u_{i+1}^k - 4u_{i-1}^k + u_{i-2}^k,
\end{aligned}$$

and similarly for the operator $\delta_t u_i^k$. Depending on the boundary conditions of the problem the boundary points are either externally specified or expressed in terms of the interior points.

In our generalized scheme we use a finite difference representation that approximates the partial differential equation (A.1b) at the point $(i\delta x, (k+\frac{1}{2})\delta t)$. A forward difference approximation is used for the time derivative, that is

$$\frac{\partial n}{\partial t} \approx \frac{1}{\delta t}\delta_t n_i^{k+\frac{1}{2}},$$

which has a leading error of $O(\delta t)$.

For approximating the other terms appearing in the parabolic equation we use a weighted average of central difference approximations at the time-steps k and $k+1$. For example, the discretisation of the diffusion term is

$$\frac{\partial^2 n}{\partial x^2} \approx \frac{1}{(\delta x)^2}\left[\phi\delta_x^2 n_i^{k+1} + (1-\phi)\delta_x^2 n_i^k\right],$$

with a leading error of $O((\delta x)^2)$ where $0 \leq \phi \leq 1$. We represent

$$\frac{\partial f}{\partial x} \approx \frac{1}{\delta x}\left[\phi\delta_x n_i^{k+1} + (1-\phi)\delta_x n_i^k\right],$$

where

$$f(x,t) = \frac{1-\theta}{1+\gamma n},$$

so

$$\begin{aligned}\frac{\partial}{\partial x}\left\{n\frac{\partial f}{\partial x}\right\} \approx\ & \frac{1}{(\delta x)^2}\left[\phi\left(n_{i+\frac{1}{2}}^{k+1}\delta_x f_{i+\frac{1}{2}}^{k+1} + n_{i-\frac{1}{2}}^{k+1}\delta_x f_{i-\frac{1}{2}}^{k+1}\right)\right. \\ & \left.+ (1-\phi)\left(n_{i+\frac{1}{2}}^{k}\delta_x f_{i+\frac{1}{2}}^{k} + n_{i-\frac{1}{2}}^{k}\delta_x f_{i-\frac{1}{2}}^{k}\right)\right],\end{aligned}$$

which is correct to $O((\delta x)^2)$.

The full finite difference approximation for the dermal cell density equation (A.1b) can now be written as

$$\begin{aligned}\frac{1}{\delta t}\delta_t n_i^{k+\frac{1}{2}} =\ & \frac{\alpha}{(\delta x)^2}\phi\left[\delta_x^2 n_i^{k+1} - \left(n_{i+\frac{1}{2}}^{k+1}\delta_x f_{i+\frac{1}{2}}^{k+1} + n_{i-\frac{1}{2}}^{k+1}\delta_x f_{i-\frac{1}{2}}^{k+1}\right)\right] \\ & + \frac{\alpha}{(\delta x)^2}(1-\phi)\left[\delta_x^2 n_i^k - \left(n_{i+\frac{1}{2}}^{k}\delta_x f_{i+\frac{1}{2}}^{k} + n_{i-\frac{1}{2}}^{k}\delta_x f_{i-\frac{1}{2}}^{k}\right)\right], \quad \text{(A.3)}\end{aligned}$$

which is valid for $0 \leq i \leq l_x$, $k \geq 0$ and $0 \leq \phi \leq 1$. Note that $\phi = 0$ gives the usual explicit finite difference scheme, $\phi = \frac{1}{2}$ the Crank-Nicholson scheme and $\phi = 1$ a fully implicit backwards time-difference scheme (see, for example, Smith 1985).

To analyse the stability and convergence properties of the above scheme we first refer to the simple linear heat equation

$$\frac{\partial n}{\partial t} = \frac{\partial^2 n}{\partial x^2}, \tag{A.4}$$

which can be written, in generalized finite difference form, as

$$\frac{1}{\delta t}\delta_t u_i^{k+\frac{1}{2}} = \frac{1}{(\delta x)^2}\left[\phi\delta_x^2 u_i^{k+1} + (1-\phi)\delta_x^2 u_i^k\right]. \tag{A.5}$$

It can be shown that this scheme is stable and convergent for $\frac{1}{2} \leq \phi \leq 1$. However, when $0 \leq \phi < \frac{1}{2}$ the condition

$$\frac{\delta t}{(\delta x)^2} \leq \frac{1}{2(1-2\phi)},$$

is required for stability and convergence (Smith 1985).

For nonlinear parabolic equations it is usually not possible to find bounds on δx and δt in terms of ϕ for which stability and convergence are ensured — even stronger bounds on δt than the above could be necessary. Although the stability properties of the linear heat equation do not necessarily carry over to nonlinear equations, one would expect the nonlinear equations to be stable and convergent when $\frac{1}{2} \leq \phi \leq 1$. For the purpose of our simulations we chose $\phi = \frac{1}{2}$.

We still have to introduce finite difference expressions for the zero-flux boundary conditions (A.2a), since in solving the equation (A.3) at $i = 0$ and $i = l_x$, we need the function values at the grid points $i = -1$ and $i = l_x + 1$. Using the approximation

$$\frac{\partial n}{\partial x} \approx \frac{1}{\delta x}\delta_x n_i^k,$$

we specify these values of n in terms of the internal points,

$$\delta_x n_0^k = \delta_x n_{l_x}^k = 0. \tag{A.6}$$

How these expressions are used to calculate the values of n^k_{-1} and $n^k_{l_x+1}$ shall be shown below.

At each time-step we also have to solve the ordinary differential equation (A.1a). Again the finite difference method is employed. As before the central difference approximations for the derivatives are used so that

$$\begin{aligned}\frac{\partial^2\theta}{\partial x^2} &\approx \frac{1}{(\delta x)^2}\delta_x^2\theta_i^k,\\ \frac{\partial^2 g}{\partial x^2} &\approx \frac{1}{(\delta x)^2}\delta_x^2 g_i^k,\end{aligned}$$

with a leading error of $O((\delta x)^2)$ and where

$$g(x,t) = \frac{n^2}{[1+\hat{\nu}(1-\theta)]^2 + cn^2}.$$

For approximating the fourth order spatial derivative of θ we use

$$\frac{\partial^4\theta}{\partial x^4} \approx \frac{1}{(\delta x)^4}\delta_x^4\theta_i^k,$$

which is correct to $O((\delta x)^4)$.

The full equation in finite difference format is written as

$$\frac{1}{(\delta x)^2}\delta_x^2\theta_i^k - \beta\frac{1}{(\delta x)^4}\delta_x^4\theta_i^k + \frac{\tau}{(\delta x)^2}\delta_x^2 g_i^k = \rho\theta_i. \tag{A.7}$$

In solving this equation at $i = 0, 1$ and $i = l_x - 1, l_x$ we need the values of θ at the grid points $i = -2$, $i = -1$ and $i = l_x + 1$, $i = l_x + 2$. As before, to find these values, we introduce the zero-flux boundary conditions (A.2). Our difference approximations for the zero-flux boundary conditions are

$$\delta_x\theta_0^k = \delta_x\theta_{l_x}^k = 0, \tag{A.8a}$$

$$\delta_x^3\theta_0^k = \delta_x^3\theta_{l_x}^k = 0. \tag{A.8b}$$

Numerical Algorithm

Now that we have approximated our system of partial differential equations (A.1) and boundary conditions (A.2) by a set of finite difference equations we can proceed to implement them as part of an algorithm.

We shall approximate a point halfway between two grid points by the average of the two closest points, for example

$$u_{i+\frac{1}{2}} = \frac{u_i + u_{i+1}}{2}.$$

Also note that by using the boundary conditions (A.6) and (A.8) the values of n_i^k, $i = -1, l_x + 1$ and θ_i^k, $i = -2, -1, l_x + 1, l_x + 2$ can be expressed in terms of the interior grid values of n and θ, for example

$$\begin{aligned} \theta_{-1}^k &= \theta_1^k \\ \theta_{-2}^k &= \theta_2^k - 2\theta_1^k + 2\theta_{-1}^k. \end{aligned}$$

At time-step $k = 0$, we specify the initial conditions for our system of equations at each grid point. Depending on the problem these could either be small random perturbations about the homogeneous steady state or an initial patterned solution. NAG FORTRAN routine G05CA5 was used to generate the random perturbations.

We now give a short descriptive outline of the algorithm used for solving the difference equations. As a first step the boundary points must be updated as is described above. Then, using the initial conditions, the finite difference equation for epithelial dilation (A.7) is solved at each grid point i, $0 \leq i \leq l_x$.

In general, at time-step k, one cannot solve (A.7) explicitly in terms of θ_i^k, since there are $l_x + 1$ nonlinear equations for the $l_x + 1$ grid points. We therefore use an iterative scheme to solve the equations numerically. As a first approximation the values of θ at time-step $k - 1$ are used. To speed up the process we make use of the Gauss-Seidel method (see, for example, Smith 1985), where the new value of a variable is used as soon as it is calculated. For example, if the nonlinear equations are iteratively updated from $i = 0$ to $i = l_x$ then in calculating say θ_2 we use the newly calculated values for θ_0 and θ_1 while the old values are used for θ_3 and θ_4. This iterative procedure is repeated until the values for θ converge. Note that after each iteration we use the boundary conditions (A.6) to update the values of θ at the points $i = -2, -1$ and $i = l_x + 1, l_x + 2$.

We also experimented with the successive over relaxation method as an alternative iterative scheme. In this scheme a relaxation factor is introduced in an attempt to accelerate the Gauss-Seidel method. Various values for the acceleration factor were tried but we failed to improve on the convergence speed of the Gauss-Seidel method.

Since equation (A.7) is nonlinear in θ_i^k, a nonlinear root finding procedure must be used to solve it at each grid point. To do this we use NAG FORTRAN routine C05AZF which locates a simple zero of a continuous function on a given interval by a combination of the methods of linear interpolation, extrapolation and bisection.

Using the solutions of the ordinary differential equations (A.7) at time-step k we proceed to solve the parabolic-type equation (A.3) for the next time-step $k+1$. Here again we have a system of l_x equations, one for each grid point, which is nonlinear in the unknown variables n_i^{k+1}. There is also an additional complication in that the value of θ^{k+1} is required in solving (A.3), although it has not yet been calculated from our ordinary differential equation at the time-step $k+1$. As an initial approximation however, we assume $\theta_i^{k+1} = \theta_i^k$.

To solve the system of l_x equations we again make use of an iterative Gauss-Seidel scheme. As before, the root of each finite difference equation (A.3) is solved using NAG routine C05AZF. As initial estimates to n_i^{k+1} we use the values calculated at the previous time-step, n_i^k. These values are then corrected iteratively until they converge. Note that after each iteration we use the boundary conditions to update the values of n at the grid points $i = -1$ and $i = l_x + 1$.

In principle one could now solve the elliptic equation at time-step $k+1$ to determine an updated value for θ_i^{k+1} as needed by the parabolic equation (A.3). This can then be used to calculate improved approximations for n at time-step $k+1$. One could repeat this procedure iteratively until the solutions converge for both n_i^{k+1} and θ_i^{k+1}. However, this would be very time-consuming. Fortunately we obtained good results without resorting to this extremely involved scheme.

Nevertheless, the procedure as described above is still very slow due to the nonlinear nature of the equations. We attempted to accelerate the computations by using a combination of an implicit and an explicit method. Rather than using a weighted average of the functions f and g, at the time-steps k and $k+1$, when solving the finite difference equations at time-step $k+1$, their values at time-step k were used. Unfortunately, this scheme proved to be unstable and we were forced to revert to the above discussed procedure.

In our computations we used time-steps of 0.01, while our space-steps varied from 0.05 to 0.01. In all the cases considered the scheme was stable and convergent. However, for spacings much smaller than the above, the scheme was unstable.

A.3 The Two-Dimensional System

Here we show how to extend the one-dimensional finite difference method to the two-dimensional problem (4.12)

$$\nabla^2\theta - \beta\nabla^4\theta + \tau\nabla^2\left\{\frac{n^2}{1+cn^2}\right\} = \rho\theta, \tag{A.9a}$$

$$\frac{\partial n}{\partial t} = D\nabla^2 n - \alpha\nabla\cdot(n\nabla(1-\theta)), \tag{A.9b}$$

where epithelial viscosity, μ, dermal logistic growth, r, and the interaction parameters γ and $\hat{\nu}$ have all been set to zero. If we restrict our problem to a rectangular domain, say $\boldsymbol{B}$, the boundary conditions are

$$(\boldsymbol{\eta}\cdot\nabla)n = 0, \quad (\boldsymbol{\eta}\cdot\nabla)\theta = 0, \quad (\boldsymbol{\eta}\cdot\nabla^3)\theta = 0, \quad \text{for } (x,y) \text{ on } \partial\boldsymbol{B} \tag{A.10}$$

where $\boldsymbol{\eta}$ is the unit normal vector on the boundary $\partial\boldsymbol{B}$, see (4.2).

We consider a rectangular spatial domain of dimensions $\boldsymbol{B} = (L_x, L_y)$ with grid spacing δx and δy in the x- and y-directions respectively. We again use the integer index i, $-2 \le i \le l_x + 2$, to discretize x into equal increments of size δx, while we use j, $-2 \le j \le l_x + 2$, to discretize y into equal increments of size δy. Now $L_x = l_x\delta x$ and $L_y = l_y\delta y$. The index k, $0 \le k \le l_t$, is again

used to discretize time into equal increments of size δt. The value of $n(\boldsymbol{x}, t)$ at the mesh point (i, j), at time-step k, is denoted by

$$n(i\delta x, j\delta y, k\delta t) = n_{i,j}^{k},$$

where $-2 \leq i \leq l_x + 2$, $-2 \leq j \leq l_y + 2$ and $0 \leq k \leq l_t$. The other variables are discretized similarly.

A finite difference approximation for the two-dimensional chemotaxis equation is

$$\frac{1}{\delta t}\delta_t n_{i,j}^{k+\frac{1}{2}} = \phi\left\{D\left(\frac{\delta_x^2}{(\delta x)^2} + \frac{\delta_y^2}{(\delta y)^2}\right) n_{i,j}^{k+1} - \alpha\left(\frac{n_{i+\frac{1}{2},j}^{k+1}\delta_x f_{i+\frac{1}{2},j}^{k+1,j} + n_{i-\frac{1}{2},j}^{k+1}\delta_x f_{i-\frac{1}{2},j}^{k+1}}{(\delta x)^2}\right.\right.$$
$$\left.\left. + \frac{n_{i,j+\frac{1}{2}}^{k+1}\delta_y f_{i,j+\frac{1}{2}}^{k+1} + n_{i,j-\frac{1}{2}}^{k+1}\delta_y f_{i,j-\frac{1}{2}}^{k+1}}{(\delta y)^2}\right)\right\} + (1-\phi)\left\{D\left(\frac{\delta_x^2}{(\delta x)^2} + \frac{\delta_y^2}{(\delta y)^2}\right) n_{i,j}^{k}\right.$$
$$\left. - \alpha\left(\frac{n_{i+\frac{1}{2},j}^{k}\delta_x f_{i+\frac{1}{2},j}^{k} + n_{i-\frac{1}{2},j}^{k}\delta_x f_{i-\frac{1}{2},j}^{k}}{(\delta x)^2} + \frac{n_{i,j+\frac{1}{2}}^{k}\delta_y f_{i,j+\frac{1}{2}}^{k} + n_{i,j-\frac{1}{2}}^{k}\delta_y f_{i,j-\frac{1}{2}}^{k}}{(\delta y)^2}\right)\right\},$$

where

$$f(x, y) = \frac{n^2}{1 + cn^2}.$$

This equation is valid for $0 \leq i \leq l_x$, $0 \leq j \leq l_y$ and $k \geq 0$. The corresponding discretized zero-flux boundary conditions are

$$\delta_x n_{0,j}^{k} = 0, \qquad \delta_x n_{l_x,j}^{k} = 0, \qquad \text{for} \quad -1 \leq j \leq l_y + 1,$$
$$\delta_y n_{i,0}^{k} = 0, \qquad \delta_y n_{i,l_y}^{k} = 0, \qquad \text{for} \quad -1 \leq i \leq l_y + 1,$$

The elliptic equation expressed in terms of a finite difference equation is

$$\frac{\delta_x^2\theta_{i,j}^{k}}{(\delta x)^2} + \frac{\delta_y^2\theta_{i,j}^{k}}{(\delta y)^2} - \beta\left\{\frac{\delta_x^4\theta_{i,j}^{k}}{(\delta x)^4} + \frac{2\delta_x^2\delta_y^2\theta_{i,j}^{k}}{(\delta x)^2(\delta y)^2} + \frac{\delta_y^4\theta_{i,j}^{k}}{(\delta y)^4}\right\} + \frac{\delta_x^2\tau g_{i,j}^{k}}{(\delta x)^2} + \frac{\delta_y^2\tau g_{i,j}^{k}}{(\delta y)^2} = \rho\theta_{i,j}^{k},$$

where

$$g(x, t) = \frac{1-\theta}{1+\gamma n}.$$

For this equation our finite difference boundary conditions (A.10), are

$$\delta_x\theta_{0,j}^{k} = 0, \qquad \delta_x\theta_{l_x,j}^{k} = 0, \quad \text{for} \quad -1 \leq j \leq l_y + 1,$$
$$\delta_y\theta_{i,0}^{k} = 0, \qquad \delta_y\theta_{i,l_y}^{k} = 0, \quad \text{for} \quad -1 \leq i \leq l_x + 1,$$

and

$$\left\{\frac{\delta_x^3}{(\delta x)^3}+\frac{\delta_x\delta_y^2}{(\delta x)(\delta y)^2}\right\}\theta_{0,j}^k=0,\quad \left\{\frac{\delta_x^3}{(\delta x)^3}+\frac{\delta_x\delta_y^2}{(\delta x)(\delta y)^2}\right\}\theta_{l_x,j}^k=0,\quad \text{for } 0\le j\le l_y,$$

$$\left\{\frac{\delta_y^3}{(\delta y)^3}+\frac{\delta_y\delta_x^2}{(\delta x)(\delta y)^2}\right\}\theta_{i,0}^k=0,\quad \left\{\frac{\delta_y^3}{(\delta y)^3}+\frac{\delta_y\delta_x^2}{(\delta x)(\delta y)^2}\right\}\theta_{i,l_y}^k=0,\quad \text{for } 0\le i\le l_x.$$

Again, as in the one-dimensional case, we approximated variable values halfway between two grid points by the average of the two closest points. The boundary points can thus be expressed in terms of the interior points, for example

$$\begin{aligned}\theta_{-1,j}^k &= \theta_{1,j}^k \quad \text{for } -1\le j\le l_y+1,\\ \theta_{-2,j}^k &= \theta_{2,j}^k-2\theta_{1,j}^k+2\theta_{-1,j}^k+\frac{(\delta x)^2}{(\delta y)^2}[\theta_{1,j+1}^k-2\theta_{1,j}^k+\theta_{1,j-1}^k\\ &\quad -\theta_{-1,j+1}^k+2\theta_{-1,j}^k-\theta_{-1,j-1}^k \quad \text{for } 0\le j\le l_y.\end{aligned}$$

A similar algorithm to the one described in the previous section for the one-dimensional system can now be used. Stable and convergent solutions were found when $\delta t = 0.01$ and $0.05 \le \delta x, \delta y \le 0.01$. However, as in the one-dimensional case, for space-steps too small the scheme becomes unstable.

References

Abercrombie, M., Heaysman, J.E.M., Pegrum, S.M. (1970). The locomotion of fibroblast in culture. III. Movements of particles on the dorsal surface of the leading lamella. *Exp. Cell Res.* **62**, 389–398.

Alberts, B., Bray, D., Lewis, J., Raff, M., Roberts, K., Watson, J.D. (1989). *Molecular Biology of the Cell.* 2nd ed. New York, London: Garland Publishing, Inc.

Atkinson, K.E. (1978). *An Introduction to Numerical Analysis.* New York: John Wiley & Sons.

Belintsev, B.N., Beloussov, L.V., Zaraisky, A.G. (1987). Model of pattern formation in epithelial morphogenesis. *J. theor. Biol.* **129**, 369–394.

Beloussov, L.V., Dorfman, J. G., Cherdantzev, V.G. (1975). Mechanical stresses and morphological patterns in amphibian embryos. *J. Embryol. exp. Morph.* **34**, 559–574.

Bentil, D.E., Murray, J.D. (1990). Pattern selection in biological pattern formation mechanisms. *Appl. Math. Lett.* **4(3)**, 1–6.

Berridge, M.J. (1988). Inositol lipids and calcium signalling. *Proc. R. Soc. Lond. (Biol.)* **234**, 359–378.

Beug, H., Gerisch, G., Kempff, S., Riedel, V., Cremer, G. (1970). Specific inhibition of cell contact formation in *Dictyostelium* by univalent antibodies. *Exp. Cell. Res.* **63**, 147–158.

Beug, H., Katz, F.E., Gerisch, G. (1973). Dynamics of antigenic membrane sites relating to cell aggregation in *Dictyostelium discoideum. J. Cell Biol.* **56**, 647–658.

Bradbury, J.M., Gross, J.D. (1989). The effect of ammonia on cell-type-specific enzyme accumulation in *Dictyostelium discoideum*. *Cell Differ. Dev.* **27**, 121–128.

Bray, D., White, J.G. (1988). Cortical flow in animal cells. *Science* **239**, 883–888.

Bretscher, M.S. (1984). Endocytosis: relation to capping and cell locomotion. *Science* **224**, 681-686.

Bretscher, M.S. (1987). How animal cells move. *Sci. Am.* **257(6)**, 44–51.

Bretscher, M.S. (1989). Particle migration on cells. *Nature* **341**, 491–492.

Brickell, P.M., Tickle, C. (1989). Morphogens in Chick Limb Development. *BioEssays* **11(5)**, 145–149.

Cheer, A., Nuccitelli, R., Oster, G.F., Vincent, J.-P. (1987). Cortical activity in vertebrate eggs. I. The activation waves. *J. theor. Biol.* **124**, 377–404.

Cheng, L.Y., Murray, J.D., Odell, G.M., Oster, G.F. (1986). The cortical tractor: a new model for epithelial morphogenesis. *Lect. Notes Biol.* **71**, 209–216.

Choung, C.-M., Edelman, G.M. (1985a). Expression of cell adhesion molecules in embryonic induction. I. Morphogenesis of nestling feathers. *J. Cell Biol.* **101**, 1009–1026.

Choung, C.-M., Edelman, G.M. (1985b). Expression of cell adhesion molecules in embryonic induction. I. Morphogenesis of adult feathers. *J. Cell Biol.* **101**, 1027–1043.

Cogger, H.G. (1975). *Reptiles and amphibians of Australia.* Sydney: A.H. & A.W. Reed.

Cooke, J., Zeeman, E.C. (1976). A clock and wavefront model for the control of the number of repeated structures during animal morphogenesis. *J. theor. Biol.* **58**, 455-476.

Cruywagen, G.C., Maini, P.K., Murray, J.D. (1992). Sequential pattern formation in a model for skin morphogenesis. *IMA J. Math. Applied in Medic. & Biol.* (submitted)

Cruywagen, G.C., Murray, J.D. (1992a). On a tissue interaction model for skin pattern formation. *J. Nonlinear Sci.* **2**, 217–240.

Cruywagen, G.C., Murray J.D. (1992b). A new tissue interaction model for dermal-epidermal skin patterns. In: *Proceedings of the 1st European Conference on the Application of Mathematics to Medicine and Biology.* (eds. J. Demongeot & V. Capasso), Heidelberg: Springer Verlag. (in press)

Darnell, J., Lodish, H., Baltimore, D. (1986). *Molecular Cell Biology.* New York: Scientific American Books.

Davidson, D. (1983a). The mechanism of feather pattern development in the chick. I. The time determination of feather position. *J. Embryol. exp. Morph.* **74**, 245–259.

Davidson, D. (1983b). The mechanism of feather pattern development in the chick. II. Control of the sequence of pattern formation. *J. Embryol. exp. Morph.* **74**, 261-273.

Dembo, M., Harris, A.K. (1981). Motion of particles adhering to the leading lamellae of crawling cells. *J. Cell Biol.* **91**, 528–536.

Dee, G., Langer, J.S. (1983). Propagating pattern selection. *Physical Review Letters* **50**, 383–386.

Devreotos, P., Zigmond, S.H. (1988). Chemotaxis in *Eukaryotic* cells. *Ann. Rev. Cell. Biol.* **4**, 649-686.

Dew, P.M., Walsh, J.E. (1981). A set of library routines for solving parabolic equations in one space variable. *ACM Trans. Math. Soft.* **7(3)**, 295–314.

Dhouailly, D. (1973). Dermo-epidermal interactions between birds and mammals: differentiation of cutaneous appendages. *J. Embryol. exp. Morph.* **30**, 587–603.

Dhouailly, D. (1975). Formation of cutaneous appendages in dermo-epidermal recombination between reptiles, birds and mammals. *Wilhelm Roux's Arch. devl. Biol.* **177**, 323–340.

Dhouailly, D., Maderson, P.F.A. (1984). Ultrastructural observations on the embryonic development of the integument of *Lacerta muralis (Lacertilia, Reptilia). J. Morph.* **179**, 203–228.

Ede, D. (1972). Cell behaviour and embryonic development. *Int. J. Neuroscience* **3**, 165–174.

Edelman, G.M. (1984). Cell adhesion and morphogenesis: The regulator hypothesis. *Proc. Natl. Acad. Sci. USA* **81**, 1460-1464.

Edelman, G.M. (1985). Cell adhesion and the molecular process of morphogenesis. *Ann. Rev. Biochem.* **54**, 135-169.

Edelman, G.M. (1986). Cell adhesion molecules in the regulation of animal form and tissue pattern. *Annu. Rev. Cell Biol.* **2**, 81–116.

Edelman, G.M. (1988). Morphoregulatory molecules. *Biochemistry* **27(10)**, 3533–3543.

Edelman, G.M., Hoffman, S., Chuong, C.-M., Cunningham, B.A. (1985). The molecular bases and dynamics of cell adhesion in embryogenesis. In: *Molecular Determinants of Animal Form.* UCLA Symposia on Molecular and Cellular Biology. (new series) vol. 31 (ed. G.M. Edelman), 195–221, New York: Alan R. Liss, Inc.

Edmund, A.G. (1969). Dentition. In: *Biology of the Reptilia.* (Morphology A) vol. 1 (eds. A. d'A. Bellairs & T.S. Parsons), 117–200. London: Academic Press.

Elsdale, T., Pearson, M. (1979). Somitogenesis in Amphibia. II. Origins in early embryogenesis of two factors involved in somite specification. *J. Embryol. exp. Morph.* **22**, 253–264.

Erikson, C.A. (1990). Cell migration and adult organism. *Curr. Op. Cell. Biol.* **2**, 67–74.

Fife, P.C. (1979). Mathematical Aspects of Reacting and Diffusing Systems. *Lect. Notes in Biomathematics* **28**, Heidelberg: Springer Verlag.

Gallin, W.J., Chuong, C.-M., Finkel, L.H., Edelman, G.M. (1986). Antibodies to liver cell adhesion molecules perturb inductive interactions and alter feather pattern and structure. *Proc. Natl. Acad. Sci. USA* **83**, 8235–8239.

Gerber, A. (1939). Die embryonale und postembryonale Pterylose der Alectromorphae. *Rev. Suisse Zool.* **46**, 161-324.

Gerish, G. (1986). Interrelation of cell adhesion and differentiation in *Dictyostelium discoideum. J. Cell Sci.* **4** (supplement), 201–219.

Gilbert, S.F. (1988). *Development Biology.* 2nd ed. Sunderland: Sinauer Associates, Inc.

Goodwin, B.C. (1984). Calcium is a candidate for the morphogen in *Acetabularia.* European Developmental Biology Congress, Southampton. *J. Embryol. exp. Morph.* **82** (supplement), 171.

Grumet, M., & Edelman, G.M. (1988). Neuron-glia cell adhesion molecules interacts with neurons and astroglia via different binding mechanisms. *J. Cell Biol.* **106**, 487-503.

Harris, A.K., Dunn, G. (1972). Centripetal transport of attached particles

on both surfaces of moving fibroblast. *Expl. Cell Res.* **73**, 519–5238.

Harris, A.K., Stopak, D., Wild, D. (1981). Fibroblast traction as a mechanism for collagen morphogenesis. *Nature* **290**, 249-251.

Hay, E. D. (1981). *Cell Biology of Extracellular Matrix.* New York: Plenum.

Hoffman, S., Edelman, G.M. (1983). Kinetics of homophylic binding by embryonic and adult forms of the neural cell adhesion molecule. *Proc. Natl. Acad. Sci. USA* **80**, 5762–5766.

Holtfreter, J. (1943). A study of the mechanics of gastrulation. Part I. *J. Exp. Zool.* **94**, 261–318.

Holtfreter, J. (1944). A study of the mechanics of gastrulation. Part II. *J. Exp. Zool.* **95**, 171–212.

Jacobson, A.G., Oster, G.F., Odell, G.M. (1985). The cortical tractor model for epithelial folding: application to the neural plate. In: *Molecular Determinants of Animal Form.* UCLA Symposia on Molecular and Cellular Biology. (new series) vol. 31 (ed. G.M. Edelman), 143–167, New York: Alan R. Liss, Inc.

Jacobson, A.G., Oster, G.F., Odell, G.M., Cheng, L.Y. (1986). Neuralation and the cortical tractor model for epithelial folding. *J. Embryol. exp. Morph.* **96**, 19–49.

Jordan, D.W., Smith, P. (1987). *Nonlinear Ordinary Differential Equations.* 2nd ed. Oxford: Clarendon Press.

Kay, R., Gross, J., Peachy, M., Jermyn, K., Dkokia, B., Kopachik, W., Brookman, J., Pogge, R. (1984). *Dictyostelium* morphogens and how they might act. European Developmental Biology Congress, Southampton. *J. Embryol. exp. Morph.* **82** (supplement), 173.

Keener, J.P. (1988). *Principles of Applied Mathematics, Transformation and*

Approximation. Reading, Mass.: Addison Wesley.

Kimelman, D., Kirschner, M. (1987). Synergistic induction of mesoderm by FGF and TGF-beta and the identification of a mRNA coding for FGF in the early *Xenopus* embryo. *Cell* **51**, 869–877.

Kolmogoroff, A., Petrovsky, I., Piscounoff, N. (1937). Étude de l'équation de la diffusion avec croissance de la quantité de matière et son application à un problème biologique. *Moscow Univ. Bull. Math.* **1**, 1–25.

Kolega, J. (1986). Effects of mechanical tension on protrusive activity and microfilament and intermediate filaments organization in an epithelium moving in culture. *J. Cell Biol.* **102**, 1400–1411.

Korn, E.D., Hammer, J.A. (1988). Myosins of nonmuscle cells. *Annu. Rev. Biophys. Biophys. Chem.* **17**, 23–45.

Lane, D.C., Murray, J.D., Manoranjan, V.S. (1987). Analysis of wave phenomena in a morphogenetic mechanochemical model and an application to post-fertilisation waves on eggs. *IMA J. Math. Applied in Medic. & Biol.* **4**, 309–331.

Landau, L.D., Lifshitz, E.M. (1970). *Theory of Elasticity.* 2nd ed. New York: Pergamon.

Lisenmayer, T. (1972). Control of integumentary patterns in the chick. *Devl. Biol.* **27**, 244–271.

Maderson, P.F.A. (1965a). The embryonic development of the squamate integument. *Acta Zool.* **46**, 275–295.

Maderson, P.F.A. (1965b). The structure and development of the squamate epidermis. In: *Symposium on the Biology of the Skin and Hair Growth.* (eds. A.G. Lyne & B.F. Short), 129–153, Sydney: Angus and Robertson.

Matkowsky, B.J. (1970). Nonlinear dynamic stability: a formal theory. *SIAM*

J. Appl. Math. **18**, 872–883.

McClay, D.R., Ettensohn, C.A. (1987). Cell adhesion in morphogenesis. *Annu. Rev. Cell Biol.* **3**, 319–345.

McKeehan, M.S. (1951). Cytological aspects of embryonic lens induction in the chick. *J. Exp. Zool.* **117**, 31–64.

McLachlan, J.C. (1980). The effect of 6-aminonicotinamide on limb development. *J. Embryol. exp. Morph.* **55**, 307–318.

Meinhardt, H. (1982). *Models of Biological Pattern Formation.* London: Academic Press.

Mollison, D. (1977). Spatial contact models for ecological and epidemic spread. *J. Roy. Stat. Soc.* **B39**, 283–326.

Mooney, J.D., Nagorcka, B.N. (1985). Spatial patterns produced by a reaction-diffusion system in primary hair follicles. *J. theor. Biol.* **115**, 229–317.

Moscana, A.A. (1952). Cell suspensions from organ rudiments of chick embryos. *Exp. Cell Res.* **3**, 536–539.

Maini, P.K., Murray, J.D. (1988). A nonlinear analysis of a mechanochemical model for biological pattern formation. *SIAM J. Appl. Math.* **48(4)**, 1064–1072.

Murray, J.D. (1977). *Nonlinear Differential Equation Models in Biology.* Oxford: Clarendon Press.

Murray, J.D. (1984). *Asymptotic Analysis.* 2nd ed. Heidelberg: Springer Verlag.

Murray, J.D. (1989). *Mathematical Biology.* Heidelberg: Springer Verlag.

Murray, J.D., Cruywagen, G.C., Maini, P.K. (1992). Pattern Formation in Tissue Interaction Models. In: *Lect. Notes in Biomathematics.* vol. **100** (ed.

S. Levin), Heidelberg: Springer Verlag. (in press)

Murray, J.D., Deeming, D.C., Ferguson, M.W.J. (1990). Size dependent pigmentation pattern formation in embryos of *Alligator Mississipiensis*: time of initiation of pattern generation mechanism. *Proc. Roy. Soc.* **B239**, 279–293.

Murray, J.D., Oster, G.F. (1984a). Cell traction models for generating pattern and form in morphogenesis. *J. Math. Biol.* **19**, 265-279.

Murray, J.D., Oster, G.F. (1984b). Generation of biological pattern and form. *IMA J. Maths. Appl. Med. & Biol.* **1**, 51-75.

Murray, J.D., Oster, G.F., Harris, A.K. (1983). A mechanical model for mesenchymal morphogenesis. *J. Math. Biol.* **17**, 125-129.

Myerscough, M.R., Murray, J.D. (1992). Analysis of propagating pattern in a chemotaxis system. *Bull. Math. Biol.* **54**, 77–94.

Nagorcka, B.N. (1984). Evidence for a reaction-diffusion system in the formation of hair fibres. *Biosystems* **16**, 323–332.

Nagorcka, B.N. (1986). The role of a reaction-diffusion system in the initiation of skin organ primordia. I. The first wave of initiation. *J. theor. Biol.* **121**, 449–475.

Nagorcka, B.N., Manoranjan, V.S., Murray, J.D. (1987). Complex spatial patterns from tissue interactions — an illustrative model. *J. theor. Biol.* **128**, 359–374.

Nagorcka, B.N., Mooney, J.D. (1982). The role of a reaction-diffusion system in the formation of hair fibres. *J. theor. Biol.* **98**, 575–607.

Nagorcka, B.N., Mooney, J.D. (1985). The role of a reaction-diffusion system in the initiation of primary hair follicles. *J. theor. Biol.* **114**, 243–272.

Novel, G. (1973). Feather pattern stability and reorganization in cultured

skin. *J. Embryol. exp. Morph.* **30**, 605–633.

Odell, G.M., Bonner, J.T. (1986). How the *Dictyostelium Discoideum Grex* crawls. *Phil. Trans. R. Soc. Lond.* **B312**, 487-525.

Odell, G.M., Oster, G., Alberch, P., Burnside, B. (1981). The mechanical basis of morphogenesis. I. Epithelial folding and invagination. *Dev. Biol.* **85**, 446–462.

Oster, G.F. (1984). On the crawling of cells. *J. Embryol. exp. Morph.* **83** (supplement), 329–364.

Oster, G.F., Murray, J.D., Harris, A.K. (1983). Mechanical aspects of mesenchymal morphogenesis. *J. Embryol. exp. Morph.* **78**, 83-125.

Oster, G.F., Murray, J.D., Maini, P.K. (1985). A model for chondrogenic condensations in the developing limb: the role of the extracellular matrix and cell tractions. *J. Embryol. exp. Morph.* **89**, 93–112.

Oster, G.F., Odell, G.M. (1984). The mechanochemistry of cytogels. *Physica* **12D**, 333–350.

Pearson, M., Elsdale, T. (1979). Somitogenesis in amphibian embryos. I. Experimental evidence for an interaction between two temporal factors in the specification of the somite pattern. *J. Embryol. exp. Morph.* **51**, 27-50.

Perelson, A.S., Maini, P.K., Murray, J.D., Hyman, J.M., Oster, G.F. (1986). Nonlinear pattern selection in a mechanochemical model for morphogenesis. *J. Math. Biol.* **24**, 525–541.

Petris, S. De. Raff, M.C. (1973). Fluidity of the plasma membrane and its implications for cell movement. In: *Locomotion of Tissue Cells*, Ciba Foundation Symposium 14 (new series) (eds. R. Porter & D.W. Fitzsimons), 27–52, Amsterdam: Elsevier (North Holland).

Petrov, K., Beloussov, L.V. (1984). The kinetics of contact polarization of

the cells in the induced tissues of amphibian embryos. *Ontogenes (Sov. J. dev. Biol.)* **15**, 643.

Plickert, G. (1980). Mechanically induced stolon branching in *Eirene Viridula* (*Thecata, Campanulinidau*). In: *Development and Cellular Biology of Coelenterates.* (eds. P. Tardent & R. Tardent), 185–190, Amsterdam: Elsevier (North Holland).

Purcell, E. (1977). Life at low Reynolds number. *Americ. J. Phys.* **45**, 1–11.

Rawles, M. (1963). Tissue interactions in scale and feather development as studied in dermal epidermal recombinations. *J. Embryol. exp. Morph.* **11**, 765–789.

Richtmyer, R.D., Morton, K.W. (1967). *Difference methods for initial value problems.* New York: Interscience Publishers.

Saxén, L., Lehtonen, E., Karkinen-Jääskeläinen, M., Nordling, S., Wartiovaara, J. (1976). Are morphogenetic tissue interactions mediated by transmissible signal substances or through cell contacts? *Nature 259*, 662–663.

Segel, L.A., Slemrod, M. (1989). The quasi-steady-state assumption: A case study in perturbation. *SIAM Review* **31(3)**, 446–477.

Sengel, P. (1976). *Morphogenesis of Skin.* Cambridge: Cambridge University Press.

Sengel, P., Mauger, A., Robert, J., Kieny, M. (1985). Extracellular matrix in skin morphogenesis. In: *Molecular Determinants of Animal Form.* UCLA Symposia on Molecular and Cellular Biology. (new series), vol. 31 (ed. G.M. Edelman), 319-347, New York: Alan R. Liss, Inc.

Shaw, L.J., Murray, J.D. (1990). Model for complex skin patterns. *SIAM J. Appl. Math.* **50(2)**, 628–648.

Sheetz, P.M., Turney, S., Qian, H., Elson, E.L. (1989). Nanometre-level

analysis demonstrates that lipid flow does not drive membrane glycoprotein movements. *Nature* **340**, 284–288.

Smith, G.D. (1985). *Numerical Solutions of Partial Differential Equations: Finite Difference Methods.* 3rd ed. Oxford: Oxford University Press.

Snyderman, R., Goetzl, E. (1981). Molecular and cellular mechanisms of leukocyte chemotaxis. *Science* **213**: 830–837.

Sternfield, J., David, C.N. (1981). Cell sorting during pattern formation in *Dictyostelium. Differentiation* **20**, 10-21.

Tickle, C., Alberts, B., Wolpert, L., Lee, J. (1982). Local application of retinoic acid to the limb bud mimics the action of the polarizing region. *Nature* **296**, 564–566.

Turing, A.M. (1952). The chemical basis of morphogenesis. *Phil. Trans. R. Soc. Lond.* **B237**, 37–72.

Walbot, V., Holder, N (1987). *Development Biology.* New York: Random House.

Wessells, N.K. (1965). Morphology and proliferation during early feather development. *Dev. Biol.* **12**, 131–153.

Wessells, N.K. (1977). *Tissue Interaction in Development.* Menlo Park: W.J. Benjamin.

Wilson, H.V. (1907). On some phenomena of coalescence and regeneration in sponges. *J. Exp. Zool.* **5**, 245-258.

Wolpert, L. (1969). Positional information and the spatial pattern of cellular differentiation. *J. theor. Biol.* **25**, 1–47.

Wolpert, L. (1971). Positional information and pattern formation. *Curr. Top. Dev. Biol.* **6**, 183–224.

Wolpert, L. (1981). Positional information and pattern formation. *Phil. Trans. Roy. Soc. Lond.* **B295**, 441–450.

Zeeman, E.C. (1974). Primary and secondary waves in developmental biology. *Lectures in Mathematics in the Life Sciences* **4**, 69–161, Rhode Island: American Mathematical Society.

Zigmond, S.H. (1978). Chemotaxis by polymorphonuclear leukocytes. *J. Cell Biol.* **77**, 269-287.

Zigmond, S.H. (1989). Cell locomotion and chemotaxis. *Curr. Op. Cell Biol.* **1**, 80–86.